Light Higgsinos at the ILC:
Precision Measurements and Detector Requirements

Dissertation

with the aim of achieving a doctoral degree

at the Faculty of Mathematics, Informatics and Natural Sciences

Department of Physics

of Universität Hamburg

submitted by

Hale Sert

2015 in Hamburg

Day of oral defense: 26.11.2015

The following evaluators recommend the admission of the dissertation:

Name : Dr. Jenny List

Name : Prof. Dr. Gudrid Moortgat-Pick

To my Family

Abstract

This thesis is based on a study of Natural Supersymmetry (SUSY) scenarios at the International Linear Collider (ILC). These scenarios are motivated by naturalness, which requires the μ parameter to be at the electroweak scale. The considered Natural SUSY scenario contains three light higgsino-like charginos and neutralinos, $\widetilde{\chi}_1^{\pm}, \widetilde{\chi}_1^0$ and $\widetilde{\chi}_2^0$, with a mass splitting of a few GeV or even sub-GeV, while all other supersymmetric particles are heavy in the multi-TeV scale. Due to the small mass difference of a few GeV, the final state consists of a large missing energy and a few very soft visible particles. Therefore, the analysis of such scenarios is extremely challenging for the LHC as well as the ILC.

In order to investigate the feasibility of observing light higgsinos at the ILC, an analysis has been performed using both fast detector simulation and full detector simulation for International Large Detector (ILD). The fast simulation results have indicated that the key observables of the higgsinos can be reconstructed with an uncertainty of a few percent. It has been shown that the results enable determining the lower limits and allowed regions for the mass parameters of the bino M_1 and the wino M_2, as well as determining the higgsino mass parameter μ to the accuracy of a few percent. The full simulation analysis has provided information about detector requirements, such as the identification of low momentum electrons and muons. The electron identification can be studied by using the ionisation energy loss of the particles per length, dE/dx, which can be obtained from the Time Projection Chamber (TPC) of ILD. The identification of low momentum muons has been studied in the context of the thesis by using the calorimeter cluster shape differences between muons and pions. As a result, a method has been developed for particles with momentum lower than 2 GeV, and its impact on the higgsino analysis has been investigated. It has been found that assuming the electrons can be identified with the same efficiency as the muons, the key observables can be reconstructed with the same precision as in the fast simulation case by taking two times more data.

The presence of soft final-state particles makes the tracking of high relevance for the analysis. Therefore, a comprehensive hardware study related to the TPC of ILD has been performed. In this study, three commonly used gas mixtures have been investigated in a small gas chamber containing a triple Gas Electron Multiplier stack, and their performance has been compared. This study has enhanced the understanding of the dependency of the charge transfer on the gas type. It has confirmed that the gas proposed to be used in the TPC is the most promising one.

Zusammenfassung

Diese Arbeit basiert auf einer Untersuchung von Natürlichen Supersymmetrie-Szenarien am International Linear Collider (ILC). Diese Szenarien sind durch Natürlichkeit motiviert, für welche es erforderlich ist, dass der μ-Parameter im Bereich der elektroschwachen Skala liegt. Das betrachtete Szenario enthält drei leichte Higgsino-artige Charginos und Neutralinos, $\widetilde{\chi}_1^\pm, \widetilde{\chi}_1^0$ und $\widetilde{\chi}_2^0$, mit einer Massenaufspaltung von wenigen GeV oder sogar weniger als einem GeV, während alle anderen supersymmetrischen Teilchen schwer sind und in der Größenordnung von mehreren TeV liegen. Aufgrund des geringen Massenunterschieds von wenigen GeV bestehen die Endzustände aus großer fehlender Energie und wenigen sehr niederenergetischen sichtbaren Teilchen zusammen mit einem harten Anfangszuslandsstrahlungs Photon. Dadurch stellt die Analyse sowohl am LHC wie auch am ILC eine Herausforderung dar.

Um zu untersuchen, ob die Beobachtung von leichten Higgsinos am ILC möglich ist, wurde eine Analyse durchgeführt, wofür sowohl schnelle Detektorsimulation als auch volle Detektorsimulation für den International Large Detector (ILD) genutzt wurden. Die Ergebnisse der schnellen Simulation haben zu erkennen gegeben, dass die Hauptobservablen der Higgsinos mit einer Unsicherheit von einigen Prozent rekonstruiert werden können. Es wurde gezeigt, dass die Ergebnisse es ermöglichen, die Untergrenzen und die erlaubten Regionen der Massenparameter des Binos M_1 und des Winos M_2 sowie den Higgsino-Massenparameter μ mit einer Genauigkeit von einigen Prozent zu bestimmen. Die Analyse mit der vollen Simulation hat Hinweise über Detektoranforderungen geliefert, wie die Identifizierung von Elektronen und Myonen mit niedrigem Impuls. Die Elektronidentifizierung kann untersucht werden, indem der Ionisationsenergieverlust pro Länge, dE/dx, genutzt wird. Dieser kann von der Zeitprojektionskammer (time projection chamber - TPC) des ILD gemessen werden. Die Identifizierung von Myonen mit niedrigem Impuls wurde im Rahmen dieser Arbeit untersucht, indem die Unterschiede der Clusterform im Kalorimeter zwischen Myonen und Pionen genutzt wurden. Als Ergebnis wurde eine Methode für Teilchen mit einem Impuls kleiner als $2\,\text{GeV}$ entwickelt. Ihr Einfluss auf die Higgsino-Analyse wurde untersucht. Unter der Annahme, dass die Elektronen mit derselben Effizienz identifiziert werden können wie die Myonen, wurde herausgefunden, dass die Hauptobservablen mit derselben Genauigkeit wie im Fall der schnellen Simulation rekonstruiert werden können, indem die doppelte Datenmenge genommen wird.

Durch das Vorhandensein der niederenergetischen Teilchen erhält die Spurrekonstruktion eine hohe Relevanz für die Analyse. Daher wurde eine umfassende Hardware-Studie im Zusammenhang mit der ILD-TPC durchgeführt. In dieser Studie wurden drei geeignete Gasgemische untersucht, und ihre Leistung wurde verglichen. Dazu wurde ein Testaufbau mit einem dreifachen Stapel von Gas-Elektronen-Vervielfachern genutzt. Diese Studie hat das Verständnis der Abhängigkeit des Ladungstransfers vom Messgas verbessert und hat bestätigt, dass das für die Nutzung in der TPC vorgesehene Gas vielversprechend ist.

Contents

Chapter 1

Introduction

The discovery of the Higgs boson with a mass of around $125\,\mathrm{GeV}$, which was made by the Large Hadron Collider (LHC) experiments in 2012, was a milestone in particle physics. With the discovery of the only missing particle of the Standard Model (SM), one could consider the SM to be complete. However, there are still open questions that cannot be explained with the known theory of the SM, but require new physics beyond the SM. One of the crucial puzzles of the SM, which is known as the hierarchy problem, is the quadratic divergence stemming from the radiative contributions to the Higgs boson mass due to interactions of the Higgs boson with the other particles, especially with the top quark due to its large Yukawa coupling ($y_t \approx 1$). Supersymmetry (SUSY) is one of the proposed theories which suppresses the quadratic divergence by introducing a superpartner for each particle with a difference in spin of one half such that the Higgs boson mass can be obtained naturally without introducing a large amount of fine-tuning.

In order to solve the hierarchy problem, SUSY requires the masses of the superpartners to be as close as possible to the mass of their SM partners to prevent regeneration of the divergence, in particular the scalar partners of the top quarks (stops) and the superpartners of the gluons (gluinos). The stops play a crucial role at one-loop level, since they have a dominant contribution to the Higgs mass due to their large Yukawa coupling. At two-loop level, the gluinos become important since they have strong couplings to the top quarks and scalar top quarks. In addition, the masses of the Z boson and of the higgsino-like gauginos have to be of the same order to avoid large fine-tuning in the mass of the Z boson. Such scenarios are called Natural SUSY. Since the LHC experiments have not found any hints of supersymmetric particles, in particular in the searches for stops and gluinos, one can conclude that the coloured spectrum of the SUSY should be rather heavy, around the TeV scale. However, a light electroweak SUSY sector as demanded by the naturalness of the Z boson mass could be still available including a SM-like Higgs boson with a mass compatible with the value measured at the LHC. These theoretical and experimental facts motivate scenarios with light higgsinos at the electroweak scale and heavy stops with a mass of a few TeV where all other particles are so heavy that they are above the currently experimentally observable region.

Such a scenario with light higgsinos, which are naturally mass degenerate, has been studied

in this thesis. If all other SUSY particles are heavy, the mass splittings of the higgsino-like charginos and neutralinos, $\widetilde{\chi}_1^\pm$, $\widetilde{\chi}_1^0$ and $\widetilde{\chi}_2^0$, can be as small as a few GeV or even less than a GeV. The presence of almost mass degenerate higgsinos causes a signature of very soft final state particles and a large missing energy. Therefore the analysis of such scenarios are extremely challenging for the LHC.

The International Linear Collider (ILC), which is a planned future electron-positron collider, would provide the possibility to search for such light and almost mass degenerate higgsinos. The ILC is designed to run at centre-of-mass energies of 200-500 GeV with an option to upgrade to 1 TeV. Due to the type of the colliding particles, it has a well-determined initial energy, democratic production of the particles and very clean final states. These provide an opportunity to measure each particle created in the collision, even those with very low momentum. The ILC has also the capability of having polarised beams which can be very useful especially for searches for new physics by suppressing the SM background and by providing information about the couplings of the higgsinos. With these features, scenarios including light higgsinos with small mass differences could be well observable at the ILC.

At a lepton collider, the light higgsinos can be produced in two processes, $e^+e^- \to \widetilde{\chi}_1^+ \widetilde{\chi}_1^- \gamma$ and $e^+e^- \to \widetilde{\chi}_1^0 \widetilde{\chi}_2^0 \gamma$ via dominantly Z boson or γ exchange in the s-channel. The lightest chargino and the heavier neutralino decay to the lightest supersymmetric particle $\widetilde{\chi}_1^0$ and off-shell W and Z bosons with $\widetilde{\chi}_1^\pm \to W^{*\pm} \widetilde{\chi}_1^0$ and $\widetilde{\chi}_2^0 \to Z^{*0} \widetilde{\chi}_1^0$, and in addition the heavier neutralino decays radiatively to $\widetilde{\chi}_2^0 \to \gamma \widetilde{\chi}_1^0$ with a large branching ratio. The hard initial state radiation (ISR) photon is required to distinguish the signal events from one of the dominant Standard Model background events stemming from the interaction of the beams. To distinguish these two signal processes, exclusive decay modes, which are the semi-leptonic decay modes of the chargino process and radiatively decays to a photon of the neutralino process have been considered.

In order to investigate whether light and nearly mass degenerate higgsinos could be observable at the ILC, as a first step an analysis has been performed using a fast detector simulation at the ILD detector. The fast simulation considers perfect particle identification, and does not include the low p_t $\gamma\gamma$ overlay and pair background which are arising from the beam-beam interaction at the ILC. Therefore, to investigate whether the analysis of such scenarios could be performed in a real experiment when the simplifications are taken into account, and to determine the detector requirements that would be needed, in a second step the analysis has been conducted in full simulation. The particle identification of low momentum particles, such as electron and muon identification, is one of the crucial requirements. In the context of this thesis, a method has been developed to identify muons with momentum lower than 2 GeV. The fast simulation part of the thesis was published in [1, 2].

The considered Natural SUSY scenarios have the signature of very soft particles with momentum below a few GeV, therefore the tracking performance for such soft particles is very important for the analysis of such scenarios. Especially, the tracking in the central tracking system, the Time Projection Chamber (TPC), of ILD is crucial since it provides information about dE/dx, which is needed for the low momentum electron identification. The TPC consists of a gas filled volume, in which the gas molecules are ionised when a charged particle goes though the sensitive

volume. In order to have a sufficient signal, the primary electrons from the ionisation should be amplified in the endplate of the TPC by using for example a Gas Electron Multiplier (GEM). In general, more than one GEM is used to provide sufficient amplification. Due to the geometrical structure of the GEMs, the particles arriving at the GEM are not transferred completely to the amplification region of the GEM, and also the transfer of the particles from the amplification region to the other side of the GEM is not 100% efficient. These transfers of the particles can be described by the so-called charge transfer coefficients. They could be influenced by the components of the gas mixtures, thus the determination of the charge transfer coefficients for different gas mixtures is crucial. For this reason, a study has been performed to enhance the understanding of the dependency of the charge transfer coefficients on the type of gas mixture by investigating three possible gases commonly considered for the ILD TPC in a small gas chamber containing a triple GEM stack.

The content of this thesis is structured as follows:

In Chapter 2, the theoretical foundations of this thesis will be introduced and the status of LHC SUSY searches will be discussed. In Chapter 3, an overview of the ILC will be given including the advantages of lepton colliders, the physics program of the ILC, and the challenging SM backgrounds. In Chapter 4, the ILD detector and the concept of particle flow reconstruction will be introduced.

The study of Natural SUSY scenarios at the ILC will be detailed in Chapters 5 to 7. In Chapter 5, the studied two benchmark points will be introduced, and the signal topology as well as the key method to distinguish it from background will be discussed. In Chapter 6, the fast simulation studies to measure the precision of the key observables will be explained for the considered benchmark points. In Chapter 7, the feasibility of the analysis, the experimental challenges and the resulting requirements on the detector design will be discussed. In Chapter 8, the measurements of charge transfer coefficiencts for the ILD TPC will be covered. The conclusions drawn from this thesis will be explained in Chapter 9.

Chapter 2

Theoretical Foundations

The Standard Model of particle physics, which was proposed by Sheldon Glashow [3], Steven Weinberg [4] and Abdus Salam [5] in 1960s, is the fundamental theory which describes the elementary matter particles that we know today and their interactions successfully. In this chapter, the theoretical background of this thesis is covered. In Section 2.1, the Standard Model will be described including its gauge symmetry as well as the electroweak symmetry breaking which explains the mass of the particles. Then the problems of the Standard Model which motivate the extension of the theory will be summarised. In Section 2.2, one of the proposed theories for extensions of the Standard Model, Supersymmetry (SUSY), will be discussed. The chapter will finish with a discussion of the status of SUSY at the LHC in Section 2.3.

2.1 The Standard Model of Particle Physics

The Standard Model (SM) consists of twelve fundamental matter particles with spin 1/2, called *fermions*, listed in Table 2.1. These fundamental matter particles are classified into two groups with six particles, called *leptons* and *quarks*. Both leptons and quarks are grouped in three generations with respect to their mass, which is the only property differing between generations. Apart from the neutrinos, the first generation particles are the lightest ones, and only these first generation particles, e.g. e, u and d quarks, constitute ordinary matter. The second and third generation fermions are heavier and unstable, therefore they decay to the lightest particles. The neutrinos were thought to be massless until recently, therefore neutrinos are assumed to be massless in the SM. However, the Super-Kamiokande experiment found evidence for neutrino mass, which is very small (at least nine orders of magnitude lighter than other fermions [6]), by studying the oscillations of the atmospheric neutrinos produced by cosmic ray interactions in 1998 [7]. The leptons exist as free particles, however the quarks, which carry fractional charges, can exist only in combinations of three quarks or a quark and an antiquark, such as proton($p - uud$) and pion($\pi^+ - u\bar{d}$). Another important property of quarks is that each flavour carries three different colours. With the help of this property, the sum of the charges of all the fundamental matter particles becomes zero which is the necessary condition to have an anomaly free theory fulfilling $Tr(Q) = 0$ (for more details see Section 2.1.1.3).

Fermions	Generation	Name		Charge ($q/|e|$)	Mass (GeV)	Flavour
	1st	e neutrino	ν_e	0	$< 10^{-9}$	$L_e = +1$
		electron	e	-1	0.0005	$L_e = +1$
Leptons	2nd	μ neutrino	ν_μ	0	$< 10^{-9}$	$L_\mu = +1$
		muon	μ	-1	0.106	$L_\mu = +1$
	3rd	τ neutrino	ν_τ	0	$< 10^{-9}$	$L_\tau = +1$
		tau	τ	-1	1.70	$L_\tau = +1$
	1st	up	u	$+\frac{2}{3}$	0.003	$--$
		down	d	$-\frac{1}{3}$	0.005	$--$
Quarks	2nd	charm	c	$+\frac{2}{3}$	0.1	$C = +1$
		strange	s	$-\frac{1}{3}$	1.3	$S = -1$
	3rd	top	t	$+\frac{2}{3}$	174	$T = +1$
		bottom	b	$-\frac{1}{3}$	4.5	$B = -1$

Table 2.1 The fundamental fermions of the SM. All neutrinos and the electron are stable particles, while the rest decays to lighter particles. Each particle has an antiparticle with opposite charge. They are denoted with a bar generally.

The fundamental fermions are described by the Dirac equation [8], which concludes that for each fundamental particle an antiparticle exists with the same mass, but with the opposite sign of all additive quantum numbers. The Dirac equation [9] is

$$E\psi = (\vec{\alpha} \cdot \vec{p} + \beta m)\psi \tag{2.1}$$

where E and $\vec{p}$ are the energy and momentum operators, ψ is a four component wave function, called spinor, which represents both a fermion and its anti-fermion with two spin substates for each. σ and β are 4×4 matrices and can be given in the Dirac-Pauli representation as follows:

$$\vec{\alpha} = \begin{pmatrix} 0 & \vec{\sigma} \\ \vec{\sigma} & 0 \end{pmatrix} \quad \text{and} \quad \beta = \begin{pmatrix} I & 0 \\ 0 & -I \end{pmatrix} \tag{2.2}$$

where $\vec{\sigma}$ denotes the Pauli spin vector which consist of three 2×2 matrices (cf. Appendix A), and I denotes the 2×2 unit matrix.

In high energy physics experiments, since the centre-of-mass energy is much larger than the mass of the particles, the mass of the light particles can be assumed to be relatively small. In the limit $E \gg m$, the Dirac equation becomes much simpler, and it can be represented in terms of two-component wave functions:

$$E\chi = -\vec{\sigma} \cdot \vec{p}\chi \tag{2.3}$$

$$E\phi = +\vec{\sigma} \cdot \vec{p}\phi. \tag{2.4}$$

Since the energy of a massless fermion is $E = |\vec{p}|$ in the case of positive energy, Eq. (2.3) becomes:

$$\frac{\vec{\sigma} \cdot \vec{p}}{|\vec{p}|}\chi = -\chi \ , \quad \text{helicity:} \quad h = \frac{\vec{\sigma} \cdot \vec{p}}{|\vec{p}|} = -1 \tag{2.5}$$

From the first equation one can define a quantity, called *helicity*. Helicity is a measure of the sign of the spin calculated by taking the projection of the spin vector onto the direction of momentum. Helicity can be either $h = -1$ or $h = +1$, which correspond to left-handed (LH) and right handed (RH) particles for massless particles, respectively. For anti-particles, one needs to consider negative energy case, which will give $h = +1$ meaning that the antiparticle will be right-handed. To summarise, Eq. (2.3) corresponds to a left-handed particle or right-handed antiparticle.

For massless particles, helicity is a quantity which is Lorentz invariant, while for massive particles it is not. The *chirality*, which has the same meaning as the helicity in case of massless particles, is a Lorentz invariant quantity independent of the particle mass. It represents the eigenvalues of the γ_5 matrices (cf. Appendix A). The eigenstates of the γ_5 matrix are defined as left-handed and right-handed *chiral states*, which are denoted with L and R subscripts. The left-handed and right-handed component of a field transform differently under gauge transformations, therefore the chirality is an important structure for the SM. Any Dirac spinor ψ can be written as a combination of left-handed and right-handed chiral states as follows;

$$\psi = \psi_R + \psi_L = P_R\psi + P_L\psi \tag{2.6}$$

where P_R and P_L are the projection operators, that project out chiral states:

$$P_R = \frac{1 + \gamma_5}{2} \quad \text{and} \quad P_L = \frac{1 - \gamma_5}{2} \ . \tag{2.7}$$

For massive particles, the left-handed and right-handed chiral states will be mixed with each other, while the massless particles can have either left-handed or right-handed chiral states.

All fundamental particles except neutrinos can have either left-handed or right-handed chiral states. However, neutrinos are completely longitudinally polarised. They exist only in the left-handed chiral state ν_L, while its antiparticle is right handed $\bar{\nu}_R$. Such pure chiral states can only be possible in the case of massless particles. Since neutrinos are considered as massless in the Standard Model, it is not surprising to have only ν_L and $\bar{\nu}_R$. This property is approximately valid for neutrinos with very small mass.

There are four types of fundamental interactions between the fundamental matter particles. The interactions are described as the exchange of a mediator particle. All the forces and mediators are listed in Table 2.2. Even though all particles feel the gravitational interaction between two individual particles, the interaction is extremely small especially at the level of particle physics, and it is not included in the SM. The weak force is experienced by all the fundamental matter particles. This means that all particles interact with others via the weak interaction by the exchange of W and Z bosons. The neutrinos, which are neutral, do not feel the electromagnetic interaction, but other particles do, and they interact with the exchange of a photon (γ). Like the

Interaction	Relative Strength	Mediator Boson		Spin/Parity	Mass(GeV)
Strong	1	Gluon	g	1^-	0
Electromagnetism	10^{-3}	Photon	γ	1^-	0
Weak	10^{-8}	W boson	W	1^-	80.4
		Z boson	Z	1^+	91.2
Gravity	10^{-37}	Graviton	G	2^+	0

Table 2.2 The fundamental interactions of the SM, including their relative strength, spin/parity and mass as well as the mediator boson of the interactions.

electromagnetic force, strong force is also experienced depending on the charge of the particles, which is colour charge in this case. Since only quarks have colour charge, only quarks interact with the strong interactions via the exchange of gluons.

In the interactions, most of the quantum numbers are conserved. Some of them which present the flavour of the particles are listed in Table 2.1. For leptons, they are called *lepton flavour number*, L_e, L_μ and L_τ, which are $L_i = +1$ for leptons, and $L_i = -1$ for anti-leptons. For quarks, they are called *quark flavour number*, C, S, T and B, which are $C = T = +1$ and $S = B = -1$ for quarks, whereas anti-quarks have opposite sign of these quantum numbers. In each interaction these quantum numbers should be conserved with one exception. In the case of quarks, when they interact via the weak interaction, quarks may change the flavour by fulfilling for example $\Delta C = \pm 1$.

The Standard Model is a *gauge theory* which expresses the SM in terms of gauge groups:

$$SU(3)_C \otimes SU(2)_L \otimes U(1)_Y \tag{2.8}$$

where each group has corresponding gauge fields which carry the properties of their group. The number of the generators gives the number of the fields in each group. Each symmetry group is represented by a charge; hypercharge, weak isospin and color for $U(1)_Y$, $SU(2)_L$, and $SU(3)_C$ in turn. These properties are given in Table 2.3. The $SU(2)_L \otimes U(1)_Y$ part of the SM, which is called the *electroweak sector*, explains the interaction of the fundamental particles, while the quantum chromodynamics part $SU(3)_C$ defines the interaction between quarks and gluons. The electroweak sector is invariant under $SU(2)_L \otimes U(1)_Y$ symmetry, the combination of weak and electromagnetic interactions. Due to the properties of the $U(1)$ abelian and $SU(2)$ non-abelian groups, the particles in the SM are written in terms of doublets (weak-isospin), and singlets:

$$\psi_e^L = \begin{pmatrix} \nu_e \\ e^- \end{pmatrix}_L, \quad \psi_\mu^L = \begin{pmatrix} \nu_\mu \\ \mu^- \end{pmatrix}_L, \quad \psi_\tau^L = \begin{pmatrix} \nu_\tau \\ \tau^- \end{pmatrix}_L \quad \text{and} \quad e_R^-, \ \mu_R^-, \ \tau_R^-, \tag{2.9}$$

$$\psi_u^L = \begin{pmatrix} u \\ d \end{pmatrix}_L, \quad \psi_c^L = \begin{pmatrix} c \\ s \end{pmatrix}_L, \quad \psi_t^L = \begin{pmatrix} t \\ b \end{pmatrix}_L \quad \text{and} \quad u_R, \ c_R, \ t_R, \ d_R, \ s_R, \ b_R. \tag{2.10}$$

Gauge Groups	Number of Generators	Gauge Fields	Gauge Bosons	Charges
$U(1)_Y$	$n^2 = 1$	B_μ	$A_\mu \equiv \gamma$	Hypercharge
$SU(2)_L$	$n^2 - 1 = 3$	$W_\mu^i, i = 1, 2, 3$	$W^\pm, Z^0$	Weak isospin
$SU(3)_C$	$n^2 - 1 = 8$	$G_\mu^a, a = 1, 2..., 8$	g^a	Color

Table 2.3 Properties of the Gauge Groups

Within these particles, only the left-handed particles participate in the charged current weak interactions. For example, the e_L^- interacts with $\nu_{e,L}$ via the exchange of a W boson. The left-handed states are invariant under both $U(1)_Y$ and $SU(2)_L$ gauge symmetries. However, the right-handed particles are only invariant under $U(1)_Y$ symmetry. Therefore, the left-handed and right-handed states of the particles transform differently under gauge transformations. The absence of the right-handed neutrinos can be seen from Eq. (2.9).

As each symmetry does, the $U(1)_Y$ and $SU(2)_L$ symmetries carry charges which are hypercharge (Y) and third component of weak isospin (T^3). These two charges were found to be related to the electromagnetic charge (Q) by Kazuhiko Nishijima and Tadao Nakano [10] in 1953 and independently by Murray Gell-Mann [11] after three years, as follows:

$$Q = T_3 + \frac{1}{2}Y. \tag{2.11}$$

which is called Gell-Mann-Nishijima relation. The charges Q, T_3 and Y are known as the generators of the corresponding groups.

2.1.1 Gauge Symmetry

As a consequences of Noether's theorem [12], each continuous symmetry transformation requires a conservation law. Not only external symmetry transformations such as translation and rotation, but also internal symmetry transformations obey this theory. The internal symmetry transformations responsible for the existence of the fundamental forces are gauge symmetries. The invariance under global gauge/phase transformations requires a conserved current which proves the conservation of charge. However, the Lagrangian of a free fermion is not invariant under local gauge transformations. In order to regain the local gauge invariance, constraints are required and they play an important role in the theory of the interactions. All fundamental interactions mainly arise due to these constraints. In the following sections, details about these transformations will be given.

2.1.1.1 Global and Local Gauge Invariance

Gauge invariance can be studied for several symmetry groups. For the Standard Model, one needs to study the invariance under both the abelian group $U(1)_Y$, and the non-abelian $SU(2)_L$ and $SU(3)_C$ groups. In an abelian group, the multiplication of two different elements of the

groups is commutative, while it is not for non-abelian groups because the generators of these groups are non-commutative. In the following, gauge invariances will be explained by first considering only an abelian group $U(1)$ symmetries, and then by considering only a non-abelian group $SU(2)$ symmetries.

Abelian Gauge Invariance

The Dirac Lagrangian density for a free fermion, which is a complex field, is given [13] by

$$\mathcal{L} = i\overline{\psi}(x)\gamma^{\mu}\partial_{\mu}\psi(x) - m\overline{\psi}(x)\psi(x). \tag{2.12}$$

where $\psi(x)$ denotes a Dirac spinor, and γ^{μ} are gamma matrices for $\mu = 0, 1, 2, 3$ as described in Appendix A. They can be represented in terms of $\vec{\alpha}$ and β matrices: $\gamma^{0} = \beta$, and $\gamma^{i} = \alpha^{i}\beta$ with $i = 1, 2, 3$.

The global phase transformation for an abelian $U(1)_Y$ symmetry states that the fermion fields should transform as:

$$\psi \rightarrow e^{igY\theta}\psi \tag{2.13}$$

where Y represent the generator of the corresponding gauge group which is hypercharge, g is the coupling constant and θ is a real constant called "phase" or "gauge". Since

$$\partial_{\mu}\psi(x) \rightarrow e^{igY\theta}\partial_{\mu}\psi(x), \tag{2.14}$$
$$\overline{\psi}(x) \rightarrow e^{-igY\theta}\overline{\psi}(x), \tag{2.15}$$

the Lagrangian in Eq. (2.12) is invariant under the global phase transformation, which gives rise to a conserved current in the form of $J_{\mu} = -gY\overline{\psi}(x)\gamma^{\mu}\psi(x)$. This can be found by considering an infinitesimal $U(1)$ phase transformation, and studying the invariance of Lagrangian under this transformation (see [13] for the derivation).

In case of *the local gauge transformation*, the transformation of a free fermion field with a phase changing as a function of the position is given by

$$\psi \rightarrow e^{igY\theta(x)}\psi. \tag{2.16}$$

The following quantities transform as:

$$\partial_{\mu}\psi(x) \rightarrow e^{igY\theta(x)}\partial_{\mu}\psi(x) + igY\psi(x)\partial_{\mu}\theta(x) \tag{2.17}$$
$$\overline{\psi}(x) \rightarrow e^{-igY\theta(x)}\overline{\psi}(x) \tag{2.18}$$

which result in that the Lagrangian is not invariant because of the additional term including $\partial_{\mu}\theta(x)$. However, the invariance of the Lagrangian can be regained by introducing a vector field (gauge field), B_{μ}. Since this field corresponds to a $U(1)$ symmetry group, the partial derivative can be replaced with the following covariant derivative:

$$D_{\mu} = \partial_{\mu} + igYB_{\mu} \qquad \text{for electron } Y = -1 \tag{2.19}$$

where g and Y are the coupling constant and hypercharge (generator) of the $U(1)_Y$ symmetry group. The vector field B_μ transforms under the phase transformation as:

$$B_\mu \rightarrow B_\mu + \frac{1}{g}\partial_\mu\theta(x). \tag{2.20}$$

Considering these replacements and transformations, the Lagrangian in (2.12) becomes invariant under the local gauge transformation. The kinetic energy term of the introduced gauge field, which is also invariant, should be added to the Lagrangian as well. Then, the Lagrangian is written as:

$$\mathcal{L} = i\overline{\psi}(x)\gamma^\mu D_\mu\psi(x) - m\overline{\psi}(x)\psi(x) - \frac{1}{4}B^{\mu\nu}B_{\mu\nu} \tag{2.21}$$

where $B_{\mu\nu}$ represents the field strength tensor of the $U(1)$ symmetry group,

$$B_{\mu\nu} = \partial_\mu B_\nu - \partial_\nu B_\mu. \tag{2.22}$$

However, the mass term of the gauge field B_μ, which is $\frac{1}{2}m_B^2 B_\mu B^\mu$, is not invariant under the local gauge transformation, therefore it is forbidden by the local invariance. From this it can be interpreted that the local gauge transformation introduces an electromagnetic interaction which has a massless boson responsible for the interaction. Expanding the covariant derivative,

$$\mathcal{L} = i\overline{\psi}(x)\gamma^\mu\partial_\mu\psi(x) - m\overline{\psi}(x)\psi(x) + gY\overline{\psi}(x)\gamma^\mu\psi(x)B_\mu - \frac{1}{4}B^{\mu\nu}B_{\mu\nu} \tag{2.23}$$

which contains the interaction term of the introduced gauge field with the fermions, where the term $gY\overline{\psi}(x)\gamma^\mu\psi(x)$ can interpreted as a conserved current $J_\mu = -gY\overline{\psi}(x)\gamma^\mu\psi(x)$, since it has the same structure as the current obtained from the global phase invariance.

Non-Abelian Gauge Invariance

Non-abelian gauge symmetries constitute the so-called Yang-Mills theories proposed by Chen Ning Yang and Robert Mills [14]. They are an extension of the abelian gauge invariance concept to the non-abelian symmetries.

In the $SU(2)_L$ case, since there are three gauge fields, three massless gauge bosons will arise after the transformation, while the $SU(3)_C$ group has eight gauge fields. In addition, the mentioned property of the non-abelian groups will give rise to interactions between the gauge bosons which are the mediators of the corresponding gauge fields.

The local gauge transformation transforms the fermion field and its derivative as:

$$\psi \rightarrow e^{ig_w\vec{T}\cdot\vec{\theta}(x)}\psi\,, \tag{2.24}$$

$$\partial_\mu\psi \rightarrow e^{ig_w\vec{T}\cdot\vec{\theta}(x)}\partial_\mu\psi + \psi\partial_\mu(e^{ig_w\vec{T}\cdot\vec{\theta}(x)})\,, \tag{2.25}$$

where $\vec{T}$ are the generators of $SU(2)$ symmetry group which are the Pauli matrices, $T_i = \sigma_i/2$. In order to make the Lagrangian invariant, the gauge-covariant derivative is introduced,

$$D_\mu = I\partial_\mu + ig_w T_i W_\mu^i \tag{2.26}$$

where I is the 2×2 unit matrix, g_w and W_μ^i denote the coupling constant and the gauge fields of the corresponding interaction respectively. The generators in the non-abelian gauge groups are not commutative, and the relation between them is given by

$$[T^i, T^j] = i\varepsilon_{ijk}T^k. \tag{2.27}$$

Here ε_{ijk} is the antisymmetric Levi-Civita symbol[1] which is also known as the structure constant of the group. In this case, the gauge fields transform as

$$W_\mu^i \rightarrow W_\mu^i + \varepsilon_{ijk}\theta^j W_\mu^k + \frac{1}{g_w}\partial_\mu\theta^i \tag{2.28}$$

while the field strength tensor denoted by $W_{\mu\nu}^i$ has the following form:

$$W_{\mu\nu}^i = \partial_\mu W_\nu^i - \partial_\nu W_\mu^i - ig_w[W_\mu^j, W_\nu^k] \tag{2.29}$$

$$W_{\mu\nu}^i = \partial_\mu W_\nu^i - \partial_\nu W_\mu^i - ig_w\varepsilon_{ijk}W_\mu^j W_\nu^k \tag{2.30}$$

which is also valid in the abelian case, since the commutator vanishes. Considering all this, the Lagrangian invariant under non-abelian local gauge transformations can be obtained as follows:

$$\mathcal{L} = i\overline{\psi}(x)\gamma^\mu D_\mu\psi(x) - m\overline{\psi}(x)\psi(x) - \frac{1}{4}W_i^{\mu\nu}W_{\mu\nu}^i. \tag{2.31}$$

To see the physical consequences, it is helpful to write the covariant derivative in the explicit form:

$$\mathcal{L} = i\overline{\psi}(x)\gamma^\mu\partial_\mu\psi(x) - m\overline{\psi}(x)\psi(x) - g_w\overline{\psi}(x)\gamma^\mu T^i W_\mu^i\psi(x) - \frac{1}{4}W_i^{\mu\nu}W_{\mu\nu}^i. \tag{2.32}$$

The third term indicates the interaction of the gauge fields with the fermion field, while the last term shows the interaction of gauge fields among themselves. This last term can be rewritten considering the components of the field strength tensor as follows;

$$\frac{1}{4}W_i^{\mu\nu}W_{\mu\nu}^i \approx W_\mu^2 + W_\mu^3 + W_\mu^4. \tag{2.33}$$

Equation (2.33) represents that there are three boson and four boson interactions in the theory which arise due to the feature of the non-abelian groups.

The most important result one can conclude from the Lagrangian in Eq. (2.32) is that the mass terms of the gauge fields $\frac{1}{2}m_W^2 W_\mu W^\mu$ are forbidden because of the invariance as in the abelian gauge invariance case. However, it was experimentally observed that the gauge bosons of the weak interactions, $W^\pm$ and Z, have mass $m_W = 80.385 \pm 0.015\,\text{GeV}$, $m_Z = 91.1876 \pm 0.0021\,\text{GeV}$ [15].

The problem of the gauge boson masses is not the only mass problem, since the fermion mass terms break the invariance of the chiral symmetry. The mass term of a fermionic field

$$\mathcal{L} \approx -m\overline{\psi}(x)\psi(x) = -m(\overline{\psi}_R(x)\psi_L(x) + \overline{\psi}_L(x)\psi_R(x)) \tag{2.34}$$

---

[1] $\varepsilon_{ijk} = 1$; $\varepsilon_{jik} = -\varepsilon_{ijk} = -1$, $\varepsilon_{jki} = \varepsilon_{ijk} = 1$

depicts the breaking of chiral invariance, since the left-handed particles are doublets while the right-handed particles are singlets. However, the fermion mass problem would not be a problem in the presence of left-right symmetric theories.

These dilemmas indicate that considering invariance under local gauge symmetries is not enough to explain the full set of the observables. In order to solve these problems, a scalar field, the *Higgs field*, which interacts with the particles to give them their masses, is introduced. For that, even though the Lagrangian is invariant under gauge transformation, the vacuum state should not be invariant, meaning the existing symmetry is broken spontaneously when the scalar field acquires its value in the vacuum. In the following section, spontaneous symmetry breaking and the mechanism, which explains the interaction of the particles with the Higgs field, will be explained.

The Higgs Field

The Higgs field is a complex scalar doublet field represented by

$$\phi(x) = \begin{pmatrix} \phi^+ \\ \phi^0 \end{pmatrix}, \quad \text{with} \quad \begin{array}{l} \phi^+ \equiv (\phi_1 + i\phi_2)/\sqrt{2} \\ \phi^0 \equiv (\phi_3 + i\phi_4)/\sqrt{2}. \end{array} \tag{2.35}$$

The Lagrangian for the Higgs scalar field is written as

$$\mathcal{L}_{Higgs} = (D_\mu \phi)^\dagger (D^\mu \phi) - V(\phi) \tag{2.36}$$

where

$$V(\phi) = -\mu^2 \phi^\dagger \phi + \lambda (\phi^\dagger \phi)^4 \tag{2.37}$$

gives the potential energy term of the Higgs field, while $(D_\mu \phi)^\dagger (D^\mu \phi)$ is the kinetic term.

2.1.1.2 Spontaneous Gauge Symmetry Breaking and the Higgs Mechanism

Spontaneous symmetry breaking takes place when the Higgs potential tends to acquire its minimum value. Therefore, to investigate the symmetry breaking, the Lagrangian for scalar fields needs to be studied. Both global and local gauge symmetry breaking will be discussed in the next sections. If the spontaneous symmetry breaking is studied for global gauge invariance, it gives rise to one massive scalar (spin zero) boson, and one or more massless scalar bosons depending on the considered symmetry group, for example; one for $U(1)$, and three for $SU(2)$. These massless bosons are called *Goldstone bosons*. Local symmetry breaking scenarios will give rise to mixing terms in the Lagrangian which will require proper gauge transformations of the Higgs field, which is called *Higgs Mechanism*. This mechanism was proposed by Peter Higgs [16], Franois Englert and Robert Brout [17], and Gerald Guralnik, Carl Richard Hagen, and Tom Kibble [18]. For simplicity, the given examples in the next subsections will be for a complex singlet scalar field, which will be called "toy model".

Global Gauge Symmetry Breaking

Global gauge symmetry breaking will be studied using a toy model including a complex scalar field $\phi = \frac{1}{\sqrt{2}}(\phi_1 + i\phi_2)$. The Lagrangian which is invariant under a global phase transformation of the complex scalar field is

$$\mathcal{L} = (\partial_\mu \phi)^\dagger (\partial^\mu \phi) - \mu^2 \phi^\dagger \phi - \lambda (\phi^\dagger \phi)^2. \tag{2.38}$$

with $V(\phi) = \mu^2 \phi^\dagger \phi - \lambda(\phi^\dagger \phi)^2$ is the potential of the field, and $\lambda > 0$ in order to ensure vacuum stability. If $\mu^2 > 0$, the vacuum will correspond to $\langle \phi \rangle = 0$, and there will a scalar boson in theory with a mass μ, which has a four-boson self-coupling vertex shown in the third term of Eq. (2.38). For $\mu^2 < 0$, the situation will be explained in the following.

In order to determine the value of the field in the vacuum, in other words the vacuum expectation value of the field, the minimum value of the potential needs to be calculated. The extremum condition for $V(\phi) = \mu^2 \phi^\dagger \phi + \lambda(\phi^\dagger \phi)^2$ gives

$$\frac{\partial V}{\partial \phi} = (\phi^\dagger + \phi)(\mu^2 + 2\lambda \phi^\dagger \phi). \tag{2.39}$$

The solution of this condition, when $\partial V / \partial \phi = 0$, is

$$\phi_1^2 + \phi_2^2 = v, \quad \text{with} \quad v = \frac{-\mu^2}{\lambda} \tag{2.40}$$

which corresponds to a circle of minima of the potential in the plane ϕ_1-ϕ_2. To proceed, one can take $\langle \phi_1 \rangle = v$ and $\langle \phi_2 \rangle = 0$, and then expand the field around the vacuum by taking into account the fluctuation in both the real ϕ_1 and imaginary ϕ_2 direction denoted by $\eta(x)$ and $\xi(x)$:

$$\phi(x) = \frac{1}{\sqrt{2}} \big[v + \eta(x) + i\xi(x) \big] \tag{2.41}$$

Using this expansion, Lagrangian becomes

$$\mathcal{L} = \frac{1}{2}(\partial_\mu \eta(x))(\partial^\mu \eta(x)) + \mu^2 \eta^2(x) + \frac{1}{2}(\partial_\mu \xi(x))(\partial^\mu \xi(x)) + const + \mathcal{O}(\eta^3, \eta^4, \xi^3, \xi^4) \tag{2.42}$$

which contains a scalar boson η including both kinetic term and mass term $(-\frac{1}{2}m^2\eta^2)$ resulting in a mass $m_\eta^2 = -2\mu^2$, and a massless scalar boson ξ including only its kinetic term. The spontaneous symmetry breaking under global invariance give rise to a massive gauge boson, but it also give rise to an additional massless gauge boson. This is known as the *Goldstone theorem* originally proposed by Yoichiro Nambu for superconductivity [19] and implemented to quantum field theory by Jeffrey Goldstone, Abdus Salam, and Steven Weinberg [20]. The theorem states that each spontaneously broken continuous symmetry gives rise to a massless scalar goldstone boson. The number of goldstone bosons is related to the number of the generators of the group in question.

Local Gauge Symmetry Breaking – Higgs Mechanism

The description of the local gauge symmetry will be explained with the same toy model including a complex scalar field $\phi = \frac{1}{\sqrt{2}}(\phi_1 + i\phi_2)$. The Lagrangian which is invariant under local gauge invariant for complex scalar field can be written as:

$$\mathcal{L} = (\partial_\mu + igB_\mu)\phi^\dagger(\partial^\mu + igB^\mu)\phi - \mu^2\phi^\dagger\phi - \lambda(\phi^\dagger\phi)^2 - \frac{1}{4}B_{\mu\nu}B^{\mu\nu}. \tag{2.43}$$

For $\mu^2 < 0$, the scalar field can be expanded around the vacuum, $\phi(x) = \frac{1}{\sqrt{2}}\big[v + \eta(x) + i\xi(x)\big]$. Substituting this expansion into the Lagrangian yields a massive h and massless ξ gauge bosons

$$\mathcal{L} = \underbrace{\frac{1}{2}(\partial_\mu\eta)^2 + \mu^2\eta^2(x)}_{\text{massive scalar boson}} + \underbrace{\frac{1}{2}(\partial_\mu\xi)^2}_{\text{kinetic term}} - \underbrace{gvB_\mu\partial^\mu\xi}_{\text{mixed term}} + \underbrace{\frac{1}{2}g^2v^2B_\mu B^\mu - \frac{1}{4}B_{\mu\nu}B^{\mu\nu}}_{\text{massive gauge boson}}. \tag{2.44}$$

At first glance, it looks like the Lagrangian contains a mass term for the B_μ vector field, however an inconsistency arises between the degrees of freedom before the breaking and after the breaking. The massive field gains a longitudinal polarisation, while there is no reduction of the number of the degrees of freedom. In addition, an interaction term between B_μ and the goldstone boson ξ arises. These inconsistencies can be resolved by transforming the vector field:

$$B_\mu \rightarrow B_\mu + \frac{1}{gv}\partial_\mu\xi, \tag{2.45}$$

which is determined from the Lagrangian itself via the following relation:

$$\mathcal{L} \approx \frac{1}{2}(\partial_\mu\xi)^2 - gvB_\mu\partial^\mu\xi + \frac{1}{2}g^2v^2B_\mu B^\mu \approx \frac{g^2v^2}{2}\left(B_\mu + \frac{1}{gv}\partial_\mu\xi\right)\left(B^\mu + \frac{1}{gv}\partial^\mu\xi\right). \tag{2.46}$$

When one writes the expanded Higgs field around the vacuum state in a different form given by

$$\phi(x) \rightarrow \frac{1}{\sqrt{2}}\big[v + \eta(x) + i\xi(x)\big] = \frac{1}{\sqrt{2}}e^{i\xi(x)/v}(v + \eta), \tag{2.47}$$

the Lagrangian is acquired as follows:

$$\mathcal{L} = \underbrace{\frac{1}{2}(\partial_\mu\eta)^2 + \mu^2\eta^2}_{\text{massive scalar boson}} + \underbrace{\frac{1}{2}g^2v^2B_\mu B^\mu - \frac{1}{4}B_{\mu\nu}B^{\mu\nu}}_{\text{massive gauge boson}} + \mathcal{O}(\eta^3, \eta^4, B_\mu^2\eta, B_\mu^2\eta^2). \tag{2.48}$$

The equation shows that the massless goldstone boson is disappeared. It contains mass terms for both the vector field B_μ and the scalar field η. The degrees of freedom of the goldstone boson are transformed into the longitudinally polarised state of the massive gauge bosons. This mechanism is called the *Higgs mechanism*, and the massive scalar gauge boson can be considered as a candidate for the *Higgs boson* ($\eta \equiv h$).

The new Lagrangian which defines the $U(1)$ theory including new massive gauge bosons can be written as follows:

$$\mathcal{L} = \underbrace{i\overline{\psi}(x)\gamma^\mu D_\mu\psi(x)}_{\text{fermion kinetic term}} - \underbrace{m\overline{\psi}(x)\cdot\phi(x)\psi(x)}_{\text{fermion mass term}} - \underbrace{\frac{1}{4}F^{\mu\nu}F_{\mu\nu}}_{\text{gauge kinetic term}} + \underbrace{(D_\mu\phi)^\dagger(D^\mu\phi) - V(\phi)}_{\text{scalar boson kinetic \& potential}} \tag{2.49}$$

where $(D_\mu\phi)^\dagger (D^\mu\phi)$ is the kinetic term of the scalar complex field, while $V(\phi) = -\mu^2|\phi|^2 + \lambda|\phi|^4$ shows the potential energy term.

Since this symmetry breaking was an example for $U(1)$ symmetry group, one needs to extend this for the electroweak symmetry, $SU(2) \otimes U(1)$, which defines the Standard Model. Therefore, electroweak symmetry breaking in the SM will be discussed in the next section.

2.1.1.3   Electroweak Symmetry Breaking

The Standard Model is based on the $SU(3)_C \otimes SU(2)_L \otimes U(1)_Y$ gauge group. $SU(3)$ group is invariant under the spontaneous symmetry breaking, but the electroweak sector $SU(2) \otimes U(1)$ is a spontaneously broken symmetry. In the theory there are four gauge fields which are massless before the symmetry breaking. The spontaneous symmetry breaking will give rise to three massless Goldstone boson which will disappear with the selection of the proper gauge transformation (unitary gauge). These bosons will give their degree of freedom to the massless gauge bosons, and the three gauge bosons W^+, W^- and Z^0 will acquire masses, while the photon stays massless.

The electroweak theory before spontaneous symmetry breaking has the following Lagrangian [13]:

$$\mathcal{L}_{SU(2)\otimes U(1)} = \mathcal{L}_{fermion} + \mathcal{L}_{scalar} + \mathcal{L}_{Yukawa} + \mathcal{L}_{gauge} \tag{2.50}$$

$$
\begin{aligned}
\mathcal{L}_{fermion} &= \overline{\psi}_{\ell_L} i\gamma^\mu D_{\mu_L} \psi_{\ell_L} + \overline{\psi}_{\ell_L} i\gamma^\mu D_{\mu_R} \psi_{\ell_L} + \overline{\psi}_{q_L} i\gamma^\mu D_{\mu_L} \psi_{q_L} + \overline{\psi}_{q_R} i\gamma^\mu D_{\mu_R} \psi_{q_R} && (2.51) \\
\mathcal{L}_{scalar} &= (D_{\mu_H} H)^\dagger (D_{\mu_H} H) - V(H) && (2.52) \\
\mathcal{L}_{Yukawa} &= -y_\ell \overline{\psi}_{\ell_L} H \psi_{\ell_R} - y_d \overline{\psi}_{d_L} H \psi_{d_R} - y_u \overline{\psi}_{u_L} H_c \psi_{u_R} + h.c. && (2.53) \\
\mathcal{L}_{gauge} &= -\frac{1}{4} B_{\mu\nu} B^{\mu\nu} - \frac{1}{4} W^i_{\mu\nu} W^{i\mu\nu}. && (2.54)
\end{aligned}
$$

where the Higgs field is denoted with $H = \begin{pmatrix} H^+ \\ H^0 \end{pmatrix}$. The Higgs field can only generate the down-type leptons and quarks, since only the lower element of the doublet has the non-zero vacuum expectation value. Therefore, for the up type quarks (neutrinos are assumed to be massless), the charge conjugate of the Higgs field is used, which is given by $H_c = -i\sigma_2 H^* = \begin{pmatrix} -H^{0*} \\ H^- \end{pmatrix}$. The potential of the Higgs field is $V(H) = \mu^2 H^\dagger H + \lambda(H^\dagger H)^2$. In Eq. (2.53), $h.c.$ stands for hermitian conjugate which is applied for each term in the equation. When $\mu^2 < 0$, the Higgs field acquires a vacuum expectation value (VEV) and can be expanded around its vacuum as before:

$$H(x) = \frac{1}{2} \begin{pmatrix} 0 \\ v + \eta(x) \end{pmatrix} \qquad \text{with} \qquad \langle H^0 \rangle = \sqrt{-\frac{\mu^2}{2\lambda}} = \frac{v}{\sqrt{2}} \tag{2.55}$$

The general structure of covariant derivatives is given by

$$D_\mu = \partial_\mu + igY B_\mu + ig_w T^i W^i_\mu \tag{2.56}$$

where Y and T^i are the generators of the $U(1)_Y$ and $SU(2)_L$ groups respectively, which are hypercharge and isospin vectors of the fields. g and g_w are the coupling constants of the corresponding group. For the right-handed fermions, the third term vanishes since they do not take part in the weak interactions. Considering the covariant derivatives and the expansion of the Higgs fields, the Lagrangian in (2.52) is used to obtain the mass and couplings of the gauge bosons $W^\pm, Z, \gamma$, and the Higgs. The so-called gauge Lagrangian ($\mathcal{L}_{gauge}$) contains $B_{\mu\nu}$ and $W^i_{\mu\nu}$ which are the field strength tensors of the $U(1)_Y$ and $SU(2)_L$ gauge groups respectively. The field strength tensors are given in Eqs. (2.22) and (2.29). The gauge term gives the kinetic energies and self interactions of the gauge bosons $W^\pm, Z$ and γ. The fermion part of the Lagrangian contains the kinetic energy and interaction terms with the gauge bosons, while the mass and couplings terms to the Higgs boson are included in the Yukawa Lagrangian ($\mathcal{L}_{Yukawa}$).

The masses of the gauge bosons can be derived from the kinetic term of the Higgs field which is $(D_{\mu_H}H)^\dagger(D_{\mu_H}H)$. The first and the second weak gauge fields mix with each other and create charged W bosons $W^\pm$ of the weak interaction with a mass:

$$ m_W \;=\; \frac{g_w v}{2} \qquad\qquad \text{for} \qquad W^\pm_\mu = \frac{1}{\sqrt{2}}(W^1_\mu \mp iW^2_\mu). \tag{2.57} $$

The third gauge field of the weak interaction and the gauge field of the electromagnetic interaction mix such that the photon remains massless, while Z acquires mass. The relation of the physical mass eigenstates with the gauge eigenstates and the mass of the physical bosons are given by

$$ m_A \;=\; 0 \qquad\qquad \text{for} \qquad A_\mu = \cos\theta_W B_\mu + \sin\theta_W W^3_\mu, \tag{2.58} $$

$$ m_Z \;=\; \sqrt{g^2 + g_w^2}\,\frac{v}{2} = \frac{m_W}{\cos\theta_W} \qquad \text{for} \qquad Z_\mu = -\sin\theta_W B_\mu + \cos\theta_W W^3_\mu. \tag{2.59} $$

where the θ_W is the weak mixing angle also referred to as Weinberg angle. It follows from the requirement of the photon to remain massless ($m_A = 0$):

$$ \sin\theta_W = \frac{g_w}{\sqrt{g^2 + g_w^2}}, \qquad \cos\theta_W = \frac{g}{\sqrt{g^2 + g_w^2}}\,. \tag{2.60} $$

From the scalar Lagrangian $\mathcal{L}_{scalar}$, the Higgs boson mass after the spontaneous symmetry breaking can be read off as

$$ m_h = \sqrt{-2\mu^2} = \sqrt{2\lambda}v\,, \tag{2.61} $$

where λ is a free parameter. The vacuum expectation value of Higgs field ($\langle H \rangle = v$) can be calculated from the experimental results of the W boson mass, m_W, and of the weak coupling constant, g_w, using the relation $m_W = \frac{g_w v}{2}$:

$$ v \simeq 246\,\text{GeV}. \tag{2.62} $$

As explained before, the breaking of the electroweak symmetry can explain the mass of the weak gauge bosons. The introduction of the Higgs field also solves the problem of the fermion

masses. The Yukawa interaction terms given in Eq. (2.53), which is invariant under the gauge symmetries, are added to the Lagrangian,

$$\mathcal{L}_{Yukawa} \in -y_\ell \bar{\psi}_{\ell_L} H \psi_{\ell_R} + h.c. \quad \text{with} \quad H = \frac{1}{\sqrt{2}} \begin{pmatrix} 0 \\ v + \eta \end{pmatrix}, \ L = \begin{pmatrix} \nu_{e_L} \\ e_L \end{pmatrix}, \ \ell_R = e_R \quad (2.63)$$

which gives the mass term of the electron for example, and interaction term with the higgs boson as:

$$\mathcal{L}_{Yukawa} \approx \underbrace{-\frac{1}{\sqrt{2}} y_e v (\bar{e}_L e_R + \bar{e}_R e_L)}_{\text{mass term}} \underbrace{-\frac{1}{\sqrt{2}} y_e \eta (\bar{e}_L e_R + \bar{e}_R e_L)}_{\text{interaction term}} \quad \text{with} \quad m_e = \frac{y_e v}{\sqrt{2}}. \quad (2.64)$$

All the above calculations are done at tree-level; however for physical values of these parameters one needs to consider loop corrections as well. This does not cause any problem in the case of the SM, because it has been shown by Gerard 't Hooft that the SM a renormalisable theory [21], which means the results of the calculation considering all higher order loop corrections will be finite. However, the loop calculations will affect the values of the mass of the particles, and the couplings corresponding to the three gauge groups of the Standard Model. Even though the couplings are constant when one considers only tree level, they are changes with the energy (momentum of the associated mediator) due to the loop corrections. This is determined with the number of fermions or bosons contributing to the self energy of the gauge bosons [6]. Due to these changes depending on the loop-level, the masses and couplings of the particles are generally called as *running masses* or *running couplings*.

The renormalisability of the SM provides a theory which is anomaly free [22]. An example of an anomaly is the anomaly of local gauge symmetry, the so-called gauge anomaly [23, 24]. It stems from the violation of the current conservation, required by gauge symmetries, at the loop-level, while it is conserved at tree-level. This violation originates from a fermion loop diagram of a triangular shape with vector currents at three vertices [25]. In order to have an anomaly free theory, the condition of $Tr(Q) = Tr(T_3^2 Y) = 0$ has to be fulfilled. In the SM, lepton and quark sectors have anomalies individually, however they are canceled by unifying the theory including both leptons and quarks. This motivates the real unification of the leptons and quarks included in the multiplets of the gauge groups which is proposed by the "Grand Unified Theories" in order to unify the electroweak and strong interactions.

2.1.2 Puzzles of the Standard Model

The Standard Model is a successful theory providing very good agreement with the experimental results. However it has some puzzles which do not have any explanation within the existing theory. One of the important ones is the so-called `the hierarchy problem` stemming from the effect of the loop contributions to the mass of the Higgs boson. The existence of `dark matter` is another issue to which the SM does not offer a solution to explain the observable amount of dark matter. Another puzzle is `the unification of the gauge couplings` as well as the lack of information to explain `the neutrino masses`. These puzzles will be explained in the following.

Dark Matter: The observations of the cosmological parameters indicated that approximately 5% of the universe consists of normal matter, while dark matter forms $\sim 27\%$ of the universe, and the rest consist of dark energy [15]. Dark matter is non-luminous and non-absorbing matter, therefore it is not visible and it can only be detected by its gravitational effects on visible matter [26]. The most convincing evidence for dark matter comes from the measurements of the rotation curves of galaxies [27, 28]. These measurements showed that the galaxies move faster than expected, and their velocity stays constant at large distances from the centre of the rotation orbit instead of decreasing by $v(r) \propto 1/\sqrt{r}$ due to the Kepler's third rule. This indicated the existence of a non-luminous matter with a mass $M(r) \propto r$.

Another evidence is the observation of clusters of galaxies. This observation includes the X-ray temperature measurements of hot gas and the measurement of gravitational lensing of background galaxies on the cluster. The former way forms the baryonic part of the clusters, while the latter represents the distortions of the light due to the existence of a massive object (dark matter) [26]. The best known example is the Bullet Cluster [29], which consists of two clusters passed through each other. The measurements from the X-rays emitted by very hot gas showed that the baryonic matter is located in the centre of the clusters. The gravitational lensing measurements indicated that the most of the mass of the cluster moved without any interaction, and these parts of the cluster are placed in the outer part of the clusters. These observations showed that the gas molecules would be decelerated while they are passing through each other due to the electromagnetic interaction of the gas molecules of the baryonic matter. However, the non-luminous part of the clusters interact only weakly, therefore those parts of the clusters moves faster than baryonic matter. This separates the baryonic matter and the non-baryonic matter from each other. This is considered as the first direct observation of dark matter.

Weakly interacting massive particles (WIMPs) is one the most popular candidates proposed in order to explain the observable amount of dark matter. These are the particles at the weak scale ($\mathcal{O}(10^2)$ GeV) interacting with normal particles by the weak interaction. They can be searched for either in cosmological experiments or in collider experiments.

Neutrino Masses: Another problem of the SM is *the absence of an explanation for the tiny neutrino masses.* In the Standard Model, they are considered as massless. However, the observation of the neutrino oscillations between the flavours of the neutrinos has proven that they are massive particles. The most known constraint on the mass of the neutrinos comes from the experimental results from cosmology and astrophysics. These experiments provide an upper limit on the sum of the neutrino masses which shows that the neutrinos should be lighter than the other fermions by a factor 10^{-6} [15, 30]. Whether neutrinos are Dirac particles like the other fermions or Majorana particles, which are their own anti-particles, has also not been determined yet. This would be determined with the observation of the neutrinoless double-β decay. If they are Dirac particles, then the smallness of the neutrino masses can be explained with the see-saw mechanism which includes both the Dirac mass term $\mathcal{L}_D = -m_D(\bar{\nu}_R \nu_L + \bar{\nu}_L \nu_R)$ in the order of other fermion masses, and the Majorana mass term $\mathcal{L}_M = -M(\bar{\nu}_R^c \nu_L + \bar{\nu}_R \nu_R^c)$ which is large in the order of $M = 10^{11}$ GeV [6]. This mechanism requires two physical neutrinos; one of them is mostly left-handed with a small mass and the other one is mostly right-handed neutrino which is heavy.

Grand Unification: As explained in Section 2.1.1.3, the couplings of the gauge groups are running as a function of energy due to loop interactions. The dependency of the gauge couplings on energy is shown in Figure 2.1. Because of the structure of the gauge groups, the couplings of $U(1)$ and $SU(2)$ groups are decreasing with energy, while the coupling of $SU(3)$ group is increasing. Therefore, they could unify at a high energy called the Grand Unification Theory (GUT) scale. In other words, at this GUT scale all the SM interactions, electromagnetic $U(1)$, weak $SU(2)$ and strong $SU(3)$, are expected to merge into a single interaction. The first suggestion of the GUT scale was made by Howard Georgi and Sheldon Glashow in 1974 [23]. They suggested that the three groups are embedded in an $SU(5)$ symmetry group, which almost unifies the couplings at $\mathcal{O}(10^{15})\,\text{GeV}$. But the convergence was not exact as shown in Figure 2.1 by the dashed lines. In a supersymmetric theory, supersymmetric particles will also contribute to the gauge boson self energy which will change the running of the couplings. In this case, it has been shown that the couplings converge at around $\mathcal{O}(10^{16})\,\text{GeV}$ as illustrated in Figure 2.1 by the coloured lines.
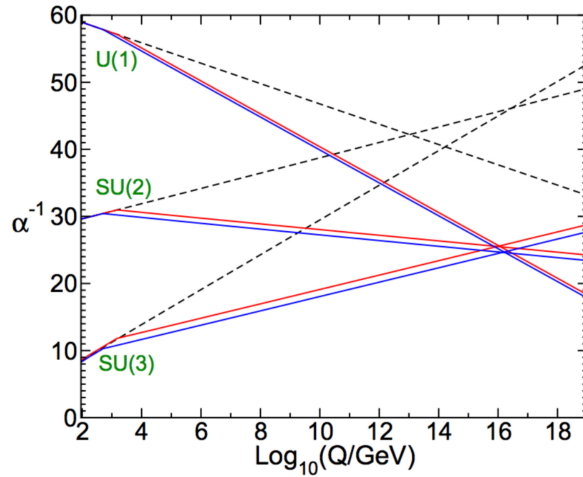
Figure 2.1 The unification of the coupling constant of the fundamental interactions. Dashed black lines are for the Standard Model, the straight coloured lines are for the minimal supersymmetric extension of the SM, the MSSM. Figure is taken from Ref. [31].

Hierarchy Problem: The ATLAS and CMS experiments measured a Higgs boson with the mass of $m_{h_{phys}} = 125.09 \pm 0.21(stat) + 0.11(syst)\,\text{GeV}$ [32]. The mass of the Higgs boson is extracted from the spontaneously symmetry breaking as $m_h = \sqrt{-2\mu^2} = \sqrt{2\lambda}v$ as seen in Equation (2.61). This is the bare mass of the Higgs boson calculated at tree level. In order to get the physical mass of the Higgs boson, the interaction of the Higgs field with itself, fermions and gauge bosons via loop effects should also be taken into account. These contributions are shown in Figure 2.2, and give corrections to the Higgs mass [33] as follows:

$$m_{h_{phsy}} = m_{h_{bare}} + \Delta m_h \tag{2.65}$$

$$m_{h_{phsy}} = m_{h_{bare}} + \mathcal{O}(\lambda, y_f^2, g_{(w)}^2)\Lambda^2 + \mathcal{O}(\lambda, y_f^2, g_{(w)}^2)\log\frac{\Lambda}{m_i} \tag{2.66}$$

where λ, y_f and g_w (g) are the Higgs-self coupling, Yukawa Higgs-fermion coupling and $SU(2)$ weak scale ($U(1)$) gauge coupling constants. m_i shows the mass of the particle interacting with the Higgs field. Λ is an ultra-violet cut-off scale until which the Standard Model is valid. It is also considered as the scale of new physics. If there is no new physics, this scale could be the Planck scale $\mathcal{O}(10^{19})\,\text{GeV}$ which is the gravitational scale when the loop effects could be important. Alternatively in a unified theory where the three fundamental interactions converge, the Λ could be at the unification scale (GUT) $\mathcal{O}(10^{16})\,\text{GeV}$. In both possibilities there is a huge difference at least in the order of 10^{30} between the bare mass of the Higgs boson and the loop corrections. This difference causes radiative divergences and is known as the *hierachy problem* of the Higgs mass.

(a) Higgs self-interaction   **(b)** Higgs-fermion interaction   **(c)** Higgs-boson interaction
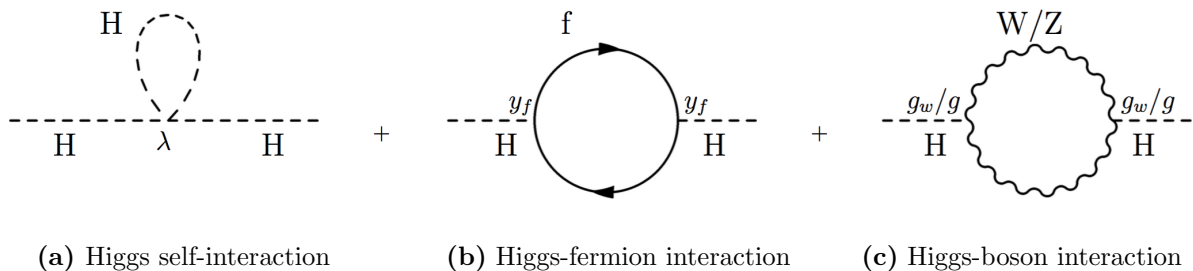
Figure 2.2 One loop radiative corrections to the Higss mass-squared value m_H^2 for (a) an interaction with a itself (b) an interaction with a fermion (c) interaction with a gauge boson.

Among these contributions, the top quark interaction is the dominant one because of its large Yukawa coupling of $y_t \approx 1$. As an example, one can consider the case where the Higgs field couples to a fermion with a mass m_f, which has a contribution to the $-y_f H \bar{\psi} \psi$ Lagrangian interaction term. The correction of this term to the Higgs mass is given [34] by,

$$\Delta m_{h_f}^2 = -\frac{y_f^2}{16\pi^2}\left[2\Lambda^2 + 6m_f^2 \log\left(\frac{\Lambda}{m_f}\right) + ...\right]. \qquad (2.67)$$

This shows that there are two main contributions to Higgs boson mass; the quadratic term Λ^2 which has a large contribution in the order of 10^{30}, and the logarithmic term $\log(\Lambda/m)$ which has a comparably mild contribution. To overcome this huge difference, the so called hierachy problem, and to obtain the physical mass from these contributions, one way is to fine tune the bare mass of the Higgs boson. However, this needs quite a large fine-tuning. Another more natural way is to introduce a scalar field S with a mass m_s which interacts with the Higgs field. This interaction will have a contribution to the Lagrangian with a term $-\lambda_s |H|^2 |S|^2$ where λ_s shows the coupling constant of a scalar field with the Higgs field, and it will give rise to a correction to the Higgs mass [34, 31] as follows:

$$\Delta m_{h_s}^2 = +\frac{\lambda_s}{16\pi^2}\left[\Lambda^2 - 2m_s^2 \log\left(\frac{\Lambda}{m_s}\right) + ...\right]. \qquad (2.68)$$

As one can see from Equations (2.67) and (2.68), the corrections coming from the Higgs-scalar interaction have an opposite sign contribution compared to the Higgs-fermion interaction. Using

this property, one can propose that if there is a scalar particle in the theory with a relation $\lambda_s = 2y_f^2$, the quadratic divergence will be naturally cancelled. If their masses would be equal to each other, logarithmic contribution to the Higgs mass would be also cancelled. This is a motivation to a new symmetry, symmetry of bosons and fermions which is called Supersymmetry.

2.2   Supersymmetry

Supersymmetry (SUSY), in contrary to the internal gauge symmetries, is a spacetime symmetry which transforms a fermion into a boson, and a boson into fermion. It proposes that each SM particles has a partner, with the same quantum number except their spin differing by 1/2, called *superpartner*. The SUSY transformations of a bosonic and fermionic states are given by

$$Q\left|Boson\right\rangle = \left|Fermion\right\rangle , \qquad Q\left|Fermion\right\rangle = \left|Boson\right\rangle . \tag{2.69}$$

Here Q is the generator of supersymmetry which is a fermionic operator (spinor) due to the conservation of spin angular momentum. Spinors are intrinsically complex objects, therefore the hermitian conjugate of Q, $Q^\dagger$, is also a symmetry generator. These generators satisfy the following commutation and anti-commutation relations arising from the extended version of Coleman-Mandula theorem [35] which combines the space-time (Poincaré) and internal symmetries:

$$\{Q, Q^\dagger\} \propto P^\mu, \tag{2.70}$$

$$\{Q, Q\} = \{Q^\dagger, Q^\dagger\} = 0, \tag{2.71}$$

$$[P^\mu, Q] = [P^\mu, Q^\dagger] = 0 . \tag{2.72}$$

P^μ is the four-momentum generator of spacetime translations which transforms as a spin-1 object under the Lorentz transformations, while the generators of the SUSY transformations transform as spin-1/2 objects.

In supersymmetric theories, a *supermultiplet* representation which contains both the SM fermions (bosons) and their superpartner bosons (fermions) is used. The commutation relation of the SUSY generators seen in Eq. (2.72) give rise to the equal mass condition of the SM particle and its superpartner if SUSY is an exact symmetry. In addition to fulfilling the above (anti-)commutation relations, the generators also commute with the generators of gauge transformations which states that the superpartners should have the same charge of each symmetry describing the SM. Another consequences of the (anti-)commutation relations is that the number of the boson and fermion states in each supermultiplet should have the same number of degrees of freedom;

$$n_B = n_F . \tag{2.73}$$

There are two simple possibilities to satisfy the above relation; one of them is to have a Weyl fermion (spin-1/2) with two spin helicity states ($n_F = 2$) and two real scalars (spin-0) with one degree of freedom each of a complex scalar field ($n_B = 2$). These kinds of supermultiplets are called *chiral (matter) supermultiplets* since they contain the SM fermions and their superpartners. The other possibility is to have a massless spin-1 boson with two degrees of freedom,

and one spin-1/2 Weyl spinor with two degrees of freedom. These are called *vector (gauge) supermultiplets* due to their gauge boson content. All the Standard Model particles and gauge interactions with their superpartners are listed in Tables 2.4 and 2.5 in terms of chiral and gauge supermultiplets, respectively. In the supermultiplet representation, only one type of helicity representation for chiral supermultiplets needs to be chosen. The common way is to represent all particles with a left-handed Weyl spinor. Therefore, the conjugates of the right-handed particles are placed in a chiral supermultiplet, since it has a left-handed structure.

Names		Spin 0	Spin 1/2	$SU(3)_C,\ SU(2)_L,\ U(1)_Y$		
Squarks , Quarks	Q_i	$(\widetilde{u}_{L_i}\ \widetilde{d}_{L_i})$	$(u_{L_i}\ d_{L_i})$	(3,	2,	1/3)
	$u^c_{R_i}$	$\widetilde{u}^*_{R_i}$	$u^\dagger_{R_i}$	($\bar{3}$,	1,	$-4/3$)
	$d^c_{R_i}$	$\widetilde{d}^*_{R_i}$	$d^\dagger_{R_i}$	($\bar{3}$,	1,	2/3)
Sleptons, Leptons	L_i	$(\widetilde{\nu}_{L_i}\ \widetilde{e}_{L_i})$	$(\nu_{L_i}\ e_{L_i})$	(1,	2,	-1)
	$e^c_{R_i}$	$\widetilde{e}^*_{R_i}$	$e^\dagger_{R_i}$	(1,	1,	2)
Higgs, Higgsinos	H_u	$(H^+_u\ H^0_u)$	$(\widetilde{H}^+_u\ \widetilde{H}^0_u)$	(1,	2,	$+1$)
	H_d	$(H^0_d\ H^-_d)$	$(\widetilde{H}^0_d\ \widetilde{H}^-_d)$	(1,	2,	-1)

Table 2.4 Chiral(Matter) supermultiplets in the minimal supersymmetric extension of the Standard Model, MSSM

Names	Spin 1/2	Spin 1	$SU(3)_C,\ SU(2)_L,\ U(1)_Y$		
Gluino, Gluons	$\widetilde{g}$	g	(8,	1,	0)
Winos, W fields	$\widetilde{W}^\pm\quad \widetilde{W}^0$	$W^\pm\quad W^0$	(1,	3,	0)
Bino, B field	$\widetilde{B}^0$	B^0	(1,	1,	0)

Table 2.5 Gauge(Vector) Supermultiplets with an unbroken symmetry in the minimal extension of the Standard Model

Table 2.4 shows the matter particles and Higgs boson together with their superparters which are called scalar leptons (sleptons), scalar quarks (squarks), and higgsinos, while Table 2.5 represents the gauge fields of the SM model and their superpartners which are called gluino, winos and binos (in general gauginos). The common quantum numbers of both the SM fields and their superpartners are also given in the tables. In Table 2.4, it is shown that there are two Higgs doublets within the standard particles:

$$\text{Higgs sector in SUSY:} \qquad H_u(x) = \begin{pmatrix} H^+_u \\ H^0_u \end{pmatrix}, \qquad H_d(x) = \begin{pmatrix} H^0_d \\ H^-_d \end{pmatrix} \qquad (2.74)$$

and two superpartners of these doublet Higgs fields:

$$\text{Superpartners of Higgs fields:} \qquad \widetilde{H}_u(x) = \begin{pmatrix} \widetilde{H}^+_u \\ \widetilde{H}^0_u \end{pmatrix}, \qquad \widetilde{H}_d(x) = \begin{pmatrix} \widetilde{H}^0_d \\ \widetilde{H}^-_d \end{pmatrix} \qquad (2.75)$$

The introduction of two Higgs doublets is necessary in supersymmetric theories for two independent reasons.

One of them is to cancel the gauge anomaly, explained in Section 2.1.1.3, which destroys the gauge invariance at loop-level. In the SM, all anomalies caused by leptons and quarks cancel each other. The inclusion of the Higgs boson does not have any effect on the anomaly, since only fermions have a contribution to the anomaly. In supersymmetry the anomaly cancellation should be consistent as well. In this case, the scalar superpartners of the fermions do not contribute, but the fermion superpartners of gauge bosons and Higgs boson do. However, the hypercharges of the gauginos are zero since their Majorana nature makes them left-right symmetric, and therefore the contribution from gauginos is zero as well due to $Tr[T_3^2 Y] = 0$. Then the only contribution left comes from the superparters of the Higgs doublets, which are the so-called higgsino doublet. One higgsino doublet is not sufficient to cancel the gauge anomaly, therefore there should be two Higgs doublets and so two higgsino doublets which give rise to two Higgs supermultiplets with opposite hypercharges Y=+1/2 and Y=-1/2, called H_u and H_d.

The second reason is the compatibility of the isospin of the neutral component of the Higgs field and the isospin of the particles that will acquire its mass by the interaction with the Higgs field. In the SM, the neutral component of the Higgs doublet with isospin of $T_3 = -1/2$ gives mass to the down-type quarks. The masses of the up-type quarks are acquired by the hermitian conjugate of the Higgs field which changes chirality of the field. In supersymmetry, in order to explain the interaction of the chiral fields including both the quarks superfields and the Higgs doublets a new function, the so-called superpotential, is introduced. The superpotential consists of the fields which are in the same chirality. Therefore, the hermitian conjugate of the existing Higgs doublet, which changes the chirality of the field, cannot be included in the theory. Because of that, the additional doublet needs to be introduced to give the up-type quarks their masses.

Depending on the number of SUSY transformations, there can be several SUSY theories. The number of supersymmetries is denoted by N, and it can be N=1, 2, 4, 8. The previous discussion considered the minimum number of transformation with N=1. For the extended version the degrees of freedom within one supermultiplet will be larger than the ones mentioned here which will correspond more SUSY generators.

Supersymmetry cannot be an exact symmetry, since no hint about the superpartners has been observed yet. However, the equal mass condition of the superpartners has an important role in the cancellation of the logarithmic correction of the quantum loop effects to the Higgs mass. Therefore, SUSY is assumed to be broken, but it is broken "softly" in order to prevent the regeneration of the divergences to the mass of Higgs boson.

2.2.1 Lagrangian of a Simplest Supersymmetric Model

A simple supersymmetic theory contains the following chiral and vector supermultiplets with the given mass dimensions of the fields;

$$\text{Chiral Supermultiplet} \quad : \quad \left(\phi^i_{(s=0)}, \; \psi^i_{(s=1/2)}\right), \tag{2.76}$$

$$\text{Vector Supermultiplet} \quad : \quad \left(A^a_{\mu_{(s=1)}}, \lambda^a_{(s=1/2)}\right), \tag{2.77}$$

where i represents each matter field, and a shows the number of generators of the corresponding symmetry group (e.g. a=3 for the SU(2) group). The full supersymmetric Lagrangian which is invariant under supersymmetry and gauge transformations can be written as

$$\mathcal{L}_{susy} = \underbrace{(D^\mu \phi^i)^* D_\mu \phi_i + i\psi^{\dagger\, i}\bar{\sigma}^\mu D_\mu \psi_i - \frac{1}{4}F^a_{\mu\nu}F^{\mu\nu a} + i\lambda^{\dagger a}\bar{\sigma}^\mu D_\mu \lambda^a}_{\text{kinetic energy terms of chiral and gauge fields}} \tag{2.78}$$

$$\underbrace{- \sqrt{2}g(\phi^* T^a \psi)\lambda^a - \sqrt{2}g\lambda^{\dagger a}(\psi^\dagger T^a \phi)}_{\text{interaction terms of chiral and gauge fields}} \tag{2.79}$$

$$\underbrace{- \frac{1}{2}\left(W^{ij}\psi_i\psi_j + W^*_{ij}\psi^{\dagger i}\psi^{\dagger j}\right)}_{\text{interaction terms of chiral fields}} \tag{2.80}$$

$$\underbrace{- F^{*\, i}F_i - \frac{1}{2}D^a D^a}_{\text{scalar potential term}} \tag{2.81}$$

where the first line contains the kinetic terms of the chiral and gauge fields including the SM fermions and their superpartner scalar fields, the gauge fields and their fermionic partner fields, the gauginos, as well as the scalar Higgs boson and its fermionic superpartners, the higgsinos. The first term of Eq. (2.78) shows the kinetic term of a scalar field as given in Eq. (2.38), while the kinetic energy of the fermionic fields presented in the second term has a different structure than Eq. (2.12). The reason of this is the difference on the representations of the fermion fields. The fermion fields in SUSY are represented with a two-component Weyl spinor instead of four-component Dirac spinor, which spoils the Lorentz invariance. To satisfy the Lorentz invariance of the theory, the kinetic term of the Weyl spinors should have the form $\psi^\dagger i\bar{\sigma}^\mu \partial_\mu \psi$ with $\bar{\sigma}^\mu = (1, -\vec{\sigma})$ where $\vec{\sigma}$ are the Pauli matrices given in Appendix A [36]. The covariant derivatives corresponding for the chiral and gauge fields are:

$$D_\mu \phi^i \quad = \partial_\mu \phi^i - igA^a_\mu T^a \phi^i \tag{2.82}$$

$$D_\mu \lambda^a \quad = \partial_\mu \lambda^a + gf^{abc}A^b_\mu \lambda^c. \tag{2.83}$$

In the third term of Eq. (2.78), $F^a_{\mu\nu}$ is the field strength tensor of the corresponding gauge symmetry, $F^a_{\mu\nu} = \partial_\mu A^a_\nu - \partial_\nu A^a_\mu + gf^{abc}A^b_\mu A^c_\nu$.

The second and third lines, which are Eqs. (2.79) and (2.80), describe the interactions of the chiral and gauge fields and non-gauge interactions including the matter field and Higgs boson interactions, and the fermion mass terms. As seen from Eq. (2.80), the interactions between chiral fields are determined by a function W_{ij}, which is the second derivative of the superpotential

with respect to scalar fields. The superpotential which shows the interaction of the chiral scalar fields can be written as:

$$W = \frac{1}{2}M^{ij}\phi_i\phi_j + \frac{1}{6}y^{ijk}\phi_i\phi_j\phi_k \,, \tag{2.84}$$

where M^{ij} is a symmetric mass matrix, and y^{ijk} is a Yukawa coupling between scalar and fermonic fields. The superpotential has a mass dimension $[M]^3$, and it does not include any complex conjugate of a field.

The last line of the SUSY Lagrangian, given in Eq. (2.81), shows the scalar potential term containing the so-called F-term determined by the Yukawa interactions and D-term determined by the gauge interactions. F-term and D-terms are a complex scalar fields without kinetic terms, therefore they are called auxiliary fields. They consist of the scalar chiral superfields, and so they contribute to the scalar potential of the theory. In contrary to the usual scalar fields, these terms have a mass dimension of 2. Their explicit form can be obtained from the equations of motion. They are originally motivated by the necessity of making the bosonic and fermionic degrees of freedom of the SUSY theory compatible off-shell. The explicit forms of the F-term and D-term are

$$F^{*\,i} = -\frac{\partial W}{\partial \phi_i} \quad \text{and} \quad D^a = -g(\phi^* T^a \phi). \tag{2.85}$$

The scalar potential corresponding to these auxiliary fields is

$$V_{scalar} = V_F + V_D \tag{2.86}$$

with

$$V_F = F^{*\,i}F_i \quad \text{and} \quad V_D = \frac{1}{2}D^a D^a \tag{2.87}$$

which determines the potential of the Higgs field in SUSY as will be given in Eq. (2.96).

This Lagrangian is valid for unbroken supersymmetry, while it is known that SUSY is a softly broken symmetry. Therefore, one needs to introduce extra terms to the Lagrangian in (2.78). These terms which break SUSY softly are given [31] by

$$\mathcal{L}_{soft} = -\underbrace{(m^2)^i_j\phi^{j*}\phi_i - \frac{1}{2}(M_a\lambda^a\lambda^a + h.c)}_{\text{mass terms}} + \underbrace{\left(\frac{1}{6}a^{ijk}\phi_i\phi_j\phi_k + \frac{1}{2}b^{ij}\phi_i\phi_j + h.c.\right)}_{\text{interaction terms}} \tag{2.88}$$

where m^2 is mass squared of the scalar fields, M_a represent the gaugino masses for each symmetry group, a^{ijk} and b^{ij} show the trilinear and bilinear scalar couplings. The soft breaking Lagrangian $\mathcal{L}_{soft}$ also contributes to the scalar potential and form the following potential;

$$V_{scalar} = V_F + V_D + V_{soft} \tag{2.89}$$

where the potential terms V_F and V_D stems from the introduced auxiliary fields with the definitions given in Equation (2.85) and V_{soft} includes the mass terms and bilinear interaction terms of the scalar Higgs fields seen in Equation (2.88).

Equation (2.89) is used to calculate the tree-level potential of the Higgs fields in SUSY theories which provides a relation between the Higgs boson and the Z boson mass. It is a nice feature of SUSY theories that the Higgs mass can be calculated from the theory. In addition the acquired scalar potential can be used to obtain relations among the mass of the Z boson, the masses of the up and down-type Higgs soft masses and the higgsino mass parameters. These relations lead to the motivation of the existence of light higgsinos in the electroweak scale that will be studied within the context of this thesis. More information about these will be given in the next section for the MSSM.

2.2.2 The Minimal Supersymmetric Standard Model

The minimal supersymmetric extension of the Standard Model, the so-called Minimal Supersymmetric Standard Model (MSSM) is based on the same gauge group structure as the SM, $SU(3)_C \otimes SU(2)_L \otimes U(1)_Y$. The field content of the MSSM can be seen in Tables 2.4 and 2.5. The particle content of the MSSM is listed in Table 2.6 including both standard model particles and their superpartners. If SUSY were unbroken, the gauge fields after the electroweak symmetry breaking would create the particles seen in the weak eigenstate column of Table 2.6. The combination of the bino field ($\widetilde{B}$) and the neutral third component of the wino field ($\widetilde{W}^0$) creates the photino ($\tilde{\gamma}$) and zino ($\tilde{Z}$) type gauginos, while the remaining components of the wino field create the charged wino bosons ($\tilde{W}^\pm$). After supersymmetry breaking the neutral and charged weak eigenstates, including the higgsinos, mix with each other and produce physical particles, the neutralinos and the charginos.

The superpotential of supersymmetric theories is a crucial function which describes the coupling of the chiral or matter particles. In the MSSM, the superpotential can be written as

$$W = \mu H_u H_d + y_e L \cdot H_d \, e_R^c + y_u Q \cdot H_u \, u_R^c + y_d Q \cdot H_d \, d_R^c \qquad (2.90)$$

where H_u, H_d, L, Q, e_R^c, u_R^c, d_R^c are the fields corresponding supermultiplets given in Table 2.4 containing both fermonic and bosonic fields, y_u, y_d and y_e are dimensionless Yukawa coupling constants. μ is the supersymmetric version of the SM Higgs mass parameter, which is called *higgsino mass parameter*. The dot stands for multiplication of two weak doublets, which can be done by using an antisymmetric parameter $\epsilon^{\alpha\beta}$. For example, $\mu H_u \cdot H_d = \mu \epsilon^{\alpha\beta}(H_u)_\alpha (H_d)_\beta$.

The superpotential given in Eq. (2.90) contains only the terms which does not violate baryon (B) or lepton (L) number. However, the renormalisable theory contains also some gauge invariant terms which violate B and L numbers. However, baryon and lepton number violating interactions have never been seen experimentally. If both violating interactions were present, the proton would decay rapidly. Proton lifetime is the most important constraint for B and L number violating terms. Therefore to forbid B and L number violation terms a new symmetry, R-parity, is introduced [31]:

$$P_R = (-1)^{3(B-L)+2s} \qquad (2.91)$$

where B, L and s represent the baryon and lepton numbers and the spin of the particle. The Standard Model particles and the Higgs bosons have even R-parity ($P_R = +1$), while the superpartners of the SM particles have odd parity ($P_R = -1$). R-parity of an interaction term is

Standard Particles			Superparters (Sparticles)				
			Weak Eigenstates		Mass Eigenstates		
Name	Symbol	Spin	Name	Symbol	Name	Symbol	Spin
Quark	q_L, q_R	1/2			Squark	$\tilde{q}_L, \tilde{q}_R$	0
Lepton	l_L, l_R	1/2			Slepton	$\tilde{l}_L, \tilde{l}_R$	0
Neutrino	$\nu_L\,(\nu_R)$	1/2			Sneutrino	$\tilde{\nu}_L\,(\tilde{\nu}_R)$	0
Gluon	g	1			Gluino	$\tilde{g}$	1/2
Photon	γ	1	Photino	$\tilde{\gamma}$	Neutralino	$\tilde{\chi}_1^0, \tilde{\chi}_2^0, \tilde{\chi}_3^0, \tilde{\chi}_4^0$	1/2
Z boson	Z^0	1	Zino	$\tilde{Z}$			
Higgs	H	0	Higgsino	$\tilde{H}_1^0, \tilde{H}_2^0$ $\tilde{H}^\pm$	Chargino	$\tilde{\chi}_1^\pm, \tilde{\chi}_2^\pm$	1/2
W boson	$W^\pm$	1	Wino	$\tilde{W}^\pm$			

Table 2.6 Particle content in the minimal supersymmetric extension of the Standard Model, MSSM. Weak state particles are the particles which would be created if the SUSY were unbroken. With the breaking of the SUSY, the weak eigenstates mix with each other and create the physics particles in the mass eigenstates, which are called neutralinos and charginos.

determined by the multiplication of R-parities of each particle in the term. The introduction of R-parity symmetry has important phenomenological consequences. One of them is that SUSY particles can only be produced in pairs. In addition, each SUSY particle should decay into an odd number of the lightest supersymmetric particles. Moreover, there should be at least one stable LSP in the final state. If it is neutral, then it could be a good candidate for dark matter. In the MSSM theories, R-parity is considered as conserved.

It has been explained in Section 2.2.1 that the SUSY is a softly broken symmetry. The soft symmetry breaking terms in the MSSM can be written as follows [31]:

$$\mathcal{L}_{soft} = -\underbrace{\frac{1}{2}\Big(M_1\tilde{B}\tilde{B} + M_2\tilde{W}\tilde{W} + M_3\tilde{g}\tilde{g} + c.c\Big)}_{\text{gaugino mass terms}} \tag{2.92}$$

$$-\underbrace{m_{H_u}^2 H_u^* H_u - m_{H_d}^2 H_d^* H_d - (bH_u \cdot H_d + c.c)}_{\text{part of Higgs potential}} \tag{2.93}$$

$$-\underbrace{\tilde{Q}^\dagger m_Q^2 \tilde{Q} - \tilde{L}^\dagger m_L^2 \tilde{L} - \tilde{\bar{u}} m_{\tilde{u}}^2 \tilde{\bar{u}}^\dagger - \tilde{\bar{d}} m_{\tilde{d}}^2 \tilde{\bar{d}}^\dagger - \tilde{\bar{e}} m_{\tilde{e}}^2 \tilde{\bar{e}}^\dagger}_{\text{sfermion mass terms}} \tag{2.94}$$

$$-\underbrace{\Big(\tilde{\bar{u}} A_u \tilde{Q} \cdot H_u - \tilde{\bar{d}} A_d \tilde{Q} \cdot H_d - \tilde{\bar{e}} A_e \tilde{L} \cdot H_d\Big)}_{\text{triple interaction terms}} \tag{2.95}$$

where M_1, M_2 and M_3 are the *bino*, *wino* and *gluino mass parameters*. The second line shows the contribution to the Higgs potential. The third line gives the mass terms of the scalar

quarks and leptons corresponding to left handed and right handed quarks and leptons. The last line represents the triple interaction of the scalar fields, where A_u, A_d, A_e are trilinear coupling constants with a mass dimension of one.

2.2.2.1 Electroweak Symmetry Breaking

The Higgs potential in the MSSM can be obtained including the F-term calculated from the superpotential, D-term obtained from the gauge interactions (see Eqs. (2.85) and (2.87)) and soft breaking term contributions (see Eq. (2.89)). It is given at tree level as follows:

$$V_{tree} = \underbrace{\mu^2(|H_u|^2 + |H_d|^2)}_{\text{F-term}} + \underbrace{m_{H_u}^2|H_u|^2 + m_{H_d}^2|H_d|^2 + b(H_u \cdot H_d + h.c)}_{\text{Soft breaking terms}}$$
$$+ \underbrace{\frac{(g^2 + g_w^2)}{8}\left(|H_u|^2 - |H_d|^2\right)^2 + \frac{g_w^2}{2}\left(|H_u|^2|H_d|^2 - |H_u \cdot H_d|^2\right)}_{\text{D-term}} \tag{2.96}$$

where $|H_i|^2 = H_i^* H_i$, g and g_w are the gauge couplings of the gauge groups of $U(1)_Y$ and $SU(2)_L$ respectively. $m_{H_u}^2$, $m_{H_d}^2$ are the mass-squared terms of the scalars and b is the bilinear scalar coupling constant. In terms of the components of the Higgs fields the Higgs potential can be written as

$$V_{tree} = (m_{H_u}^2 + \mu^2)(|H_u^0|^2 + |H_u^+|^2) + (m_{H_d}^2 + \mu^2)(|H_d^0|^2 + |H_d^-|^2) + [b(H_u^+ H_d^- - H_u^0 H_d^0) + h.c]$$
$$+ \frac{(g^2 + g_w^2)}{8}\left(|H_u^0|^2 + |H_u^+|^2 - |H_d^0|^2 - |H_d^-|^2\right)^2 + \frac{g_w^2}{2}\left(|H_u^+ H_d^{0*} + H_u^0 H_d^{-*}|^2\right). \tag{2.97}$$

The Higgs fields can be extended around the vacuum as:

$$H_u \equiv \frac{1}{\sqrt{2}}\begin{pmatrix} H_u^+ \\ v_u + \eta_u(x) + i\xi_u(x) \end{pmatrix} \qquad H_d \equiv \frac{1}{\sqrt{2}}\begin{pmatrix} v_d + \eta_d(x) + i\xi_d(x) \\ H_d^- \end{pmatrix} \tag{2.98}$$

where v_u and v_d are the vacuum expectation values of the neutral components of the Higgs fields, while $\eta_{u,d}(x)$ and $\xi_{u,d}(x)$ denote the fluctuations around the vacuum in the real and imaginary axis respectively. As in the SM case, the neutral components of the Higgs fields acquire a non-vanishing value at the minimum of the potential. The vacuum expectation values of the Higgs fields can be denoted with

$$\langle H_u^0 \rangle = \frac{v_u}{\sqrt{2}}, \quad \langle H_u^+ \rangle = 0, \quad \langle H_d^0 \rangle = \frac{v_d}{\sqrt{2}}, \quad \langle H_d^- \rangle = 0. \tag{2.99}$$

The ratio of the vacuum expectation values $\langle H_u^0 \rangle$ and $\langle H_d^0 \rangle$ is defined as $\tan\beta$, which is an important parameter in SUSY theory, as:

$$\tan\beta = \frac{v_u}{v_d} \tag{2.100}$$

Due to the vanishing of the expectation values of $\langle H_u^+ \rangle$ and $\langle H_d^- \rangle$, they do not contribute to the electroweak breaking. Therefore the charged component of the Higgs fields in Eq. (2.97) can be eliminated. The equation becomes;

$$
\begin{aligned}
V_{tree} = {} & (m_{H_u}^2 + \mu^2)|H_u^0|^2 + (m_{H_d}^2 + \mu^2)|H_d^0|^2 + b(H_u^0 H_d^0 + h.c) \\
& + \frac{(g^2 + g_w^2)}{8} \left(|H_u^0|^2 - |H_d^0|^2 \right)^2 .
\end{aligned}
\tag{2.101}
$$

In the MSSM, because of the additional Higgs doublet, there are eight degrees of freedom in total. When electroweak symmetry is broken, three of the degrees of freedom become goldstone bosons and they are transformed into the longitudinal polarisation states of the $W^\pm$ and Z bosons. The remaining degrees of freedom give rise to five Higgs bosons. Two of them are the CP even (scalar) neutral Higgs bosons h and H, one of them is the CP odd (pseudoscalar) neutral Higgs boson A and two of them are charged Higgs bosons $H^\pm$. The masses of these Higgs bosons can be derived from the scalar potential given in Eq. (2.97) by writing down the mass squared matrices produced due to the mixing between two Higgs doublet H_u and H_d, denoted by $\mathbf{M}_{H_n}^2$. The mass squared matrices and the mixing between the component of the Higgs fields can be shown as

$$
\mathcal{L} \ni \begin{pmatrix} H_u^i & H_d^j \end{pmatrix} \mathbf{M}_{H_n}^2 \begin{pmatrix} H_u^i \\ H_d^j \end{pmatrix} \quad \text{considering} \quad \mathcal{M}_{ab}^2 = \left(\frac{\partial^2 V_{tree}}{\partial H_a^i \partial H_b^j} \right)_{H_{a(b)} \to v_{u(d)}}
\tag{2.102}
$$

where $\mathcal{M}_{ab}$ shows the components of the mass squared matrices. The indices a and b of $\mathcal{M}_{ab}$ run over the up- or down-type components of the Higgs doublets $a, b = u, d$. $\mathbf{M}_{H_n}^2$ is a 2×2 mass matrix with the index n representing the type of Higgs boson. Depending on the type of Higgs boson, the fields H_u^i and H_d^j correspond to the different components of Higgs doublets; either the charged, or the neutral. The mass matrices are obtained for each real and imaginary part of the Higgs field which is expanded around the vacuum for example as $H_u^0 \approx v_u + \eta + i\xi$. Diagonalisation of the mass matrices then give the mass of the Higgs bosons [31]. Diagonalisation of the mass matrices then give the mass of the Higgs bosons [31]:

$$
m_{A^0}^2 \quad = \quad 2|\mu|^2 + m_{H_u}^2 + m_{H_d}^2 = 2b/\sin(2\beta)
\tag{2.103}
$$

$$
m_{h^0, H^0}^2 \quad = \quad \frac{1}{2}\left(m_{A^0}^2 + m_Z^2 \pm \sqrt{(m_{A^0}^2 - m_Z^2) + 4m_Z^2 m_{A^0}^2 \sin^2(2\beta)} \right)
\tag{2.104}
$$

$$
m_{H^\pm}^2 \quad = \quad m_{A^0}^2 + m_W^2
\tag{2.105}
$$

The prediction of the Higgs mass in SUSY (m_h): The Higgs boson mass is a free parameter in the SM. However, it is constrained from above in the MSSM, while the masses of the H^0, A^0 and $H^\pm$ can be arbitrarily large. It is predicted to be within the range [37, 38, 39]:

$$
m_h^{max} \approx m_Z |\cos 2\beta| + \text{radiative corrections} \lesssim 110 - 135 \, \text{GeV}
\tag{2.106}
$$

which states that without radiative corrections the Higgs boson can have a mass similar to the Z mass. However, the radiative corrections increase the value of the tree-level mass of the Higgs boson up to the maximum of about 135 GeV.

The prediction of the higgsino mass in SUSY (μ): The extra Higgs doublet field has an effect on the mass definition of the other particles as well. For example; the Z boson mass relation, obtained in the SM as seen in 2.59, becomes;

$$m_Z^2 = (g^2 + g_w^2)\frac{v}{4} \tag{2.107}$$

where $v^2 = v_u^2 + v_d^2$. The Z boson mass can be also written in terms of the mass of the Higgs fields and $\tan\beta$ by minimising the scalar potential given in Equation (2.97) and using Eqs. (2.100) and (2.107). The following minimum conditions

$$\left.\frac{\partial V}{\partial H_u^0}\right|_{\langle H_u\rangle=\frac{v_u}{\sqrt{2}}} = \left.\frac{\partial V}{\partial H_d^0}\right|_{\langle H_d\rangle=\frac{v_d}{\sqrt{2}}} = 0 \tag{2.108}$$

give two equations:

$$m_{H_u}^2 + |\mu|^2 - b\cot\beta - (m_Z^2/2)\cos 2\beta = 0 \tag{2.109}$$
$$m_{H_d}^2 + |\mu|^2 - b\tan\beta + (m_Z^2/2)\cos 2\beta = 0\,. \tag{2.110}$$

These give a relation between the Z boson mass and Higgs boson masses at tree level

$$m_Z^2 = 2\frac{m_{H_u}^2\tan^2\beta - m_{H_d}^2}{1 - \tan^2\beta} - 2|\mu|^2\,. \tag{2.111}$$

This equation shows a direct relation between the higgsino mass parameter μ and Z boson mass. It motivates that in order to have a natural theory without introducing large fine-tuning, the higgsinos in the theory should be in the electroweak scale as the Z boson. More details about naturalness will be discussed in Section 2.2.4. In order to explain the structure of the higgsinos, the chargino and neutralino sector will be discussed in the next section.

2.2.3   Chargino and Neutralino Sector in the MSSM

The gauginos and higgsinos mix with each other after electroweak symmetry breaking. The neutral parts of the gaugino fields, bino ($\widetilde{B}^0$) and third component of the wino ($\widetilde{W}^0$) combine with the neutral components of the Higgs fields ($\widetilde{H}_u^0$ and $\widetilde{H}_d^0$) and form the *neutrinos*. The charged components which are the charged component of the winos ($\widetilde{W}^\pm$) mix with the charged Higgsino components and form the charged physical mass eigenstate particles, the *charginos*. The mass matrices of the neutrinos and charginos driven due to the mixing can be obtained from the related terms in the Lagrangian [40, 41, 42]

$$\mathcal{L} \ni -\frac{1}{2}\begin{pmatrix} \widetilde{B}_R & \widetilde{W}_R^0 & \widetilde{H}_{d_R}^0 & \widetilde{H}_{u_R}^0 \end{pmatrix}\mathbf{M}_{\widetilde{\chi}^0}\begin{pmatrix} \widetilde{B}_L \\ \widetilde{W}_L^0 \\ \widetilde{H}_{d_L}^0 \\ \widetilde{H}_{u_L}^0 \end{pmatrix} + h.c\,, \tag{2.112}$$

where indices R and L correspond to the left handed and right components of the fields. The neutralino mass matrix in the $(\widetilde{B}, \widetilde{W}^0, \widetilde{H}_d^0, \widetilde{H}_u^0)$ basis is given by

$$
\mathbf{M}_{\widetilde{\chi}^0} = \begin{pmatrix} M_1 & 0 & -m_Z \cos\beta \sin\theta_W & m_Z \sin\beta \sin\theta_W \\ 0 & M_2 & m_Z \cos\beta \cos\theta_W & -m_Z \sin\beta \cos\theta_W \\ -m_Z \cos\beta \sin\theta_W & m_Z \cos\beta \cos\theta_W & 0 & -\mu \\ m_Z \sin\beta \sin\theta_W & -m_Z \sin\beta \cos\theta_W & -\mu & 0 \end{pmatrix}
\tag{2.113}
$$

at tree level [40]. M_1 and M_2 denote the $U(1)$ bino mass parameter and the $SU(2)$ wino mass parameter, while μ is the higgsino mass parameter. $\tan\beta$ is the ratio of the vacuum expectation values of the two Higgs fields (cf. Eq. (2.99)), and θ_W denotes the weak mixing angle. $\sin\theta_W$ and $\cos\theta_W$ are given in Eq. (2.60) in terms of gauge coupling of the electroweak groups of the SM. The matrix $\mathbf{M}_{\widetilde{\chi}^0}$ is complex symmetric, and it can be diagonalised by one unitary matrix N via $\mathcal{M}_{\widetilde{\chi}^0} = N^* \mathbf{M}_{\widetilde{\chi}^0} N^\dagger$;

$$
\begin{pmatrix} \widetilde{\chi}_{1L}^0 \\ \widetilde{\chi}_{2L}^0 \\ \widetilde{\chi}_{3L}^0 \\ \widetilde{\chi}_{4L}^0 \end{pmatrix} = N \begin{pmatrix} \widetilde{B}_L \\ \widetilde{W}_L^0 \\ \widetilde{H}_{d_L}^0 \\ \widetilde{H}_{u_L}^0 \end{pmatrix}, \qquad \begin{pmatrix} \widetilde{\chi}_{1R}^0 \\ \widetilde{\chi}_{2R}^0 \\ \widetilde{\chi}_{3R}^0 \\ \widetilde{\chi}_{4R}^0 \end{pmatrix} = N^* \begin{pmatrix} \widetilde{B}_R \\ \widetilde{W}_R^0 \\ \widetilde{H}_{d_R}^0 \\ \widetilde{H}_{u_R}^0 \end{pmatrix}
\tag{2.114}
$$

where the matrix $\mathcal{M}_{\widetilde{\chi}^0}$ contains the neutralino masses $M_{\widetilde{\chi}_i^0}$ on the diagonal. The mixing matrix N relates the neutralino mass eigenstates to the neutral gauge eigenstates.

The chargino mass matrix in the $(\widetilde{W}^+, \widetilde{H}^+)$ basis is also obtained from the Lagrangian including the following interaction terms [40, 41, 42];

$$
\mathcal{L} \ni -\frac{1}{2} \begin{pmatrix} \widetilde{W}_R^+ & \widetilde{H}_{u_R}^+ \end{pmatrix} \mathbf{M}_{\widetilde{\chi}^\pm} \begin{pmatrix} \widetilde{W}_L^- \\ \widetilde{H}_{d_L}^- \end{pmatrix} + h.c
\tag{2.115}
$$

where the mass matrix is given [43] by

$$
\mathbf{M}_{\widetilde{\chi}^\pm} = \begin{pmatrix} M_2 & \sqrt{2} m_Z \cos\theta_W \sin\beta \\ \sqrt{2} m_Z \cos\theta_W \cos\beta & \mu \end{pmatrix} .
\tag{2.116}
$$

$\mathbf{M}_{\widetilde{\chi}^\pm}$ is not a symmetric matrix and it can be diagonalised via the bi-unitary transformation $\mathcal{M}_{\widetilde{\chi}^+} = U^* X V^\dagger$. U and V relate the chargino mass eigenstates to the charged gauge eigenstates as

$$
\begin{pmatrix} \widetilde{\chi}_{1R}^- \\ \widetilde{\chi}_{2R}^- \end{pmatrix} = U_R \begin{pmatrix} \widetilde{W}_R^- \\ \widetilde{H}_{d_R}^- \end{pmatrix}, \qquad \begin{pmatrix} \widetilde{\chi}_{1L}^+ \\ \widetilde{\chi}_{2L}^+ \end{pmatrix} = V_L \begin{pmatrix} \widetilde{W}_L^+ \\ \widetilde{H}_{u_L}^+ \end{pmatrix}
\tag{2.117}
$$

The terms of $\mathcal{M}_{\widetilde{\chi}^\pm}$ on the diagonal give the mass of the charginos.

Depending on the amount of mixing, charginos and neutralinos can behave either bino-like, wino-like or higgsino-like [44]. According to the values of the electroweakino mass parameters, M_1, M_2, and μ, one can classify three limiting cases as an example:

- In the case $|M_1| < |M_2| \ll |\mu|$ with $|M_1| < |M_2| \approx \mathcal{O}(10^2\,\text{GeV})$ and $\mu \approx \mathcal{O}(\text{TeV})$, one obtains $|M_1| \approx M_{\widetilde{\chi}_1^0}$ with a bino-like $\widetilde{\chi}_1^0$, $|M_2| \approx M_{\widetilde{\chi}_2^0}, M_{\widetilde{\chi}_1^\pm}$ with wino-like $\widetilde{\chi}_2^0$ and $\widetilde{\chi}_1^\pm$, higgsino-like heaviest states with masses $|\mu| \approx M_{\widetilde{\chi}_{3,4}^0}, M_{\widetilde{\chi}_2^\pm}$.

- The hierarchy $|M_2| < |M_1| \ll |\mu|$ leads to the lightest two states being nearly mass-degenerate and wino-like, $|M_2| \approx M_{\widetilde{\chi}_1^0}, M_{\widetilde{\chi}_1^\pm}$ but a bino-like $\widetilde{\chi}_2^0$ with mass $|M_1| \approx M_{\widetilde{\chi}_2^0}$, while $\widetilde{\chi}_{3,4}^0$ and $\widetilde{\chi}_2^\pm$ remain higgsino-like and heavy as before.

- Choosing $|\mu| \ll |M_1| < |M_2|$ (or $|\mu| \ll |M_2| < |M_1|$) with $\mu \approx \mathcal{O}(10^2\,\text{GeV})$ and $|M_{1,2}| < |M_{2,1}| \approx \mathcal{O}(\text{TeV})$, leads to nearly mass-degenerate lightest states with $|\mu| \approx M_{\widetilde{\chi}_{1,2}^0}, M_{\widetilde{\chi}_1^\pm}$ but $|M_1| \approx M_{\widetilde{\chi}_3^0}$ (or $|M_1| \approx M_{\widetilde{\chi}_4^0}$) and $|M_2| \approx M_{\widetilde{\chi}_2^\pm}, M_{\widetilde{\chi}_4^0}$ (or $|M_2| \approx M_{\widetilde{\chi}_2^\pm}, M_{\widetilde{\chi}_3^0}$). The lighter neutralinos and the lightest chargino are then mostly higgsino-like and have unsuppressed couplings to the SM gauge bosons.

In this thesis, the last scenario, which has a relatively small μ in the order of the electroweak scale and large M_1 and M_2 in the order of a few TeV, will be investigated. This limiting case requires a light electroweak SUSY sector and a heavy coloured sector. Such scenarios can be constructed easily from the unconstrained MSSM, by simply choosing sufficiently large values for the squark, slepton, and gluino masses. The soft SUSY breaking terms (masses, mixing angles, complex phases) can be chosen independently in an unconstrained MSSM due to the absence of any assumptions about the SUSY breaking mechanism [45]. The mixing of the electroweak gauginos, which are higgsino-like charginos and neutralinos in this case, will be explained in the following.

2.2.3.1 Higgsino-Like Charginos and Neutralinos

One of the possible scenarios stemming from the case $|\mu| \ll |M_1| < |M_2|$ could have three light and higgsino-like charginos and neutralinos, $\tilde{\chi}_1^\pm$, $\tilde{\chi}_1^0$ and $\tilde{\chi}_2^0$. The explicit form of the tree-level masses of the three light higgsino-like particles, $M_{\widetilde{\chi}_1^\pm}$, $M_{\widetilde{\chi}_1^0}$, and $M_{\widetilde{\chi}_2^0}$ can be calculated by diagonalising the mass matrices of Eqs. (2.113) and (2.116) [2] as follows:

$$M_{\widetilde{\chi}_{1,2}^0} = \eta_{1,2}\left(|\mu| \mp \frac{m_Z^2}{2}\left(1 \pm \sin 2\beta\ \text{sign}(\mu)\right)\left(\frac{\sin^2\theta_W}{M_1} + \frac{\cos^2\theta_W}{M_2}\right)\right), \qquad (2.118)$$

$$M_{\widetilde{\chi}_1^\pm} = |\mu| - \sin 2\beta\ \text{sign}(\mu)\ \cos^2\theta_W\ \frac{m_Z^2}{M_2}, \qquad (2.119)$$

up to terms suppressed by higher powers of M_1 and M_2. From the diagonalisation of the neutralino mass matrices, the neutralino masses can have either positive or negative values. Therefore to distinguish this from the physical masses, an extra factor $\eta_{1,2}$, which denotes the sign of the mass eigenvalue, is introduced:

$$M_{\widetilde{\chi}_{1,2}^0} = \eta_{1,2} M_{\widetilde{\chi}_{1,2}^0}' \qquad (2.120)$$

where $M_{\widetilde{\chi}_{1,2}^0}'$ shows the physical neutralino masses. The factors $\eta_{1,2}$, where $\eta_{1,2} = \pm 1$, depend on the CP-quantum numbers of the corresponding neutralino [46].

Equations (2.118) and (2.119) give the dependency of the chargino and neutralino mass parameters on the model parameters. In the higgsino case, since $|\mu| \ll |M_1| < |M_2|$, the contribution from the second terms is small which indicates that the masses mostly depend on the μ parameter, while they have a weak dependency on $\tan \beta$, M_1 and M_2. Especially in the large $\tan \beta$ limit, the dependency of the masses on $\tan \beta$ can be seen clearly since $\sin 2\beta \to 2/\tan \beta$ and $\cos 2\beta \to 1$.

The mass eigenstates of the charginos and neutralinos can be written in terms of the weak interaction eigenstates as [2]

$$
\begin{aligned}
\chi_1^0 &= \frac{1}{\sqrt{2}} \left(\widetilde{H}_d^0 - \widetilde{H}_u^0 \right) + \frac{\sin \beta + \cos \beta}{\sqrt{2}} \frac{m_Z}{M_1} \sin \theta_W \, \widetilde{B} - \frac{\sin \beta + \cos \beta}{\sqrt{2}} \frac{m_Z}{M_2} \cos \theta_W \, \widetilde{W}^0 , \\
\chi_2^0 &= \frac{1}{\sqrt{2}} \left(\widetilde{H}_d^0 + \widetilde{H}_u^0 \right) - \frac{|\sin \beta - \cos \beta|}{\sqrt{2}} \frac{m_Z}{M_1} \sin \theta_W \, \widetilde{B} + \frac{|\sin \beta - \cos \beta|}{\sqrt{2}} \frac{m_Z}{M_2} \cos \theta_W \, \widetilde{W}^0 , \\
\chi_1^+ &= \widetilde{H}_u^+ - \sqrt{2} \sin \beta \frac{m_W}{M_2} \, \widetilde{W}^+ , \\
\chi_1^- &= \widetilde{H}_d^- - \sqrt{2} \cos \beta \frac{m_W}{M_2} \, \widetilde{W}^- .
\end{aligned}
\tag{2.121}
$$

Equation 2.121 explicitly shows the higgsino and gaugino mixing. The terms corresponding to the bino and wino component have small contributions of the order of $m_Z/M_{1,2}$. Therefore, the chargino and the neutralinos are called higgsino-like. Another consequence of multi-TeV gaugino masses is that the mass splittings are of the order of 1-10 GeV. The tree level mass difference between lightest neutralino and the lightest chargino can be explicitly given for $\mu > 0$ [2] as follows:

$$
M_{\widetilde{\chi}_1^\pm} - M_{\widetilde{\chi}_1^0} = \frac{m_Z^2}{2} \left[\sin 2\beta \left(\frac{\sin^2 \theta_W}{M_1} - \frac{\cos^2 \theta_W}{M_2} \right) + \left(\frac{\sin^2 \theta_W}{M_1} + \frac{\cos^2 \theta_W}{M_2} \right) + \mathcal{O}\left(\frac{\mu}{M_i^2} \right) \right] .
\tag{2.122}
$$

Since the last term has a negligible effect, the mass difference depends on the bino and wino mass parameters, M_1 and M_2, and $\tan \beta$. For $\tan \beta \gg 1$, the mass difference further simplifies to

$$
M_{\widetilde{\chi}_1^\pm} - M_{\widetilde{\chi}_1^0} = \frac{m_Z^2}{2} \left(\frac{\sin^2 \theta_W}{M_1} + \frac{\cos^2 \theta_W}{M_2} \right) + \mathcal{O}\left(\frac{\mu}{M_i^2}, \frac{1}{\tan \beta} \right) ,
\tag{2.123}
$$

which indicates that the mass difference has a weak dependency on $\tan \beta$. The mass difference between two higgino-like neutralinos is given by

$$
M_{\widetilde{\chi}_2^0} - M_{\widetilde{\chi}_1^0} = m_Z^2 \left(\frac{\sin^2 \theta_W}{M_1} + \frac{\cos^2 \theta_W}{M_2} \right) + \mathcal{O}\left(\frac{\mu}{M_i^2} \right) .
\tag{2.124}
$$

The neutralino mass difference has a different dependency on the model parameters as seen from Eqs. (2.122) and (2.124) such that the neutralino mass difference does not depend on $\tan \beta$. This difference will give some advantages in the determination of electroweakino parameters explained in Section 6.4.

Mass parameters M_1, M_2 and μ are complex-valued parameters in general. The complex phases of soft breaking parameters can be rotated away through a redefinition of the fields [47]. It is

one of the ways to reduce the number of free parameters in SUSY. M_2 can be made real and positive without loss of generality by a suitable rotation of the gaugino and higgsino fields. In this study, M_1 and μ are also assumed to be real, which means that no new sources of CP violation are introduced. The sign of the μ parameter has a negligible effect on observables, since the contribution from the second term of Eqs. (2.118) and (2.119) is negligible in the case of large M_1 and M_2. Therefore the positive values of μ are considered, while both positive and negative values of M_1 are taken into account. The negative values of M_1 will reduce the wino contribution to the neutralino mass seen in Eq. (2.119) which may result in different mass pattern. Especially at low $\tan\beta$ values, the lightest neutralino can be heavier than the lightest chargino, $M_{\widetilde{\chi}_1^\pm} < M_{\widetilde{\chi}_1^0}$. This can be seen easily from Eqs. (2.118) and (2.119) considering $\tan\beta = 1$.

2.2.4 Natural Supersymmetry

The hierarchy problem explained in Section 2.1.2 is one of the main problems that the Standard Model has. Supersymmetry solves this problem by introducing superpartners of each SM particle with 1/2 spin difference. Even though the quadratic divergent terms are cancelled by introducing the superpartners, the logarithmic contribution stays due to the fact that SUSY must be broken. It is assumed that SUSY is broken softly in order to prevent regeneration of the divergence. This requires the scalar particles to be not so heavy compared to their corresponding partners. The dominant contribution to the Higgs mass comes from the top quark and scalar top quark masses, since the top quark has a large Yukawa coupling ($y_t \sim 1$). The gluino contributes to the scalar top quark mass at one-loop level, thus it has an effect on Higgs mass at two-loop level. All other superpartners do not have a significant contribution to the Higgs boson mass. Therefore, naturalness puts upper limits only on stops and gluinos, while the first and second generation squarks and sleptons can be heavier. This type of models are called Natural SUSY [48, 49, 50].

Another important variable to comment on for the naturalness is the Z boson mass given at one-loop level [48] (for tree level formula see Eq. (2.111)) as follows:

$$m_Z^2 = 2\frac{(m_{H_u}^2 + \Sigma_u)\tan^2\beta - m_{H_d}^2 - \Sigma_d}{1 - \tan^2\beta} - 2|\mu|^2, \qquad (2.125)$$

where Σ_u and Σ_d are the loop corrections calculated by minimisation of one-loop corrections to the scalar tree-level potential given in Eq. (2.97) in the vacuum (as in Eq. (2.108)). Due to the large Yukawa coupling, the largest contribution to the loop correction terms Σ_u, Σ_d comes from the scalar top quarks. This contribution is given [48] by

$$\Sigma_u \sim \frac{3y_t^2}{16\pi^2}m_{\tilde{t}_i}^2\left(\ln\left(\frac{m_{\tilde{t}_i}}{\Lambda^2}\right) - 1\right). \qquad (2.126)$$

In general, naturalness requires the extraction of the experimental results, such as Higgs boson or Z boson masses, from the theory without large amount of fine-tuning. This demands that the Z boson mass and values of each parameter on the right hand side of Eq. (2.125) should be of the same order. In the limit of large $\tan\beta$, the Z boson mass can be written as

$$m_Z^2 = -2(m_{H_u}^2 + \Sigma_u + |\mu|^2), \qquad (2.127)$$

where m_Z is directly proportional to the up type Higgs soft mass, the loop correction and the higgsino mass parameter μ. Following the naturalness requirement, this equation requires the higgsinos to be light, in the same order with the Z boson mass, as well as the mass of the scalar top quarks and also the gluino mass related with the loop correction of stop quarks should be below a few TeV.

At two-loop level, additional statements about the stop quark mass arise as explained in [50]. In this case, the Higgs mass receives also contribution from the mixing between two stops corresponding to the left-handed and right-handed top quarks, $X_t = A_t - \mu \cot \beta$. This contribution has the power to give sufficient correction to the Higgs mass in order to obtain its measured value without large fine-tuning. The contribution depends on the stop masses as shown in Figure 2.3a. The figure displays the status of the phenomenological MSSM for the maximum Higgs boson mass value as a function of a ratio of stop-mixing $X_t = A_t - \mu \cot \beta$ over SUSY breaking scale defined as $M_S = \sqrt{m_{\tilde{t}_1} m_{\tilde{t}_2}}$. As seen from the figure, for small stop masses (sub-TeV) corresponding to $M_S < 1\,\mathrm{TeV}$, the ratio X_t/M_S should be close to its maximum around two to three. However, smaller and higher values than this would be possible if the stops are heavy (a few TeV) corresponding to $M_S < 3\,\mathrm{TeV}$. It is indicated that very small mixing of stop quarks are excluded for the pMSSM model. Especially for $M_S < 1\,\mathrm{TeV}$, only large mixing cases are allowed. However, in the case of large mixing, large fine-tuning would be necessary with respect to the trilinear coupling constant A_t. Therefore, large stop masses in the order of a TeV with reasonable mixing is the most natural scenario from the theoretical point of view.

(a)   (b)
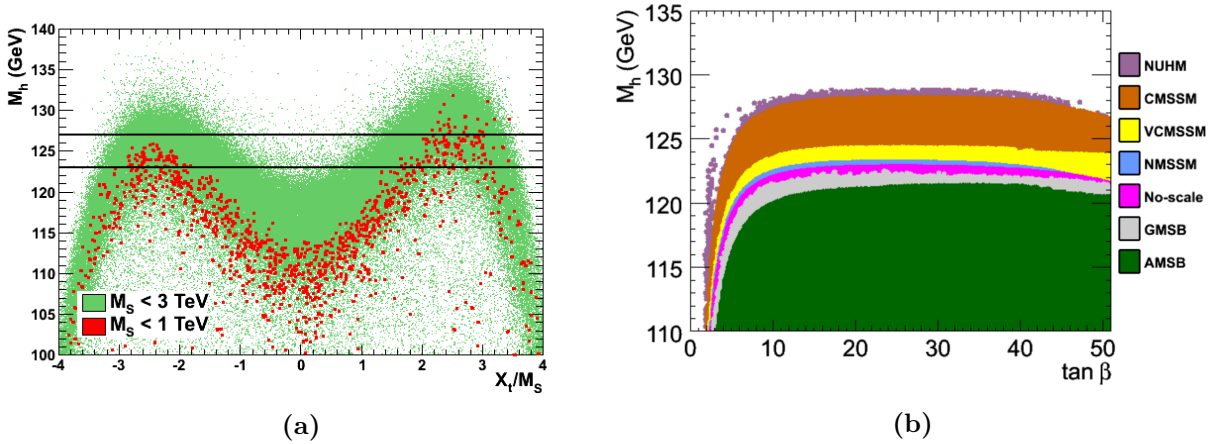
Figure 2.3 The maximum value of the Higgs boson mass (a) as a function of X_t/M_S where X_t is the mixing of stops, and $M_S = \sqrt{m_{\tilde{t}_1} m_{\tilde{t}_2}}$, taken from Ref. [39] (b) as a function of $\tan \beta$ in various constrained MSSM scenarios, taken from Ref. [51].

Since supersymmetry has many free parameters in the order of 100, generally simplified versions of supersymmetric models are considered. One of them is the phenomenological MSSM (pMSSM) [52, 53] stemming from the MSSM (unconstrained model) with a few restrictions such as the absence of CP and flavour violation, which reduces the number of free parameters to 19 in addition to the SM free parameters. The constrained MSSM (CMSSM) [54, 53] is another

simplified model that takes into account the various SUSY breaking scenarios. SUSY is considered as broken at a high scale and then it is transmitted to the low scale by the mediators. Depending on the type of the mediator, there are three main scenarios which are gravity mediated mSUGRA, gauge mediated GMSB and anomaly mediated AMSB supersymmetry breaking scenarios.

The Higgs boson mass in the MSSM given in (2.106) has an upper bound which is set by the loop corrections. Due to this dependency on the radiative corrections, the measured value of the Higgs mass has a significant effect on the parameters of the MSSM, and because of this constraint, some of the known MSSM models are excluded [39]. The situation on various constrained models such as GMSB, AMSB and mSUGRA (shown as CMSSM in the plot) and several special cases, is represented in Figure 2.3b [51]. Figure 2.3b shows that the GMSB and AMSB model are excluded. In addition, most of the mSUGRA models are also excluded apart from the general mSUGRA model and NUHM model which is more general model than mSUGRA with two additional free parameters. All in all, these plots display that the measured value of the Higgs boson mass has a significant effect on the studied models. This conclusion has motivated the extension of the minimal GMSB models. A hybrid gauge and gravity mediated model [55, 56] can be an alternative way to explain the Higgs boson mass. This hybrid model requires light higgsinos in the theory. This is one of the motivations in the top down perspective for the scenario analysed in this thesis.

2.3 Status of Supersymmetry at the LHC

There were many searches during the first run of the LHC at 7 TeV and 8 TeV centre-of-mass energies for $\sim 5\,\text{fb}^{-1}$ and $\sim 20\,\text{fb}^{-1}$ integrated luminosity respectively. Due to the requirement of the R-parity conservation, SUSY particles can be only produced in pairs, such as $\tilde{q}\tilde{q}, \tilde{g}\tilde{g}, \tilde{l}\tilde{l}, \tilde{\chi}\tilde{\chi}$. The cross sections of the possible production channels are given in Figure 2.4 as a function of the mass of the corresponding SUSY particle. As seen from the plots, the channels of strongly interacting particles have higher cross sections compared to the channels of weakly interacting particles.

The searches can be classified under several groups: searches of gluino and squark pair production with various dominant final states, third generation squark-pair production searches, searches of electroweak production, and exotic SUSY searches including long-lived SUSY particle searches. The LHC experiments have not observed any sign of the SUSY yet, therefore the results of the searches are converted into the exclusion limits. The status of the searches is summarised for instance in [53].

The gluino and squark pair production searches are generally interpreted in the models such as the CMSSM. In constrained models, the generalisation of the results to other models or event topologies is difficult. The interpretation of the searches with generic signatures such as $E_T^{miss} + \text{jets}$ or $\text{jets} + \text{same-sign leptons} + E_T^{miss}$ in the context of the CMSSM model excludes squark and gluino masses below $M_{\tilde{g}} = 1.2\,\text{TeV}$ and $M_{\tilde{q}} = 1.8\,\text{TeV}$ [53, 57, 58]. In CMSSM models, mass scales of all sfermions and gauginos are coupled to each other separately. This
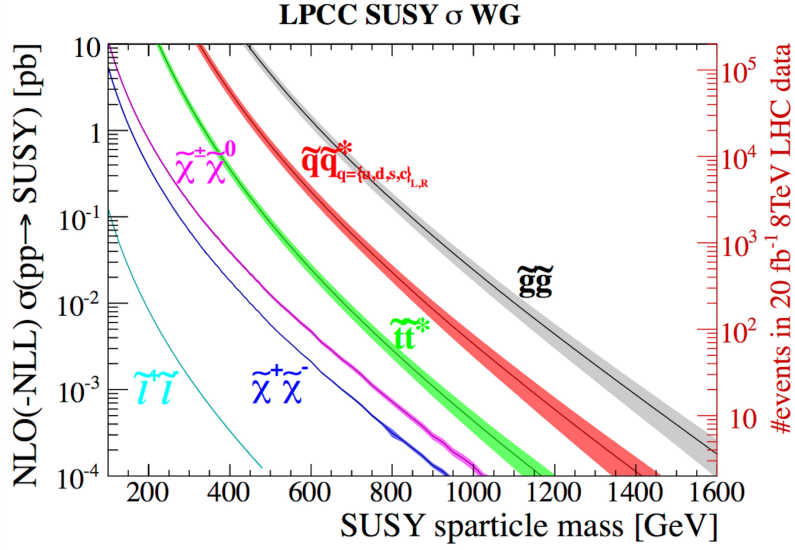
Figure 2.4 The cross sections of possible production channels of SUSY particles as a function of the particle mass. In general, channels which experience the strong interaction have higher cross sections, while gauginos and sleptons have the smallest cross section since they do not participate in strong interactions. Figure is taken from Ref. [53].

means that if one excludes the higher mass of the first generation squarks, light sleptons and third-generation squarks will be also excluded.

Alternatively, another approach can be used which is called simplified model searches (SMS) for interpretation of the searches. This approach is based on one particular event topology for example $pp \to \tilde{q}\tilde{q} \to q\tilde{\chi}_1^0 q\tilde{\chi}_1^0$. The only free parameters are the masses of the scalar particles involved in the chain which are $\tilde{q}$ and $\tilde{\chi}_1^0$, hence these models are quite simple to interpret. From the interpretations of the searches with E_T^{miss} + jets in simplified models of $pp \to \tilde{q}\tilde{q} \to q\tilde{\chi}_1^0 q\tilde{\chi}_1^0$, and $pp \to \tilde{g}\tilde{g} \to q\bar{q}\tilde{\chi}_1^0 q\bar{q}\tilde{\chi}_1^0$ the squarks and gluinos can be excluded up to 800 GeV and 1.3 TeV [53, 59, 57].

The next group of SUSY searches is the third generation production. The production cross section of the third generations is lower than the first and second generation of the squark-pair production as seen in Figure 2.4. This stems form the negligible heavy-quark content of the proton which reduces the possible production channels. The $\tilde{t}_{1,2}$ and $\tilde{b}_{1,2}$ can only be produced in the s-channel with the exchange of a gluon. They cannot be produced in the s-channel via a quark exchange or in the t-channel. Typical production channels of the stop-pairs are $pp \to \tilde{t}_2\tilde{t}_2$ where $\tilde{t}_2 \to \tilde{t}_1 h/Z$, and $pp \to \tilde{g}\tilde{g}$ where $\tilde{g} \to t\tilde{t}\tilde{\chi}_1^0$. The stop quark decays depending on the mass difference between the stop and the LSP, $\Delta m = m_{\tilde{t}} - m_{\tilde{\chi}_1^0}$ into $\tilde{t}_1 \to \tilde{\chi}_1^0 t \to \tilde{\chi}_1^0 bW$, $\tilde{t}_1 \to \tilde{\chi}_1^\pm b \to b\tilde{\chi}_1^0 b\tilde{\chi}_1^0 W^{(*)}$, or $\tilde{t}_1 \to \tilde{\chi}_1^0 c$ with the exchange of $\tilde{\chi}_1^\pm - W - b/s$ loop. For instance if the mass difference is larger than the mass of the top quark, $\Delta m > m_t$, the decay mode $\tilde{t}_1 \to \tilde{\chi}_1^0 t$ is the dominant one. There exists a large variety of searches which can be found in [57, 60, 61, 62, 63, 64, 65, 66, 67, 68, 69]. The collection of some of these searches is given in Figure 2.5. It shows that the mass of the stops can be excluded up to ~ 700 GeV depending on
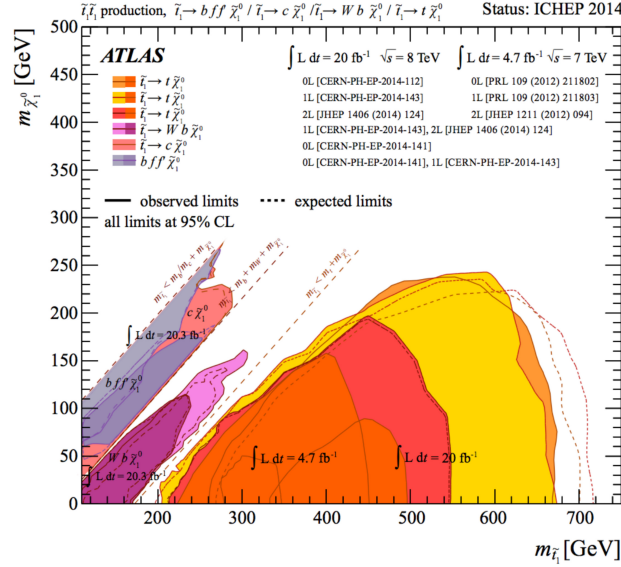
the kinematics of the existing theory.

Figure 2.5 A collection of excluding limits for selected searches from the ATLAS experiment [62, 63, 67, 68, 70, 71, 72]. Figure is taken from Ref. [53].

The electroweak production searches are also interpreted in the context of simplified models. The possible production channels in this class are $pp \to \widetilde{\chi}_1^{\pm}\widetilde{\chi}_2^0$ and $pp \to \widetilde{l}\widetilde{l}$ via decay channels of $\widetilde{\chi}_1^{\pm} \to W^{\pm}\widetilde{\chi}_1^0$, $l\tilde{\nu}$ and $\widetilde{\chi}_2^0 \to Z/H\,\widetilde{\chi}_1^0$, $l\tilde{l}$ where $\tilde{l} \to l\widetilde{\chi}_1^0$ and $\tilde{\nu} \to \nu\widetilde{\chi}_1^0$. As seen from Figure 2.4, the production cross section of slepton-pairs is suppressed compered to gaugino-pairs by a factor of 100. One of the reason for this is that gauginos can couple to protons directly, while the sleptons need an intermediate SM gauge boson to couple to the partons in the beam proton. Depending on the decay products of the W and Z gauge bosons and H boson, there are several different final states one can study. The available searches can be found in [73, 74, 75, 76, 77, 78].

Another possible way to search for the superpartners of the electroweak gauginos, the so-called electroweakinos, is the exotic SUSY searches including the searches for long-lived SUSY particles. Long-lived particles can produced in models which have a very small mass difference between a charged NLSP and the neutral LSP. These scenarios are possible in the pMSSM model with $M_2 < M_1, \mu$ requiring almost degenerate wino-like NLSP and LSP. Another possibility is a model with the relation $\mu < M_1, M_1$ which would give rise to `nearly mass degenerate higgsino-like LSP and NLSP`. As explained before this corresponds to the model studied in this thesis. Displaced signatures can be used to search for these kinds of models. As an example, one possible scenario is the decay of a chargino via $\widetilde{\chi}_1^{\pm} \to W^{\pm*}(\to ff')\widetilde{\chi}_1^0$. Since the mass difference is small, the visible particles will be very soft and their observation is not be possible. In this case if the lifetime of the NLSP particle is long enough to go through a few layers of the tracker, a disappearing track or a kink could be used to search for them. Up to now, no excess has been observed in these kinds of searches.

The absence of any sign of the discovery at the LHC puts some constraints on the mass reach of

the so-called electroweakino particles. Figure 2.6 shows the exclusion limits of the electroweaki-
nos where the chargino $\widetilde{\chi}_1^\pm$ and the heavier neutralino $\widetilde{\chi}_2^0$ decays via W and Z bosons [76, 78],
since these channels are related to the context of this thesis. The figure shows the limits in the
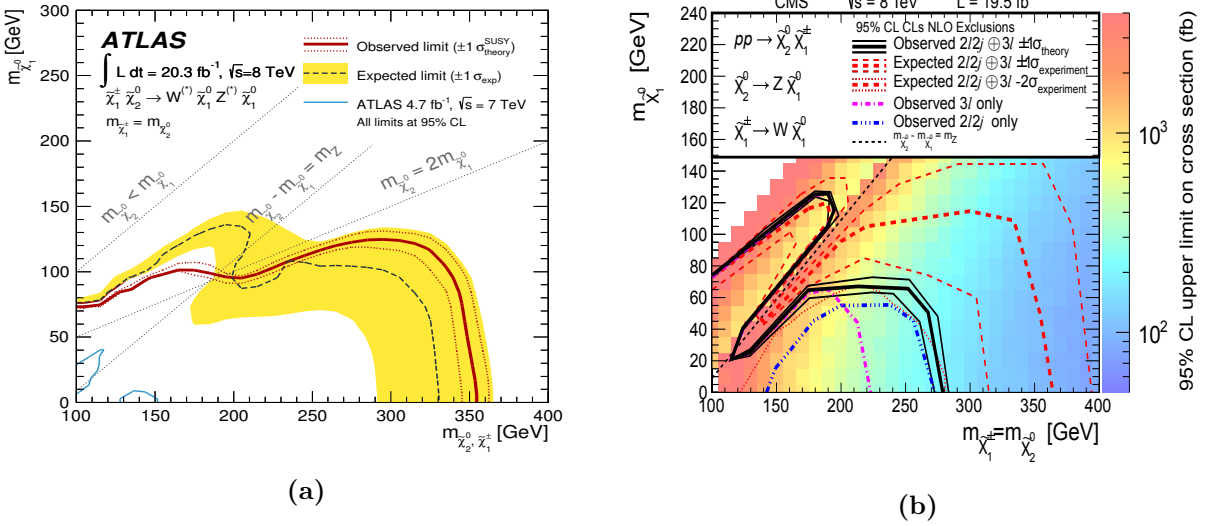

Figure 2.6   The exclusion limits of the electroweakino productions in the context of the
simplified models at $\sqrt{s} = 8\,\mathrm{TeV}$ centre-of-mass energy and an integrated luminosity of (a)
$\mathcal{L} = 20.3\,\mathrm{fb}^{-1}$ for ATLAS, taken from [76] (b) $\mathcal{L} = 19.5\,\mathrm{fb}^{-1}$ for CMS, taken from [78]

$M_{\widetilde{\chi}_1^0} - M_{\widetilde{\chi}_1^\pm}/M_{\widetilde{\chi}_2^0}$ plane assuming the chargino and the second lightest neutralino are degenerate
in mass. It is seen that for low values of the lightest neutralino $M_{\widetilde{\chi}_1^0} \lesssim 100$ with the condition
$M_{\widetilde{\chi}_1^0} < M_{\widetilde{\chi}_1^\pm} = M_{\widetilde{\chi}_2^0}$, the mass of the chargino and second lightest neutralino can be excluded
up to $\approx 350\,\mathrm{GeV}$ with a 95% confidence level. If the mass difference between $M_{\widetilde{\chi}_1^0}$ and $M_{\widetilde{\chi}_1^\pm}$ is
small, and all three gauginos are nearly mass degenerate, small values of the gauginos, even the
value of $100\,\mathrm{GeV}$, are still allowed. At the high luminosity LHC, the obtained discovery reach
of charginos and neutralinos can be extended from $350\,\mathrm{GeV}$ to $800\,\mathrm{GeV}$ [79, 80, 81].

Since the LHC experiments have not found any hint for supersymmetry especially in squarks
and gluino searches, one can conclude that the coloured SUSY spectrum should be rather heavy,
in a few TeV scale. Nevertheless, there are still large allowed regions for a light electroweak
SUSY sector including a SM-like Higgs boson with a mass compatible with the current LHC
measured value $m_h = 125.09 \pm 0.21(\mathrm{stat.}) \pm 0.11(\mathrm{sys.})\,\mathrm{GeV}$ [32]. The main motivation for this
kind of scenarios, `Natural SUSY`, is the naturalness explained in Section 2.2.4. As an example,
the scenarios in which the higgsino mass parameter μ is much smaller than the electroweak
gaugino masses M_1 and M_2, could be given.

In this thesis, Natural SUSY scenarios including light higgsino-like charginos and neutralinos,
$\widetilde{\chi}_1^\pm, \widetilde{\chi}_1^0$ and $\widetilde{\chi}_2^0$, which are at the electroweak scale, and heavy coloured third generation particles,
which are in the currently experimentally non-observable region, have been investigated. One
of the key feature of such scenarios is that the particles in the electroweak sector are very close

in mass, and this results in very soft decay products. Due to this feature, such scenarios are very challenging for the LHC, while they may be observable at the International Linear Collider [48, 82, 83]. The details about the feasibility of such scenarios for the International Large Detector (ILD) of the ILC will be discussed throughout the chapters of this thesis.

Chapter 3

The International Linear Collider

The International Linear Collider (ILC) is a planned linear electron-positron collider which will be designed to run at various centre-of-mass energies within the range of 200-500 GeV with a possible upgrade to 1 TeV. The layout of the ILC will be described in the following section. Lepton colliders have some advantages compared to hadron colliders, and these will be explained in Section 3.2. After that, the physics goals of the ILC will be clarified by focusing on a few important examples in Section 3.3. In Section 3.4, the main beam parameters will be considered in various aspects. The chapter will be finalised by explaining the challenging backgrounds for the considered analysis.

3.1   Overview of the ILC

The schematic layout of the ILC is shown in Figure 3.1. The figure indicates the subsystems
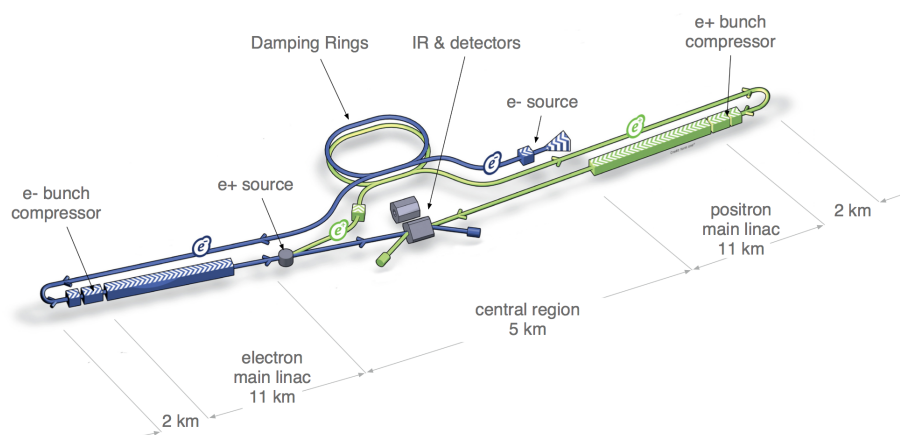

Figure 3.1 Schematic layout of the ILC showing all the subsystem and their length information. In total, it is about 31 km long. Figure is taken from Ref. [84].

43

of the ILC: electron and positron sources, damping rings, main linear accelerators for electron and positron, and beam delivery systems including interaction region (IR) and detectors. These apart from the detectors will be introduced in the following, while the detector which the analysis based on will be explained in detail in next chapter. The detailed description can be found in the ILC Technical Design Report Volume 1, Volume 3.II and Volume 4 [84, 85, 86].

Particle Sources

The electrons are produced by shining a polarised laser onto a GaAs photocathode in a DC gun. When the polarised photons are sent to the photocathode, the electrons are emitted by the photoelectric effect. The polarisation of the produced electrons is determined by the laser polarity. All in all, the electrons with 90% longitudinal polarisation can be produced by this way. Since the energy of the electrons in this step is very low, they undergo a process utilising normal conducting structures for bunching and pre-acceleration. After that, a superconducting linear accelerator (linac) accelerates the bunch trains up to 5 GeV before sending them to the damping ring.

The positron source is placed after the main linac of the electrons. The accelerated electrons with energies up to $150 - 250\,\text{GeV}$ are passed through a superconducting helical undulator ($\sim 150\,\text{m}$) which generates circularly polarised photons with energies $10 - 30\,\text{MeV}$. The photons are directed to a target where they create electron-positron pairs. While the produced electrons and left-over photons are dumped, the positrons are kept and pre-accelerated to $400\,\text{MeV}$ before transport to the next linac. Then they are accelerated to $5\,\text{GeV}$ in the same way as the electrons. With the design length of the undulator, 30% polarisation can be obtained; however, it can be increased up to 60% by increasing the length of the undulator to $\sim 220\,\text{m}$.

Damping Rings

There are one electron and one positron damping ring with a circumference of $3.2\,\text{km}$ which will be located in the same tunnel. Since the emittance of the produced bunches is not sufficiently small to achieve the desired luminosity, they need to be made more compact. Therefore, the produced electron and positron bunches go through the damping rings by emitting synchrotron radiation. After the $5\,\text{GeV}$ electron and positron bunches are compressed in the damping rings, they are sent to the next systems, the so-called Ring to Main Linac.

Ring to Main Linac

This system consists of several parts: $\sim 15\,\text{km}$ straight transport line for $5\,\text{GeV}$ beam particles, a $180\,^\circ$ turning point, spin rotators which turn the beam polarisation to the desired direction, and a two-stage bunch compressor to reduce the longitudinal beam size even further from several millimetres to a few hundred micron. In addition, the two-stage compressor accelerates the bunches from $5\,\text{GeV}$ to $15\,\text{GeV}$. Then they are sent to the main linacs.

Main Linacs

The bunches injected $15\,\text{GeV}$ are accelerated up to $250\,\text{GeV}$ in the two Main Linac systems for the electron and positron beams. The Main Linacs are based on $1.3\,\text{GHz}$ superconducting radio-frequency technology. The superconducting nine-cell niobium cavities are $1\,\text{m}$ long with

an average gradient of 31.5 GeV and a pulse length of 1.6 ms. In total ~ 7400 cavities are needed to form the main linac of the ILC.

Beam Delivery Systems

The Beam Delivery Systems (BDS) (2.2 km long) consist of several main subsystems. The first subsystem includes emittance measurement and correction, and polarisation and energy diagnostics. The measurement of the polarisation and energy before the collision is performed in this system. The final focus constitutes an other subsystem. It uses superconducting quadrupoles to focus the beam at the IP. In addition, the BDS contains two detectors that will use a common interaction region with the help of a "push-pull" arrangement. The final subsystem consists of the extraction line for the beam dump, and polarisation and energy diagnostic to measure them after the collision.

3.2   Advantages of Lepton Colliders

Lepton colliders are in general the complementary experiments to hadron colliders. The main advantages of hadron colliders are the collisions of high energetic particles ($\sqrt{s} = 13$ TeV has been reached by LHC experiments nowadays), and high rates of the processes of interest. Nevertheless, lepton colliders cannot have such high energies due to the large amount of synchrotron radiation for circular lepton colliders and due to cost limitations in case of linear lepton colliders. The rates are lower as well. However, they have advantages which turn this into a big benefit for lepton colliders. These advantages will be summarised in the following. The details can be found in Ref. [87].

`Well-determined initial four-momentum and spin:` The initial state at the lepton colliders is well determined. This is not the case for hadron colliders where the colliding particles are composite, and only some fraction of their energies determined with the parton distribution function (PDF) of the hadrons plays a role in the collision. This feature of lepton colliders provides an opportunity to use the recoil method, which will be used to reconstruct the mass of the higgsino-like charginos in the considered analysis as explained 6.2.2.

`Democratic production of particles:` The particles created from the electron-positron annihilation are produced at similar rate, because the photon couples to all species of quarks and leptons as well as new particles with about the same strength. In the hadron-hadron collision, the couplings of the gluon to all quark species are equal as well, but not the leptons. However, the democratic production of the particles is not the case for hadron-hadron collisions. Due to the compositeness of the hadrons, the PDF provides high cross sections for the production of light particles, while the production of heavy particles has lower cross section. Thus, the heavy particles constitute a small fraction of the total produced particles, which require a trigger system in order to reduce the amount of the uninteresting events. At the ILC, due to the production of various processes with the similar cross sections, it is possible to distinguish the interesting events from the others without requiring any trigger. This means that all the produced final state particles can be reconstructed at the ILC, therefore the absolute branching values or total widths can be measured directly, contrary to the LHC. In addition, the final states with very

soft particles which are vetoed at the LHC can be studied. This is an indispensable feature of the ILC which makes the analysis of Natural SUSY scenarios with a signature of large amount of missing energy and a few very soft visible particles possible.

`Clean final state:` The final state of ILC events is very clean compared to the LHC. At the LHC energies, the total cross section of the proton-proton collision is 100 mb. Proton bunches are crossing in every 25 ns, where each bunch crossing creates 30 proton-proton collisions. These pp collisions produces hundreds of particles. At the ILC, the dominant background is the photon-photon collisions which have a production cross section of 100 nb. Bunch crossings of the beam particles is 300 ns, and at each bunch crossing only about one photon-photon collision is expected which will produce a few final state particles. Therefore, the ILC has a very clean final state compared to the LHC. This feature is important to make the observation of challenging final states of the considered scenarios feasible. Otherwise, it would be very difficult to resolve the soft signal particles from the background particles.

`Polarisation Capability:` The ILC will supply polarised electron and positron beams, which offers an opportunity to study the processes depending on the polarisation state of both initial and final state particles. Although the matter particles are considered as a single objects, the left-handed and right-handed components of them actually behave differently, in particular at energies higher than the Z boson mass, where the weak interaction starts to play a role. While this dependency cannot be studied explicitly at the LHC, it is one of the significant advantages of the ILC. This property of the ILC is important especially for new physics searches, since it helps to suppress the background events as will be explained in 3.4.3. Therefore, it is an important feature for the analysis of the Natural SUSY scenarios.

3.3   Physics Goals

The guaranteed physics program of the ILC is precision measurements of the Higgs boson, the top quark, and the W and Z bosons. These precision measurements could provide evidence for the existence of new physics. The ILC also aims to search for new physics as well by looking for new particles directly. A complete overview can be found in the Physics Volume of the Technical Design Report of the ILC [87], and in a general detailed review [88] as well as a recent summary of the physics case [89]. There are several planned running scenarios of the ILC which will be explained in Section 3.4. In this section, only a few important physics goals will be summarised.

3.3.1   Higgs Physics

The mass of the Higgs boson has been determined up to 0.2% accuracy by the LHC experiments [32]; however, the properties of the particle are still heavily under investigation in order to learn more about it and maybe to discover new physics. Therefore, it is important to be able to determine them as precise as possible.

At the ILC, there are two dominant production processes of Higgs bosons which are Higgsstrahlung ($e^+e^- \to Zh$) and WW-fusion ($e^+e^- \to \nu_e\nu_e h$). The Higgsstrahlung process, which

offers the model-independent measurement of the Higgs boson mass, is by far the dominant process at around $\sqrt{s} \approx 250\,\text{GeV}$. The WW-fusion process, which is getting dominant at high energies, is used for the precise Higgs coupling measurements and contributes to the total width measurements of the Higgs boson. The model-independent determination of the Higgs mass does not depend on any kind of the decay product of the Higgs boson. Therefore, it offers an opportunity to study invisible decays of the Higgs, such as dark matter or long-lived particles that do not couple to the SM interactions, even for a branching ratio below 1%.

The Higgs physics studies provide an indirect way to probe new physics by searching for any deviation from the SM prediction of the parameters, such as couplings of the Higgs boson to other particles. Different new physics models would cause different deviation patterns from the SM expectation, therefore it would be possible to distinguish what kind of new physics model the deviations refer to. In the presence of the higgsino-like charginos in the electroweak scale, those charginos would circulate in the $h\gamma\gamma$ loop. Therefore, the deviations of the Higgs couplings to photons ($h\gamma\gamma$) from their SM values could be used to search for the higgsino-like charginos [90].

3.3.2 Top Physics

Precision measurements of the top quark mass and couplings are other very important physics topics for both the SM and beyond the SM. Since the top quark is the particle with the strongest coupling to the Higgs field due to its high mass, it has a dominant contribution to the Higgs mass in the loop level. So, a better precision on the top quark mass will improve the Higgs boson mass and as a result, a precise measurement of the top quark mass up to 100 MeV will be able to clarify the question of the stability of the SM [87].

The ILC offers an important tool to measure the top quark with high precision, which is the threshold scan of the $t\bar{t}$ production at around 350 GeV. The LHC cannot do such measurements due to the uncertainty on the initial centre-of-mass energy. From the threshold scan measurements, the $\overline{\text{MS}}$ mass can be determined to an accuracy of 10 MeV [89] at the ILC. In contrast, it would be determined to an accuracy of 500 MeV at the High Luminosity LHC [89, 91]. In addition to the $\overline{\text{MS}}$ mass, the mass of the top quark m_t can be determined to 17 MeV precison, while the width Γ_t and Yukawa coupling of top quark can be determined up to 26 MeV and 4.2% precision, respectively [89].

3.3.3 Beyond the Standard Model

New physics beyond the SM can be searched for either indirectly from the precision measurements or directly from the searches for new particles at the ILC [89]. In the precision physics, one can search for any shift from the SM expectation of the parameters; such as couplings of the Higgs bosons to other particles. This is already explained in Section 3.3.1. In the latter way, there are several ongoing studies. One of the important ones is the dark matter searches.

The dark matter can be searched with an initial state gluon in the case of LHC and an initial state photon in the case of ILC recoiling against invisible particles [89]. At the LHC, this

analysis suffers from the large SM background from the production of a Z boson which decays to neutrinos, especially in Drell-Yan processes. However, since there is no background from the strong interaction, and the existing amount of background can be reduced using a suitable polarisation combination, it is a well observable analysis at the ILC [92].

Another way to search for dark matter is to consider an electrically charged particle which decays to neutral dark matter particle and visible products. If the mass difference between charged and neutral particles is sufficiently large, then the decay product of the process would be visible at the LHC [76, 78]. However, generally the annihilation cross section of the lightest neutral particle is small to explain the observed amount of the dark matter. In order to explain it, the coannihilation of the lightest neutral particle and the charged one should be possible, which require a mass difference in the order of 20 GeV. Since such low energetic visible decay products do not pass the trigger cut, it is a challenging scenario for the LHC. However, at the ILC due to absence of trigger cuts, such kind of scenario would be observable. A full simulation study where lightest supersymmetric particle is the dark matter and it coannihilates with the supersymmetric partner of tau lepton $\tilde{\tau}$ has been performed for a centre-of-mass energy $\sqrt{s} = 500$ GeV and an integrated luminosity of $\int \mathcal{L}dt = 500$ fb^{-1} [93]. The scalar tau lepton decays to a tau lepton and LSP where $\Delta(M_{\tilde{\tau}} - M_{\tilde{\chi}}) = 11$ GeV. It has been found that the cosmic relic density of the dark matter can be predicted to 0.2% accuracy [89].

Another crucial new physics study is the search for the so-called hidden higgsinos. The observation of the higgsinos, which are required to be degenerate in mass and in the electroweak scale by naturalness, is challenging for the LHC due to the same reasons as the dark matter: small mass gap, large background. Therefore, hidden higgsinos with small mass splittings of a few GeV can only be studied at the ILC. In this thesis, the ability of the ILC to search for the hidden higgsinos will be studied in detail.

3.4 Top Level Beam Parameters

In this section the main parameters of the colliders for physics, which are energy, luminosity and polarisation, will be discussed in various aspects. The measurement procedures for these parameters will be summarised at the end of the section.

3.4.1 Beam Energy

The design centre-of-mass energy range of the ILC is $200-500$ GeV with a possibility to extend it to 1 TeV. The maximum value of the centre-of-mass energy is high compared to previous lepton colliders. For example the SLC experiment (1989-1998) had a maximum centre-of-mass energy 91.2 GeV with a linear accelerator, while LEP (1989-2000) reached a centre-of-mass energy of 209 GeV with a storage ring. The circular accelerator is a challenging technology for lepton colliders due to the synchrotron radiation loss, which is proportional to the fourth power of a ratio of the energy and mass of the circulating particle and inversely proportional to the radius ($\delta E \sim E^4/Rm^4$). Therefore, the amount of the energy loss by the synchrotron radiation for light particles limits the highest possible energy for a circular lepton accelerator in order to

keep the cost in a reasonable level by avoiding to build an accelerator with large radius. This explains why the planned future lepton collider at energies significantly larger than the LEP centre-of-mass energy will be a linear accelerator.

For studying different processes at the ILC, different centre-of-mass energies are needed. This can be seen from Figure 3.2, which displays the cross section of the various physics processes as a function of the centre-of-mass energy. For the best performance, the energy values corresponding to the maximum cross section of a given process are chosen for detailed studies. For example, as seen from the figure, $q\bar{q}$ production has a peak around the Z boson mass, while the W-pair production has maximum cross section around $160\,\text{GeV}$. Therefore, the precision measurements of the Z and W bosons are done at $91\,\text{GeV}$ and $160\,\text{GeV}$. Because of this dependency, different running scenarios of the ILC will provide different results.
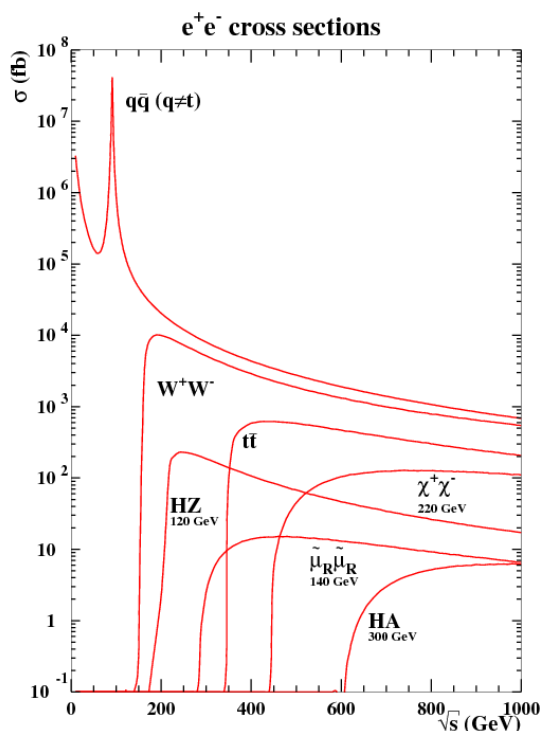

Figure 3.2 The production cross section of the various SM and new physics processes as a function of centre-of-mass energy at the ILC. It shows the production cross section of $q\bar{q}$ ($q \neq t$), W-pair production (W^+W^-), Higgsstrahlung (HZ) for $m_H = 120\,\text{GeV}$, $t\bar{t}$ production, and three new physics processes. Figure is taken from Ref. [94].

Table 3.1 shows three different operating scenarios in the time interval of 20 years [95].

It contains both $\sqrt{s} = 500\,\text{GeV}$ stage and luminosity upgrade of this stage. It has three main running time with centre-of-mass energies of 500, 350, and 250 GeV in turn. Scenario G-20 starts data-taking at $\sqrt{s} = 500\,\text{GeV}$, and collects data for an integrated luminosity of $1\,\text{ab}^{-1}$, and continues at the top-threshold $\sqrt{s} = 350\,\text{GeV}$, and then at the Higgsstrahlung maximum

cross section $\sqrt{s} = 250\,\text{GeV}$. After that in the luminosity upgrade, data is taken only at $500\,\text{GeV}$ for $\int \mathcal{L}dt = 4\,\text{ab}^{-1}$. It is optimised in order to obtain quick results on the processes which require $\sqrt{s} = 500\,\text{GeV}$ including top quark related measurements and new physics searches. The other two scenarios H-20 and I-20 collect less amount of data at $\sqrt{s} = 500\,\text{GeV}$ in order to have an early luminosity upgrade. With the saved luminosity from $500\,\text{GeV}$, data is taken at $250\,\text{GeV}$ and $350\,\text{GeV}$ as well after the luminosity upgrade, which yield an opportunity to have more precise result from the physics processes dominant at these energies.

3.4.2 Beam Luminosity

Since the production cross sections shrink with increasing centre-of-mass energy as seen in Figure 3.2, higher luminosity is required in order to have high statistics which is necessary for the precision measurements. The design luminosity for $\sqrt{s} = 500\,\text{GeV}$ is around $2 \times 10^{34}\,\text{cm}^{-2}\text{s}^{-1}$ To achieve such high luminosity is a challenging issue. The luminosity can be estimated with the following formula [96, 97]:

$$\mathcal{L} = \frac{n_b N^2 f_{rep}}{4\pi \sigma_x \sigma_y} H_D \qquad (3.1)$$

where n_b and N are the number of colliding bunches and the number of particles per bunch, f_{rep} is the pulse repetition rate, σ_x and σ_y are the bunch sizes in the transverse direction. The values of these parameters at $\sqrt{s} = 500\,\text{GeV}$ are given in Table 3.2. H_D shows the enhancement factor which takes into account the beam-beam interaction effect as explained in the next section. One of the important influences of the beam-beam interaction is the radiation of photons which are called "beamstrahlung" [96, 98].

3.4.2.1 Beamstrahlung

At the ILC, in order to achieve the required luminosity the beam sizes should be small (cf. Eq. (3.1)), which give rise to strong static electric fields around the bunches. At relativistic energies,

	Stage	500			Run Time	500 LumiUP		
Scenario	$\sqrt{s}$ [GeV]	500	350	250	bef. LumiUP	500	350	250
G-20	$\int \mathcal{L}dt\ [fb^{-1}]$	1000	200	500		4000	-	-
	time [years]	5.5	1.3	3.1	9.9	8.3	-	-
H-20	$\int \mathcal{L}dt\ [fb^{-1}]$	500	200	500		3500	-	1500
	time [years]	3.7	1.3	3.1	8.1	7.5	-	3.1
I-20	$\int \mathcal{L}dt\ [fb^{-1}]$	500	200	500		3500	1500	-
	time [years]	3.7	1.3	3.1	8.1	7.5	3.4	-

Table 3.1 The planned operating scenarios of the ILC. The energies and corresponding luminosities are given in the running order, which means all the scenarios will start to run at $500\,\text{GeV}$. The sixth column shows the total run time before the luminosity upgrade. Table is adapted from Ref. [95].

the boost of the electric field induces the magnetic field as well. Due to the induced strong electromagnetic field of a bunch, the particles in the other bunch are accelerated towards the oncoming bunch, the so-called *pinch effect* demonstrated in Figure 3.3. This focuses the beams focus and reduces the bunch sizes even further, which increases the luminosity. This is taken into account with the so-called beam enhancement factor H_D seen in Eq. (3.1), which is in the order of two for typical beam parameter sets [99].
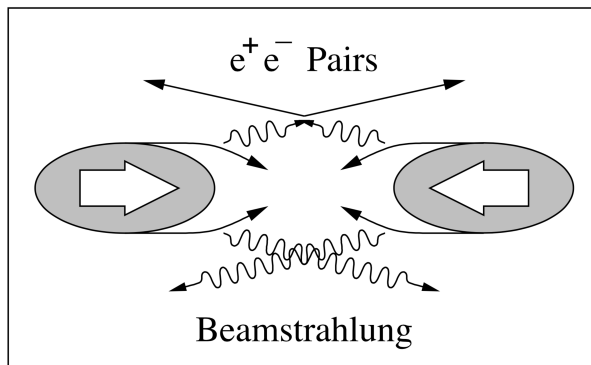

Figure 3.3 Demonstration of pinch effect with beamstrahlung and e^+e^--pair creation. Figure is taken from [99].

While the particles within the bunches are bending, they emit real photons which are called *beamstrahlung*. The energy of the photons corresponds to the energy loss of the particle and changes depending on the place of the particle emitting a photon. For example, if it is emitted from a particle away from the centre of the bunch, its energy would be higher, while it could have a low energy when it is emitted form a particle very close to the centre of the bunch. The energy loss caused during the beam-beam interaction is inversely proportional to the square of sum of the beam sizes as follows [97]:

$$\delta E \approx 0.86 \frac{r_e N^2 \gamma}{\sigma_z (\sigma_x + \sigma_y)^2} \tag{3.2}$$

where r_e and γ are the classical electron radius and the relativistic factor $E_{beam}/m_e c^2$, while σ_z is the bunch length. This energy loss of the beam particles results in a spectrum, the so-called *beam energy spectrum* or *luminosity spectrum*, with a tail towards lower energies in addition to a peak in the centre-of-mass energy distribution which needs to be taken into account in analyses. Only 58% of the collisions happen in the region which is within 1% of the centre-of-mass energy, 500 GeV for the ILC [84]. The spectrum for the ILC is simulated using `GuineaPig` [100].

Equation (3.1) shows that the most effective way to achieve the required luminosity is to reduce the size of beams, σ_x and σ_y. However, there is a limitation on the size of the beams coming from the energy loss due to the beamstrahlung photons (see Eq. (3.2)). In order to increase the luminosity while keeping the energy loss as small as possible, flat beams are required at the ILC.

Name of the Parameter	Symbol	Unit	Value
centre-of-mass energy	E_{CM}	GeV	500
Luminosity	L	$cm^{-2}s^{-1}$	1.8×10^{34}
Fraction of L in top 1% E_{CM}	$L_{0.01}/L$	%	58
Luminosity pulse repetition rate	f_{rep}	Hz	5
Number of bunches	n_b	-	1312
Bunch population	N	-	2×10^{10}
Bunch separation	Δt_b	ns	554
Linac bunch interval	n_b	-	554
RMS bunch length	σ_z	μm	300
RMS horizontal beam size at IP	σ_x^*	nm	474
RMS vertical beam size at IP	σ_y^*	nm	5.9

Table 3.2 Summary of the baseline parameters of the ILC at $\sqrt{s} = 500\,\text{GeV}$. Table is adapted from Ref. [84].

3.4.3 Beam Polarisation

At the ILC, the beams are foreseen to be longitudinally polarised. The production cross section of a process for longitudinally polarised beams can be calculated by [101]:

$$\sigma(P_{e^+}, P_{e^-}) = \frac{1}{4}\Big\{(1 + P_{e^+})(1 - P_{e^-})\sigma_{RL} + (1 - P_{e^+})(1 + P_{e^-})\sigma_{LR} \tag{3.3}$$
$$+ (1 + P_{e^+})(1 + P_{e^-})\sigma_{RR} + (1 - P_{e^+})(1 - P_{e^-})\sigma_{LL}\Big\}$$

where σ_{ij} $(i, j \in L, R)$ refers to the polarised cross sections. Here index i corresponds to positron polarisation, while j shows the electron polarisation. For instance; σ_{RL} means the positron beam is completely right-handed, i.e. $P_{e^+} = +1$, and the electron beam is completely left-handed polarised, $P_{e^-} = -1$.

In annihilation diagrams, which are represented by s-channel diagram, the helicities of the incoming particles are coupled with each other, while in the exchange diagrams indicated with t-channel, the helicities of the incoming beams couple with the outgoing particle helicities. In the SM, the former case allows only LR or RL polarisation combinations due to the vector structure of the mediator (J=1). However in the new physics case, the mediator could be a spin zero (J=0) particle as well. In this case, LL and RR combinations would be possible. In the t-channel case, the helicity of one vertex does not have any effect from the helicity of the other initial particle. Therefore, the exchange particle could be either a vector, or a fermion, or a scalar, which allows not only LR and RL configuration but also LL and RR helicity configurations of the initial particles. Within the SM, the single W production and Bhabha scattering can be given as examples for this [101].

The beam polarisation offers a possibility to suppress the SM background in new physics searches. Using a proper combination the background can be suppressed, while the signal is

either enhanced or not depending on the signal [101]. The influence of the polarisation on the number of events can be parametrised with a scaling factor, f_{pol} defined by [101]:

$$f_{pol} = \frac{\sigma(P_{e^+}, P_{e^-})^a}{\sigma(P_{e^+}, P_{e^-})^b} \qquad (3.4)$$

where the indices a and b correspond to cases when only electrons are polarised, and both beams are polarised in turn, which results in a value between 0 and 2 [101].

The above statement on signal enhancement and background suppression is only valid when the polarisation dependency of the background and signal events are not the same. In the cases where both signal and background are enhanced with the same polarisation configuration, the beam polarisation still helps by increasing the significance of the events according to $S/\sqrt{B}$ as shown with an example in Table 3.3. In the first case, it is clear that the polarisation configuration has a significant influence on the number of events, while in the latter case even though both signal and background are enhanced, it increases the significance $S/\sqrt{B}$ by $\sqrt{2}$ times.

Polarisation Dependency	Signal (S)	Background (B)	S/B	$S\sqrt{B}$
S enhanced & B decreased	$2 \times S$	$0.5 \times B$	$4 \times S/B$	$2\sqrt{2} \times S/\sqrt{B}$
S enhanced & B enhanced	$2 \times S$	$2 \times B$	$1 \times S/B$	$\sqrt{2} \times S/\sqrt{B}$

Table 3.3 An example showing the gain in the S/B and $S/\sqrt{B}$ using the scaling factor obtained by the comparison of the case when both beams are polarised in the case when only the electron is polarised. In one case, the signal is enhanced while the background is decreased with the selected configuration, in the other both the signal and background are enhanced with the selected configuration. Table is adapted from [101].

3.4.4 Measurement of Top Level Beam Parameters

Since the ILC is designed for precision physics, the measurement of the top level beam parameters is very important. To achieve the envisaged precisions required by the physics analyses, the integrated luminosity, the beam energy and the polarisation should be measured with precisions of $\Delta\mathcal{L}/\mathcal{L} = 10^{-3}$, $\Delta E/E = 10^{-4}$, and $\Delta P/P = 2.5 \times 10^{-3}$ at $\sqrt{s} = 500\,\text{GeV}$, respectively [102, 103]. For the GigaZ option, which is planned for precision measurements at $\sqrt{s} \approx m_Z$, the precision of the luminosity and beam polarisation should be even better, $\Delta L/L = 10^{-4}$ [104] and $\Delta P/P = 10^{-3}$ [86]. The methods foreseen for the ILC to achieve the required precisions will be explained in the following.

The luminosity is measured in one of the forward detectors specialised for this purpose, the so-called LumiCal. The precise measurement of the luminosity (10^{-3}) is done by counting the number of Bhabha scattering events, $e^+e^- \to e^+e^-(\gamma)$, within a certain polar angle range. In order to extract the integrated luminosity from the equation $N_B = \sigma_B \int \mathcal{L}dt$ [102], the cross section of the process needs to be determined. This can be done theoretically using the polar angle of the scattered electron [104]. Therefore, the determination of the polar angle range is crucial. The acceptance region of the inner radius of the calorimeter determines the minimum

value of the polar angle. The maximum is determined from the amount of the events such that the available amount of data will provide the desired statistical precision. In counting Bhabha scattering events, the reconstruction of each particle (electron, positron, photon) plays a significant role. This necessitates a small Moilère radius to have a more compact electromagnetic showers.

There are three ways of measuring the beam energy [103]. The first two measurements are obtained using an upstream energy spectrometer before the collision and a downstream energy spectrometer after the collision in order to take into account collision effects, with spectrometers including different magnet setups. Using the deflection of the beams due to the magnetic fields and the relation between magnetic field and energy, the beam energy can be reconstructed (for details see [103]). The third one is the average beam energy, which is measured directly from the annihilation data using the radiative Z return events, $e^+e^- \to Z\gamma \to \mu^+\mu^-\gamma$, as the Z boson mass is known very precisely ($\delta m_Z = 2.1\,\mathrm{MeV}$). If it is assumed that only one photon is radiated, the mass of the $\mu^+\mu^-$ system can be reconstructed from the angles between each muon and photon [105]. The centre-of-mass energy can be obtained from the Z boson mass and these angles.

The beam polarisation can be measured directly using the upstream and downstream Compton polarimeters [103]. The procedure can be briefly explained as in the following: a circularly polarised laser is shot onto the beam, and the backscattered electrons and positrons are detected by several counting Cherenkov detectors. The sign of the laser polarisation is constantly switched. The polarisation of the beam is then obtained from the cross section asymmetry corresponding to the left and right handed laser polarisations. In addition, spin transport is a necessary step in order to relate the polarisation measured in the polarimeters and that at the IP [106]. For physics analysis, *the luminosity weighted polarisations* are used, which are determined by weighting the measured polarisation with the luminosity.

3.5 Beam-Induced Background

The beamstrahlung photons are generally very well collimated along the beam pipe. So, most of them leave the detector through the beam pipe. However, secondary particles created by the beamstrahlung photons might have a significant impact on the detector performance. These backgrounds arising from secondary particles are known as beam-induced background.

The beam-induced backgrounds include two main backgrounds which arise due to soft e^+e^-−pair creation via the interaction of emitted photons and low p_t photon photon interaction creating hadrons. These photons can be either real beamstrahlung photons or virtual photons emitted from the particles within the bunches.

3.5.1 Soft e$^+$e$^-$-Pair Background

The interaction of the real or virtual photons with each other create low energetic *electron-positron pairs* as can be seen from Figure 3.3. The creation of the electron-positron pairs can be

classified in two groups; coherent pair creation [107] and incoherent pair creation [108]. In the coherent creation, the beamstrahlung photons create e^+e^--pairs due to the effect of the field. In the incoherent creation, two photons interact and create e^+e^--pairs. Depending on the type of the photon, there are three possible processes as seen in Figure 3.4; the interaction of two real beamstrahlung photons, the so-called *Breit-Wheeler process*; the interaction of one real photon and one virtual photon which is called *Bethe-Heitler process*; and the interaction of two virtual photons, the so-called *Landau-Lifshitz process*. The coherent pair creation is almost negligible for the ILC [109], while the incoherent creation is dominant, especially for the last two processes [110].
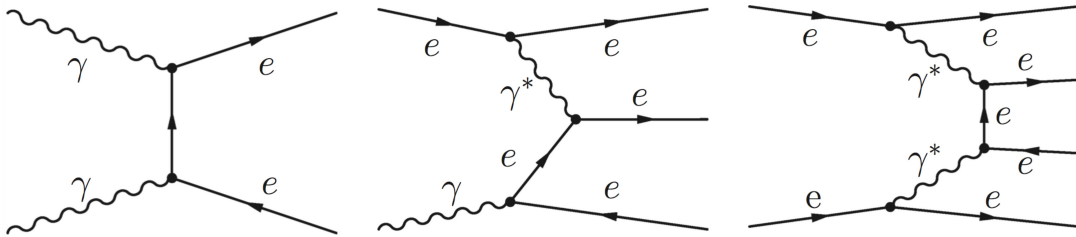

Figure 3.4 Feynman diagrams of the possible e^+e^--pair creation processes: real-real photon collision (Breit-Wheeler process), virtual-real photon collision (Bethe-Heitler process), and virtual-virtual photon collision (Landau-Lifshitz process).

At the ILC with $\sqrt{s} = 500\,\text{GeV}$ centre-of-mass energy, approximately 10^5 e^+e^--pairs are created per bunch crossing with an average energy of 2.5 GeV per particle [86]. The produced pairs cause many background hits in the detectors. The hit rates of each subdetector provide information to understand which part of the detector will be mostly influenced by the pair background. The amount of hits for the beam parameters used in the Detailed Baseline Design (DBD) can be found in Ref. [111]. Those hits are reconstructed as background tracks.

The soft e^+e^--pairs are mostly collimated in the forward region, but not as strongly as the beamstrahlung photons. After the collision of two very forward photons, the created pairs may be scattered in any angle, and they create tracks in vertex detector and in the Time Projection Chamber (TPC) of the ILC, which will be explained in Chapter 4. However, since they are soft particles, they mostly curl and travel along the field lines of the applied magnetic field, which is used mainly in order to determine the transverse momentum of the particles. Therefore, mostly the forward region of the detector is influenced by these pair particles. However, they may also backscatter into the vertex detector or into the TPC due to interactions with the material in the endcap.

Another effect of the e^+e^--pairs is the focusing and defocusing of the pair particles due to the effect of the electromagnetic field of the bunches. When the soft pairs, which are created with a small angle against to the beam axis, are travelling within the electromagnetic field of the other bunch, the opposite-signed particle of the pair with respect to the bunch will be deflected with a large angle (if it has a low p_t) such that it will be detected, while the same-signed particle is

focused to the beam itself. These charged particles of pairs with low p_t will have a significant contribution to the beam-induced background [112, 113].

Since the pair particles are considered as background tracks for any kind of physics analysis, they have to be taken into account. For high energetic signal particles, these background tracks can be reduced by vetoing the low energetic particles. In the case of soft particles, the pair background tracks have a significant effect which requires more investigation. The impact of the pair-background on the tracking of soft particles will be discussed in Section 7.3.

3.5.2   Low p_t $\gamma\gamma$ Overlay

The collisions of two beamstrahlung or bremsstrahlung photons may also produce hadrons in various interactions: direct, vector meson dominance (VMD), anamolous or generalised VMD and deep inelastic scattering. These are explained in [114] in detail. The dominant direct and VMD interactions will be explained in the following.

The parton component of the photons, described by the photon structure function, plays a crucial role in this type of $\gamma\gamma$ collisions. In addition to the direct quark-antiquark production via electromagnetic interaction of point-like photons (direct-direct), the photons can also turn into hadrons before the collision [115]. This process is known as *Vector-Meson Dominance* [116]. If one of the photons interacts hadronically, a parton of the created hadron collides with a photon directly (VMD-direct). Moreover, both photons can turn into hadrons, and their parton components can collide with each other (VMD-VMD) to produce hadronic final states. This type of background arises when the transferred four-momentum to a photon is very low, which will be shown in Section 5.2. Since in this case the photons will be very soft, the possibility to produce this kind of event is so large that the production cross section of these kind of processes diverges, especially when they have very small polar angle.

At the ILC for $\sqrt{s} = 500\,\text{GeV}$ using the TDR nominal parameters, there are in average $\langle N \rangle = 1.2$ events per bunch crossing (BX) coming from this background. However, the previous estimation of $\langle N \rangle = 1.7$ events per BX, the so-called standard overlay, is used in the SM background samples. Because of the huge cross section, this background needs to be generated and simulated separately and to be added at analysis level. However, in the fast simulation part of this thesis it is not included. The effect of this background on the signal and the proposed ways in order to suppress these events will be discussed in Section 7.2.3.1.

Chapter 4

International Large Detector

The ILD detector concept for the ILC is mainly optimised for a method to reconstruct the particles produced in the collisions, the so-called Particle Flow concept, which requires highly granular calorimeters and very precise tracking system. This results in a requirement on the asymptotic momentum resolution of $\sigma_{1/p_t} = 2 \times 10^{-5}\,\mathrm{GeV}^{-1}$, with the p_t dependence as shown in Table 4.1. The Particle Flow concept is motivated by the precision physics goals of the ILC, which require a jet energy resolution of $\sigma_E/E \sim 3 - 4\%$ (equal to $30\%/\sqrt{E}$ at $100\,\mathrm{GeV}$). More details about the Particle Flow concept will be explained in Section 4.2. Another important requirement is the efficient identification of heavy quark jets, in particular based on displaced vertices due to the long lifetime of the particles. This leads to a requirement on the impact point resolution in the order of $\mathcal{O}(\mu\mathrm{m})$ as seen in Table 4.1. In the optimisation of the detector, each of these main requirements lead to specific demands on the sub-detectors as given in Table 4.2.

Parameter	Symbol		Resolution
Jet Energy	$\frac{\sigma_E}{E}$	$\sim$	$3 - 4\,\%$
Momentum	σ_{1/p_t}	$=$	$2 \times 10^{-5} \oplus \frac{1 \times 10^{-3}}{p_t \sin\theta}\,[1/\mathrm{GeV}]$
Impact Parameter	$\sigma_{r\phi}$	$<$	$5 \oplus \frac{10}{p \sin^{3/2}\theta}\,[\mu\mathrm{m}]$

Table 4.1 The main characteristics of the ILD detector. For momentum and impact parameter resolutions the parametrised dependence on momentum and polar angle of the particles are given in the table. Table is adapted from Ref. [86].

This chapter includes the following topics: in Section 4.1, the interaction of particles with matter will be described; in Section 4.2, the reconstruction algorithm introduced above will be explained; and it concludes by explaining the sub-detector systems of the ILD detector in Section 4.3.

Main Resolution	Variables		Resolution
	Spatial Resolution	$\lesssim$	$3\,[\mu\mathrm{m}]$
Impact Parameter	Material Budget	$\lesssim$	$0.15 X_0\,\%$ per layer
Vertex Detector	First Layer, R	$\sim$	$1.6\,[\mathrm{cm}]$
	Pixel Occupancy	$\lesssim$	a few $\%$
Momentum	TPC Momentum Resolution $|_{B=3.5\,T}$	$\lesssim$	$10^{-4}\,[1/\mathrm{GeV}]$
Tracking, TPC	Point Resolution $|_{r\phi}$	$\lesssim$	$100\,[\mu\mathrm{m}]$
	Double Hit Resolution $|_{r\phi}$	$\lesssim$	$2\,[\mathrm{mm}]$

Table 4.2 Sub-detector specific resolutions arising from the main resolution requirements. Table is adapted from Ref. [86].

4.1 Interaction of Particles with Matter

The interaction of particles with matter in high energy particle physics experiments is used to detect and identify the produced particles in a collision event. Depending on the type and energy of the particles, they interact with matter in various ways. Some of them will be summarised in this section.

Charged particles traversing a medium interact with the atomic electrons and lose their energies by the ionisation of atoms. The ionisation energy loss of a single charged particle travelling with a velocity of $v = \beta c$ in a medium with atomic number Z and atomic mass number A is given per length by the Bethe-Bloch equation [15];

$$-\left\langle \frac{dE}{dx} \right\rangle = \frac{e^4 N_A}{4\pi\epsilon_0 m_e c^2} q^2 \frac{Z}{A} \frac{1}{\beta^2} \left[\ln\left(\frac{2m_e c^2 \beta^2 \gamma^2}{I_0} \right) - \beta^2 - \frac{\delta}{2} \right] \qquad (4.1)$$

where the used parameters are described in the following:

e	Elementary charge	β	speed v/c
q	Charge of the incident particle	γ	Lorentz factor $1/\sqrt{1-\beta^2}$
m_e	Electron mass	I_0	Mean excitation energy of the atom
N_A	Avogadro's number	Z	Atomic number of medium
ϵ_0	Dielectric constant	A	Atomic mass of medium
E_C	Critical energy for ionisation	δ	Density effect correction to ionisation energy loss

The ionisation energy loss of a particle depends on the velocity proportional to $1/\beta^2$. The distribution of the ionisation energy loss, $-dE/dx$, as a function of $\beta\gamma$ as well as a function of momentum of various particles is shown in Figure 4.1. The inversely proportional relation can
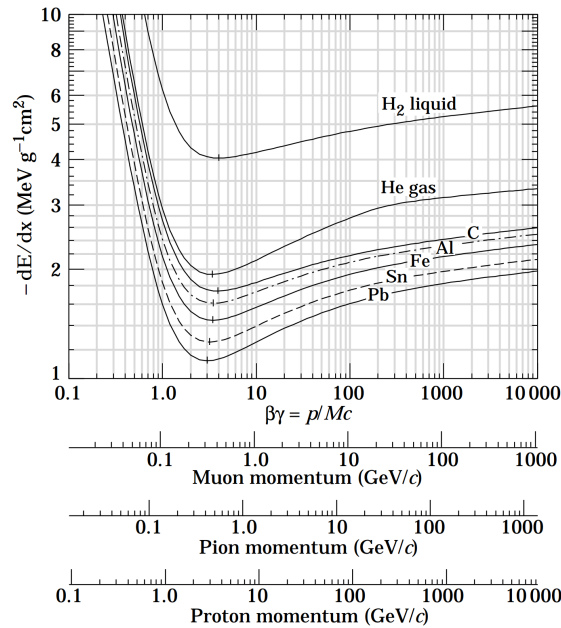
Figure 4.1 The ionisation energy loss curve for a charged particle traversing different mediums. Figure is taken from Ref. [15].

be seen from the figure for $\beta\gamma < 2-3$. For relativistic particles where $v \approx c$, the loss dE/dx grows logarithmically with velocity. This is shown in the high velocity region of Figure 4.1 for $\beta\gamma > 2-3$. In the region where the particles have $\beta\gamma \approx 3-4$, they have the minimum ionisation energy loss and are referred to as minimum ionising particles (MIPs). As can be seen from the figure, this $\beta\gamma$ value corresponds to different momentum values for different particles due to their masses. Both the distribution of the energy loss and the $\beta\gamma$ value which has minimum ionisation are dependent on the material.

All charged particles lose energy through the ionisation of the medium, however other mechanisms also play role in the loss of energy depending on the particle type. For example, the fractional energy loss of electrons or positrons for various processes are depicted in Figure 4.2a as a function of their energies. The figure indicates that there are many processes that contribute to the energy deposition of the electrons. At low energies, the ionisation is the dominant process up to the so-called *critical energy* E_C, which depends on the material type ($E_C^e \approx 10\,\mathrm{MeV}$ for lead). Above the critical energy, the bremsstrahlung becomes the dominant energy loss mechanism. Therefore, the high energetic electrons lose their energy mostly by emitting photons. For muons, the critical energy is around $E_C^\mu \approx 100\,\mathrm{GeV}$ which is quite high compared to electrons due to their higher mass. Below that energy the ionisation is the dominant mechanism for muons. As a consequence of the high critical energy, muons travel through the whole detector ionising the material at almost minimum level.

Figure 4.2b shows the total production cross section of photons as a function of their energies for the main interaction types of the photon with matter. It displays that for low energetic

photons the interaction via photoelectric effect is the dominant contribution. For the photons with moderate energy, the Compton scattering has a significant contribution. At high energies, the pair production $\gamma \to e^+ e^-$ becomes the dominant process. There are two possible sources for the production of pairs: either due to the effect of the field of a nucleus (κ_{nuc}) or due to the effect of the field of an electron (κ_e).

(a) Fractional energy loss of e^- and e^+

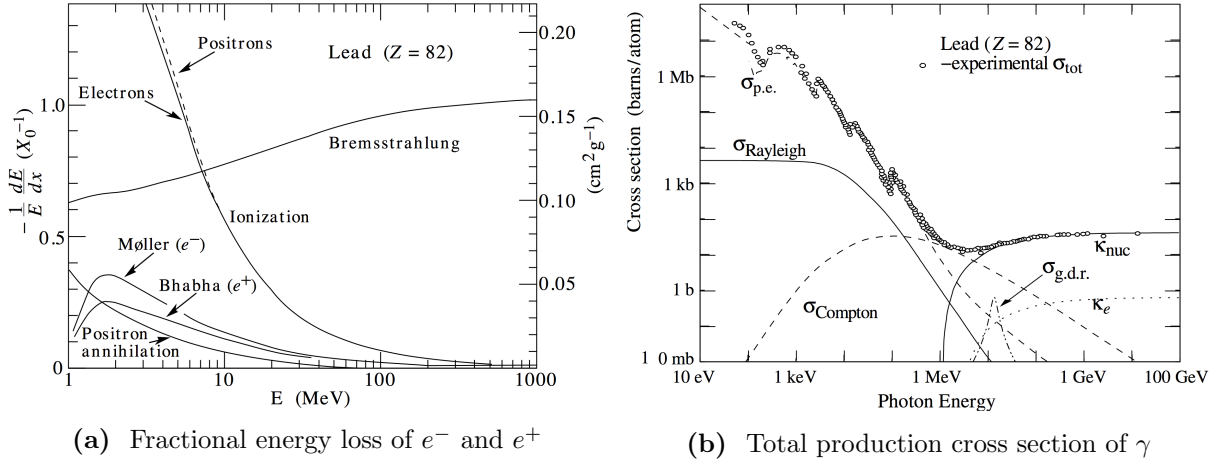**(b)** Total production cross section of γ

Figure 4.2 (a) Fractional energy loss of electrons or positrons as a function of their energies. (b) Total production cross section of photons as a function of energy. p.e denotes the photoelectric effect, κ_{nuc} shows the pair production in the nuclear field, κ_e the pair production in the electron field, and g.d.r indicates photo nuclear interactions (Giant Dipole Resonance). Figure is taken from Ref. [15].

As it is explained above, high energetic electrons emit photons, while the high energetic photons produce $e^+ e^-$ pairs. When these two processes take place successively, it leads to the development of an electromagnetic shower. These showering processes are repeated until the energy of the final state particles falls below the critical energy of electrons, and then the electrons lose their energy by ionisation. The distance between two subsequent processes are determined by the radiation length X_0, which is the average distance over which the electron loses its energy by a factor of $1/e$ by bremsstrahlung.

In contrast to leptons, charged hadrons lose energy by the ionisation process continuously. In addition to this, the charged and neutral hadrons interact strongly with a nucleus of the medium, and the interactions lead to a hadronic shower. The average distance between two strong interactions of hadrons that create hadronic showers is the nuclear interaction length λ_I. The nuclear interaction length is significantly larger than the radiation length, therefore hadronic showers cover a larger volume depending on the density of the material. Another important property of hadronic showers is that they can have many different final states, contrary to the uniformly produced electromagnetic showers. They can also have some electromagnetic component due to the decay of $\pi^0 \to \gamma\gamma$.

In the detection and determination of the momentum of the particles, different kinds of tracking detectors can be used: either large gaseous detectors or detectors based on semiconductor

technology using silicon pixels or strips. In the ILD detector of the ILC, both types of tracking detectors are foreseen. They will be explained in Section 4.3.1.

4.2 Particle Flow Concept

The precision measurements at the ILC require a jet energy resolution $\sigma_E/E \lesssim 3.5\%$ for $50 - 500\,\text{GeV}$ jet energies. In order to be able to achieve such a good precision, calorimeters of the ILC (see Section 4.3.2) are designed by taking into account the requirments of the *Particle Flow Concept* [117, 118]. The main idea behind this concept is to reconstruct each particle in a jet individually, which requires highly granular calorimeters and sophisticated software algorithms in order to separate the energy deposition of each particle from the other particles.

In the particle flow concept, the energies of the charged particles are measured from the tracker measurements, while the photon energy is measured in the electromagnetic calorimeter (ECAL). Only the energies of neutral hadrons need to be measured in the hadronic calorimeter (HCAL), which has a poor resolution compared to the ECAL and tracker measurements. The reconstruction of jets using both the Particle Flow calorimeter (left plot) and the traditional calorimeter (right plot), where all energies are measured in the calorimeters ECAL and HCAL, are shown in Figure 4.3.
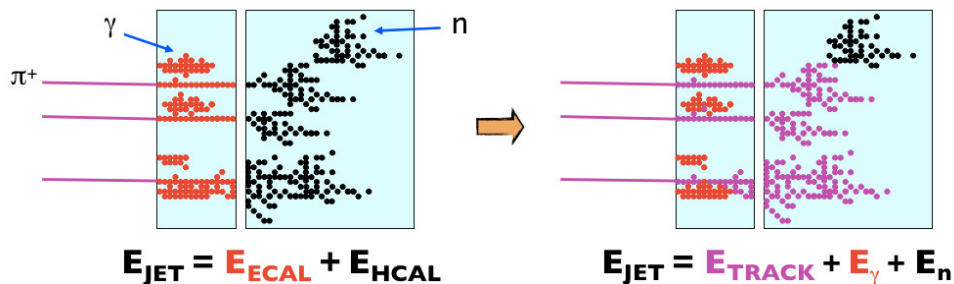

Figure 4.3 The jet energy reconstruction using (left) the traditional method, and (right) using the particle flow method (with fine granularity flow calorimetry). Figure is taken from Ref. [118].

According to the information provided by the LEP experiments from jet fragmentation measurements [119], a traditional jet contains 62% charged particles which are mainly hadrons, 27% photons, 10% long-lived neutral hadrons, and 1.5% neutrinos. This means that using the particle flow calorimetry only 10% of the jet energy will be reconstructed from the HCAL measurements, while it is 72% in the case of typical reconstruction algorithms. Since the design energy resolution of the tracker is $\sigma_E/E = 0.01\%E$, and the energy resolution of the ECAL and HCAL calorimeters are respectively $\sigma_E/E = 15\%/\sqrt{E(\text{GeV})}$, and $\sigma_E/E = 55\%/\sqrt{E(\text{GeV})}$, a typical jet energy can be measured with a theoretical resolution of $\sigma_E/E = 20\%/\sqrt{E(\text{GeV})}$, which corresponds to a better precision than the desired value of $\sigma_E/E \lesssim 3.5\%$ considering the perfect reconstruction case. However, some *confusions* may exist in the reconstruction due to

wrongly merged or split clusters. The important ones can be classified in two classes leading to *loss of energy* and *double counting of energy.*

Figure 4.4 shows these confusions by indicating charged hadrons, photons, and neutral hadrons in violet, red and black colour. The first two sketches correspond to the class leading to a loss of reconstructed energy. In both cases neutral particles, either photon or neutral hadrons, cannot be resolved from charged particles which are close to the neutral particles themselves. In the presence of such confusion, the energy of the neutral clusters is not counted since the reconstructed energy is measured only from the track information of the charged particles, therefore it leads to energy loss. The last sketch of Figure 4.4 shows the case when some of the energy deposition of the charged clusters are split as separate neutral hadrons. In this case, the energy of the separated neutral hadronic cluster will be counted twice: once from the energy of the neutral cluster, and once as the track information of the original charged particle. Therefore this leads to double counting of reconstructed energy.
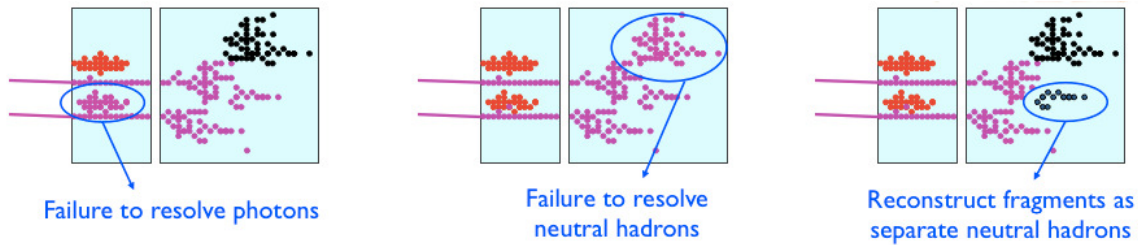

Figure 4.4 The possible confusions in a reconstruction performed with particle flow algorithm. Figure is taken from Ref. [118].

In order to have a good performance of particle flow calorimetry, the confusions needs to be reduced as much as possible. This implies some optimisation on both the calorimeter hardware, to separate electromagnetic and hadronic showers of individual particles, in addition to an accurate tracking detector and software pattern recognition algorithms to yield a good quality of matching between the cluster and track. After matching, the Particle Flow Objects, the so-called Pandora PFOs, are created from the obtained information of the matching. The reconstruction and identification algorithms of the Pandora Particle Flow Algorithm (`PandoraPFA`) will be explained in Section 7.1.

4.3 Subdetectors of ILD

The envisaged resolutions mentioned in the beginning of this chapter result in an ILD detector which has a high precision tracking system including very precise vertex detector, silicon and TPC trackers, followed by a segmented calorimeter system located within a large solenoid. The system is completed with an instrumented iron yoke serving as muon system and tail catcher. For low momentum particles as expected in the search for higgsinos with small mass splittings, the whole tracking system as well as the calorimeters, especially forward calorimeters, plays a significant role.

The overall view and a detailed quadrant view of the ILD detector are displayed in Figure 4.5. The detailed explanation of these sub-detectors are given in the Technical Design Report of the ILC [86]. In the following sections, a brief explanation of them will be presented.
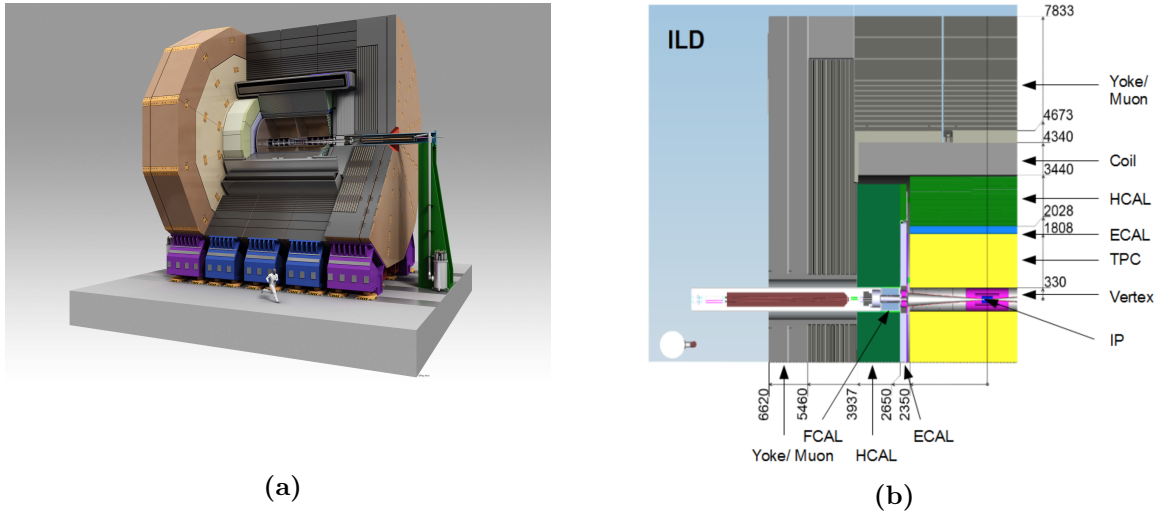

(a)

(b)

Figure 4.5 (a) A view of the ILD detector. (b) Quadrant view of the ILD detector. Figure is taken from Ref. [86].

4.3.1 Tracking Detectors

The tracking system of ILD consists of three sub-detector systems: the vertex detector (VTX), a silicon tracking system consisting of three components, and the time projection chamber (TPC). Each of them will be explained in the following sections in turn.

4.3.1.1 Vertex Detector System

The main aim of the vertex detector (VTX) is to reconstruct the decay vertices of short-lived particles in order to be able to identify them, such as b or c quarks and tau leptons. This feature plays an important role in the ILC precision physics, for example for studies on top quarks, since they decay to b quarks and W bosons. In addition, it is also significant for the reconstruction of particles with low momentum. Therefore, the vertex detector of ILD is optimised for very precise measurements. The performance of a vertex detector is indicated by the resolution of the impact parameter of charged particles, which depends on the momentum and polar angle of the particles as follows:

$$\sigma_{r\phi} = 5\,\mu\text{m} \oplus \frac{10\,(\text{GeV})}{p\,(\text{GeV})\sin^{3/2}\theta}\,\mu\text{m} \tag{4.2}$$

The given resolution leads to some necessities for the ILD detector: the spatial resolution near the interaction point (IP) should be better than $3\,\mu$m, the material budget should be below

0.15% of a radiation length (X_0) per layer, the first layer of the detector should be located at a radius of nearly 1.6 cm to be as close as possible to the beam pipe, and pixel occupancy should not exceed a few percent. In addition, the power consumption should be low to be able to use cooling systems with low material budget such as air cooling.
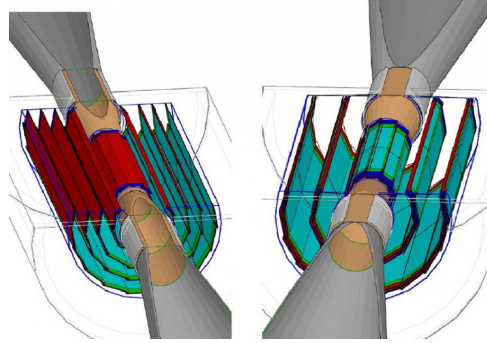

Figure 4.6 The proposed Vertex detector geometries: (left) five single layers, and (right) three double layers. Figure is taken from Ref. [120].

The ILD vertex detector is designed with cylindrical, concentric layers [121]. According to the number and type of the layers, there are two proposed geometries: either three double-sided layers as seen on the right of Figure 4.6, or five single-sided layers as on the left of Figure 4.6. The former geometry with double-sided layers has pixel sensors on both sides and therefore provide six measured positions, while the latter can have five points corresponding to each layer. The radii of the layers change from 15/16 mm to 60 mm in both geometries.

There are three sensor technologies that are studied for the ILD vertex detector. These are Complementary Metal-Oxide-Semiconductor (CMOS) Pixel Sensor (CPS) [122], Fine Pixel Charged Coupled Device (FPCCD) sensor [123], and Depleted Field Effect Transistor (DEPFET) sensor [124] technologies. CPS and DEPFET technologies use a power-pulsed readout, which is performed between bunch trains and reduces the power consumption. In principle the same readout method could be used for FPCCD technology as well. However since FPCCD has a slow readout due to the large amount of pixels arising from the very small pixel size of 5 μm pitch, one needs to be careful to be able to read out the data between bunch trains [86].

In the determination of the pixel type and readout, three main properties explained above need to be taken into account: high spatial resolution, fast readout, and low power consumption. In the case of CPS technology, for the innermost layer two different pixel sensors are situated on both sides where they serve for two different necessities of the vertex detector. One of the pixel sensors is chosen to have high spatial resolution, while the other one is optimised for fast readout. The high precision pixels, which are square pixels with 17×17 μm^2, provide a spatial resolution smaller than 3 μm and have a readout time of 50 μs [86]. The fast sensors, which are rectangular pixels with 17×85 μm^2, provide a better time resolution up to 10 μs due to the less amount of pixels, and yield an increased spatial resolution of nearly 6 μm. For the outer layers, the pixels are optimised to minimise the power consumption. The pixels with 34×34 μm^2 yield a spatial resolution of 4 μm, while providing the readout in 100 μs [86].

CMOS is the technology used in detector simulation studies for the DBD[1]. Even though it is optimised for fast read out, it still samples ~ 15 bunch crossings (BX) in each image. This might cause problems in the physics analysis due to high amount of the background collected from each bunch collision, especially for an analysis including low momentum particles. As explained in Section 3.5.1, it is not straightforward to suppress this background in this kind of analysis.

FPCCD technology [123] also uses a double-sided layer design, but the same pixels are used on both sides of the layer. Since the pixel pitch is very small it has quite high (sub-micron) spatial point resolution. The feature of having small pixels also provides an excellent separation for two tracks. As in the case of CPS, a larger pixel size is used for the outer layers, which is two times larger in the case of FPCCD.

DEPFET technology [124] follows the design of single-sided layers and uses a silicon sensor with self-supporting layers. Since there is no other external supporting material, this leads to a very good mechanical properties, for example reduced mechanical stress due to the absence of any mismatching of thermal coefficients, and minimum material budget. In order to keep the power consumption low, the readout is performed using a shutter which leaves only one single row of the pixels active during the operation. The current row readout time achieved is 80 ns which corresponds to slower frame readouts compared to other two technologies. However, the R&D studies aim to achieve approximately 40 ns row readout time corresponding a frame readout of 50 μs and 100 μs for the innermost and outer layers [86]. One of the proposed approaches in order to improve the readout speed is to read out two rows in parallel.

4.3.1.2   Silicon Tracking

The silicon tracking consists of three silicon detectors, which are the Silicon Inner Tracker (SIT) and Silicon External Tracker (SET) placed in the barrel part, and the Forward Tracker (FTD) situated in the forward region. The SIT and SET are located between the vertex detector and the TPC, and between the TPC and the barrel electromagnetic calorimeter (ECAL), respectively. They provide precise matching for the hits between the VTX detector and the TPC, and between the TPC and the ECAL clusters. They improve the momentum resolution of the overall tracking system. In addition to this, they also enable time-stamping information by combining the hits form these silicon detectors with the TPC hits. Moreover, the SIT improves the reconstruction of the low p_t charged particles which may not reach sufficiently far in the TPC, and the long-lived stable particles, which decay within the tracking system, by extending the tracking acceptance down to the vertex detector.

These three central region silicon components are made of layers, each with two single-sided strip layers tilted by a small angle with respect to each other, the so-called 'false' double-sided layers. The SIT has two such layers, while the SET includes just one, providing in total three precise space points for central tracks. In all of the silicon central tracking system, the same micro-strip sensors and the same mechanical design for the basic detector unit are used.

---

[1]Detailed Baseline Design

The last silicon detector FTD is located in the very forward region where the TPC does not have any coverage. It consists of seven tracking disks between the beam pipe and the inner field cage of the TPC, which one can see from Figure 4.5a. The first two of the disks are made of pixels and the last five disks are strip detectors. It provides precise tracking down to angles of approximately 7 degrees. This feature of the ILD detector provides an important key ingredient for the physics studies, especially for the new physics. However, since the magnetic field orientation is not useful for bending the charged particles moving in forward direction, the momentum resolution is not as precise as the central region. In addition to this, the jets going to this region stay closer to each other due to the reduced effectiveness of the magnetic field, which results in larger occupancies. Another challenge is the presence of high backgrounds, since the disks are located very close to the beam axis.

The first two disks use pixel detectors to deal with the expected high occupancies. As explained in Section 4.3.1.1, there are three possible pixel technologies under study; CPS, FPCCD, and DEPFET. Instead of the layer structure of the vertex detector, the technologies are implemented to the petal concepts for the forward tracker disks. For the last five disks micro-strip detectors are used in order to achieve the best momentum resolution despite the mentioned difficulties, since the micro-strip detectors provide the most precise $r\phi$ measurement within the tight material budget.

4.3.1.3   Time Projection Chamber

The central tracker of the ILD detector is a Time Projection Chamber (TPC) which enables continuous, three dimensional tracking in (r, ϕ, z) directions. The TPC consists of a gas-filled large sensitive volume with low material budget including a cathode in the middle and two anodes in the endplates. A sketch of half of the TPC is displayed in Figure 4.7 and shows the working principle. It is based on the ionisation of gas atoms when the charged particles pass through the sensitive volume and interact with the atoms of the gas. The ionisation causes the production of electron-ion pairs, which move by the effect of an homogeneous electric field applied between the anode and cathode. The electrons created in the primary ionisation travel towards to the anode, while the ions travel in the opposite direction. In addition to the electric field, a high magnetic field with a strength of 3.5 T will be applied as well in order to determine the momentum of the particles. The electrons reach the anode, which includes both amplification and readout planes. The readout of the amplified signal electrons gives two-dimensional projections of the initial particle trajectories. For the third dimension, an external trigger is used to measure the time between the primary ionisation of the atom and arrival of the created electron to the readout system. Since the drift velocity of the gas is known, the third dimension can be obtained using information of both time and drift velocity.

The momentum resolution is a key parameter for particle physics experiments. To acquire a good momentum resolution, the detector is therefore placed within a superconducting solenoid coil which provides maximum 3.5 T central magnetic field. This results in a design momentum resolution of the TPC of $10^{-4}\,\mathrm{GeV^{-1}}$. The point resolution is better than $100\,\mu\mathrm{m}$, and a smaller than 2 mm double-hit resolution which indicates how well one can distinguish two very close hits of the TPC under these conditions (see Table 4.2).
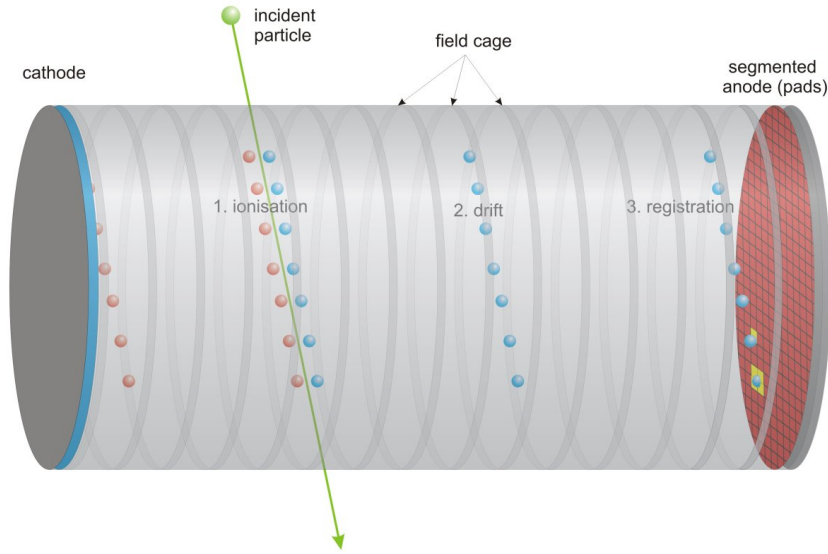
Figure 4.7 A sketch of a TPC showing its working principle. Figure is taken from Ref. [125].

The point resolution and double-hit resolution of a TPC are moderate compared to silicon tracking, however they are easily compensated by continuous tracking. The ability of having continuous tracks allows the reconstruction of non-pointing tracks, which are very important for the particle flow measurements and for the physics analysis. The amount of material of the TPC is at a much lower level compared to other tracking detectors, which provides not only the desired material budget for the particle flow calorimetry, but also superior resolution at small p_t. In addition, the TPC also offers particle identification using dE/dx with an estimated resolution of 5% [86].

The main parts of the TPC are shown in the right sketch of Figure 4.7. The TPC mainly consists of two endplates that serve as anodes, a central electrode as cathode, and a field cage covering the barrel part of the TPC volume which contains field strips. The strips provide an homogeneous electric field within the drift region of the TPC, and their potential is determined by a voltage divider. One missing part in this sketch is the technology for gas amplification.

There are two main options for the gas amplification under investigation, Micromegas [126, 127] and Gas Electron Multipliers (GEM) [127]. They both use pads with size of $\approx 1 \times 6\,\mathrm{mm}^2$, resulting in 10^6 pads per endplate. If the amplified charges are spread over the pads, a good point resolution could be achieved. In the case of GEMs, two or three GEM foils are stacked on top of each other in order to obtain the sufficient amplification. The transverse diffusion within the GEM stack is enough to spread the charge over several 1 mm wide pads, which provides a good point resolution. For Micromegas, a single structure is enough to amplify the signal sufficiently, but the spreading of signals on the readout plane is very small. Therefore, a resistive coating on the anode surface is used in order to spread the charge over several pads [128].

In the resolution of the TPC, the gas also plays an important role. Depending on the properties
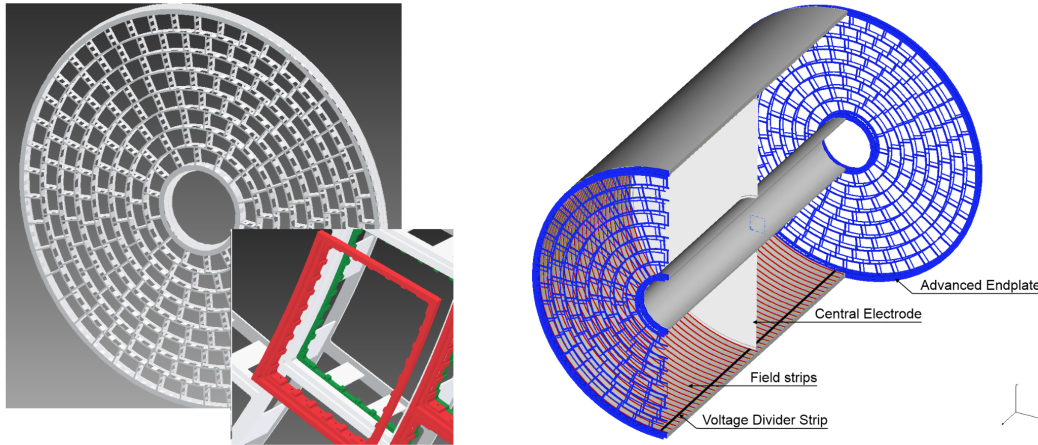
Figure 4.8 (a) Sketch of the endplate of the TPC with a zoomed version showing the supporting dead part (gray material) of the readout modules (red). (b) Sketch of the TPC which shows the main components of the TPC. Figure is taken from Ref. [86].

of gases, the drift velocity and the transverse diffusion changes. Therefore, the gas is chosen with the aim of minimising the diffusion and maximising the drift velocity. There are three commonly studied TPC gases which are T2K : $Ar(95\%), CF_4(3\%), C_4H_{10}(2\%)$, P5 : $Ar(95\%), CH_4(5\%)$, and TDR : $Ar(93\%), CH_4(5\%), CO_2(2\%)$. Due to the properties explained above, T2K gas is chosen as a promising candidate. More details about the properties of these three gases will be explained in Section 8.3.

The endplates support the modular readout and amplification system as sketched in Figure 4.7. In the zoomed sketch, one can clearly see the supporting mechanical structure.

One of the challenges of the TPC is that ions produced during the primary ionisation or during the amplification drift back to the cathode and cause field distortions for the electrons. The effect of the ions from the primary ionisation are negligible. However, the ions produced during the amplification form ion discs because of the drift velocity differences between electrons and ions (since the ions are heavy, they drift slowly) as seen in the upper half of Figure 4.9, and shift the transverse direction of the electrons. One proposed solution is to use ion gates to prevent the ions from entering the drifting volume as shown in the lower half of Figure 4.9. Since in this case there are significantly less ions drifting back, there are no distortions on the direction of the electrons.

4.3.1.4 Performance

The whole tracking system covers the polar angle region down to $7°$ as seen in Figure 4.10a. However, the central tracking detector TPC functions only down to $\theta \approx 37°$ with full performance, while the forward FTD detector plays an important role for the small polar angle region. The VTX detector provides a coverage down to $\theta \approx 16°$. Figure 4.10b displays the momentum resolution of the tracking system in total for different polar angle values as a function of the mo-
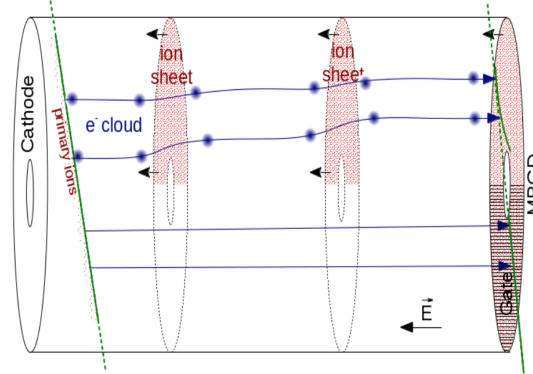
Figure 4.9 Ion discs and their effect on the electrons (upper half of the figure), as well as ion gate solution to compensate for these effects (lower half of the figure). Figure is taken from Ref. [86].

mentum. The points display the results of the full simulation performed using muons generated at given certain polar angles within a momentum range of $1 - 200\,\text{GeV}$, while the lines show the result from the parametrisation given in Table 4.1. The figure indicates that especially for high momenta the obtained precision is compatible with the design resolution.
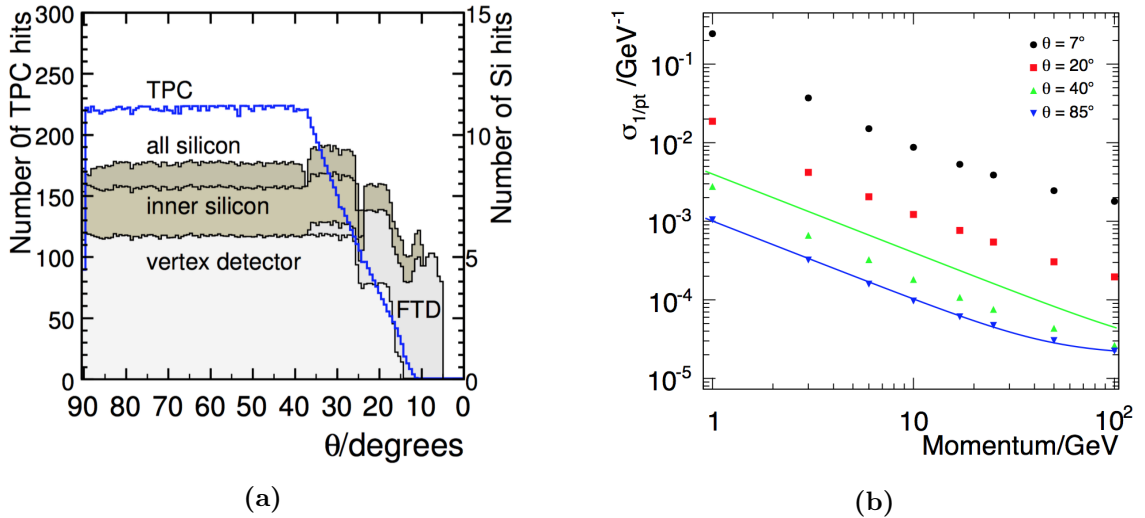

(a)   (b)

Figure 4.10 (a) The number of hits of 100 GeV muons in the tracking detectors as a function of polar angle θ in the ILD detector and (b)Transverse momentum resolution for a single muon events as a function of transverse momentum for different polar angles. The points indicate the results of the full simulation performed as it is explained in the text. The lines show the foreseen parametric resolution for $\theta = 40°$ and $\theta = 85°$. Figure is taken from Ref. [86].

The track reconstruction efficiency of simulated high multiplicity $t\bar{t} \rightarrow 6$ jets events in the presence of pair background at $\sqrt{s} = 500\,\text{GeV}$ and $\sqrt{s} = 1\,\text{TeV}$ is shown in Figure 4.11 as a function of momentum and the cosine of the polar angle. The figure shows that the tracks can be
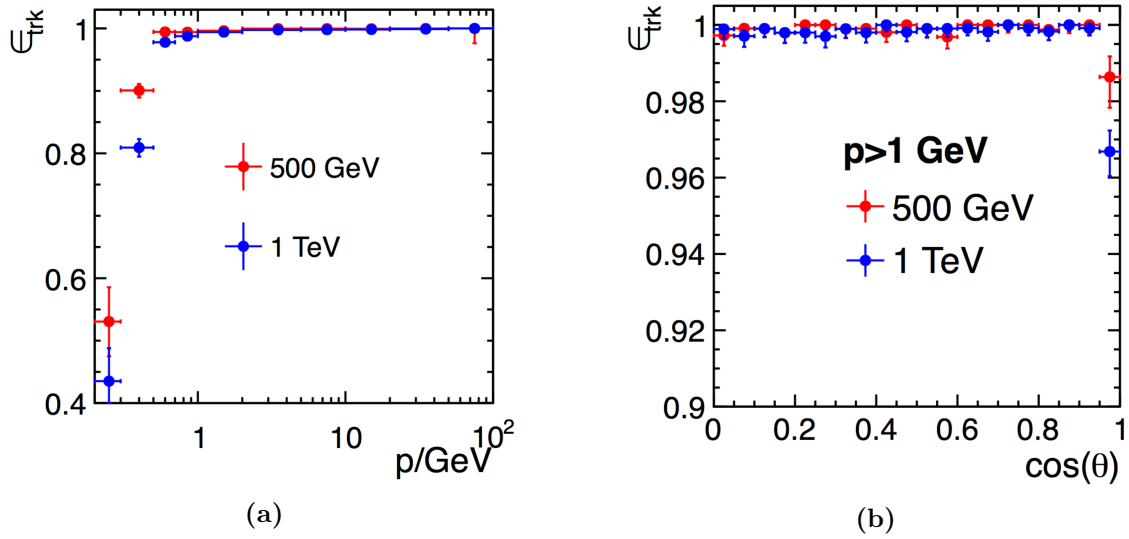
Figure 4.11 Tracking efficiency for $t\bar{t} \to 6$ jets events including pair background for centre-of-mass energies of $\sqrt{s} = 500\,\mathrm{GeV}$ and $\sqrt{s} = 1\,\mathrm{TeV}$ as a function of (a) momentum and (b) $\cos\theta$ for $p > 1\,\mathrm{GeV}$. Figure is taken from Ref. [86].

reconstructed with on average 97% efficiency for tracks having momenta larger than $p > 1\,\mathrm{GeV}$ and for $\cos\theta < 0.95$. For tracks with lower momenta than $p < 1\,\mathrm{GeV}$ the efficiency goes down to $\sim 40\%$ for $p = 0.2\,\mathrm{GeV}$. The tracking efficiency of tracks for $p < 0.2\,\mathrm{GeV}$ has not been studied yet. However, these low momentum particles are crucial for the subject of this thesis. There are ongoing studies on the reconstruction of such low momentum particles, and they will be summarised in Section 7.3.

4.3.2   Calorimeters

The calorimeter system of ILD contains two main calorimeters which are an electromagnetic calorimeter (ECAL) and a hadronic calorimeter (HCAL) located on the barrel and on two end-caps after the external silicon tracking system. Both ECAL and HCAL are sampling calorimeters consisting of an absorber used to absorb the energy of the traversing particles and an active medium used to generate the signal. The reason to use sampling calorimeters is that they respond well to the requirement of high granularity needed for the particle flow and to the requirement of compactness in order to reduce the size of the coil that covers the calorimeters, for cost reasons.

At very small polar angles, there are three dedicated calorimeters, LumiCAL, BeamCAL and LHCAL, which are called forward calorimeters. They are used to measure luminosity, pairs from beamstrahlung and neutral hadrons, and to determine the nominal beam parameters. In addition, they also help to close the gaps to achieve hermeticity, which is especially important for low p_t particles since they go mostly through the forward region.

A detailed explanation of the ILD calorimeter system is given in [86]. In the following sections, the sub-systems and their main properties will be summarised.

4.3.2.1   Electromagnetic Calorimeter

The electromagnetic calorimeter is mainly responsible for identification of photon and measurement of the photon energies as a consequence of the particle flow. Therefore, it is optimised for these two main tasks. The Molière radius (R_M) of the chosen material is one of the key parameters in the optimisation. A small Molière radius helps to separate the showers close to each other in transverse direction. The ECAL serves not only for photon reconstruction but also for the reconstruction of the detailed shower properties, which will be useful in order to distinguish the electromagnetic (EM) showers from hadronic showers which have already started showering in the ECAL. In that sense, a large ratio of interaction length (λ) to radiation length (X_0) is used to optimise the separation of the showers. The reason for this is that the large interaction length will reduce the fraction of the hadronic showers starting in the ECAL, while the small radiation length will cause the EM showers to start earlier.

Considering the above conditions, a tungsten absorber has been chosen for the ILD baseline design, since it is compact and has a large ratio of interaction length to radiation length with $\lambda_I = 99\,$mm, $X_0 = 3.5\,$mm and small Molière Radius of $R_M = 9\,$mm. In the longitudinal direction the ECAL has 30 readout layers with total thickness of 24 radiation lengths, $24X_0$. In the baseline design, silicon pixels with a size of $5 \times 5\,$mm^2 have been chosen. An alternative to the baseline design are scintillator strips with a size of $5 \times 45\,$mm^2, which are arranged in alternative directions such that the effective granularity will corresponds to $5 \times 5\,$mm^2.

4.3.2.2   Hadronic Calorimeter

The hadronic calorimeter of ILD is optimised to distinguish the charged and neutral hadronic showers, and to determine the energy of the neutral hadrons. In addition, each hadronic shower will also have some electromagnetic energy due to emitted photons along showering, which needs to be taken into account.

In the baseline design of the hadronic calorimeter (HCAL), steel is used as an absorber, while either scintillator tiles or gaseous devices are proposed for the active medium. Compared to the ECAL absorber tungsten, steel has a moderate ratio of interaction length of $\lambda_I = 17\,$cm, and a radiation length ratio of $X_0 = 1.8\,$cm, which results in a fine longitudinal sampling in terms of X_0 with in total 48 readout (active) layers, corresponding to 6 times the interaction length $6\lambda_I$. This fine sampling helps with the measurement of the EM energy part of the hadronic showers and for the determination of the shower structure with a good resolution. The scintillator tiles option has an analogue readout system (AHCAL) segmented by $3 \times 3\,$cm^2 cells in the transverse direction, and gaseous devices have a semi-digital readout system (SDHCAL) with $1 \times 1\,$cm^2 cells. The AHCAL readout system has been considered in the simulations for the DBD analyses.

For the barrel region, two absorber geometries are proposed; with longitudinally 2 rings and azimuthally 16 modules, or with longitudinally 5 rings and azimuthally 8 modules. In the DBD design, the first geometry option is used for the scintillator tiles.

4.3.2.3   Forward Calorimeters

There are two main calorimeters dedicated for the very forward region of the ILD detector as seen in Figure 4.12; LumiCal[2] located in a circular hole of the ECAL endcap covering polar angles between 31 and 77 mrad, and BeamCal placed in front of the final focus quadrupole near the beam pipe with an angular coverage from 5 to 40 mrad. In addition to these, there is an extra hadron calorimeter specified for the low angle region, LHCAL, which extends the angular coverage of the HCAL to the same range as the LumiCal.
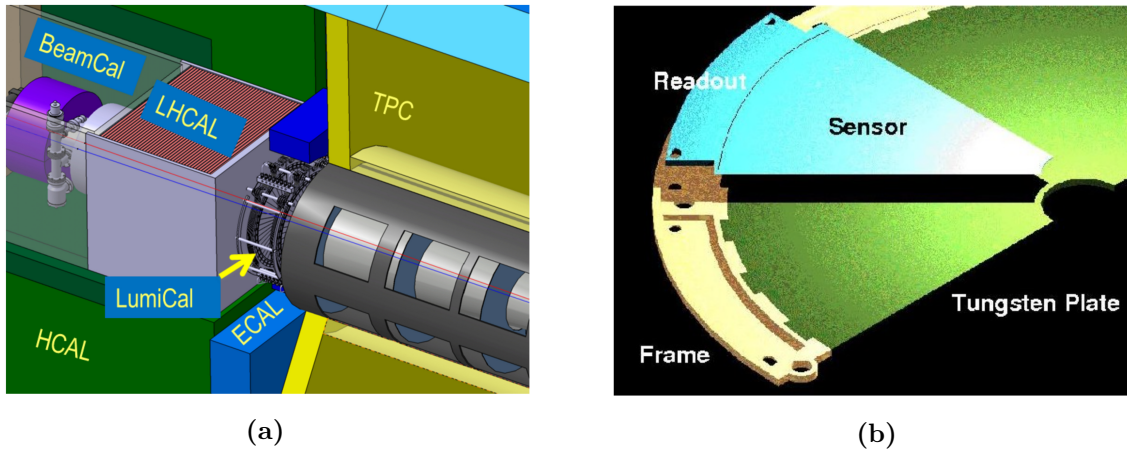

(a)   **(b)**

Figure 4.12 (a) Forward detectors of the ILD. (b) A half layer sketch including absorber and sensor structure. Figure is taken from Ref. [86].

The LumiCal is designed to measure the luminosity with a precision better than 10^{-3} at centre-of-mass energy of $\sqrt{s} = 500\,\text{GeV}$ using Bhabha scattering events. The measurement is done as explained in Section 3.4.4.

The BeamCal serves for two purposes using the deposited energy information from the beamstrahlung pairs explained in Section 3.5; one of them is the estimation of the bunch-by-bunch luminosity, and the other one is the determination of the beam parameters with a precision of 10%. Moreover, it is also used to suppress the background for measurements of high energetic electrons in the very forward region. Therefore, it carries crucial importance for new physics searches based on large missing energy as in the context of this thesis.

Figure 4.13a shows the distribution of the energy deposition by beamstrahlung pairs superimposed with a high energetic electron. It shows that the amount of the hits caused by the

---

[2]The LumiCal should be centred around the outgoing beam, since it is supposed to measure the polar angle of the scattering beam particles.
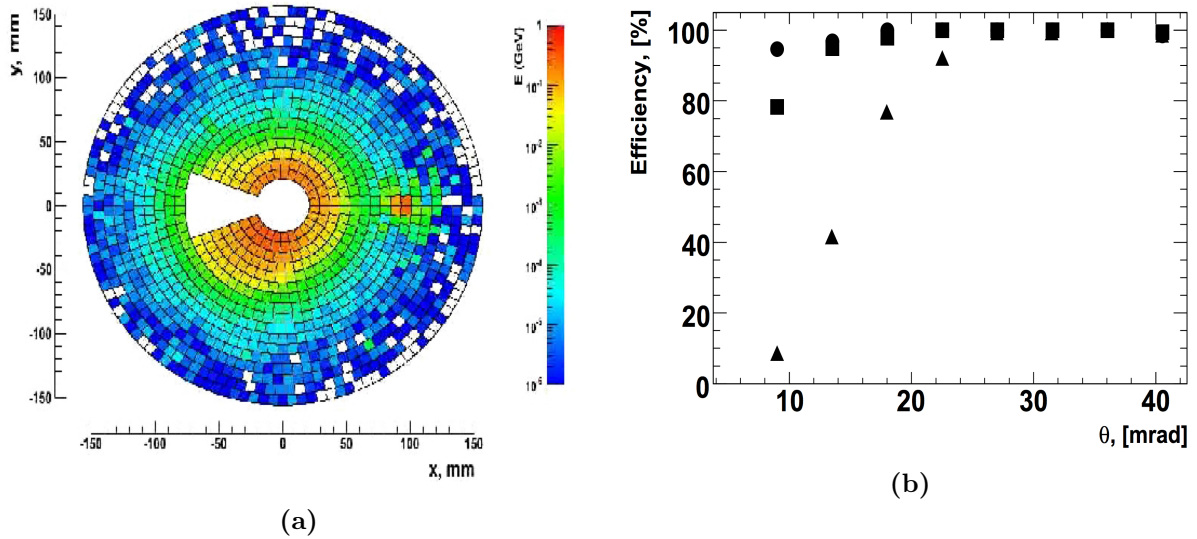
(a)

(b)

Figure 4.13 The distribution of the energy deposited by beamstrahlung pairs after one bunch crossing in the BeamCal. A single high energy electron deposition is superimposed as well, seen as red spot on the right side around $(x, y) \approx (100, 0)$. (b) The detection efficiency of single high energy electrons in the presence of the pair background for various electron energies as a function of polar angle. The triangles, squares and circles denotes respectively the electron energies of 75 GeV, 150 GeV, and 250 GeV. Figure is taken from Refs. [86, 104], in turn.

background is quite large, especially in the centre region. The high energetic electrons come from the electrons scattered under a small angle, especially from $\gamma\gamma$ and $e\gamma$ type of processes. This signature can be distinguished from the pair backgrounds due to its energy and also the position of the energy deposition in the BeamCal, as seen in the right side of Figure 4.13a around $(x, y) \approx (100, 0)$ as a red spot. The efficiency to detect a high energetic electron on top of the pair background is shown in Figure 4.13b for various electron energies. The triangles shows the 75 GeV electrons, the squares shows the electrons with 150 GeV, and the circles denotes the electron energies of 250 GeV. It depicts that when the electron energy decreases, the efficiency to detect it decreases as well. The electrons with $E \approx 150$ GeV can be detected by $\sim 95\%$ efficiency down to 15 mrad, while the same efficiency can be acquired for $E \approx 75$ GeV electrons down to 24 mrad. This feature of the BeamCal will be used in the preselection step of the analysis that will be explained in Section 6.1.

Both LumiCal and BeamCal detectors are cylindrical sandwich calorimeters made of tungsten absorber triangular discs of one X_0 thickness, and followed by silicon (LumiCal) or gallium arsenide (BeamCal) triangular sensor planes as seen in Figure 4.12b. Both need fast readout, because of high occupancy stemming from beamstrahlung and two-photon processes. Especially the BeamCal experiences a large number of electrons due to its angular coverage in very forward region. Therefore, the sensors which will be used in the design of the BeamCal should be radiation hard.

In order to reduce the amount of pair background, the detector is designed so that the pairs leave the detector through the beam pipe. Because of that, an anti-DID (Detector Integrated Dipole) field is applied for focusing the pairs along the beam pipe.

4.3.2.4   Performance

The jet energy resolution of the ILD detector has been tested with the separation of the $\nu_e \bar{\nu}_e WW$ and $\nu_e \bar{\nu}_e ZZ$ events via the reconstructed invariant mass of di-jets [129]. Figure 4.14a and 4.14b show the reconstructed invariant mass of di-jets and the average reconstructed di-jet mass distribution at $\sqrt{s} = 1\,\text{TeV}$ centre-of-mass energy. The figures indicate that the jet energy resolution is good enough to separate the W and Z bosons decaying hadronically.
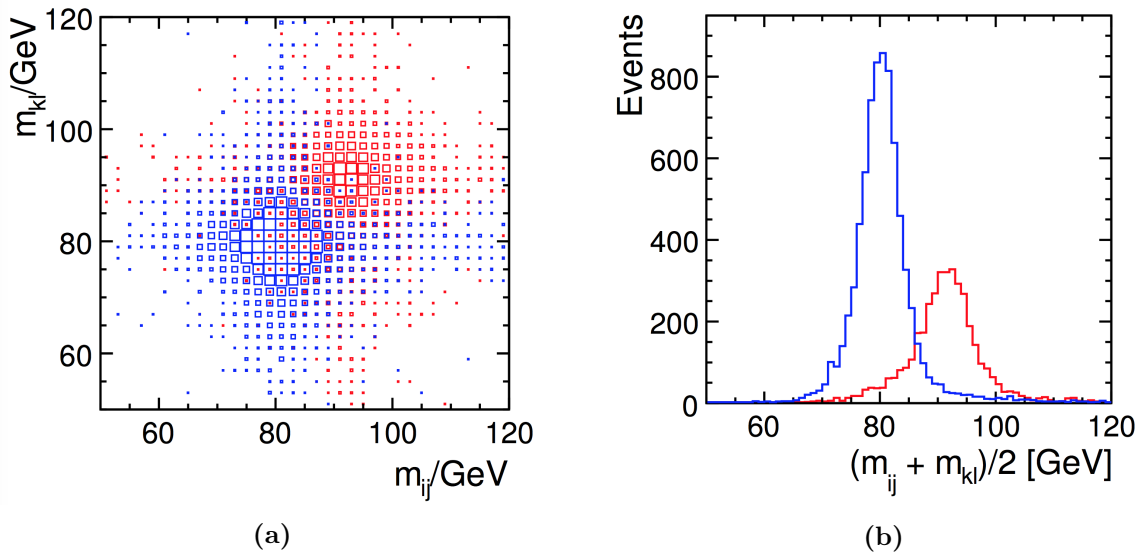

Figure 4.14 (a) The reconstructed di-jet mass distributions for the best jet pairing in $\nu_e \bar{\nu}_e WW$ (blue) and $\nu_e \bar{\nu}_e ZZ$ (red) events at centre-of-mass energy of $\sqrt{s} = 1\,\text{TeV}$. (b) Average reconstructed di-jet mass distribution for the best jet-pairing in $\nu_e \bar{\nu}_e WW$ (blue) and $\nu_e \bar{\nu}_e ZZ$ (red) events. Figure is taken from Ref. [86].

4.3.3   Muon System

The muon system of ILD consists of two separate parts which are made of iron including sensitive layers in between: the first part consists of 10 layers spaced 14 cm apart for both barrel and endcap, while the second part includes three (barrel) and two (endcap) layers spaced by 60 cm as shown in Figure 4.15. The first part of the muon system also serves as tail catcher in order to recover the energy leaking from the calorimeters, whereas the second part is responsible only for muon system. The barrel part of the muon system has one extra sensitive layer in front of it which is not shown in the figure, with the aim of maximising the performance of the tail catcher which is limited by the material of the coil. For the sensitive layers, two main options exist; scintillator strips with wavelength-shifting fibres and readout with silicon photomultipliers

from both sides, or alternatively a gaseous detector resistive plate chambers, which has excellent granularity of $1 \times 1\,\mathrm{cm}^2$.
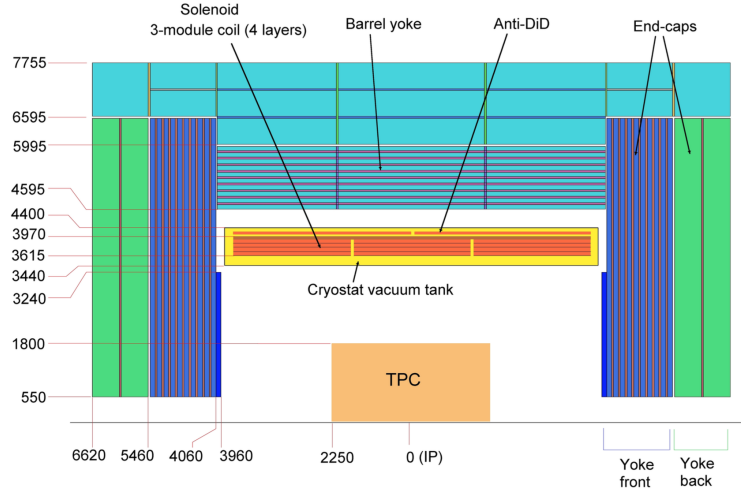

Figure 4.15 Muon system of ILD, dimensions are in mm. Figure is taken from Ref. [86].

The primary task of the muon system is the identification of isolated muons. Most of the misidentified muons are pions, which decay to muons or go through the detectors, and are detected in the muon system. The efficiency of the muon identification considering the pion contamination for low energetic particles as a function of the energy of the particles is shown in Figure 4.16a. The blue lines correspond to the first 11 layers of the muon system, and the green

(a) μ ID efficiency and π contamination

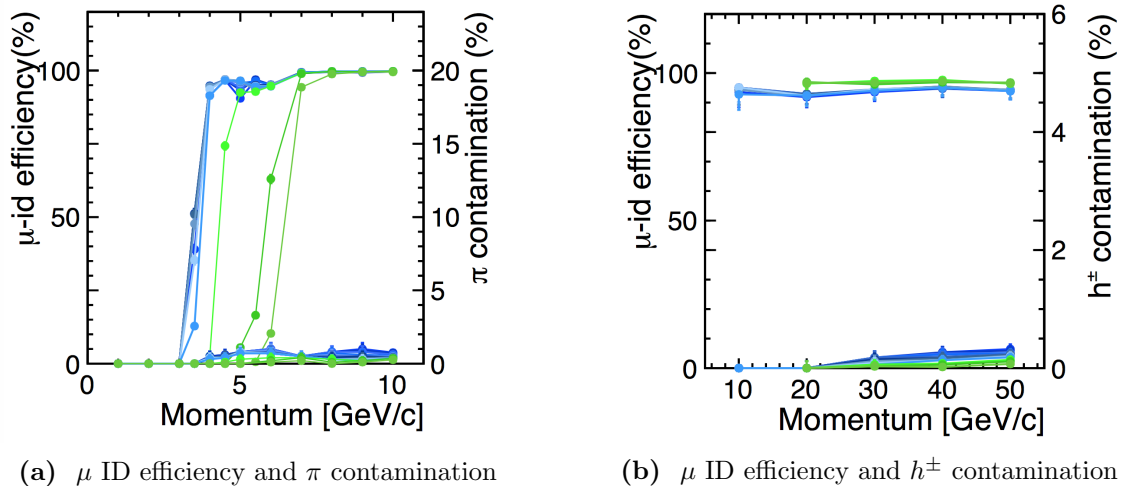**(b)** μ ID efficiency and $h^{\pm}$ contamination

Figure 4.16 Simulated muon identification efficiencies and contaminations as a function of momentum. The blue lines correspond to the first 11 layers of the muon system, and the green lines show the remaining part of the muon system. In hadron contamination, semileptonic decay products of b-quarks are used. Figure is taken from Ref. [86].

lines show the rest part of the muon system. It indicates that only the muons with $p > 7\,\text{GeV}$ can go through all the layers of the muon system. Low momentum muons below $4\,\text{GeV}$ cannot reach the second part of the system. The pion contamination for $p > 7\,\text{GeV}$ is around 20%.

Since the muon in a jet is accompanied by hadronic background, the muons have a hadronic contamination in this case. This is studied using the semileptonic decays products of the b quarks, and the results are depicted in Figure 4.16b. It shows that the high energetic muons ($p > 7\,\text{GeV}$) can be identified with 97% efficiency, whereas there are a few percent hadron contamination.

Figure 4.16 indicates that the muon identification can be done very efficiently for high momentum particles ($p > 7\,\text{GeV}$), whereas the muon system cannot be used for the particles with lower momentum than that, especially lower than $p < 4\,\text{GeV}$. In this case, the high granularity of the ILD detector, which provides MIP-like track signatures for the muons, can be used to identify muons which can not reach the muon system. The proposed method to identify low momentum muons below $2\,\text{GeV}$ will be explained in Section 7.4.

Chapter 5

Natural Supersymmetry with Light Higgsinos

Natural supersymmetry is a well motivated scenario by naturalness as explained in Section 2.2.4. It leads to a light electroweak SUSY sector and a rather heavy coloured SUSY sector beyond the LHC discovery range, by requiring the higgsino mass parameter μ at the electroweak scale. The μ parameter has two important features which make higgsinos distinct from the other MSSM superpartners of the Standard Model (SM) particles. First, the higgsino mass parameter μ is allowed by unbroken SUSY (cf. Equation (2.90)), and therefore the size of it is not necessarily related to the scale of SUSY breaking. It is the only dimensionful MSSM parameter in unbroken SUSY because of this property. Second, since μ enters the tree-level Higgs potential (cf. Equation (2.96)), it is directly connected to the electroweak scale. This can be also seen from the Z boson mass given at tree level as follows (please see Equation (2.125) for one-loop level):

$$m_Z^2 = 2\frac{m_{H_u}^2 \tan^2\beta - m_{H_d}^2}{1 - \tan^2\beta} - 2|\mu|^2. \tag{5.1}$$

In the large $\tan\beta$ limit, the Z boson mass is given by the following equation:

$$m_Z^2 = -2(m_{H_u}^2 + |\mu|^2)\,, \tag{5.2}$$

where m_Z is directly proportional to the up-type Higgs mass which is the SM-like Higgs boson and higgsino mass parameter μ. In the equation, each term should be at the electroweak scale to obtain the Z boson mass without introducing large fine-tuning. The higgsino mass parameter at the electroweak scale requires to have light higgsinos in the theory. Since this fine-tuning does not depend on the masses of the other MSSM superpartners, in principle all of the squark, slepton, and gluino masses can be much larger. However, there is another important parameter determining the naturalness of the theory which is the Higgs boson mass at loop level. The hierarchy problem states that the Higgs boson mass has a large contribution from the top quark loop due to the large Yukawa coupling, that cause quadratic divergence. In supersymmetric theories, this loop contribution is cancelled by the stop loop contribution in the case of equal

mass condition ($m_t = m_{\tilde{t}}$). But, since supersymmetry is not an exact symmetry, the soft SUSY breaking requires the stops to be not much heavier than the top quark so that the cancellation of the top quark loop contribution to the Higgs mass will be in a reasonable level to avoid the quadratic divergence. Therefore, generally the stop mass is also considered to be light, while the stop quarks can be excluded up to 650 GeV by the LHC experiment results [64]. In the content of this thesis, the most challenging scenario especially for the LHC, which has light higgsinos and no other supersymmetric particles below a TeV, will be studied.

The structure of this chapter is as follows. In the next section, the mixing of charginos and neutralinos will be discussed for the higgsino scenarios. In Section 5.1, the phenomenology of natural SUSY models with light higgsinos including the production and decay channels will be described. In Section 5.2, the SM backgrounds considered in the analysis will be explained with examples of possible Feynman diagrams. The initial state radiation method, which is used to distinguish the signal from the SM background with very similar signature, will be discussed in Section 5.3. After explaining the generation of the events in Section 5.4, the simulation and reconstruction of the events based on both fast and full detector simulations will be discussed in Sections 5.5 and 5.6, respectively. Finally, the weighting of the events and data samples will be explained in Section 5.7.

5.1   Phenomenology of Light Higgsinos at the ILC

The light higgsino-like charginos and neutralinos, which are at the electroweak scale and nearly mass degenerate, can be observable at the International Linear Collider (ILC). Due to the advantages of lepton colliders explained in Section 3.2, each particle coming out from the collision can be measured. Therefore even very soft particles can be observed. The polarisation capability of the ILC improves the precisions by enhancing the signal and suppressing the background events. In order to investigate the dependency of the analysis on the level of mass degeneracy, two scenarios with different mass splittings between higgsinos have been studied. In the next subsections, the benchmark scenarios will be discussed, and the production processes of higgsinos at the ILC and their decay modes will be explained.

5.1.1   Benchmark Scenarios

In this thesis two benchmark scenarios with a lightest Higgs boson mass of 124 GeV and 127 GeV are studied. Both are compatible with the LHC discovery ($m_h = 125.09 \pm 0.21$(stat.)± 0.11(syst.) [32]) within the theory uncertainty of the MSSM prediction of 2 GeV. In the higgsino case, the lightest chargino $\widetilde{\chi}_1^{\pm}$ and the first two lightest neutralinos $\widetilde{\chi}_1^0, \widetilde{\chi}_2^0$ are almost mass degenerate, and therefore the mass difference is a discriminative parameter between the scenarios. Because of that the considered scenarios are respectively referred to as dM1600 and dM770, according to their mass difference between the chargino and the lightest neutralino. The unstable higgsinos $\widetilde{\chi}_1^{\pm}$ and $\widetilde{\chi}_2^0$ have a non-zero lifetime in the order of 8.5 ps (0.3 ps) and 100 ps (0.7 ps) for the dM1600 (dM770) scenario, respectively. In addition to the motivation by naturalness argument, this kind of scenarios can be also obtained from high scale models, e.g. hybrid gauge-gravity mediated supersymmetry breaking [55, 56]. The spectrum of the model has been obtained using

the high-scale parameters of this hybrid model as explained in [2]. These kind of scenarios with light and nearly mass degenerate higgsinos are also motivated by hybrid gauge and gravity mediated SUSY breaking models. The electroweakino mass parameters and the mass spectrum of the particles for both scenarios are given in Table 5.1. The Les Houches files of the spectrum can be found in Appendix B.

	$M_1[\text{TeV}]$	$M_2[\text{TeV}]$	$\mu[\text{GeV}]$	$\tan\beta|_{m_Z}$
dM1600	1.70	4.36	165.89	44
dM770	5.30	9.51	167.40	48

	$M_{\widetilde{\chi}_1^\pm}[\text{GeV}]$	$M_{\widetilde{\chi}_1^0}[\text{GeV}]$	$M_{\widetilde{\chi}_2^0}[\text{GeV}]$	$m_h[\text{GeV}]$
dM1600	165.77	164.17	166.87	124
dM770	167.36	166.59	167.63	127

Table 5.1 Elecktroweakino mass parameters and mass spectrum for the dM1600, and the dM770 scenario including one-loop corrections. The spectrum is calculated by `SOFTSUSY` [130].

As mentioned before, the bino and wino mass parameters, M_1 and M_2, in turn are quite high compared to the higgsino mass parameter μ, which is the reason why the lightest chargino and the first two lightest neutralinos are higgsino-like. Since the higgsinos are nearly mass degenerate, one can expect to have small mass splittings between them. The mass differences are: $M_{\widetilde{\chi}_1^\pm} - M_{\widetilde{\chi}_1^0} = 770\,\text{MeV}$ (1.6 GeV) and $M_{\widetilde{\chi}_2^0} - M_{\widetilde{\chi}_1^0} = 1.04\,\text{GeV}$ (2.7 GeV) in the dM770(dM1600) scenario. The feature of having small mass splittings will result in soft particles in the final state in addition to lots of missing energy, since the chargino decays to the LSP and a virtual W boson, $\widetilde{\chi}_1^\pm \to \widetilde{\chi}_1^0 W^{\pm*}$. More details about the decay modes will be given in Section 5.1.3. Because of this signal topology, a hard initial state radiation (ISR) photon with a certain angle is introduced in order to distinguish the signal events from background events with the same final state, represented by $\gamma\gamma \to 2f$ events, as discussed in Section 5.2.2. The details about the ISR method will be explained in Section 5.3.

The full mass spectrum in Figure 5.1 can be given as an example for the considered benchmark scenarios. These scenarios are experimentally the most challenging scenarios in two different aspects. One of them is the requirement of heavy scalar third generation quarks in the order of TeV scale. In this case, there are only higgsinos within the observable region, and the observation of the decay products of the higgsinos is extremely difficult for the LHC experiment since there are only a few soft particles with lower than 2 GeV in the final state [56]. The second one is related with the chosen mass differences. For larger mass differences, the analysis would be easier, because the final state particles would be more energetic which makes their observation easier. The applied ISR method will be valid for higher mass differences of a few GeV as explained in [79]. If the mass difference gets even larger, the analysis can be done even without the requirement of the ISR photon [79]. For smaller mass differences such as $\Delta M < 150\,\text{MeV}$, the only possible decay mode of the chargino is $\widetilde{\chi}_1^\pm \to \widetilde{\chi}_1^0 e^- \nu$ as seen in Figure 5.6 which results in longer lifetime of the chargino. In that case, the charginos will fly into the detector and decay
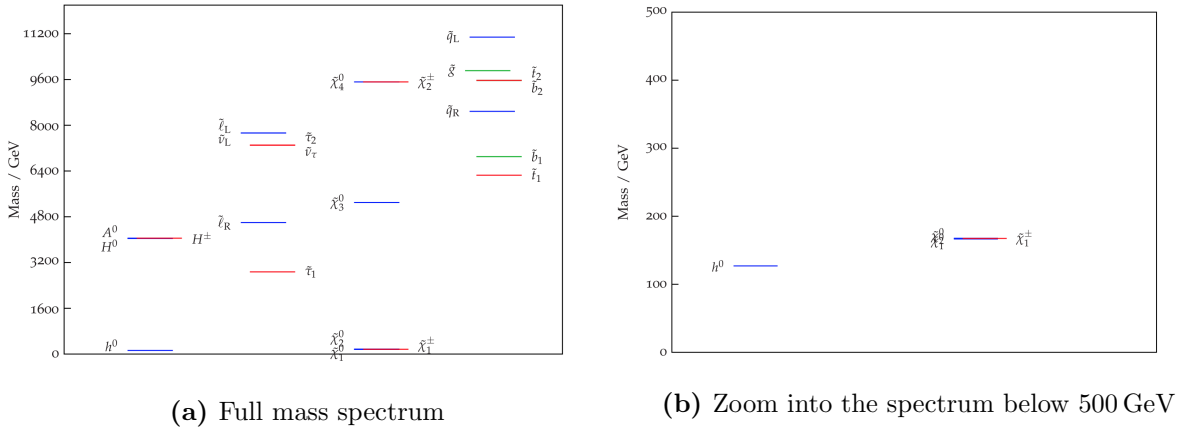
(a) Full mass spectrum

(b) Zoom into the spectrum below $500\,\mathrm{GeV}$

Figure 5.1 Mass spectrum of Natural SUSY scenarios including light higgsinos. An example for scenarios motivated by hybrid gauge and gravity mediated SUSY breaking models. Figure is taken from Ref. [131].

after leaving some signature on the tracking detectors. Because of the invisible decay product of the chargino, a kink between the tracks of the chargino and the visible decay product of the chargino will be observed at the decay point. Another important signature in this case is the energy loss by ionisation dE/dx, which is explained in Section 4.1. The value of dE/dx for charginos will be huge since they are very heavy compared to the decay products of the charginos. Thus, both the observed kink and the so-called anomalous ionisation [132, 133] can be used to identify the charginos with small mass splitting. Such scenarios have already been studied by the LEP experiments [134, 135, 136, 137]. The combined limit [138] excludes the higgsino-like charginos below approximately $92\,\mathrm{GeV}$ for small mass differences between chargino and LSP.

5.1.2 Higgsino Production Processes at the ILC

Higgsinos can be produced in $e^+e^- \to \widetilde{\chi}_1^+ \widetilde{\chi}_1^-$ and $e^+e^- \to \widetilde{\chi}_1^0 \widetilde{\chi}_2^0$ channels via Z boson or γ exchange in the s-channel, see Figure 5.2. Chargino pairs can be produced via the exchange of both Z boson and γ, while only Z boson exchange is possible for neutralinos. Even though t-channel and u-channel exchange of selectrons and sneutrinos is possible, they are suppressed in the higgsino case due to the large mass of the scalar neutrinos $\tilde{\nu}_e$ and scalar electrons $\tilde{e}$, and small Yukawa coupling between higgsinos and sleptons.

The production cross sections of the chargino and neutralino processes, which are calculated by `Whizard 1.95` [139] using the ILC set-up provided by the ILC Generator Group are given in Table 5.2. The calculation has been performed by including soft initial state radiation (ISR) and beam spectrum corresponding to the ILC Technical Design Report [86]. In addition to soft ISR photons, one photon is included in hard matrix element with a minimal invariant mass of $4\,\mathrm{GeV}$ with the corresponding beam electron, but the energy cut which is required to be larger than $10\,\mathrm{GeV}$ is not included on the generator level. The values given in the table correspond to
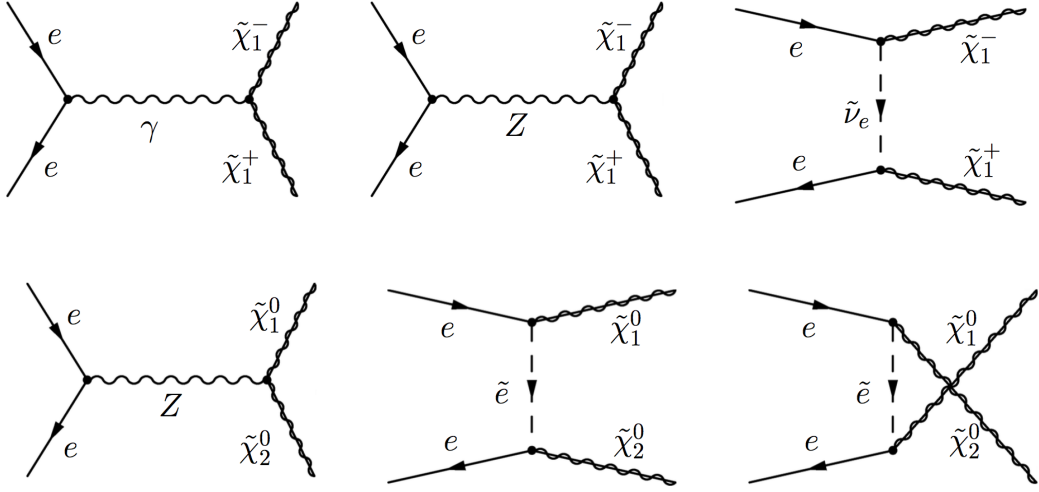
Figure 5.2 Chargino (upper row) and neutralino (lower row) production graphs at tree level. Note that t- and u-channel selectron/sneutrino exchange graphs are negligible in our scenario due to a small Yukawa coupling between sleptons and higgsinos, and their large masses.

100% polarisation of the beam electron and positron either right handed or left handed. The cross sections with the same-sign helicity (RR or LL) are zero, $\sigma_{RR} = \sigma_{LL} = 0$, because of the s-channel production. Therefore they are not shown in Table 5.2. Since technically it is not possible to have 100% polarised electron and positron beams, partial polarisation combinations $P(e^+, e^-) = (\pm 30\%, \mp 80\%)$ are considered in the analysis. To obtain samples with partially

	dM1600		dM770	
Processes	σ_{RL} [fb]	σ_{LR} [fb]	σ_{RL} [fb]	σ_{LR}[fb]
$e^+e^- \to \widetilde{\chi}_1^+ \widetilde{\chi}_1^-$	132.97	26.83	130.05	26.28
$e^+e^- \to \widetilde{\chi}_1^0 \widetilde{\chi}_2^0$	80.11	61.66	70.16	60.92

Table 5.2 Production cross sections in two different polarisation combinations for dM1600 and dM770 scenarios at $\sqrt{s} = 500\,\text{GeV}$ and $\int \mathcal{L}dt = 500\,\text{fb}^{-1}$. I.e. σ_{RL} refers to the situation when the positron is 100% right handed polarised, and the electron is 100% left handed polarised. The cross sections are calculated by `Whizard 1.95` including soft ISR photons and beam spectrum corresponding to ILC TDR, as well as one ISR photon in the hard matrix element with a minimal invariant mass of 4 GeV with the corresponding beam electron.

polarised beam electrons[1], the produced fully polarised samples are mixed according to Eq. (3.3). As a result the cross section values are reduced as seen in Table 5.3. These values

---

[1]Beam electrons refer to both beam electron and beam positron, unless stated otherwise.

correspond to the polarised cross sections, which are sufficiently large to be searched for as can be seen when it is compared with Figure 3.2 indicating the production cross sections of several processes at lepton colliders.

	dM1600		dM770	
Processes	$\sigma\,[\,\text{fb}\,]$			
$P(e^+, e^-)$	$(+0.3, -0.8)$	$(-0.3, +0.8)$	$(+0.3, -0.8)$	$(-0.3, +0.8)$
$e^+e^- \to \widetilde{\chi}_1^+ \widetilde{\chi}_1^-$	78.73	20.35	77.00	19.92
$e^+e^- \to \widetilde{\chi}_1^0 \widetilde{\chi}_2^0$	49.03	38.88	48.44	38.41

Table 5.3 Production cross sections in two different polarisation combinations $P(e^+, e^-) = (\mp 0.3, \pm 0.8)$ for dM1600 and dM770 scenarios at $\sqrt{s} = 500\,\text{GeV}$ and $\int \mathcal{L}dt = 500\,\text{fb}^{-1}$.

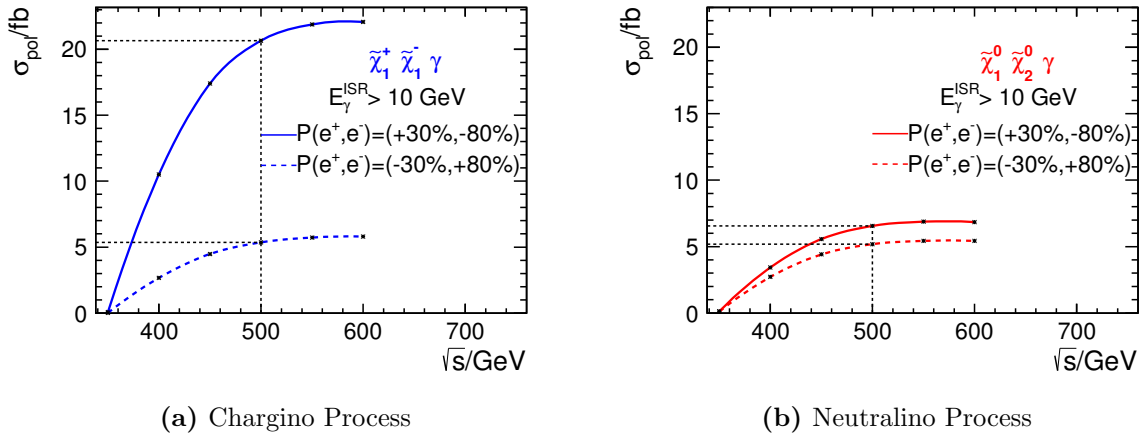**(a)** Chargino Process **(b)** Neutralino Process

Figure 5.3 (a) Chargino and (b) neutralino production cross section in scenario dM770 for $P(e^+, e^-) = (-30\%, +80\%)$ and $P(e^-, e^+) = (+30\%, -80\%)$ as a function of the centre-of-mass energy.

The polarised production cross sections as a function of the centre-of-mass energy are shown in Figure 5.3. While obtaining the cross section values, the required ISR photon has already been included in the hard matrix element. In addition, an energy cut $E_\gamma > 10\,\text{GeV}$ has been applied on the generator level while obtaining the cross sections used in Figure 5.3 (see Section 5.4). Therefore, the cross section values are substantially smaller than the values in Table 5.3. The figure indicates that choosing the proper polarisation combination, the production cross sections for the signal processes can be enhanced significantly, especially in the chargino case. This polarisation dependency of the charginos mainly comes from the interference between the two possible s-channel production modes via the exchange of a Z boson or γ. Because only the production mode with Z boson exchange is possible in the neutralino case, the polarisation dependency of the cross section is quite small compared to the chargino case.
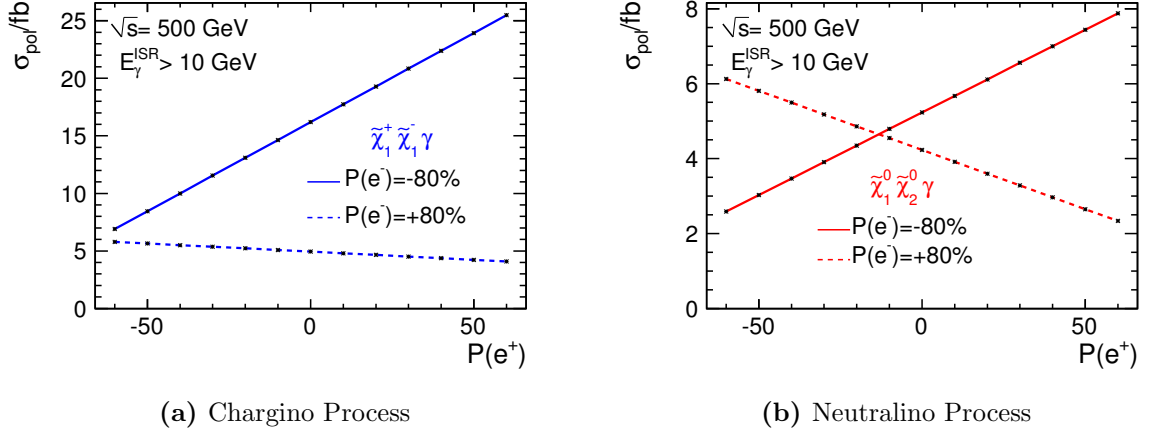
(a) Chargino Process

(b) Neutralino Process

Figure 5.4 (a) Chargino and (b) neutralino production cross section in scenario dM770 at $\sqrt{s} = 500\,\mathrm{GeV}$ as a function of the positron polarisation for $P(e^-) = +80\%$ and $P(e^-) = -80\%$.

Figure 5.4 shows the cross section at $\sqrt{s} = 500\,\mathrm{GeV}$ as a function of positron polarisation with a fixed electron polarisation to $P(e^-) = +80\%$ and $P(e^-) = -80\%$. There is a linear relation between the cross section and positron polarisation with changing slopes depending on the electron polarisation. The same-sign polarisation combination of the electron and positron reduce the cross section compared to the case when the positron is unpolarised, while the opposite sign combination increase it, which is expected due to the dominant s-channel contribution. The quantitate cross section values for the cases where positron is unpolarised and where it is polarised 30% and 60% as left-handed and right-handed are given in Table 5.4. Compared to

Processes	$P(e^-)$	$P(e^+)$				
		-60%	-30%	0%	30%	60%
$e^+e^- \rightarrow \widetilde{\chi}_1^+ \widetilde{\chi}_1^- \gamma$	-80%	6.9	11.5	14.6	19.3	23.9
$e^+e^- \rightarrow \widetilde{\chi}_1^+ \widetilde{\chi}_1^- \gamma$	+80%	5.8	5.4	4.9	4.5	4.1
$e^+e^- \rightarrow \widetilde{\chi}_1^0 \widetilde{\chi}_2^0 \gamma$	-80%	2.6	3.9	5.2	6.6	7.9
$e^+e^- \rightarrow \widetilde{\chi}_1^0 \widetilde{\chi}_2^0 \gamma$	+80%	6.1	5.2	4.2	3.3	2.3

Table 5.4 Chargino and neutralino production cross sections in scenario dM770 at $\sqrt{s} = 500\,\mathrm{GeV}$ for electron beam polarisations of $P(e^-) = -80\%$ and $P(e^-) = +80\%$ and various polarisations of positron beam.

the case considered in the analysis $P(e^+, e^-) = (\pm 30\%, \mp 80\%)$, unpolarised positron reduces the cross section approximately $\sim 30\%$, while the increased positron polarisation to $P(e^+) = 60\%$ would enhance the cross section nearly $\sim 20\%$ for left-handed polarised electrons. If the electron is right-handed, the amount of changes on the cross sections decreases significantly for the charginos, but more moderately in the neutralino case.

5.1.3 Higgsino Decay Channels

The decay of the lightest chargino $\widetilde{\chi}_1^\pm$ and the neutralino $\widetilde{\chi}_2^0$ to the lightest supersymmetric particle, $\widetilde{\chi}_1^0$ and off-shell W and Z bosons are shown in Figure 5.5. The decay of the neutralino to the lightest chargino associated with a virtual W boson, $\widetilde{\chi}_2^0 \rightarrow W^{\pm *}\widetilde{\chi}_1^\pm$, is also possible but has small branching ratios since it is kinematically highly suppressed (cf. Table 5.6). Another decay mode which is very important for small mass splittings is the radiative decay $\widetilde{\chi}_2^0 \rightarrow \widetilde{\chi}_1^0 \gamma$ via a W-chargino loop as shown in the rightmost Feynman diagram of Figure 5.5 [140].

(a) $\widetilde{\chi}_1^\pm \rightarrow \widetilde{\chi}_1^0 W^{\pm *}$ **(b)** $\widetilde{\chi}_2^0 \rightarrow \widetilde{\chi}_1^0 W^{\pm *}$ **(c)** $\widetilde{\chi}_2^0 \rightarrow \widetilde{\chi}_1^0 \gamma$
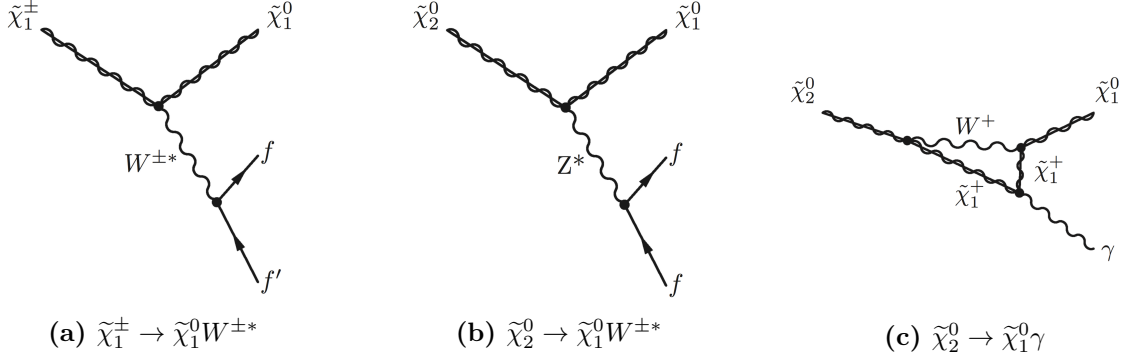
Figure 5.5 Decay channels of the lightest chargino and second lightest neutralino.

The branching ratios for charginos and neutralinos are given in Tables 5.5 and 5.6 for the dM1600 and dM770 scenarios, respectively. In the dM770 scenario, which has a sub-GeV mass splitting, charginos predominantly decay to $\pi\widetilde{\chi}_1^0$ including a single π, while $\gamma\widetilde{\chi}_1^0$ decay is dominant by far in the neutralino case. In the dM1600 scenario, those decay modes are not that dominant anymore. Other decay modes start to have significant contributions as well. The dominant decay modes of the chargino process for each scenario can be also seen in Figure 5.6, which shows branching ratios of the chargino decays as a function of the mass difference between $\widetilde{\chi}_1^\pm$ and $\widetilde{\chi}_1^0$. The detailed discussion of the branching ratios and their effect on the analysis will be given in Chapter 6.

Since the higgsinos are nearly mass degenerate, the decay products of the virtual W/Z bosons are very soft, and they are generally produced centrally. Figure 5.7 shows the transverse momentum distribution of the visible decay products of the chargino and neutralino processes on the generator level for both scenarios. It indicates that both benchmark scenarios have low momentum visible decay products, especially in the dM770 scenario the final state particles have a transverse momentum smaller than 2 GeV ($p_t < 2\,\mathrm{GeV}$).

All these considered, the expected signature of the signal samples consists of a few very soft fermions, a large amount of missing energy due to LSPs and one hard ISR photon.

5.2 Standard Model Background

The SM processes at the ILC can be classified in terms of their initial and final states. Because of the induced strong electromagnetic field between bunches, many photons will be emitted

$\widetilde{\chi}_1^+$ decay mode	BR(dM1600)	BR(dM770)
$e\nu\widetilde{\chi}_1^0$	17.3%	15.0%
$\mu\nu\widetilde{\chi}_1^0$	16.6%	13.7%
$\pi^+\widetilde{\chi}_1^0$	16.5%	60.4%
$\pi^+\pi^0\widetilde{\chi}_1^0$	28.5%	7.3%
$\pi^+\pi^0\pi^0\widetilde{\chi}_1^0$	7.5%	0.03%
$\pi^+\pi^+\pi^-\widetilde{\chi}_1^0$	7.1%	0.03%
$\pi^+\pi^+\pi^-\pi^0\widetilde{\chi}_1^0$	2.4%	–
$\pi^+\pi^0\pi^0\pi^0\widetilde{\chi}_1^0$	0.5%	–
$K^+\widetilde{\chi}_1^0$	1.2%	3.5%
$K^0\pi^+\widetilde{\chi}_1^0$	1.0%	0.03%
$K^+\pi^0\widetilde{\chi}_1^0$	0.5%	0.02%

Table 5.5 Chargino $\widetilde{\chi}_1^+$ decay modes according to `Herwig++ 2.6.0`.

$\widetilde{\chi}_2^0$ decay mode	BR(dM1600)	BR(dM770)
$\gamma\widetilde{\chi}_1^0$	23.6%	74.0%
$\nu\bar{\nu}\widetilde{\chi}_1^0$	21.9%	9.7%
$e^+e^-\widetilde{\chi}_1^0$	3.7%	1.6%
$\mu^+\mu^-\widetilde{\chi}_1^0$	3.7%	1.5%
hadrons $+\widetilde{\chi}_1^0$	44.9%	12.7%
$\widetilde{\chi}_1^\pm + X$	1.9%	0.4%

Table 5.6 Neutralino $\widetilde{\chi}_2^0$ decay modes according to `Herwig++ 2.6.0`.

before the collision as introduced in Section 3.4.2.1. Hence, not only e^+e^-, but also $e^\pm\gamma$ and $\gamma\gamma$ collisions will take place (cf. Section 3.5). Depending on the source of photons and the transferred momentum to the photons, they can be either real or virtual. There are two common sources emitting photons, which are bremsstrahlung and beamstrahlung. The mentioned three initial states constitute the classes of the SM backgrounds considered in this study. In the $e^\pm\gamma$ and $\gamma\gamma$ type of backgrounds, either one or both of the beam electrons will go through the beam pipe and will not be visible by the detector. These SM backgrounds will be explained in detail in the following.

Figure 5.8a shows a Feynman diagram of the Standard Model based on photon exchange. The diagram helps to understand differences between the e^+e^-, $e^\pm\gamma$, and $\gamma\gamma$ classes. $Q_{1,2}^2$ is a momentum scale which represents the transferred four-momentum to the corresponding photon, $Q_{1,2}^2 = -p_\gamma^2$, and also the virtuality of the photon. In case of real photon it should be zero,
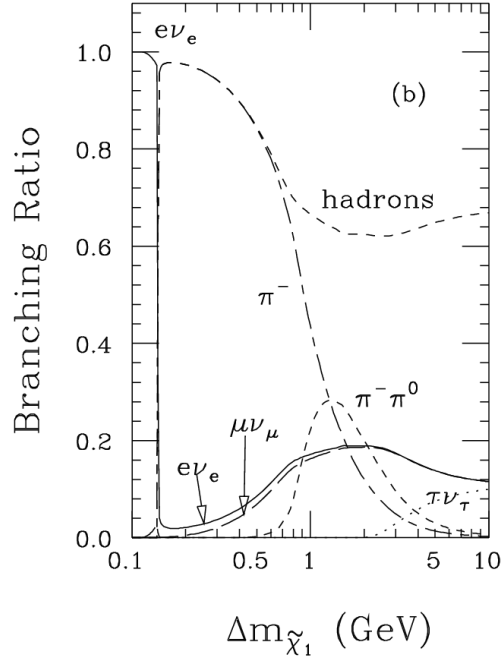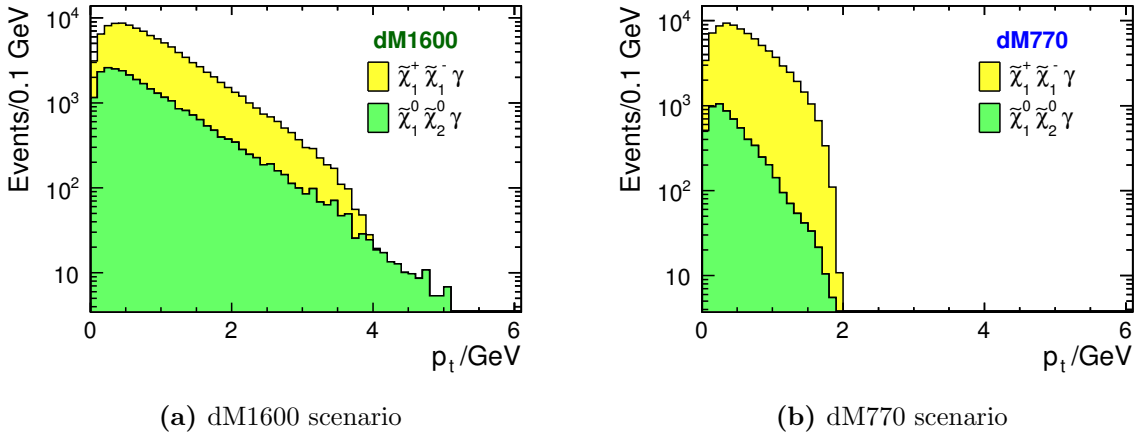
Figure 5.6 Branching ratios of the chargino decay as a function of mass difference between the chargino and the LSP, $\Delta m_{\widetilde{\chi}_1} = \Delta M_{\widetilde{\chi}_1^\pm - \widetilde{\chi}_1^0} = M_{\widetilde{\chi}_1^\pm} - M_{\widetilde{\chi}_1^0}$. Figure is taken from Ref. [82].

(a) dM1600 scenario

(b) dM770 scenario

Figure 5.7 p_t spectrum of visible chargino and neutralino decay products on the generator level for the two scenarios.

$Q_{1,2}^2 \approx 0$. On the other hand, as noted in footnote (2) it can be interpreted as a measure of the angle between incoming and outgoing beam electrons. That means that if the transferred momentum is large enough, this makes the scattering angle of the outgoing electrons larger such that they will be within the acceptance of the detector. If not, the outgoing beam electrons will go though the beam pipe. Figure 5.8b displays a sketch of the transferred momenta in
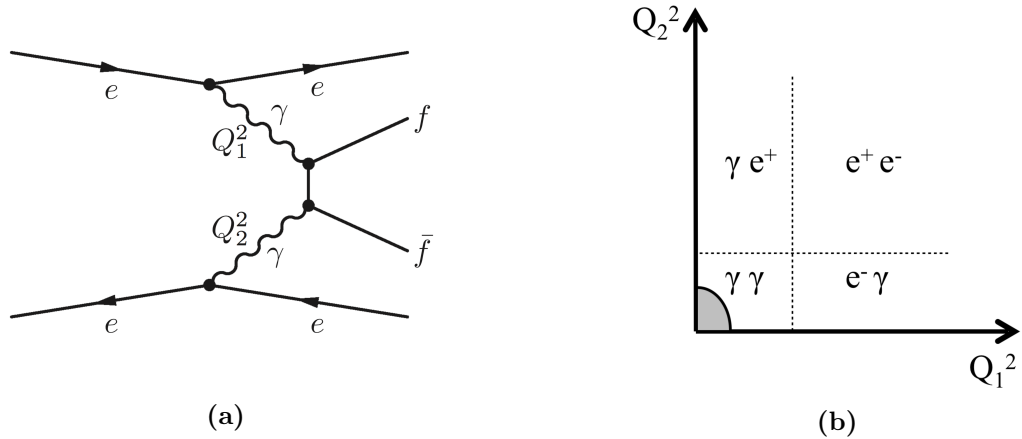
(a)

(b)

Figure 5.8 (a) An example of Feynman diagram of SM background displaying all three classes. $Q_{1,2}^2$ is a measure of the transferred four-momentum to the corresponding photon, $Q_{1,2}^2 = -p_\gamma^2$, which has a relation with the angle between incoming and outgoing beam electrons[2]. The value of this parameter classifies the SM backgrounds. This classification is shown in (b). The shaded area indicates the region where the low p_t $\gamma\gamma \to$ hadrons overlay events stem from (cf. Section 3.5.2).

the $Q_1^2 - Q_2^2$ frame. If the beam electrons transfer small momentum to the photons, the beam electrons could go through the beampipe. However, if both of the beam electrons transfer enough momentum to the photons, the beam electrons are scattered with a large angle such that they become visible by the detector. Those backgrounds are called e^+e^-. When this is valid only for one beam electron, then it is called $e^\pm\gamma$ background. Otherwise, the background is named $\gamma\gamma$. The given Feynman diagram in Figure 5.8a shows only one of the possible backgrounds including virtual photons. The example processes considering real photons are represented in Figure 5.9 for $e^+e^- \to 4f$, $e^-\gamma \to 3f$ and $\gamma\gamma \to 2f$ classes. In general, for e^+e^- and $\gamma\gamma$ backgrounds, there is an even number of fermions in the final state: $2f$, $4f$, $6f$, ..., while the final state of $e^\pm\gamma$ has an odd number of fermions: $1f$, $3f$, $5f$, ... In the analysis, the following SM background classes are considered: $e^+e^- \to (2f, 4f, 6f)$, $e^\pm\gamma \to (1f, 3f, 5f)$ and $\gamma\gamma \to (2f, 4f)$.

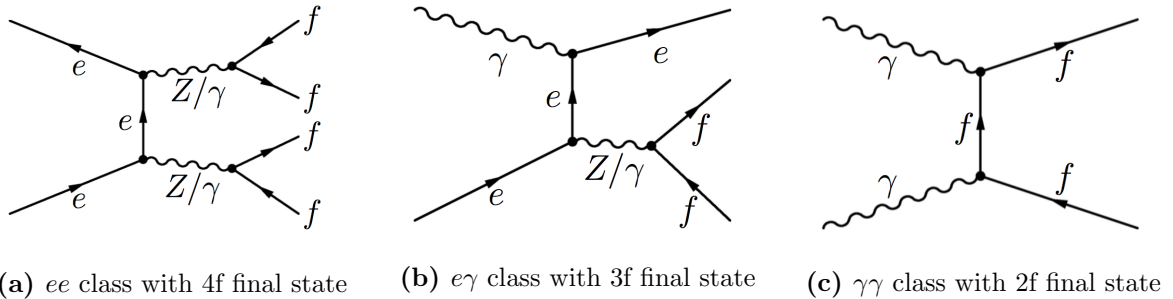**(a)** *ee* class with 4f final state   **(b)** *eγ* class with 3f final state   **(c)** *γγ* class with 2f final state

Figure 5.9 Example of Feynman diagrams of SM backgrounds in three different classes grouped in terms of their initial states; *ee*, *eγ* and *γγ* with real photons. For more information see [141].

There are two types of SM background giving the same signature as the signal, which consists of a few low energetic particles and no other activity. One of them contains events with large amounts of energy in invisible neutrinos, while the other one contains events where a large fraction of the energy escapes with particles going in un-instrumented regions of the detector, which are mainly the beam pipes. In this section these type of backgrounds will be discussed within the concept of initial state classification.

5.2.1   e$^+$e$^-$ Initial State

Most of the events in this class can be suppressed easily with the preselection determined from the topology of the signal samples (cf. Section 6.1). However, since the $\tau^+\tau^-$ events have the same signature as the chargino and neutralino signals, they are expected to be a dominant background. These events stem from $e^+e^- \to \tau^+\tau^-$ and $e^+e^- \to \tau^+\tau^-\nu_\tau\bar{\nu}_\tau$ processes for instance, which are subsets of $e^+e^- \to 2f$ and $e^+e^- \to 4f$ classes. In these events, τ-leptons decay to a virtual W boson and ν_τ, where the W bosons can decay either leptonically or hadronically. This corresponds to the first type of background including high energetic neutrinos and low energetic fermions as it is in the signal events. If the τ-pairs come from the e^+e^- class, their cross section is nearly 20 times larger $\mathcal{O}(2000)$ fb than the signal $\mathcal{O}(100)$ fb for the left handed electron case. However, since there is no missing energy threshold for τ decays, the neutrinos can carry an unknown amount of energy away. The case where the neutrinos carry lots of energy away and the τ-leptons decay to very soft visible particles is rare. This property of τ-pairs allows to suppress them without too strong cuts on the event topology. It is important to note that if τ-pairs come from $e^\pm\gamma$ or $\gamma\gamma$ classes, then the cross section of τ-pairs is much larger than e^+e^- case $\mathcal{O}(10^4)$ fb. The possibility of decaying to very soft particles is not that small any more due to the properties of these kind of classes which will be explained in the following sections. Therefore some additional cuts will be applied to suppress these kind of backgrounds.

5.2.2 $\gamma\gamma$ Initial State

The $\gamma\gamma$ events constitute the second type of background which is the most severe one with a high cross section of $\mathcal{O}(10^6)$ fb for $\gamma\gamma \to 2f$, and with a cross section in the order of $\mathcal{O}(100)$ fb for $\gamma\gamma \to 4f$. The dominant background of this type is $\gamma\gamma \to 2f$ class, which can be obtained from e^+e^- as $e^+e^- \to e^+e^-\gamma^*\gamma^* \to e^+e^-f\bar{f}$. In such events, both beam electrons have low transverse momentum such that they go through the beam pipes by carrying a large amount of the full beam energy. However, the $f\bar{f}$ pair can be emitted at any angle, and generally they have low momentum since the beam electrons take away most of the initial energy. In that sense, these events have almost the same final states as the signal as shown in Figure 5.10 (see Section 5.3 for more details). To distinguish these kind of events from the background an ISR emitted by one of the beam electrons at a a certain angle and energy which is high enough to be detected is introduced. The electron or positron which emits a photon will recoil against the ISR photon,

---

[2]p_γ is four momentum of photon. Considering the beam electrons as massless at high energy, p_γ is calculated as $p_\gamma^2 = -2E_{e_i}E_{e_o}(\sin^2\frac{\theta}{2})$, where E_{e_i}, E_{e_o} is the energy of incoming and outgoing beam electrons, and θ is the angle between incoming and outgoing beam electrons.

and will be deflected into the acceptance of the detector if the ISR photon has sufficient energy. This method will be explained in detail in the next section.

In the other case of $\gamma\gamma \to 2f$ where the initial photons are real photons from the photon component of beams, emission of an ISR photon is not be possible since there are no charged particle in the initial state. Therefore, after requiring an ISR photon those events can be suppressed in the event selection since they have a different signature than the signal events.

5.2.3 $e^{\pm}\gamma$ Initial State

This type of background has also a very similar signature to the signal events, especially after the requirement of an ISR photon. The $e^{\pm}\gamma \to 3f$ class, in particular from the t-channel diagram with an incoming real photon as seen in Figure 5.9b, is the dominant class with a cross section in the order of 10^5 fb, while $e^{\pm}\gamma \to 5f$ class has a cross section around $\mathcal{O}(100)$ fb. In these events, the ISR photon can be emitted only from one initial state particle, since there is no charged particle on the other side. In contrary to the $\gamma\gamma \to 2f$ class, the hard ISR photon does not recoil against the beam electron, but the $f\bar{f}$ pair which is produced via the exchange of a Z boson or photon, like in the signal. The beam electron, which emits a photon, itself carries away most of the beam energy while it is going through the beam pipe, and transfers small fraction of the beam energy to the real photon. This causes large missing energy in the events which is also similar to the signal. Therefore, the requirement of an ISR photon does not help much to suppress these kind of backgrounds.

5.3 Initial State Radiation Method

The ISR method, introduced in Section 5.2, is essential to suppress the $\gamma\gamma \to 2f$ background. For the mass degenerate charginos and neutrinos, the ISR method has been used before in [142]. The detector sketches of the expected signatures for both the signal and the $\gamma\gamma \to 2f$ class called "two-photon background" are displayed in Figure 5.10. In the signal case, there are only a few very soft particles since the LSPs are invisible. In the two-photon case when they are virtual, both beam electrons go through the beam pipe which cause large missing energy, and there are only remnants of the two photon interaction visible in the detector which are very soft.

Introducing a hard ISR photon can solve the problem of having similar final states. The ISR photon should have a certain angle to be within the acceptance of the tracking system to be able to distinguish photons and electrons. In addition the energy of the ISR photon should be sufficiently high, such that the outgoing beam electron will be deflected into the acceptance of the detector. While it changes the signature of the two-photon background due to additional beam electron made seen with the help of the ISR photon, it will not make crucial differences in the signal signature. The detector sketches of the signatures in this case, which show the differences clearly, is represented in Figure 5.11. It shows that the ISR method works to suppress this type of background, which originally has very similar signature to the signal.

The required ISR photon reduces the production cross section significantly (cf. Section 5.1.2), and changes the signal topology. In addition to the large missing energy and a few very soft
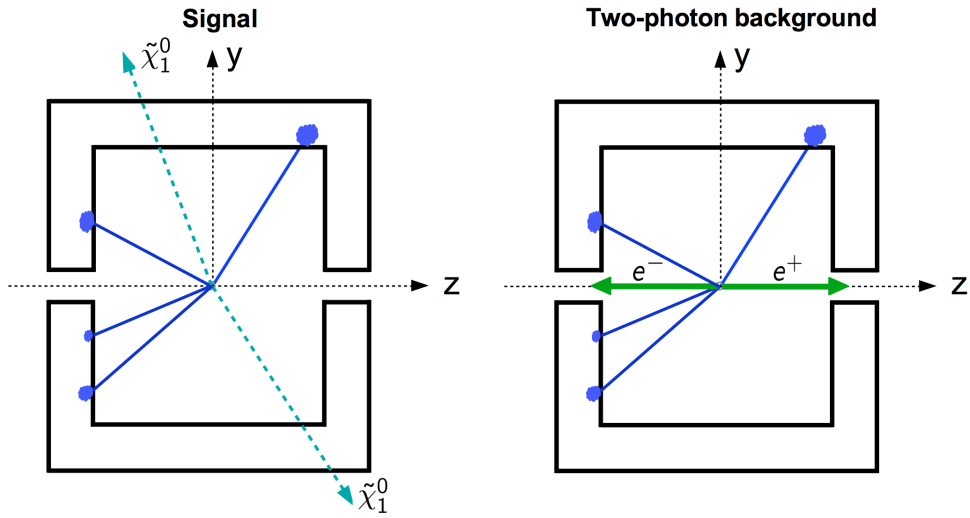
Figure 5.10 Detector sketches of the final state particles for signal and two-photon background $(\gamma\gamma \to 2f)$ events. In the signal case, there is large missing energy due to LSPs, and only few soft visible particles. In the case of two-photon background, there is large missing energy because the beam electrons escape through the beam pipes, and only few soft visible particles just in the case of signal.

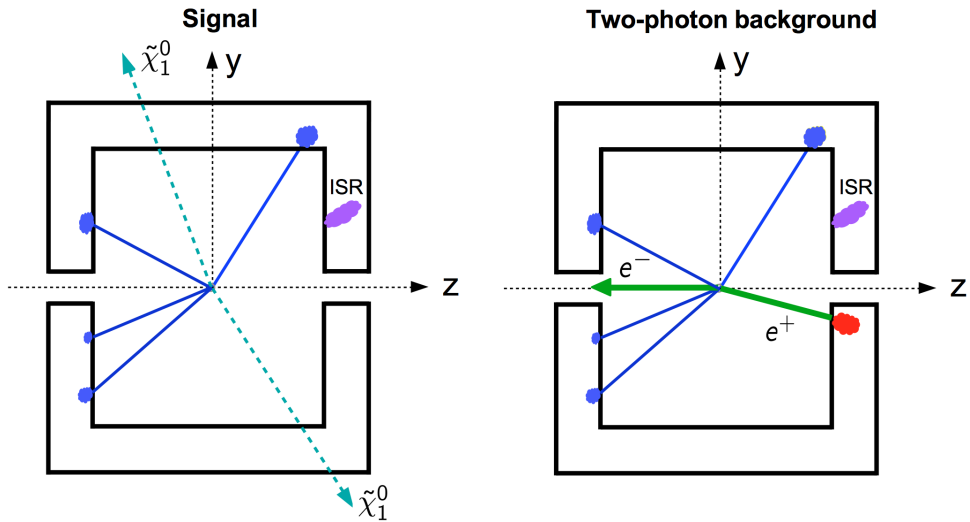**Figure 5.11** Detector sketches of the final state particles for signal and two-photon background events after requiring an ISR photon. The ISR photon makes one of the beam electrons visible by the detector in the two-photon background case, while it slightly changes the signal topology due to existence of a hard photon.

fermions, there will be a hard ISR photon in the final state. The signal processes can be written

in this case as

$$e^+e^- \rightarrow \widetilde{\chi}_1^+ \widetilde{\chi}_1^- \gamma\,,$$
$$e^+e^- \rightarrow \widetilde{\chi}_1^0 \widetilde{\chi}_2^0 \gamma\,,$$

where γ refers to the ISR photon. The Feynman diagrams of both the signal and the two-photon background are given in Figure 5.12.

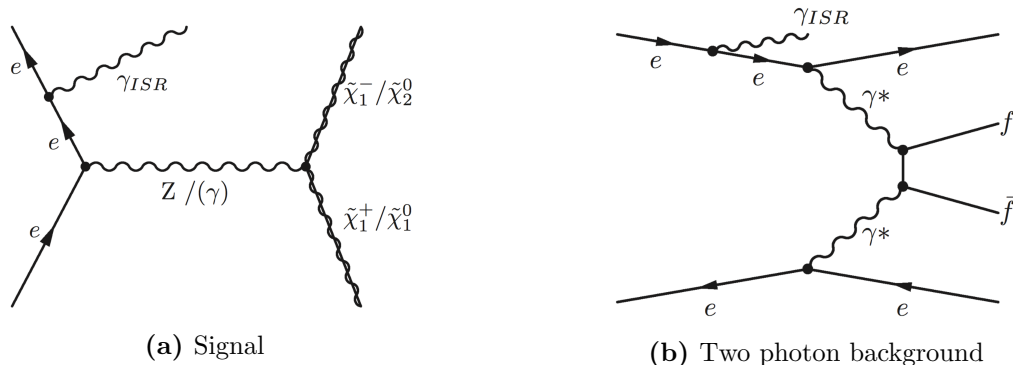**(a)** Signal   **(b)** Two photon background

Figure 5.12 Feynman diagrams with the initial state radiated photon for signals $e^+e^- \rightarrow \widetilde{\chi}_1^+ \widetilde{\chi}_1^+$, $e^+e^- \rightarrow \widetilde{\chi}_1^0 \widetilde{\chi}_2^0$, and $\gamma\gamma \rightarrow 2f$ background. In the neutralino case only Z boson exchange is possible, while both Z and γ are possible for charginos.

5.4 Building Signal Samples

As mentioned in Section 5.1.1, both the general tree-level spectrum of the scenarios, and the physical chargino and neutralino masses including one-loop corrections are calculated using the spectrum generator `SOFTSUSY` [130].

As the cross section calculation, the events are generated by using `Whizard 1.95` [139] with the ILC set-up provided by the ILC Generator Group [86]. `Whizard` accepts the SUSY Les Houches Accord input format (SLHA) [143] for supersymmetric models, in particular for the MSSM. This input file can be calculated by using either `SOFTSUSY` or `Herwig`. The file includes information about the model, SUSY breaking parameters, mass spectrum, mixings, partial widths and decay branching ratios, and is used as an input file in `Whizard`.

`Whizard` generates matrix elements by using `O'Mega` [144], to calculate the scattering amplitudes of the processes in the presence of polarised beams. With the help of this tool, tree level matrix elements are generated. Many ILC specific cases such as, beamstrahlung, ISR and beam polarisation has been already implemented into `Whizard`. The beam spectrum of the beam electron and positron is another important property of the ILC which gives the effective initial centre-of-mass energy by taking into account the beamstrahlung effects. The beam spectrum simulated by `GuineaPig` [100] is included as well.

Fragmentation and hadronisation of the final state have been performed with an interface to `Pythia` [114]. And the outputs are written in `StdHep` format [145].

In the higgsino case, both signal and background events were generated with `Wizard 1.95` in the context of the ILC TDR [86]. Since the higgsinos are nearly mass degenerate, the $\widetilde{\chi}_1^\pm/\widetilde{\chi}_2^0$ decay via highly virtual W/Z bosons. In this case the hadronisation process is not the same as in case of having on-shell W/Z bosons. This is implemented in the event generator `Herwig++` for τ leptons decaying to hadrons in the SM which have a very similar situation to the chargino case [146, 147]. Therefore, the decay widths and branching ratios of the chargino decays were calculated with `Herwig++`. For the chargino decays, this implementation is used, while the standard procedure is followed for the neutralino decays. In `Whizard`, the decays of the charginos and neutralinos were simulated by `Pythia`, and the branching ratios used in `Pythia` are the ones calculated by `Herwig++`. The required ISR photon is included in the hard matrix element with an invariant mass cut of 4 GeV with respect to the corresponding beam electron. However, the energy cut applied for the cross section calculation was not included in the event generation step in order to be able to estimate the experimental acceptance after the reconstruction.

Some SM backgrounds deserve detailed discussion in terms of their production. The possibility of radiative Bhabha events, e.g. $e^+e^- \rightarrow e^+e^-\gamma$, is very high, especially in the very forward region. Therefore, in the production of these events, both the invariant masses between any two of the final state particles and the momenta transferred between the incoming and outgoing beam particles are required to be larger than $4\,\mathrm{GeV}(M_{inv} > 4\,\mathrm{GeV},\ Q^2 > 4\,\mathrm{GeV})$, which exclude the region with very small scattering angle. Some backgrounds are not included in the production, which could have an important contribution. These are mainly the events including photon(s) in the final state; events with pure photon final states, with only neutrinos and photons, and QED Compton events. In these events, either with the conversion of photon(s) to fermions or in particular by the addition of the $\gamma\gamma \rightarrow$ hadrons overlay they can have a similar final state as the signal. However, the events that pass the exclusive decay selection are expected to be rather rare if the analysis is performed with full simulation including the low p_t $\gamma\gamma \rightarrow$ hadrons overlay. Since the analysis is performed with fast simulation and $\gamma\gamma \rightarrow$ hadrons overlay is not included, these backgrounds do have an negligible effect on the results.

5.5   Simulation and Reconstruction with SGV

One of the available detector simulations in order to simulate the detector response of the ILD detector of the ILC is `SGV` [148] which is a fast detector simulation based on a simplified description of the detector geometry. `SGV` can generate an event approximately $\mathcal{O}(10^3)$ times faster than the full simulation. The details about the tracking and the simulation of the calorimeters will be explained in the following. `SGV` can internally call `Pythia` and `Whizard`. It accepts the `StdHep` format as an input file and it is able to generate the output in `LCIO-DST` format.

5.5.1   Tracking in SGV

Track parametrisation in the ILD detector has been done at the perigee, which is the point on the track where the projection onto the $x-y$ plane is at minimum distance to the interaction point. The geometrical so-called perigee parameters are track curvature $\Omega = 1/R$, impact parameters d_0 and z_0, and direction parameters ϕ_0 and $\tan\lambda = 1/\tan\theta$ [149].

The same parametrisation is used in `SGV` as well, and the response of the ILD tracking system has been simulated. There exist two uncertainties which affect the parameters of a track. One of them is the measurement errors arise from the difference between the measured hit point and the extrapolated point, and from the limited resolution of the detector. The errors are smaller for high momentum particles due to larger number of hits. The other one is the errors originating from the multiple scattering which cannot be reduced below some values due to unavoidable scatterings within the volume of the detector because of the presence of some gas at atmospheric pressure or the existence of some denser parts in the sensitive detector volume [150]. The particles with higher momenta are scattered with a large angle which causes higher errors. These uncertainties give rise to some correlations between the track parameters. To take into account these correlations, the perigee parameters are smeared according to the covariance matrix. `SGV` can calculate the full covariance matrix of the track parameters including both measurement errors and multiple scattering errors with the help of the generated particles and the ILD detector geometry.

To calculate the covariance matrix, the track helix is followed through the detector, and the layers that are hit by the particles are determined as seen from the sketch in Figure 5.13a. The
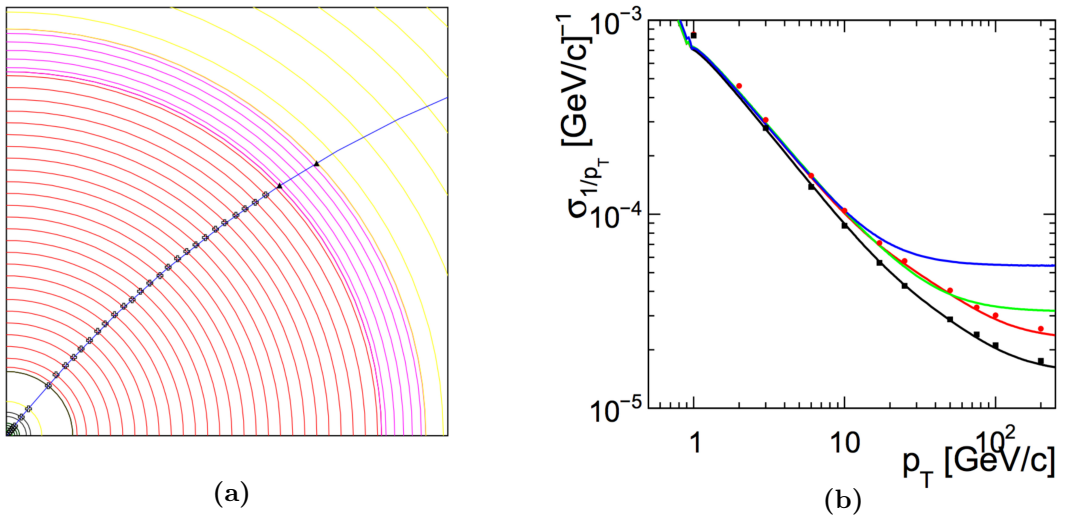

<div align="center">(a)</div> <div align="center">(b)</div>

Figure 5.13 (a) $R\phi$ projection of a quadrant of the ILD detector, (b) The momentum resolution σ_{1/p_t} as a function of transverse momentum p_t for different detector configurations. The lines indicate the SGV results, while the dots show the results from the full simulation. The blue line shows the case where only the TPC is considered, the green line includes the VTX detector as well, while the red and black lines correspond to the cases where SET and SIT are taken into account, respectively. Figure is taken from Ref. [148].

helix is followed from the outside, starting at the outer-most tracking detector surface. At each intersection, the measurement errors are stored to the relevant elements, then the matrix is inverted, and the effects of multiple scattering are added to the relevant elements of the matrix. For the multiple scattering effects, the inverse of the matrix is taken since their contribution is in the opposite direction compared to the measurement errors. After that, the matrix is inverted

again and translated along the helix to the next intersection point, and the same procedure is applied again and again until all intersection points are covered. For each layers, the obtained errors are summed and the covariance matrix is obtained.

The performance of the tracking can be seen in Figure 5.13b, where the lines show momentum resolution obtained from the full simulation, and the dots show the results of the `SGV`. It is clear that they agree with each other quite well.

5.5.2 Simulation of the Calorimeters in SGV

For the calorimeter simulation all particles are extrapolated to the intersections with the calorimeters. What kind of response the detectors will give is determined using the given properties of particles; whether the particle will be detected as a minimum ionising particle (MIP), or it will create an electromagnetic or hadronic shower, or it will stay below threshold to be detected. After determining the response type, the detector response is simulated using the parameters given in the geometry description input file. Throughout this process, the program generates random errors on the detected energy, on the shower position and on the shape of the shower, merges clusters based on the positions and shapes of the showers, and accommodates errors in the association between clusters and tracks.

In the default version of the `SGV` simulation none of the confusion effects explained in Section 4.2 are included. SGV offers a possibility to consider the effect of confusion by taking into account the so-called association errors stemming from the merging or splitting of the clusters, or wrongly association of clusters to tracks (for details see [148]). However, since the higgsino samples have low multiplicity, confusion effects are not an issue and the default version of the `SGV` was used.

In the analysis part of this thesis which will be explained in Chapter 6, `SGV` is used for the simulation of the detector response. In Chapter 7, the differences between SGV and full `Geant-4` based detector simulation, which will be explained in the next section, will be highlighted and their effect in the analysis will be discussed in detail.

5.5.3 Implementation of the Tracking Efficiency into SGV

In the context of this analysis the tracking efficiency in full simulation was implemented into `SGV` by taking into account the dependency on the polar angle. By default, SGV reconstructs a track for every particle in an event. However, the tracking efficiency for soft particles stemming from the small mass splitting of higgsinos is not 100%, while it is almost 100% for larger momenta as seen in Figure 4.11. Therefore in the context of DBD studies, tracking efficiency for small momenta including e^+e^- pair background from beamstrahlung was determined in full simulation and reconstruction of the ILD detector. To determine the efficiency $t\bar{t}$ events are chosen due to their high multiplicity, since the determination of tracks is more challenging in this case. Figure 5.14 shows the obtained tracking efficiency as a function of transverse momentum and as a function of cosine of the polar angle with $p_t < 5\,\text{GeV}$. One can see
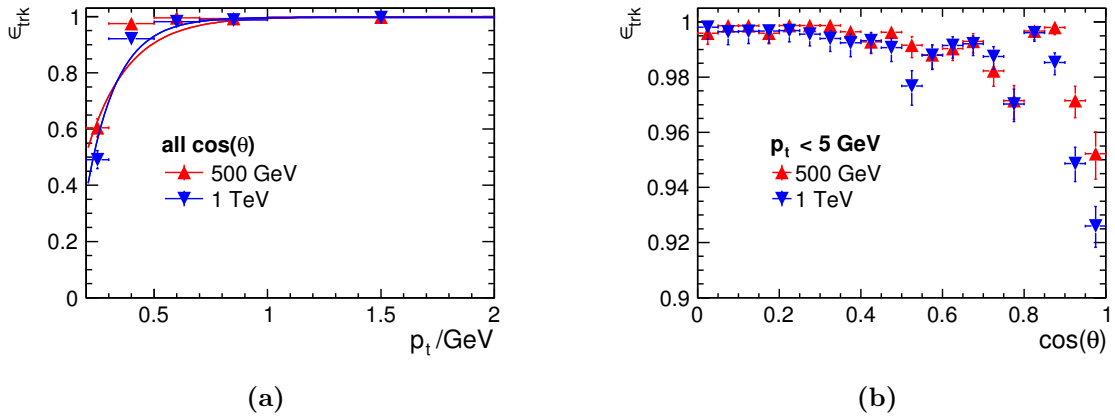
Figure 5.14 Tracking efficiency in $t\bar{t}$ events in the presence of pair background from beam-strahlung for $\sqrt{s} = 500\,\text{GeV}$ and $\sqrt{s} = 1\,\text{TeV}$, which is obtained from full simulation of the ILD detector, assuming TDR beam parameters. It is shown (a) as a function of the transverse momentum p_t, and (b) as a function of the cosine of the polar angle $|\cos\theta|$ for tracks with $p_t < 5\,\text{GeV}$. Figure is taken from Ref. [2].

on the left plot that tracking efficiency is quite high down to $400\,\text{MeV}$, while it is degrading to approximately 60% between $200\,\text{MeV}$ and $350\,\text{MeV}$. Since the tracking efficiency below $p_t < 200\,\text{MeV}$ has not been studied, it is set to zero in the analysis. Figure 5.14b displays that the average tracking efficiency for all angles is larger than 99%, while it is dropping slightly in the transition region between the barrel and the endcap, but staying larger than 95% everywhere in the geometric acceptance of the tracking system. This shows that the tracking efficiency is dependent on the polar angle. [86] Thus, Figure 5.14b was divided in four regions; $|\cos\theta| \in (0°, 20°), (20°, 40°), (40°, 60°), (60°, 90°)$. In each interval tracking efficiency was plotted as a function of p_t and is fitted with $y(x) = p_2 - p_1 \cdot \exp(-p_0 \cdot x)$ as seen in Figures 5.15 and 5.16. The parameters obtained from the fit function are stored in each polar angle region, and these four different parametrisations are used in the implementation of the tracking efficiency into SGV. Tracking efficiency in SGV is applied to the signal samples and dominant background classes, namely $e^{\pm}\gamma \to 3f$ and $\gamma\gamma \to 2l$ processes, since they are the only type of events remaining after the selection.

After reconstruction of the samples using SGV, the analysis is done by using the Marlin (Modular Analysis and Reconstruction for the LINear collider) [86, 151] framework which provides a package called LCTuple in order to create a ROOT-based TTree data structure.

Implementation of the BeamCal Tagging into SGV

The BeamCal, which is one of the very forward detectors of the ILC (cf. Section 4.3.2.3), has an important role in reducing background events with high energetic electrons scattered under a small angle, especially from $\gamma\gamma$ and $e^{\pm}\gamma$ classes. In addition to high energetic electrons, this calorimeter will be also hit by the beamstrahlung photons from pair background. Therefore, the
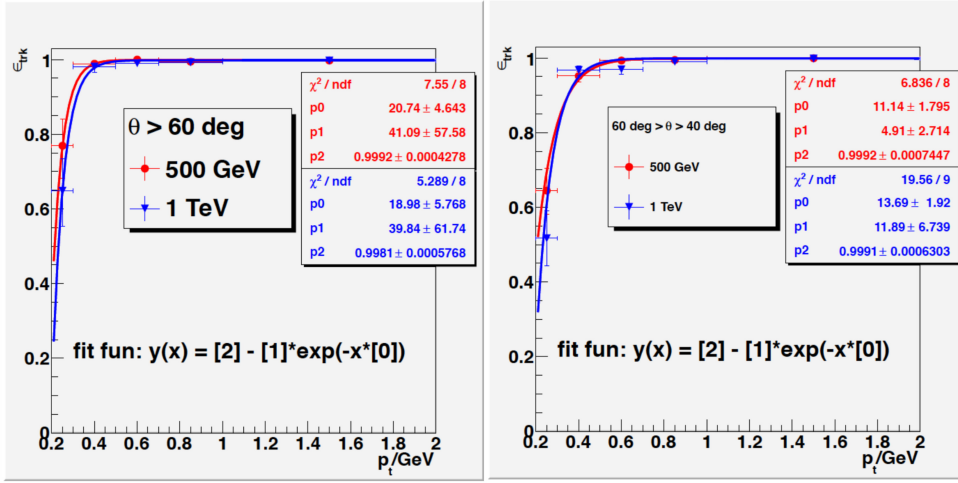
Figure 5.15 Tracking efficiency in $t\bar{t}$ events in the presence of pair background from beamstrahlung for $\sqrt{s} = 500\,\text{GeV}$ and $\sqrt{s} = 1\,\text{TeV}$, which is obtained from full simulation of the ILD detector, assuming TDR beam parameters. It is shown as a function of the transverse moment p_t for (a) $60° < \theta < 90°$ and (b) $40° < \theta < 60°$.
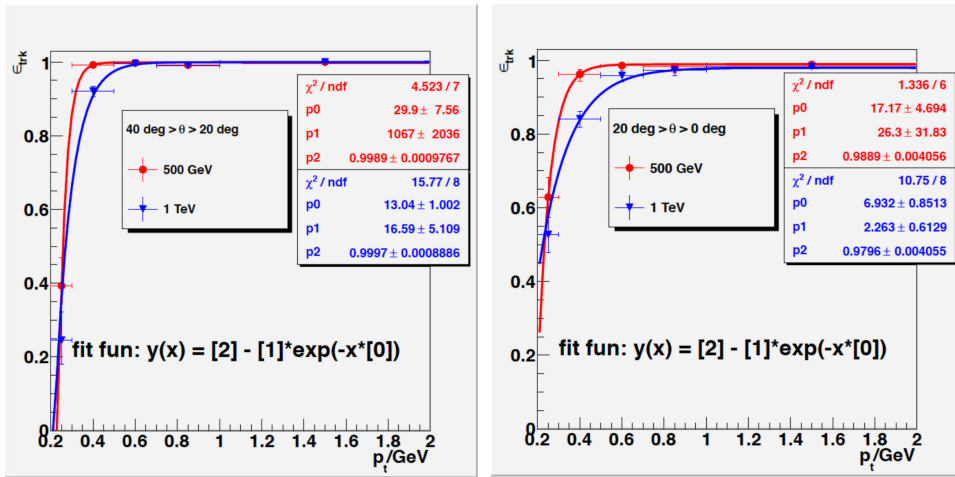

Figure 5.16 Tracking efficiency in $t\bar{t}$ events in the presence of pair background from beamstrahlung for $\sqrt{s} = 500\,\text{GeV}$ and $\sqrt{s} = 1\,\text{TeV}$, which is obtained from full simulation of the ILD detector, assuming TDR beam parameters. It is shown as a function of the transverse moment p_t for (a) $20° < \theta < 40°$ and (b) $0° < \theta < 20°$.

deposited energy on the BeamCal sensors per bunch crossing will be significant large, as can be seen in Figure 4.13a. Because of that these events are not simulated on physics events, an additional processor is added to `Marlin` after the reconstruction of samples by `SGV`, the so called *BeamCalTagEfficiency*. The processor mainly tags any event with a high energetic electron or photon (higher than $40\,\text{GeV}$) in the BeamCal.

The working principle of the algorithm can be summarised as follows: It takes the electrons and photons from the interaction point (IP) and propagates them to the BeamCal in the magnetic field. It stores the energy and momentum information of these particles in the collection which collects the reconstructed particles. The algorithm calculates the BeamCal detection probability according to the expected occupancy from the beamstrahlung and it is stored for each event. While doing this, it sums over the energy density of beamstrahlung radiation for each layer where the particle travels through the detector and compares the sum with the background. From the comparison, the probability to detect an electron or a photon is parametrised in SGV.

After running Marlin, the BeamCal particles can be found in the reconstructed particle collection, since it is merged with the reconstructed particles of the physics events.

5.6 Simulation and Reconstruction with Mokka & Marlin

All the software necessary for the steps after the event generation: simulation of the detector response, reconstruction of the simulated data, and its analysis, are collected within a software framework called ILCSoft[3] [152]. There exists a common persistency framework LCIO (Linear Collider Input/Output) [86, 153] for linear collider simulations. The idea behind building such a framework was to be able to compare the results of similar studies. This framework includes all the steps after the generation of the samples (simulation, reconstruction and analysis) in a very simple way.

5.6.1 Event Data Model

The *Event Data Model (EDM)* is defined in LCIO. An overview of the event data model is given in Figure 5.17. It consists of four different steps from the Monte Carlo level to the reconstruction and analysis. The first step contains the *MCParticle* main class which includes the list of the generated particles as well as the simulated ones, and the *SimTrackerHit* and the *SimCalorimeterHit* classes including the simulated hit information. The Raw Data step was implemented to be able to use the framework for real data from test beam and future running experiments. The third step is the digitisation, which is used to obtain the simulated data as close as possible to real data by smearing hits and including noise. This procedure is applied for the simulated hits and the results are stored in the *CalorimeterHit* and *TrackerHit* classes. The hits in these classes are combined by using pattern recognition and reconstruction algorithms into *Cluster* and *Track* classes in the reconstruction and analysis step. The main class of this step is *ReconstructedParticle* which contains a list of reconstructed particles, tracks, clusters and its particle identiy.

Detector Simulation

In order to simulate the detector response of the ILD detector of the ILC, the Mokka software [154, 155] is used. Mokka performs a detailed full detector simulation based on Geant4 toolkit [86,

---

[3]In Detailed Baseline Design (DBD) mass production v01_16_02 version of the ILCSoft was used.
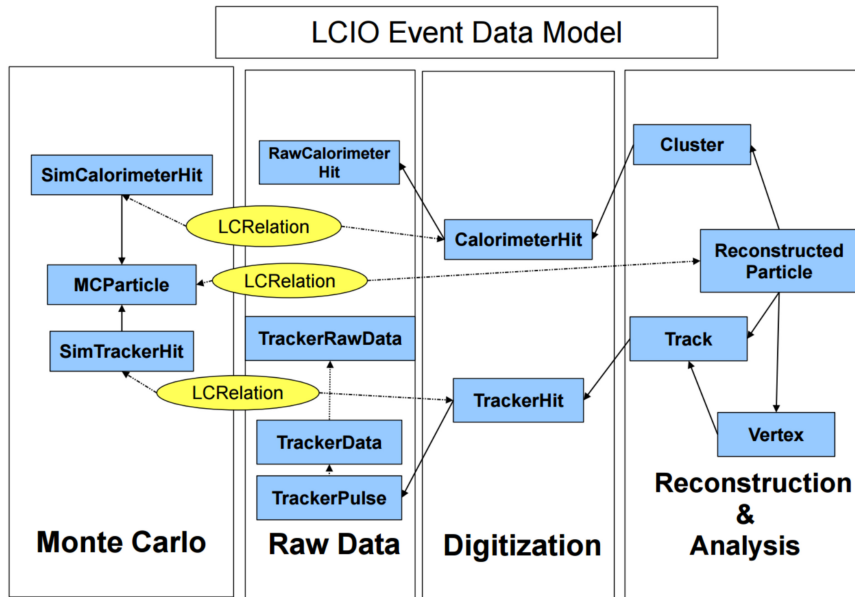
Figure 5.17 Overview of the data model defined by LCIO. The boxes shows the data classes and the arrows denote relationships between them. Figure is taken from Ref. [153]

156, 157]. `Geant4` simulates the interaction of a particle with matter. Due to the requirements of `Geant4`, `Mokka` defines the detector geometry and stores the necessary output which is determined by *Gear* toolkit in a steering file to be used in the reconstruction step, and a physics list which contains the possible processes depending on the type of the collider. There is an available list for linear collider physics processes, `LCPhys`. `Mokka` has also an interface called *Particle Gun* to generate Monte Carlo particles directly without using any event generation. The output files of `Mokka` are written in `LCIO-SIM` format.

In the studies explained in Chapter 7, both the general `Mokka` simulation and the *Particle Gun* property of `Mokka` was used. The `Mokka` version is the DBD version `08-00-03`, which performs the simulation for the `ILD_o1_v05` version of the ILD detector.

Reconstruction of Samples

After the simulation of events with full detector simulation, `Marlin` (Modular Analysis and Reconstruction for the LINear collider) [86, 151] is used for the digitisation and event reconstruction of the simulated data. This is done in several steps: first digitisation, second tracking, and third clustering. Each step is performed with the help of *processors*. All objects in each event, which have different structures such as hits, tracks, PandaroPFOs, are hold in separate *collections*. The *processors* read the data individually from the input *collections*, run their algorithms, and add the output information to the corresponding output *collections*. The transitions of the data from one *processor* to another, and between *processor* and *collection* are done with the `LCIO` event data model. `Marlin` access the information about the detector geometry via the *Gear* file.

For the event reconstruction, there is the `MarlinReco`[4] package which reconstructs the events according to *PandoraPFA*. The algorithms applied for the reconstruction of tracks and particle flow objects are introduced in detailed in Section 7.1.

The output files of `Marlin` are written in both the `LCIO-REC` and `LCIO-DST` formats. `LCIO-REC` format contains all the information obtained from the simulation and reconstruction including hits, while the `LCIO-DST` format is a more simplified version of this, containing only necessary information for the analysis.

5.7 Data Samples

The signal and background samples were generated with `Whizard 1.95` using the ILC set-up at $\sqrt{s} = 500\,\text{GeV}$ centre-of-mass energy for fully polarised beam electrons. The SM backgrounds were generated in the context of the Detailed Baseline Design (DBD) mass production. The signals were generated for an integrated luminosity of $\int \mathcal{L}dt = 500\,\text{fb}^{-1}$, but this is not the case for the SM backgrounds. Most of the SM backgrounds are generated for an integrated luminosity lower than $\int \mathcal{L}dt = 500\,\text{fb}^{-1}$, such as $e^+e^- \to 2f, 4f$, while only rare processes are generated with higher integrated luminosities than $\int \mathcal{L}dt = 500\,\text{fb}^{-1}$.

Throughout the studies of the thesis, the generated events were simulated and reconstructed both with `SGV` and with full simulation using `Mokka` and `MarlinReco` software packages. The versions of the softwares used in the analysis are given in Table 5.7.

Whizard	SGV	ILCSoft	Mokka	MarlinReco	ILD Detector
1.95	3.0	v01_16_02	08_00_03	v01_06	ILD_o1_v05

Table 5.7 The version of the event generator, fast simulation `SGV`, ILC software, and simulation and reconstruction software packages used in the full simulation. The version of the ILD detector used in `Mokka` is also depicted in the last column. The versions correspond to the ones used in the DBD production as well.

The analysis has been performed at $\int \mathcal{L}dt = 500\,\text{fb}^{-1}$ integrated luminosity for two polarisation combinations of $P(e^+, e^-) = (\pm 30\%, \mp 80\%)$ using `SGV` simulation in the first part of the study explained in Chapter 6. The obtained samples are represented in detail in Appendix C. In the stage of the analysis, the events obtained from the simulation (seen in Appendix C) were weighted to consider the partial polarisations and in order to take into account the luminosity difference between the expected integrated luminosity $\int \mathcal{L}dt = 500\,\text{fb}^{-1}$, and the ones obtained from the simulation as seen in Appendix C. The procedure of luminosity and polarisation weighting will be explained in the following.

In the second part of the study explained in Chapter 7, the signal samples are simulated and reconstructed with full simulation, and the simplification of `SGV` is investigated. For further

---

[4]DBD production version of `MarlinReco` is `v01_06`.

investigation and improvement of the analysis, the pure particles are generated directly using a feature of `Mokka`, the *particle gun*.

Luminosity and Polarisation Weights

For most of the processes of the SM background the available statistic corresponds at least to an integrated luminosity of $\int \mathcal{L}dt = 500\,\text{fb}^{-1}$, however some of them do not have enough statistics. Therefore, all samples were assigned to a luminosity weighting. This weighting was done for each process, and for each helicity combination as well, since the processes are generated in all possible helicity combinations $h(e^+, e^-) \in \{RR, LL, LR, RL\}$. The assigned luminosity weight for a given process, denoted by "proc", and helicity combination "h" is calculated by

$$w_{\text{lumi}|proc,h} = \frac{\int \mathcal{L}dt \cdot \sigma_{prod|proc,h}}{N_{prod|proc,h}} \tag{5.3}$$

where $\sigma_{prod|proc,h}$ and $N_{prod|proc,h}$ are the production cross section and number of events corresponding to a given process "proc" and helicity combination "h". The ratio N_{prod}/σ_{prod} can be interpreted as Monte Carlo luminosities, whereas $\int \mathcal{L}dt$ is the experimentally desired luminosity.

In addition to the luminosity, the polarisation of the processes should be also taken into account, since the polarisation fractions are different depending on their helicities as seen in Equation (3.3). The formula given in Eq. (3.3) can be simplified in terms of the cross section containing completely polarised electron and positron beams, and a fraction of them according to their desired polarisations as follows:

$$\sigma(P_{e^+}, P_{e^-}) = w(e_R^+\, e_L^-)\sigma_{RL} + w(e_L^+\, e_R^-)\sigma_{LR} + w(e_R^+\, e_R^-)\sigma_{RR} + w(e_L^+\, e_L^-)\sigma_{LL}. \tag{5.4}$$

The coefficients of the fully polarised cross section correspond to the weights that one need to assign in order to calculate the partial polarised cross sections. Hence, the polarisation weights w_{pol} can be written using the individual partial polarisations of the positron and electron beam for each process and helicity combination;

$$w_{\text{pol}|proc,h} = \frac{1}{4}(1 \pm P_{e^+})(1 \pm P_{e^-}). \tag{5.5}$$

	Polarisations $P(e^+, e^-)$		
Weights	$(0.0, 0.0)$	$(-0.3, +0.8)$	$(+0.3, -0.8)$
$w(e_R^+ e_L^-)$	0.25	0.035	0.585
$w(e_L^+ e_R^-)$	0.25	0.585	0.035
$w(e_R^+ e_R^-)$	0.25	0.315	0.065
$w(e_L^+ e_L^-)$	0.25	0.065	0.315

Table 5.8 Polarisation weights used in this analysis compared to the unpolarised case.

In Equation (5.5), a (positive) negative sign corresponds to (right-) left-handed polarisation of the beam electrons. The polarisation weights for the unpolarised case and partial polarisations used in the analysis are given in Table 5.8. If one wants the beams to be unpolarised, than the contribution of the fully polarised beams would be equal. In the higgsino case, since only s-channel production modes are possible, the contributions from σ_{RR} and σ_{LL} are zero.

The weight factor, which will be used in the analysis to have consistent samples, is calculated by multiplying all considered weights as follows:

$$w|_{proc,h} = w_{\text{lumi}|_{proc,h}} \cdot w_{\text{pol}|_{proc,h}}. \tag{5.6}$$

All the samples given in Appendix C are weighted by using this weight in the analysis stage.

Chapter 6

Event Selection, Mass Reconstruction and Results from Fast Simulation

In this chapter, the event selection, the measurement of masses and cross sections as well as the determination of supersymmetry (SUSY) parameters will be discussed. The signal topology consists of a few low energetic particles due to the degeneracy of the higgsinos, and large amount of missing energy coming from the lightest neutralinos (LSP). This topology provides similar final state with one of the Standard Model (SM) background, $\gamma\gamma \to 2f$. Therefore, one hard ISR photon is required to disentangle the signal and the $\gamma\gamma \to 2f$ background, which has similar signature to the signal. Besides the ISR photon, only very little activity should be present in the detector, and in particular no high energetic electron or positron should be detected in the low angle calorimeter (BeamCal). In order to suppress the majority of the SM background events, a preselection is applied without distinguishing the two signal processes. After that, exclusive decay modes are chosen to separate the two signal processes. Based on these selections, the precision on the reconstruction of the mass of the chargino $M_{\widetilde{\chi}_1^{\pm}}$ and the heavier neutralino $M_{\widetilde{\chi}_2^0}$, the mass difference between the chargino and the LSP $\Delta M_{\widetilde{\chi}_1^{\pm} - \widetilde{\chi}_1^0}$, and on the polarised cross sections for the chargino and neutralino processes are determined. Then, the electroweakino parameters M_1, M_2, μ and $\tan\beta$ are determined using the results of the first part to see how well the parameter can be estimated.

6.1   Preselection

As explained in Chapter 5, the signal consists of an ISR photon, large missing energy, and a few soft visible particles. In order to suppress the SM background, a preselection including several cuts has been applied. In the following, each of the preselection cut will be explained in detail.

- **Initial State Radiation Photon:** The initial state radiation (ISR) photon is required in

order to distinguish the similarity between the signal and the SM background as explained in Section 5.3. The photon candidate is required to be within the tracking performance of ILD with $|\cos\theta_{ISR}| < 0.9397$ corresponding to $7°$, and to have an energy $E_{\gamma_{ISR}} > 10\,\text{GeV}$. The polar angle requirement is necessary to ensure that the photon is within the acceptance of the tracking system in order to be able to distinguish photons and electrons. The highest energetic photon fulfilling these criteria is considered as a hard ISR photon.

- **BeamCal Particles:** The BeamCal is one of the forward detectors of ILD as introduced in Section 4.3.2.3 [86]. Since it is hit by the large amount of e^+e^--pair background (cf. Section 3.5.1), the BeamCal needs special consideration. In the signal events, the incoming electrons annihilate, and hence there is no significant activity in the BeamCal, even when a hard ISR photon is required. Therefore, the events which has an activity in the BeamCal are vetoed. This cut suppresses the events with high energetic electrons or photons scattered under a small angle, such as $\gamma\gamma$ and $e\gamma$ type of processes.

- **Low Multiplicity Events:** Since there are only a few final state particles in the signal, the total number of reconstructed particles (N_{RP}) can be used to suppress the SM background. Figure 6.1 displays the number of reconstructed particles for both scenarios. Since the value of N_{RP} is smaller for signals, the number of events are required to be less than $N_{RP} < 15$. The excluded region is shown with the shaded area, and it indicates that the required cut reduces most of the SM background events with high multiplicity, especially $ee \to 6f$ and $e\gamma \to 5f$.

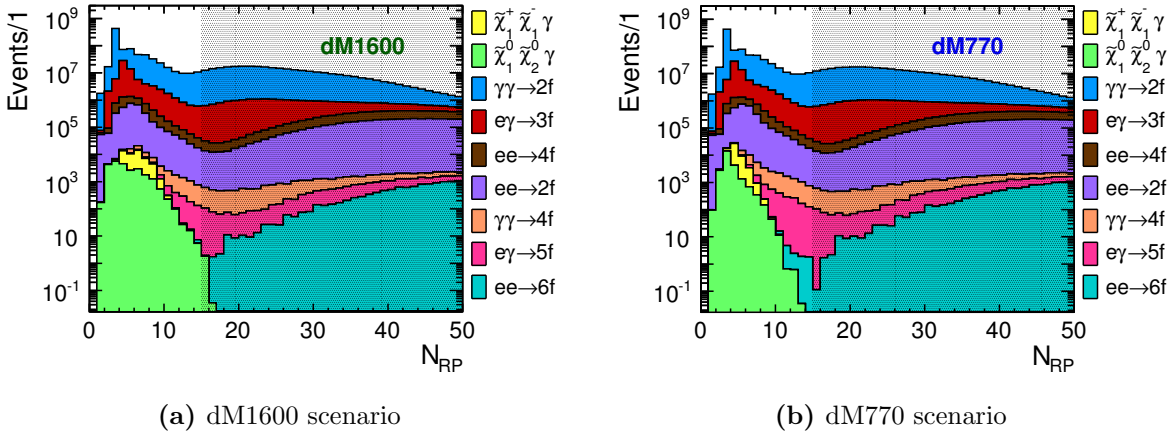(a) dM1600 scenario

(b) dM770 scenario

Figure 6.1 Number of reconstructed particles after requiring hard ISR photon for integrated luminosity of $\int \mathcal{L}dt = 500\,\text{fb}^{-1}$ at $\sqrt{s} = 500\,\text{GeV}$ with $P(e^+, e^-) = (+30\%, -80\%)$. The number of particles are required to be $N_{RP} < 15$. The shaded area shows the excluded region.

- **Four-Momentum of Soft Particles:** In each event, any other reconstructed particles apart from the ISR photon are required to be at least $20°$ away from the beam axis to be within the more efficient tracking system by fulfilling $|\cos\theta_{soft}| < 0.9397$. Otherwise, only forward tracking detector (FTD) which does not have high momentum resolution will be responsible for the tracking [129]. The related plot for the polar angle acceptance of the tracking detectors is shown in Figure 4.11a. If there is any event which has a particle in that region, it is vetoed.

This cut does not effect the signal events as much as the SM background, since the signal processes are produced centrally. The angular distribution of both the signal events as well as background events are shown in Figure 6.2. It shows the maximum value distribution of $\cos\theta$ for charged reconstructed particles. The excluded region is shown with a shaded area, which displays that a significant amount of the SM background is suppressed.
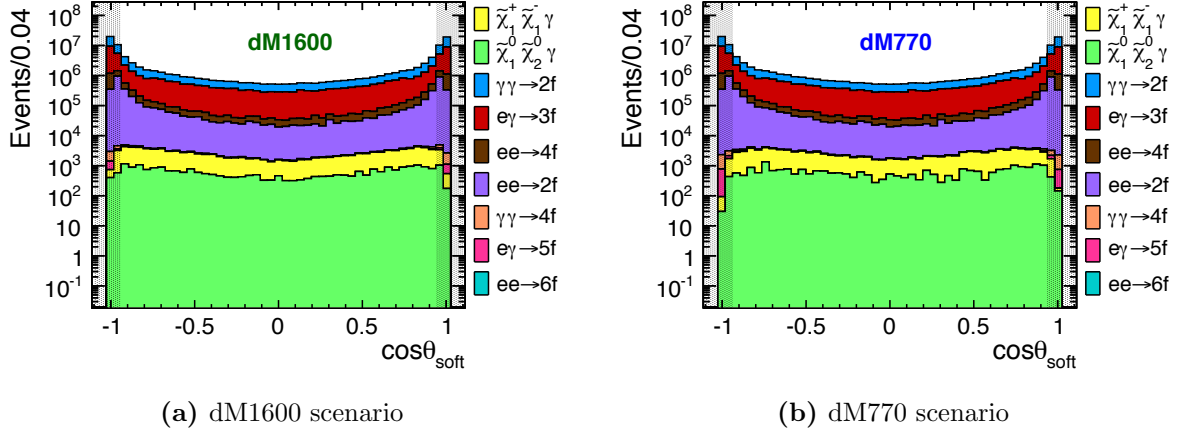

(a) dM1600 scenario

(b) dM770 scenario

Figure 6.2 The maximum value of $\cos\theta$ distribution of the reconstructed charged particles after $N_{\mathrm{RP}} < 15$ requirement at $\sqrt{s} = 500\,\mathrm{GeV}$ and $\int \mathcal{L}dt = 500\,\mathrm{fb}^{-1}$ with $P(e^+, e^-) = (+30\%, -80\%)$ for the dM770 and dM1600 scenario. The reconstructed soft particles fulfilling $|\cos\theta_{\mathrm{soft}}| < 0.9397$ corresponding $20°$ are selected. The excluded region is shown with the shaded area.

(a) dM1600 scenario
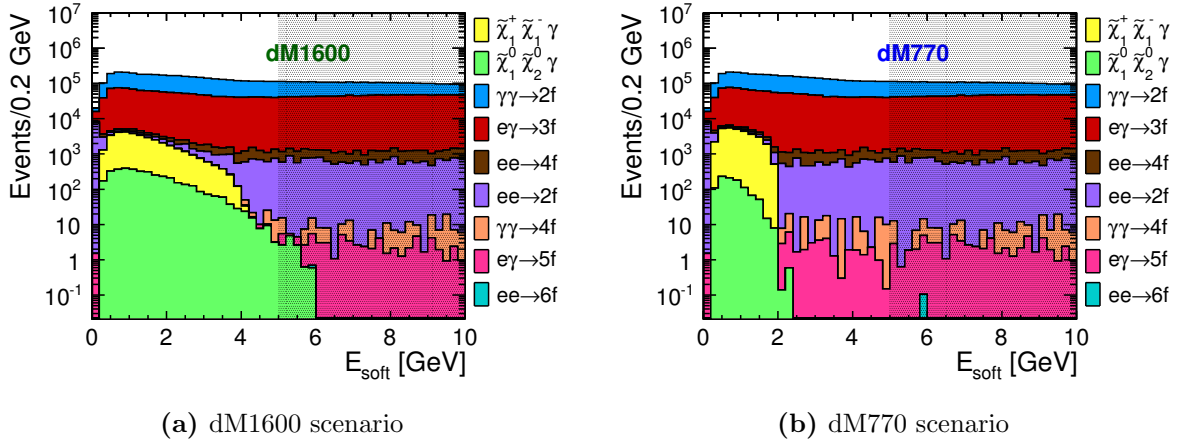
(b) dM770 scenario

Figure 6.3 The maximum energy distribution of the reconstructed charged particles after $|\cos\theta_{\mathrm{soft}}| < 0.9397$ requirement at $\sqrt{s} = 500\,\mathrm{GeV}$ and $\int \mathcal{L}dt = 500\,\mathrm{fb}^{-1}$ with $P(e^+, e^-) = (+30\%, -80\%)$ for dM1600 and dM770 scenarios. The energy of the reconstructed soft particles is required to be $E_{\mathrm{soft}} < 5$. The shaded area shows the excluded region.

Due to the mass degeneracy of the higgsinos, it is expected that the final state particles are very soft. Therefore, only the events, which have very soft reconstructed particles fulfilling

$E_{\text{soft}} < 5\,\text{GeV}$, are required. Figure 6.3 shows the energy distribution of most energetic charged reconstructed particles in each event after the cut applied on the polar angle of soft particles. It clearly indicates that this feature of the signal topology has a large contribution to the suppression of the SM background.

- **Missing Four-Momentum:** Since there is large amount of missing energy in the signal events due to missing LSPs, the events with large missing energy are considered. By requiring $E_{\text{miss}} > 300\,\text{GeV}$, the events where either the beam electron or positron with an energy nearly $250\,\text{GeV}$ is scattered under very small angles and goes through the beam pipe can be rejected. The missing energy distribution of the signal and SM background events is shown in Figure 6.4. This cut reduces a large fraction of the $\gamma\gamma \to 2f$ and $e\gamma \to 3f$ SM background.

(a) dM1600 scenario
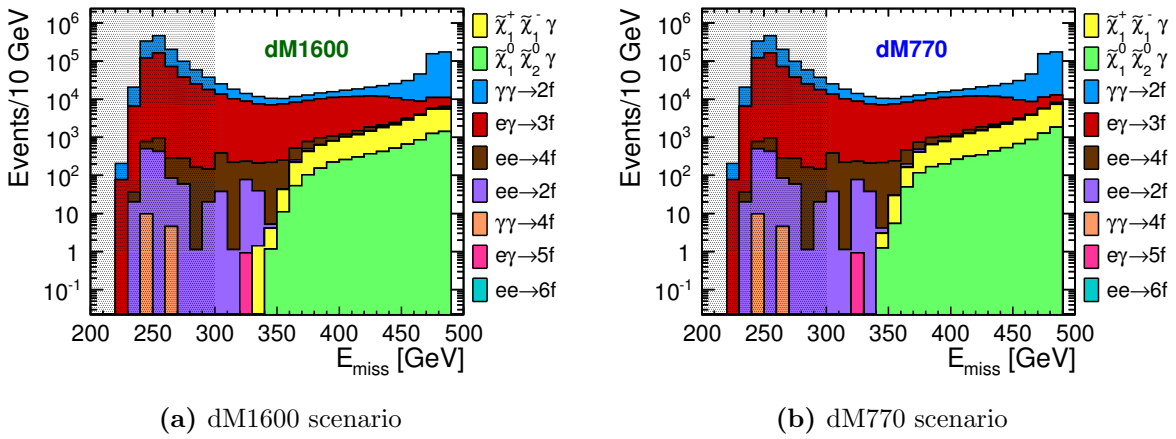
(b) dM770 scenario

Figure 6.4 Missing energy in each event after requiring $E_{\text{soft}} < 5\,\text{GeV}$ at $\sqrt{s} = 500\,\text{GeV}$ and $\int \mathcal{L}dt = 500\,\text{fb}^{-1}$ with $P(e^+, e^-) = (+30\%, -80\%)$ for dM1600 and dM770 scenarios. The excluded area fulfilling $E_{\text{miss}} < 300$ is shown with a shaded area.

In order to be sure that the missing energy is not due to particles escaping along the beam pipe, the missing momentum vector is required to be within the acceptance region of the detector by fulfilling $|\cos\theta_{\text{miss}}| < 0.992$. The distribution of $\cos\theta$ is displayed in Figure 6.5.

Cut-Flow Tables

The applied cuts in the preselection are explained above, and the corresponding numbers of events remaining after each cut are given in Table 6.1 and Table 6.3 for the centre-of-mass energy of $\sqrt{s} = 500\,\text{GeV}$, the integrated luminosity of $\int \mathcal{L}dt = 500\,\text{fb}^{-1}$, and two combinations of polarisations $P(e^+, e^-) = (+30\%, -80\%)$ and $P(e^+, e^-) = (-30\%, +80\%)$, respectively. The numbers of events for the signals are given in both scenarios, while the SM backgrounds are grouped in terms of their initial states as explained in Section 5.2. In Table 6.2 and Table 6.4, the numbers of events in each SM background subgroup are summarised as well. The tables show the weighted number of events to take into account the luminosity and polarisation differences as explained in Section 5.7.
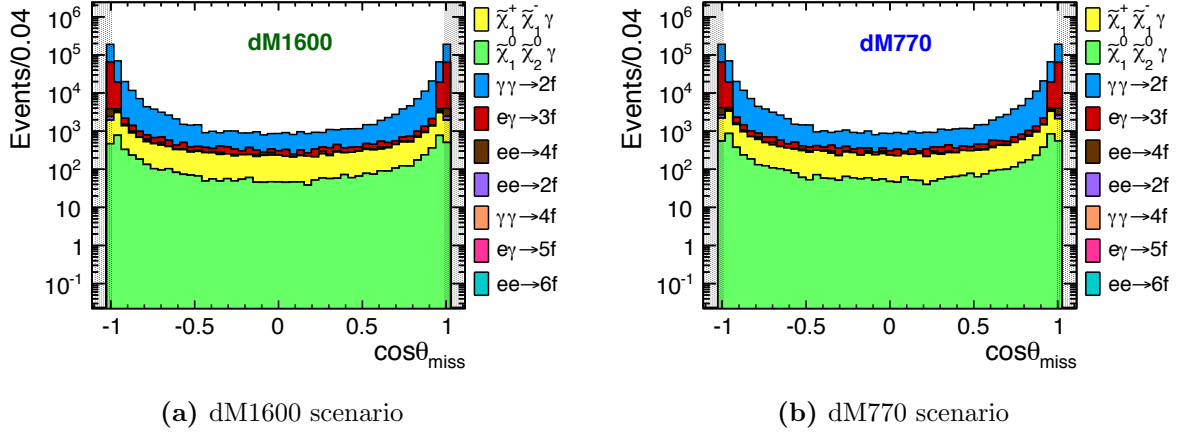
(a) dM1600 scenario

(b) dM770 scenario

Figure 6.5 $\cos\theta$ distribution of missing four-momentum for each event after requiring $E_{\text{miss}} > 300\,\text{GeV}$ at $\sqrt{s} = 500\,\text{GeV}$ and $\int \mathcal{L}dt = 500\,\text{fb}^{-1}$ with $P(e^+, e^-) = (+30\%, -80\%)$ for dM1600 and dM770 scenarios. The excluded area is shown with a shaded area.

In Table 6.1, the combined SM backgrounds in terms of their initial states are shown, while the SM background with different final states are separated in Table 6.2. Table 6.2 clearly shows that the $e\gamma \to 3f$ and $\gamma\gamma \to 2f$ are the dominant SM backgrounds. The biggest decrease on the signal is the requirement of the ISR photon since the energy requirement of the ISR photon is applied at analysis level. At generator level, there is only a minimal cut of $4\,\text{GeV}$ on the invariant mass of the photon with respect to the beam electron/positron which helps to exclude events having an ISR photon either in the very forward region or with very low energy. The requirement of the ISR photon suppresses approximately 95% of the $\gamma\gamma \to 2f$ background and at least 50% of the other SM backgrounds. Table 6.2 displays that the high multiplicity backgrounds, such as $ee \to 6f$ and $e\gamma \to 5f$ are suppressed with the cut applied on the number

	dM1600		dM770		Standard Model		
	$\widetilde{\chi}_1^+\widetilde{\chi}_1^-\gamma$	$\widetilde{\chi}_1^0\widetilde{\chi}_2^0\gamma$	$\widetilde{\chi}_1^+\widetilde{\chi}_1^-\gamma$	$\widetilde{\chi}_1^0\widetilde{\chi}_2^0\gamma$	$ee \to 2, 4, 6f$	$e\gamma \to 3, 5f$	$\gamma\gamma \to 2, 4f$
no cut	38672	24250	38130	23940	2.6434×10^7	8.8820×10^7	9.7554×10^8
BeamCal veto	38591	24187	38054	23874	2.6284×10^7	8.8178×10^7	9.6757×10^8
$N_{\text{RP}} < 15$	38591	24185	38054	23874	6.4968×10^6	6.5811×10^7	6.6308×10^8
$N_{\text{ISR}} = 1$	30058	9551	29675	9317	3.1640×10^6	1.5074×10^7	1.7752×10^7
$|\cos\theta_{\text{soft}}| < 0.9397$	21501	7318	23117	7458	7.1453×10^5	4.5646×10^6	4.7083×10^6
$E_{\text{soft}} < 5\,\text{GeV}$	20611	6615	22156	7110	9092	5.9732×10^5	1.2390×10^6
$E_{\text{miss}} > 300\,\text{GeV}$	20611	6615	22156	7110	6462	1.5822×10^5	4.6306×10^5
$|\cos\theta_{\text{miss}}| < 0.992$	19872	6365	21558	6872	5731	1.1837×10^5	3.3051×10^5

Table 6.1 Cut-flow table of the preselection for an integrated luminosity of $\int \mathcal{L}dt = 500\,\text{fb}^{-1}$ at $\sqrt{s} = 500\,\text{GeV}$ and $P(e^+, e^-) = (+30\%, -80\%)$.

	$ee \to 2, 4, 6f$			$e\gamma \to 3, 5f$		$\gamma\gamma \to 2, 4f$	
	$ee \to 2f$	$ee \to 4f$	$ee \to 6f$	$e\gamma \to 3f$	$e\gamma \to 5f$	$\gamma\gamma \to 2f$	$\gamma\gamma \to 4f$
no cut	12083300	13807900	543272	88773300	46247	975467000	77144
BeamCal veto	11997000	13745400	541827	88132700	45189	967496000	74450
$N_{\mathrm{RP}} < 15$	3076440	3420380	18	65805200	5354	663052000	25848
$N_{\mathrm{ISR}} = 1$	1698270	1465720	9	15072400	1676	17748700	3383
$\lvert\cos\theta_{\mathrm{soft}}\rvert < 0.9397$	449873	264658	2	4564270	368	4707720	592
$E_{\mathrm{soft}} < 5\,\mathrm{GeV}$	3082	6010	0	597321	2	1239020	14
$E_{\mathrm{miss}} > 300\,\mathrm{GeV}$	1982	4480	0	158216	2	463060	0
$\lvert\cos\theta_{\mathrm{miss}}\rvert < 0.992$	1734	3997	0	118363	2	330511	0

Table 6.2 Cut-flow table of the preselection for the Standard Model subgroups for an integrated luminosity of $\int \mathcal{L}dt = 500\,\mathrm{fb}^{-1}$ at $\sqrt{s} = 500\,\mathrm{GeV}$ and $P(e^+, e^-) = (+30\%, -80\%)$.

of reconstructed particles by almost 100% and 88%. The other preselection cuts applied on the soft particles and on the missing four-momentum suppress a large fraction of the SM background as well. However, these cuts do not remove the $\gamma\gamma \to 2f$ and $e\gamma \to 3f$ processes entirely. These will be reduced in the selection of the signal processes.
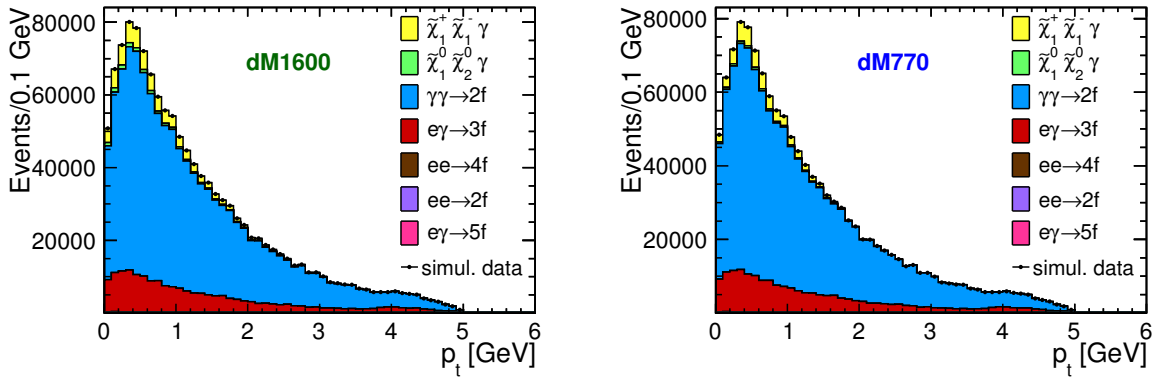
Figure 6.6 shows the p_t distribution of the final state particles apart from the ISR photon after the preselection for both scenarios. The SM background was by far dominant before the preselection. The preselection reduces a large amount of the SM background and makes the signal visible on top of the Standard Model background, although the SM contribution is still high.

	dM1600		dM770		Standard Model		
	$\widetilde{\chi}_1^+ \widetilde{\chi}_1^- \gamma$	$\widetilde{\chi}_1^0 \widetilde{\chi}_2^0 \gamma$	$\widetilde{\chi}_1^+ \widetilde{\chi}_1^- \gamma$	$\widetilde{\chi}_1^0 \widetilde{\chi}_2^0 \gamma$	$ee \to 2, 4, 6f$	$e\gamma \to 3, 5f$	$\gamma\gamma \to 2, 4f$
no cut	9817	19071	9792	18773	1.1640×10^7	8.3999×10^7	9.7554×10^8
BeamCal veto	9796	19023	9770	18727	1.1559×10^7	8.3408×10^7	9.6757×10^8
$N_{\mathrm{RP}} < 15$	9796	19021	9770	18727	4.6395×10^6	6.4208×10^7	6.6308×10^8
$N_{\mathrm{ISR}} = 1$	7640	7551	7663	7350	2.4127×10^6	1.4912×10^7	1.7752×10^7
$\lvert\cos\theta_{\mathrm{soft}}\rvert < 0.9397$	5483	5816	5970	5897	4.2021×10^5	4.4720×10^6	4.7083×10^6
$E_{\mathrm{soft}} < 5\,\mathrm{GeV}$	5265	5248	5724	5605	7468	5.8726×10^5	1.2390×10^6
$E_{\mathrm{miss}} > 300\,\mathrm{GeV}$	5265	5248	5724	5605	5078	1.5158×10^5	4.6306×10^5
$\lvert\cos\theta_{\mathrm{miss}}\rvert < 0.992$	5090	5038	5571	5434	4329	1.1284×10^5	3.3051×10^5

Table 6.3 Cut-flow table of the preselection for an integrated luminosity of $\int \mathcal{L}dt = 500\,\mathrm{fb}^{-1}$ at $\sqrt{s} = 500\,\mathrm{GeV}$ and $P(e^+, e^-) = (-30\%, +80\%)$.

	$ee \to 2, 4, 6f$			$e\gamma \to 3, 5f$		$\gamma\gamma \to 2, 4f$	
	$ee \to 2f$	$ee \to 4f$	$ee \to 6f$	$e\gamma \to 3f$	$e\gamma \to 5f$	$\gamma\gamma \to 2f$	$\gamma\gamma \to 4f$
no cut	8007910	3396260	235363	83970800	28665	975467000	77144
BeamCal veto	7948160	3376180	234691	83379900	28032	967496000	74450
$N_{\mathrm{RP}} < 15$	2708880	1930610	32	64204000	4007	663052000	25848
$N_{\mathrm{ISR}} = 1$	1517100	895588	9	14911100	1257	17748700	3383
$|\cos\theta_{\mathrm{soft}}| < 0.9397$	372946	47260	2	4471820	211	4707720	592
$E_{\mathrm{soft}} < 5\,\mathrm{GeV}$	2798	4670	0	587259	2	1239020	14
$E_{\mathrm{miss}} > 300\,\mathrm{GeV}$	1698	3380	0	151578	2	463060	0
$|\cos\theta_{\mathrm{miss}}| < 0.992$	1326	3003	0	112833	2	330511	0

Table 6.4 Cut-flow table of the preselection for the Standard Model subgroups for an integrated luminosity of $\int \mathcal{L}dt = 500\,\mathrm{fb}^{-1}$ at $\sqrt{s} = 500\,\mathrm{GeV}$ and $P(e^+, e^-) = (-30\%, +80\%)$.

(a) dM1600 scenario   (b) dM770 scenario

Figure 6.6 p_t distribution of the final state particles after preselection excluding the ISR photon at $\sqrt{s} = 500\,\mathrm{GeV}$ and $\int \mathcal{L}dt = 500\,\mathrm{fb}^{-1}$ with $P(e^+, e^-) = (+30\%, -80\%)$. Only the remaining SM backgrounds are labeled in the plots, however, some of them are suppressed by the others.

6.2 Chargino Process

6.2.1 Chargino Selection

Exclusive decay modes of the signal processes give the opportunity to distinguish them (see Section 5.1.3 for decay modes of the charginos). The semi-leptonic final state is used to select chargino events, since it is not possible to have such a final state in the case of neutralino pair production. The comparable decay mode of the neutralino is the one decaying to the LSP and the virtual Z boson which can decay only fully leptonically or fully hadronically. Therefore the semi-leptonic decay mode helps to suppress the neutralino process which is considered as SUSY background for the chargino selection. As shown in Table 5.5, single pion decay is the

dominant decay mode especially in the dM770 scenario. Therefore, the final states including one π and one e or μ are considered as the chargino signature. The main SM background to this semi-leptonic signature is τ-lepton pairs, from either $e^+e^- \to \tau^+\tau^-$, $e^\pm\gamma \to e^\pm\tau^+\tau^-$ or $\gamma\gamma \to \tau^+\tau^-$, since τ leptons decay to both leptons and hadrons just like charginos. The decay process of τ is $\tau \to \nu_\tau W^*$, where W^* decays leptonically to $e\nu_e$ and $\mu\nu_\mu$ with branching ratios of $BR(\tau \to l\nu_l\nu_\tau) = 17\%$, and hadronically to $\pi^\pm$ and $\pi^\pm\pi^0$ with branching ratios of 10% and 25%, respectively [158]. One of the W^* bosons could decay hadronically while the other one decays leptonically. This means that τ-pairs can have the similar final state to the signal. Because of this similarity, a special treatment is necessary to suppress this kind of background which will be explained in the following.

Figure 5.6 shows the branching ratios of the chargino decay modes as a function of the mass difference between chargino and LSP [82]. For the mass differences between the mass of the pions and $1\,\text{GeV}$, the single charged pion decay is the dominant decay mode, while the branching ratio of this mode is getting small for the values larger than $1\,\text{GeV}$. This can be seen from Table 5.5 for both of the benchmark scenarios. Because of this dependency of the branching ratios on the mass differences, one would need to use different decay modes for scenarios having various $\Delta M_{\widetilde{\chi}_1^\pm - \widetilde{\chi}_1^0}$. In the dM770 scenario, the single charged pion decay mode is chosen for the hadronic part since $\Delta M_{\widetilde{\chi}_1^\pm - \widetilde{\chi}_1^0} = 770\,\text{MeV}$. Including the leptonic decay modes of the other chargino, it consists of the 35% of the chargino pair events. In the case of dM1600, the branching ratio of the chargino pair events with this decay mode is 11% which is significantly lower than the other scenario due to the larger mass difference. Because of that another decay mode to one charged and one neutral pion, which has a quite large BR, is considered in addition to the single charged pion decay in the dM1600 scenario. The $\pi^\pm\pi^0$ decay channel rises the branching ratio of the semi-leptonic decay mode to 30%. Using the same decay channel in the dM770 scenario would increase the total branching ratio by only 4%, which is too small to balance the increase on the SM background, and therefore only the single pion decay mode is considered in this scenario. The cut flow table for chargino selection is given for $\sqrt{s} = 500\,\text{GeV}$ centre-of-mass energy and $\int \mathcal{L}dt = 500\,\text{fb}^{-1}$ integrated luminosity in Table 6.5 for polarisation combination of $P(e^+, e^-) = (+30\%, -80\%)$ and in Table 6.6 for polarisation combination of $P(e^+, e^-) = (-30\%, +80\%)$.

Against the τ-events which are the main background, a variable that represents the boosted energy of the hadronic chargino decay products (only $\pi^\pm$ in the dM770 scenario, both $\pi^\pm$ and π^0 in the dM1600 scenario) into the rest frame of the chargino pair can be used. More information about this variable will be given in Section 6.2.3. The boosted energy in the case of dM770 scenario is calculated as follows:

$$E_\pi^* = \frac{(\sqrt{s} - E_\gamma)E_\pi + \vec{p}_\pi \cdot \vec{p}_\gamma}{\sqrt{s'}}. \tag{6.1}$$

Here, $\sqrt{s'}$ is the reduced centre-of-mass (CM) energy of the system after emission of the ISR photon. It is defined as $s' = s - 2\sqrt{s}E_\gamma$ as seen in section 6.2.2, where $\sqrt{s} = 500\,\text{GeV}$ is the nominal centre-of-mass energy. E_π and $\vec{p}_\pi$ are the energy and the 3-momentum of the charged pion in the laboratory frame, while $\vec{p}_\gamma$ is the 3-momentum of the ISR photon in that frame. In case of the additional π^0, the reconstructed four-momentum of the two photons from the π^0 decay are added to the charged pion four-momentum. Figure 6.7 shows the value of
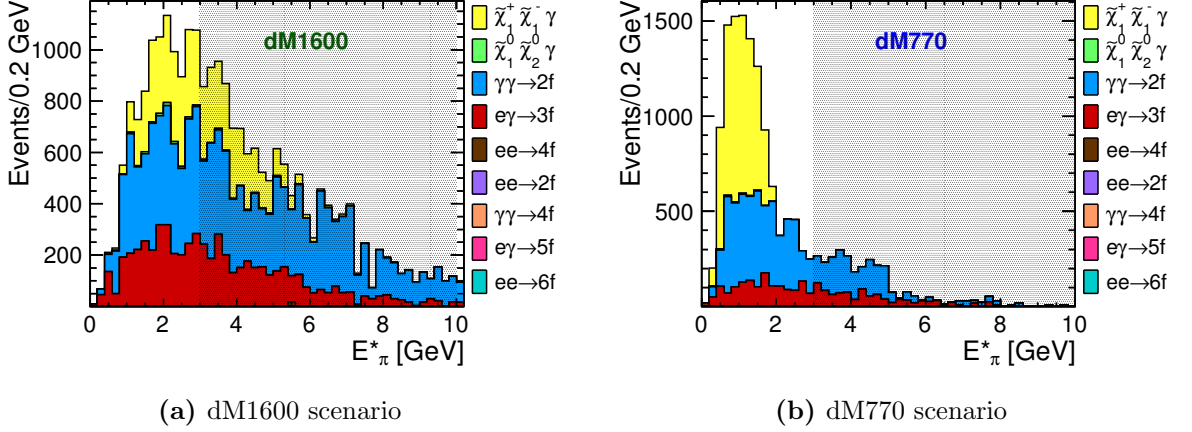
(a) dM1600 scenario   **(b)** dM770 scenario

Figure 6.7 Energy of pions boosted into the rest frame of the chargino pairs after semi-leptonic decay channel selection at $\sqrt{s} = 500\,\text{GeV}$ and $\int \mathcal{L}dt = 500\,\text{fb}^{-1}$ with $P(e^+, e^-) = (+30\%, -80\%)$ (only $\pi^{\pm}$ in the dM770 scenario, both $\pi^{\pm}$ and π^0 in the dM1600 scenario). The shaded area indicates the excluded region.

this variable in both scenarios. In the dM770 scenario, it is only a few GeV for pions from chargino decays, while it can take large values as well for τ decays. The value of it is spread in the dM1600 scenario since the mass gap between higgsinos are large in this case and there is an additional decay channel which influences the boosted energy of pions for both the signal and the background. The boosted energy is required to be $E_{\pi}^* < 3\,\text{GeV}$ in order to reduce the dominant SM background. This cut is fully efficient for dM770 scenario since it keeps the signal events as they are while reducing the number of SM background by approximately 30-40%. However, it is not that efficient for dM1600 scenario because it reduces the number of signal events also. The reason of this is that E_{π}^* is directly proportional to $\Delta M_{\tilde{\chi}_1^{\pm} - \tilde{\chi}_1^0}$ which will be explained in Section 6.2.3. Since the mass difference is two times larger in the latter case than the first case, the value of E_{π}^* gets higher; however, the events which have a high E_{π}^* are generally in the less relevant region for the analysis which is the region with higher $\sqrt{s'}$ values seen and discussed later in Figure 6.13. Therefore, it does not affect the result of the analysis. The remaining dominant SM background comes from $\gamma\gamma$ events, mainly $\gamma\gamma \to \tau^+\tau^-$ events which are back-to-back in the transverse plane due to the momentum conservation and have high $\sqrt{s'}$. The events with lower $\sqrt{s'}$ have already been excluded with the requirement of the ISR photon. The remaining events come from the case when the ISR photon has low energy such that it cannot make the beam electron visible to the detector. To suppress these events, the acoplanarity angle which is the angle between the decay products of two mother particles in the transverse plane is required to be smaller than 2 rad with a combination of $\sqrt{s'} < 480\,\text{GeV}$. For the semileptonic final state, the acoplanarity angle can be calculated from the momentum of the leptonic and hadronic decay as follows:

$$\Phi_{acop} = \arccos\left(\frac{\vec{p}_{\text{lep}} \cdot \vec{p}_{\text{had}}}{|\vec{p}_{\text{lep}}||\vec{p}_{\text{had}}|}\right) \tag{6.2}$$

where $\vec{p}_{\text{lep}} = \vec{p}_{x_{\text{lep}}} + \vec{p}_{y_{\text{lep}}}$ and $\vec{p}_{\text{had}} = \vec{p}_{x_{\text{had}}} + \vec{p}_{y_{\text{had}}}$ in the transverse plane. Figures 6.8 and 6.9

show the acoplanarity angle Φ_{acop} and $\sqrt{s'}$ distributions for both scenarios at the stage after the boosted energy cut. The combined cut reduces the SM background of $\gamma\gamma$ by a factor of four and six in the dM1600 and dM770 scenarios, respectively.

	dM1600		Standard Model		
	$\widetilde{\chi}_1^+\widetilde{\chi}_1^-\gamma$	$\widetilde{\chi}_1^0\widetilde{\chi}_2^0\gamma$	$ee \to 2,4,6\text{f}$	$e\gamma \to 3,5\text{f}$	$\gamma\gamma \to 2,4\text{f}$
after preselection	19872	6365	5731	1.1837×10^5	3.3051×10^5
$l^\pm\pi^\pm(\pi^0)$	5509	134	38	6197	13991
$E_\pi^* < 3\,\text{GeV}$	4435	103	0	2635	6162
$\Phi_{\text{acop}} < 2$ or $\sqrt{s'} < 480\,\text{GeV}$	3813	97	0	2564	1452
$E_{\text{miss}} > 350\,\text{GeV}$	3812	97	0	1016	511

	dM770		Standard Model		
	$\widetilde{\chi}_1^+\widetilde{\chi}_1^-\gamma$	$\widetilde{\chi}_1^0\widetilde{\chi}_2^0\gamma$	$ee \to 2,4,6\text{f}$	$e\gamma \to 3,5\text{f}$	$\gamma\gamma \to 2,4\text{f}$
after preselection	21558	6872	5731	1.1837×10^5	3.3051×10^5
$l^\pm\pi^\pm$	5489	38	19	2478	6754
$E_\pi^* < 3\,\text{GeV}$	5489	38	0	1465	4755
$\Phi_{\text{acop}} < 2$ or $\sqrt{s'} < 480\,\text{GeV}$	4600	36	0	1417	782
$E_{\text{miss}} > 350\,\text{GeV}$	4599	36	0	536	218

Table 6.5 Cut flow tables of the chargino selection in the two scenarios for an integrated luminosity of $\int \mathcal{L}dt = 500\,\text{fb}^{-1}$ and $P(e^+, e^-) = (+30\%, -80\%)$ following the preselection (cf. Table 6.1)

(a) Acoplanarity Angle
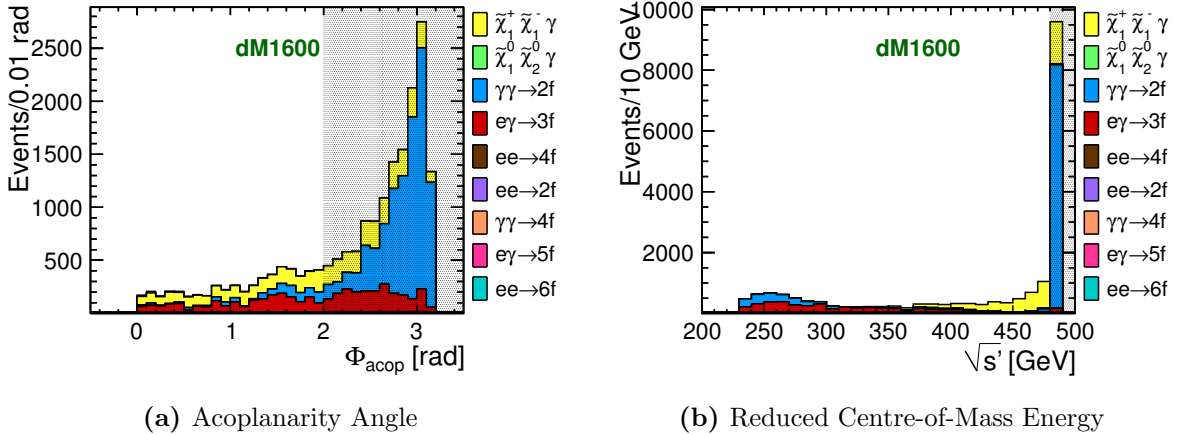
(b) Reduced Centre-of-Mass Energy

Figure 6.8 Acoplanarity angle between the leptonic and hadronic decays and reduced centre-of-mass energy distribution in the dM1600 scenario at $\sqrt{s} = 500\,\text{GeV}$ and $\int \mathcal{L}dt = 500\,\text{fb}^{-1}$ with $P(e^+, e^-) = (+30\%, -80\%)$.

	dM1600		Standard Model		
	$\widetilde{\chi}_1^+ \widetilde{\chi}_1^- \gamma$	$\widetilde{\chi}_1^0 \widetilde{\chi}_2^0 \gamma$	$ee \to 2,4,6\mathrm{f}$	$e\gamma \to 3,5\mathrm{f}$	$\gamma\gamma \to 2,4\mathrm{f}$
after preselection	5090	5038	4329	1.1284×10^5	3.3051×10^5
$l^\pm \pi^\pm (\pi^0)$	1359	110	2	6146	13991
$E_\pi^* < 3\,\mathrm{GeV}$	1092	80	0	2596	6162
$\Phi_{\mathrm{acop}} < 2$ or $\sqrt{s'} < 480\,\mathrm{GeV}$	930	77	0	2517	1452
$E_{\mathrm{miss}} > 350\,\mathrm{GeV}$	929	77	0	1034	511

	dM770		Standard Model		
	$\widetilde{\chi}_1^+ \widetilde{\chi}_1^- \gamma$	$\widetilde{\chi}_1^0 \widetilde{\chi}_2^0 \gamma$	$ee \to 2,4,6\mathrm{f}$	$e\gamma \to 3,5\mathrm{f}$	$\gamma\gamma \to 2,4\mathrm{f}$
after preselection	5571	5434	4329	1.1284×10^5	3.3051×10^5
$l^\pm \pi^\pm$	1408	32	1	2673	6754
$E_\pi^* < 3\,\mathrm{GeV}$	1408	32	0	1696	4755
$\Phi_{\mathrm{acop}} < 2$ or $\sqrt{s'} < 480\,\mathrm{GeV}$	1190	32	0	1634	782
$E_{\mathrm{miss}} > 350\,\mathrm{GeV}$	1190	32	0	683	218

Table 6.6 Cut flow tables of the chargino selection in the two scenarios for an integrated luminosity of $\int \mathcal{L}dt = 500\,\mathrm{fb}^{-1}$ and $P(e^+, e^-) = (-30\%, +80\%)$ following the preselection (cf. Table 6.1)

(a) Acoplanarity Angle

(b) Reduced Centre-of-Mass Energy
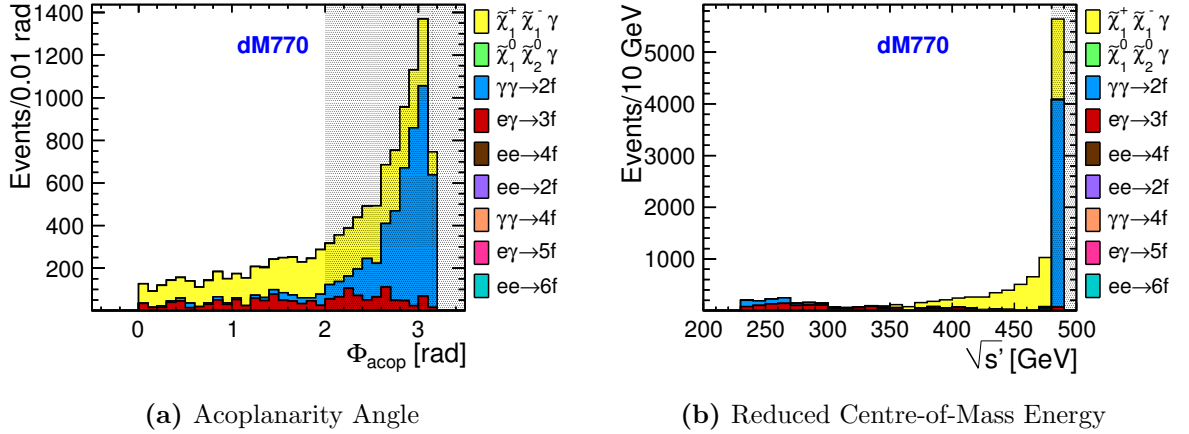
Figure 6.9 Acoplanarity angle between the leptonic and hadronic decays and reduced centre-of-mass energy distribution in the dM770 scenario at $\sqrt{s} = 500\,\mathrm{GeV}$ and $\int \mathcal{L}dt = 500\,\mathrm{fb}^{-1}$ with $P(e^+, e^-) = (+30\%, -80\%)$.

The chargino mass is reconstructed at this stage of the cuts, while for the reconstruction of the mass difference between the chargino and the LSP an additional cut on the energy of the

missing particles $E_{\mathrm{miss}} > 350\,\mathrm{GeV}$ is applied. The performance of the chargino selection can be seen in Figure 6.10 which shows the p_t distribution of the decay products after all the cuts. The figure and Table 6.5 illustrate that both the SM background and most of the neutralino $\widetilde{\chi}_1^0 \widetilde{\chi}_2^0 \gamma$ events are suppressed, and the chargino events can be selected clearly especially in the dM770 scenario. In the dM1600 scenario, the remaining SM background, which is more than in the other scenario because of the additional decay channel, is almost in the same p_t region with the signal. As seen from the figure the remaining neutralino background is really small in both scenario. To be able to achieve such small contribution from the new physics background is very important, because at the time of ILC running, we expect to be able to model electroweak SM processes very accurately, while we cannot assume that we know the background contribution from the other new physics processes perfectly.
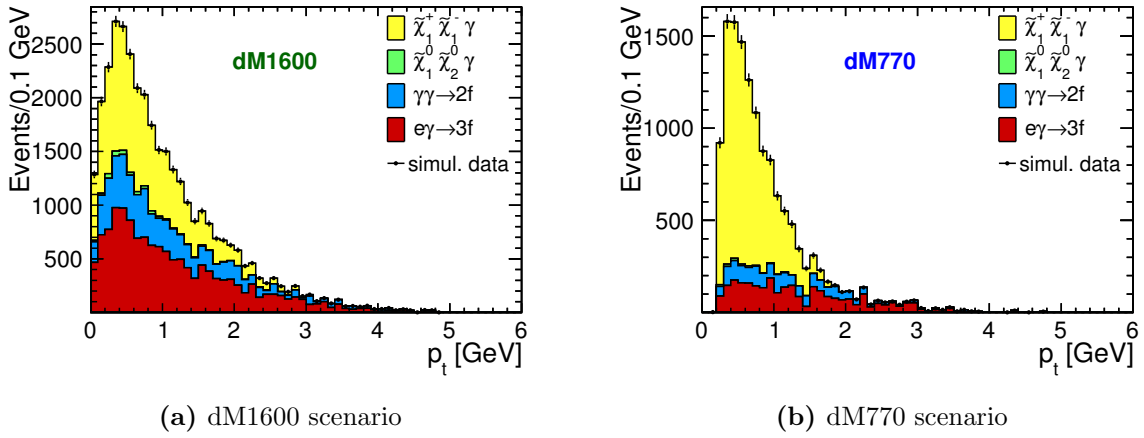

(a) dM1600 scenario

(b) dM770 scenario

Figure 6.10 p_t distribution of the final state particles after the chargino selection at $\sqrt{s} = 500\,\mathrm{GeV}$ and $\int \mathcal{L} dt = 500\,\mathrm{fb}^{-1}$ with $P(e^+, e^-) = (+30\%, -80\%)$.

6.2.2 Chargino Mass Reconstruction

The chargino mass is reconstructed using the reduced centre-of-mass energy defined in the previous section as $\sqrt{s'} = \sqrt{s - 2\sqrt{s}E_\gamma}$. One can derive the relation between the $\sqrt{s'}$ and the chargino mass from the invariant products of the four vectors considering the cases before and after the collision,

$$s = p^\mu_{\mathrm{bef}} \, p_{\mu_{\mathrm{bef}}} = p^\mu_{\mathrm{aft}} \, p_{\mu_{\mathrm{aft}}}. \tag{6.3}$$

For the $e^+ e^- \to \widetilde{\chi}_1^+ \widetilde{\chi}_1^- \gamma$ process, the energy momentum four vectors of the total system in the centre-of-mass frame can be written assuming the speed of light $c = 1$ as:

$$p^\mu_{\mathrm{bef}} = \left(2E, 0, 0, 0\right) \tag{6.4}$$

$$p^\mu_{\mathrm{aft}} = \left(E_{\widetilde{\chi}_1^+} + E_{\widetilde{\chi}_1^-} + E_\gamma, 0, 0, 0\right) \tag{6.5}$$

where E is the beam energy, $2E = \sqrt{s}$. The energy and momentum relations of the particles are given as;

$$E^2_{\widetilde{\chi}^+_1} = M^2_{\widetilde{\chi}^+_1} + \vec{p}^{\,2}_{\widetilde{\chi}^+_1} \tag{6.6}$$

$$E^2_{\widetilde{\chi}^-_1} = M^2_{\widetilde{\chi}^-_1} + \vec{p}^{\,2}_{\widetilde{\chi}^-_1} \tag{6.7}$$

$$E^2_\gamma = \vec{p}^{\,2}_\gamma, \tag{6.8}$$

while the energy and momentum conservation relations are

$$E_{\widetilde{\chi}^+_1} + E_{\widetilde{\chi}^-_1} + E_\gamma = \sqrt{s} \tag{6.9}$$

$$\vec{p}_{\widetilde{\chi}^+_1} + \vec{p}_{\widetilde{\chi}^-_1} + \vec{p}_\gamma = 0. \tag{6.10}$$

Using the above equations, the relation between the ISR photon and the charginos can be derived as follows:

$$4E^2 = (E_\gamma + E_{\widetilde{\chi}^+_1} + E_{\widetilde{\chi}^-_1})^2 \tag{6.11}$$

$$s = E^2_\gamma + 2E_\gamma(E_{\widetilde{\chi}^+_1} + E_{\widetilde{\chi}^-_1}) + (E_{\widetilde{\chi}^+_1} + E_{\widetilde{\chi}^-_1})^2 \tag{6.12}$$

$$s = -E^2_\gamma + 2E_\gamma(E_\gamma + E_{\widetilde{\chi}^+_1} + E_{\widetilde{\chi}^-_1}) + E^2_{\widetilde{\chi}^+_1} + E^2_{\widetilde{\chi}^-_1} + 2E_{\widetilde{\chi}^+_1}E_{\widetilde{\chi}^-_1} \tag{6.13}$$

$$s = -\vec{p}^{\,2}_\gamma + 2E_\gamma\sqrt{s} + \vec{p}^{\,2}_{\widetilde{\chi}^+_1} + M^2_{\widetilde{\chi}^+_1} + \vec{p}^{\,2}_{\widetilde{\chi}^-_1} + M^2_{\widetilde{\chi}^-_1} + 2E_{\widetilde{\chi}^+_1}E_{\widetilde{\chi}^-_1} \tag{6.14}$$

With the help of the momentum conservation, $\vec{p}_\gamma$ can be written in terms of the momenta of the charginos. After that, collecting the parameters related with the charginos on the left hand side and the others on the right hand side the following equation is obtained:

$$s - 2E_\gamma\sqrt{s} = -(\vec{p}_{\widetilde{\chi}^+_1} + \vec{p}_{\widetilde{\chi}^-_1})^2 + \vec{p}^{\,2}_{\widetilde{\chi}^+_1} + M^2_{\widetilde{\chi}^+_1} + \vec{p}^{\,2}_{\widetilde{\chi}^-_1} + M^2_{\widetilde{\chi}^-_1} + 2E_{\widetilde{\chi}^+_1}E_{\widetilde{\chi}^-_1} \tag{6.15}$$

$$s - 2E_\gamma\sqrt{s} = M^2_{\widetilde{\chi}^+_1} + M^2_{\widetilde{\chi}^-_1} + 2(E_{\widetilde{\chi}^+_1}E_{\widetilde{\chi}^-_1} - \vec{p}_{\widetilde{\chi}^+_1}\vec{p}_{\widetilde{\chi}^-_1}) \tag{6.16}$$

The right hand side of this equation gives the invariant mass of the chargino pair system. Therefore, this can be considered as the mass of the system recoiling the ISR photon. The value of it can be calculated using the CM energy and the energy of the ISR photon as seen from the left hand side of Equation (6.16). Hence, the recoil mass of the ISR photon which can be interpreted as the reduced centre-of-mass energy, $\sqrt{s'}$ is defined as:

$$M^2_{recoil} = s - 2E_\gamma\sqrt{s} \qquad (M_{recoil} = \sqrt{s'}). \tag{6.17}$$

The minimum value of the reduced centre-of-mass energy $\sqrt{s'}$ can be found if both charginos $\widetilde{\chi}^\pm_1$ are produced at rest. Since the charginos have the same mass, one finds:

$$\sqrt{s'}|_{\text{thresh}} = 2 \times M_{\widetilde{\chi}^\pm_1} \tag{6.18}$$

$$M_{\widetilde{\chi}^\pm_1} = \frac{1}{2}\sqrt{s'}|_{\text{thresh}} = \frac{1}{2}\sqrt{s - 2\sqrt{s}E_\gamma|_{\text{thresh}}}. \tag{6.19}$$

The obtained relation between $\sqrt{s'}$ and $M_{\widetilde{\chi}_1^\pm}$ is used to determine the mass of the charginos. Figure 6.11 shows the distributions of $\sqrt{s'}$ for the $\int \mathcal{L}dt = 500\,\text{fb}^{-1}$ integrated luminosity at $\sqrt{s} = 500\,\text{GeV}$ with $P(e^+, e^-) = (+30\%, -80\%)$ after the selection described in Section 6.2.1. The chargino signal shown in yellow can be clearly seen on top of the SM background represented in red while there is a little neutralino contribution which is shown in green. The seen sharp edge of the SM background comes from the applied cut on missing energy, $E_{\text{miss}} > 300\,\text{GeV}$. The cut on E_{miss} is kept loose to have a region independent from the signal region. This makes it possible to fix the SM background level by fitting an exponential function with two free parameters, $f_{SM}(x) = p_1 \cdot e^{-p_2 \cdot x}$ shown with a blue line. Then, a straight line fit function is added on top of the exponential SM fit function to model the signal contribution. The new fitting function becomes $f_{data}(x) = p_1 + p_2 \cdot x + p_3 \cdot e^{-p_4 \cdot x}$. In this second step, the two SM free parameters p_3 and p_4 are fixed to the values obtained from the SM only fit, and after that the combined fit is applied to the simulated data as shown with a red line. The fit ranges and the bounds on the background parameters are varied by $5\,\text{GeV}$ and $10\,\text{GeV}$ in both sides and the effect of these on the fit results are checked. It has been observed that the values are stable against the changes of the SM background bounds and fit ranges except the changes on the lower limit of the fit range. Since the interested region is close to the intersection point, this puts a limit on the allowed region of the lower fit range. However the results look stable within $5\,\text{GeV}$ changes.

The intersection point which is the threshold value of the signal distribution is used to obtain the chargino mass. The fitted values of the chargino mass for $\int \mathcal{L}dt = 500\,\text{fb}^{-1}$ integrated luminosity at $\sqrt{s} = 500\,\text{GeV}$ centre-of-mass energy with $P(e^+, e^-) = (+30\%, -80\%)$ are given for both scenarios in the following:

$$\text{dM1600 scenario:} \qquad M_{\widetilde{\chi}_1^\pm}^{\text{fit}} = 168.0 \pm 1.4 \ \ \text{GeV} \qquad\qquad (6.20)$$

$$\text{dM770 scenario:} \qquad M_{\widetilde{\chi}_1^\pm}^{\text{fit}} = 168.6 \pm 1.0 \ \ \text{GeV}. \qquad\qquad (6.21)$$

The central values of the fitted chargino masses are agree with the input values, which are $M_{\widetilde{\chi}_1^\pm} = 165.77\,\text{GeV}$ and $M_{\widetilde{\chi}_1^\pm} = 167.36\,\text{GeV}$ in the dM1600 and dM770 scenarios, within 1.6 and 1.2 standard deviations, respectively. Since the formula showing the relation between the chargino mass and the reduced centre-of-mass energy obtained after some approximations, such as assuming the chargino energies are equal and considering the nominal CM energy exactly $\sqrt{s} = 500\,\text{GeV}$ by neglecting the beamstrahlung, a slight bias is not unexpected. To compensate this, we investigated the dependency of the fitted values on the input mass values by producing more samples with different input chargino masses. Since the mass difference is really important in these kind of scenarios, all higgsino masses were changed simultaneously to keep the mass differences the same. Otherwise, this could change the model, namely the momentum and the energy distribution of the decay products, and even the branching ratio of the chargino pair events which will affect the reconstruction and introduce an additional bias.

The new signal samples were generated by changing the higgsino masses around the input values, and the analysis was repeated for each sample. In total, there are 10 new signal samples from each scenario and five of them are chosen considering the higher masses than the model input
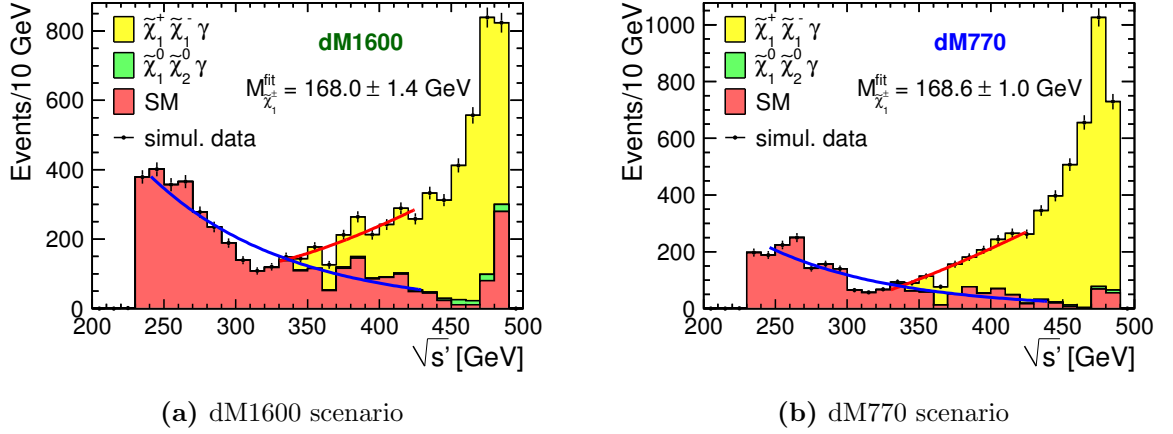
(a) dM1600 scenario

(b) dM770 scenario

Figure 6.11 Distribution of the reduced centre-of-mass energy ($\sqrt{s'}$) of the system recoiling against the hard ISR photon for all events passing the chargino selection for an integrated luminosity of $\int \mathcal{L}dt = 500\,\mathrm{fb}^{-1}$ with $P(e^+, e^-) = (+30\%, -80\%)$. $M_{\widetilde{\chi}_1^\pm}$ is determined from a linear fit to the distribution near the endpoint.

values, while the rest is chosen for lower masses as given in Table 6.7. The results of these 10 varied higgsino masses are shown in Figure 6.12. The plots show the obtained fitted values from the reconstruction, which is explained above, as a function of the true input mass values. The calibration curves are obtained by applying a linear fit for each dM1600 and dM770 scenario separately since the chosen decay channels are different. The curve obtained from the relation between fitted and true values should be diagonal if the method did not need any calibration. Apparently, this is not the case in this analysis as expected due to the assumptions explained before. The calibrated mass values and their uncertainties can be found from the projection of

Particle	Mass Values [GeV]										
					dM1600						
$\widetilde{\chi}_1^0$	159.68	160.68	161.68	162.68	163.68	-	164.68	165.68	166.68	167.68	168.68
$\widetilde{\chi}_2^0$	162.37	163.37	164.37	165.37	166.37	-	167.37	168.37	169.37	170.37	171.37
$\widetilde{\chi}_1^\pm$	161.26	162.26	163.26	164.26	165.26	-	166.26	167.26	168.26	169.26	170.26
					dM770						
$\widetilde{\chi}_1^0$	164.09	164.59	165.09	165.59	166.09	-	167.09	167.59	168.09	168.59	169.09
$\widetilde{\chi}_2^0$	165.13	165.63	166.13	166.63	167.13	-	168.13	168.63	169.13	169.63	170.13
$\widetilde{\chi}_1^\pm$	164.86	165.36	165.86	166.36	166.86	-	167.86	168.36	168.86	169.36	169.86

Table 6.7 Mass values of higgsinos for mass calibration. The dashed lines correspond to the range where the model masses lie. In dM1600 scenario, $M_{\widetilde{\chi}_1^0} = 164.18\,\mathrm{GeV}$, $M_{\widetilde{\chi}_2^0} = 166.87\,\mathrm{GeV}$, and $M_{\widetilde{\chi}_1^\pm} = 165.76\,\mathrm{GeV}$. In dM770 scenario, $M_{\widetilde{\chi}_1^0} = 166.59\,\mathrm{GeV}$, $M_{\widetilde{\chi}_2^0} = 167.83\,\mathrm{GeV}$, and $M_{\widetilde{\chi}_1^\pm} = 167.36\,\mathrm{GeV}$.

the fitted values onto the x-axis. The slope of the curve gives the relation between the statistical errors on the fitted and on the calibrated masses. The straight lines show the fitted values on the y-axis, and corresponding calibrated values projected on the x-axis, while the dashed lines show the uncertainties of the fitted and calibrated masses. While comparing the errors one needs to be careful about the axis range of the figures, since they do not have the same ranges. Even though the length of error bars looks larger in the dM770 scenario, actually it is smaller than in the dM1600 scenario, which corresponds less fluctuation from the true value.
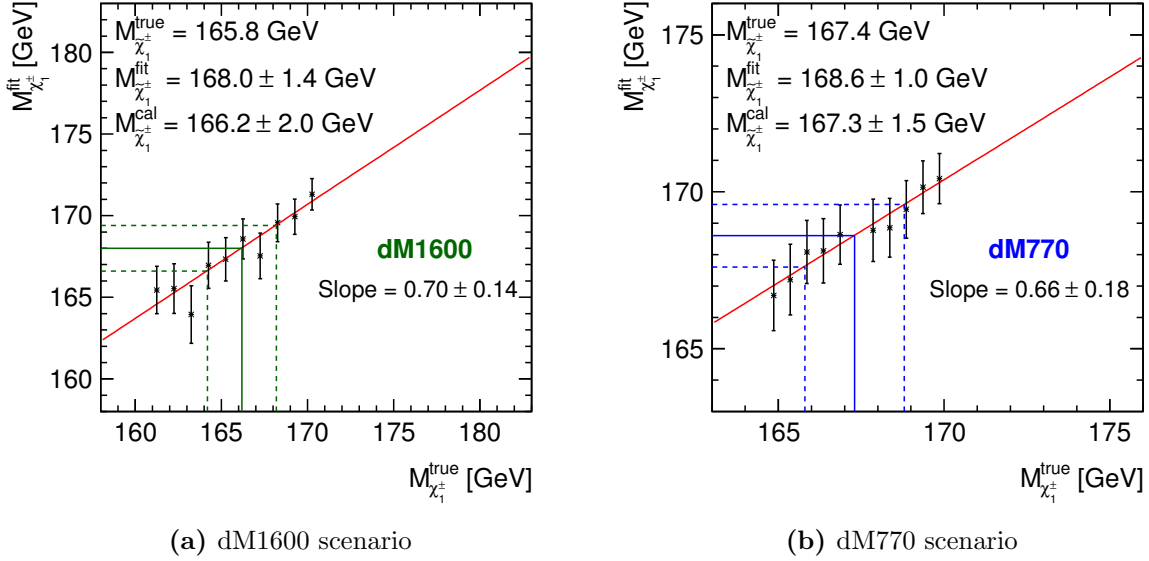

(a) dM1600 scenario

(b) dM770 scenario

Figure 6.12 Calibration of the $\sqrt{s'}$ method for the chargino mass determination. The x-axis shows the true mass values of the chargino for different samples obtained by varying the mass of the higgsinos, while the y-axis shows the results of the reconstruction, the so-called fitted mass values. The calibrated $M_{\tilde{\chi}_1^\pm}$ is obtained by projecting the fitted value of the reconstructed mass of the model onto the y-axis. The lines show the central values, and the dashed lines indicate the uncertainties.

The obtained calibration curves can be described by $y = 0.70(\pm 0.14)x + 51.83(\pm 23.11)$ in the dM1600 scenario, and $y = 0.66(\pm 0.18)x + 59.00(\pm 30.68)$ in the dM770 scenario. Both the slopes and offsets of the calibration curves are equal within the uncertainty. Since the changes in slopes and in offsets balance the difference between curves, they give similar results when only one of the curves is used for both scenarios.

The calibrated chargino masses show an excellent agreement with the input values while increasing the uncertainty by approximately 50%. The calibrated chargino masses and true values of them are given as follows at $\sqrt{s} = 500\,\text{GeV}$ and the integrated luminosity of $\int \mathcal{L}dt = 500\,\text{fb}^{-1}$ for polarisation combination of $P(e^+, e^-) = (+30\%, -80\%)$.

$$\text{dM1600 scenario:} \quad M_{\tilde{\chi}_1^\pm}^{\text{cal}} = 166.2 \pm 2.0 \ \text{GeV} \quad (M_{\tilde{\chi}_1^\pm}^{\text{true}} = 165.8 \ \text{GeV}) \tag{6.22}$$

$$\text{dM770 scenario:} \quad M_{\tilde{\chi}_1^\pm}^{\text{cal}} = 167.3 \pm 1.5 \ \text{GeV} \quad (M_{\tilde{\chi}_1^\pm}^{\text{true}} = 167.4 \ \text{GeV}) \tag{6.23}$$

6.2.3 Reconstruction of the Chargino-LSP Mass Difference

For the reconstruction of the chargino-LSP mass difference the missing energy cut is tightened to $E_{\mathrm{miss}} > 350\,\mathrm{GeV}$ in order to reduce the number of SM background events in the interesting region. The remaining number of events are shown in the last line of Table 6.5.

Even though the mass difference between the chargino and the LSP is very small, it can be obtained using the energy of the chargino decay products boosted into the rest frame of the chargino pair introduced in Equation (6.1). The boosted energy can be calculated using the Lorentz transformation,

$$
E_\pi^* \;=\; \gamma(E_\pi - \vec{\beta} \cdot \vec{p}_\pi) \tag{6.24}
$$

$$
E_\pi^* \;=\; \frac{1}{2M_{\widetilde{\chi}_1^\pm}}\Big[E_{\widetilde{\chi}_1^\pm} \cdot E_\pi - \vec{p}_{\widetilde{\chi}_1^\pm} \cdot \vec{p}_\pi \Big] \tag{6.25}
$$

where $\gamma = E_{\widetilde{\chi}_1^\pm}/M_{\widetilde{\chi}_1^\pm}$ and $\vec{\beta} = \vec{p}_{\widetilde{\chi}_1^\pm}/E_{\widetilde{\chi}_1^\pm}$. To be able to calculate the boosted energy of a final state particle, one needs to write the boosted energy E^* equation in terms of the variables which will exist in the final state considering the following assumptions. At the rest frame of the charginos, chargino energies can be assumed to be equal, which gives the relation $2E_{\widetilde{\chi}_1^\pm} = \sqrt{s} - E_\gamma$ using the energy conservation. If one considers the chargino pair as a system recoiling against the ISR photon, the relation $\vec{p}_{\widetilde{\chi}_1^\pm} = -\vec{p}_\gamma/2$ can be obtained. Using these relations, the above equation becomes

$$
E_\pi^* = \frac{1}{2M_{\widetilde{\chi}_1^\pm}}\Big[(\sqrt{s} - E_\gamma) \cdot E_\pi + \vec{p}_\gamma \cdot \vec{p}_\pi \Big]. \tag{6.26}
$$

Taking into account the reduced CM energy definition at the threshold value $\sqrt{s'} = 2M_{\widetilde{\chi}_1^\pm}$, the general formula for boosted energy can be obtained as following, which is also given in Equation (6.1),:

$$
E_\pi^* = \frac{(\sqrt{s} - E_\gamma) \cdot E_\pi + \vec{p}_\gamma \cdot \vec{p}_\pi}{\sqrt{s'}}. \tag{6.27}
$$

If the charginos are actually produced at rest, E_π^* can take only one value which can be calculated using the kinematics determining the case where the chargino decays to a neutralino and a pion. Conservation of momentum and energy in this situation is given as:

$$
E_{\widetilde{\chi}_1^\pm} \;=\; E_\pi + E_{\widetilde{\chi}_1^0} \tag{6.28}
$$

$$
\vec{p}_{\widetilde{\chi}_1^\pm} \;=\; 0 \tag{6.29}
$$

$$
\vec{p}_{\widetilde{\chi}_1^0} \;=\; -\vec{p}_\pi. \tag{6.30}
$$

Starting from the equation (6.25), and using the above equations, E^* becomes:

$$
E_\pi^* \;=\; \frac{1}{M_{\widetilde{\chi}_1^\pm}}\Big[E_{\widetilde{\chi}_1^\pm} \cdot (E_{\widetilde{\chi}_1^\pm} - E_{\widetilde{\chi}_1^0}) \Big] \tag{6.31}
$$

$$
E_\pi^* \;=\; \frac{1}{M_{\widetilde{\chi}_1^\pm}}\Big[E_{\widetilde{\chi}_1^\pm}^2 - E_{\widetilde{\chi}_1^\pm} \cdot E_{\widetilde{\chi}_1^0} \Big] \tag{6.32}
$$

where $E_{\widetilde{\chi}_1^\pm}^2 = M_{\widetilde{\chi}_1^\pm}^2$ since the charginos are at rest. To find the second term of Equation (6.32) in terms of mass of the higgsinos and pion, the conservation of four momentum can be used, $p_\pi = p_{\widetilde{\chi}_1^\pm} - p_{\widetilde{\chi}_1^0}$. Taking the square of this equation gives the below relation:

$$E_{\widetilde{\chi}_1^\pm} \cdot E_{\widetilde{\chi}_1^0} = \frac{M_{\widetilde{\chi}_1^\pm}^2 + M_{\widetilde{\chi}_1^0}^2 - m_\pi^2}{2} \tag{6.33}$$

which results in the following boosted energy equation in terms of higgsino and pion masses:

$$E_\pi^* = \frac{(M_{\widetilde{\chi}_1^\pm} - M_{\widetilde{\chi}_1^0})(M_{\widetilde{\chi}_1^\pm} + M_{\widetilde{\chi}_1^0}) + m_\pi^2}{2M_{\widetilde{\chi}_1^\pm}} = \frac{\Delta(M)\Sigma(M) + m_\pi^2}{2M_{\widetilde{\chi}_1^\pm}} \tag{6.34}$$

wherein $\Delta(M)$ and $\Sigma(M)$ are the difference and the sum of the chargino and the LSP masses, respectively. Considering $\Delta(M) + \Sigma(M) = 2M_{\widetilde{\chi}_1^\pm}$, the below equation is obtained;

$$E_\pi^* = \frac{1}{1/\Delta(M) + 1/\Sigma(M)} + \frac{m_\pi^2}{2M_{\widetilde{\chi}_1^\pm}} . \tag{6.35}$$

Since the mass difference between higgsinos is so small compared to the sum of higgsino masses, $1/\Sigma(M)$ in the first term can be neglected. Following the same thought, the second term is also negligible since there is a large difference between the pion mass m_π and the higgsino mass. Hence, E_π^* becomes equal to the mass difference to a very good approximation:

$$E_\pi^* \approx \Delta M_{\widetilde{\chi}_1^\pm - \widetilde{\chi}_1^0}. \tag{6.36}$$

The value of E_π^* where the charginos are produced at rest, corresponds to the threshold value of the reduced CM energy. Figure 6.13 shows the E_π^* distribution as a function of $\sqrt{s'}$ in the upper row. The signal shown in black has a triangular shape, and the peak point gives the mass difference. The blue arrow showing the true value of the mass difference corresponds to the peak point as seen from the figure.

Since the region around the peak point is interesting in order to determine the mass difference, higher values of $\sqrt{s'}$ can be excluded with a cut $\sqrt{s'} < 345\,\text{GeV}$ to focus on the entries around the peak point. The cut value determination procedure, required for $\sqrt{s'}$, will be explained in the following subsection. After applying the obtained cut, events left in the chosen region are projected onto the E_π^* axis, as seen in the lower row of the Figure 6.13. In these plots SM background is subtracted from the signal since the limited amount of it is available in the time of the simulation. While doing this, we assume that we will have sufficient Monte Carlo statistics and precisely known theoretical prediction for the SM background at the time of the ILC running. However, even precisely known standard model background will have the statistical uncertainty. Therefore, the errors from the statistical fluctuation of the SM background were also included in the error bars seen in the plots. It is important to note that the considered errors from the SM background will be smaller at the time of the ILC due to the assumed high precision. In the case of dM1600 scenario, even though the significance before $\sqrt{s'} < 345\,\text{GeV}$ cut is very large ($\sim 50\sigma$), the requirement of the reduced centre-of-mass energy cut for the

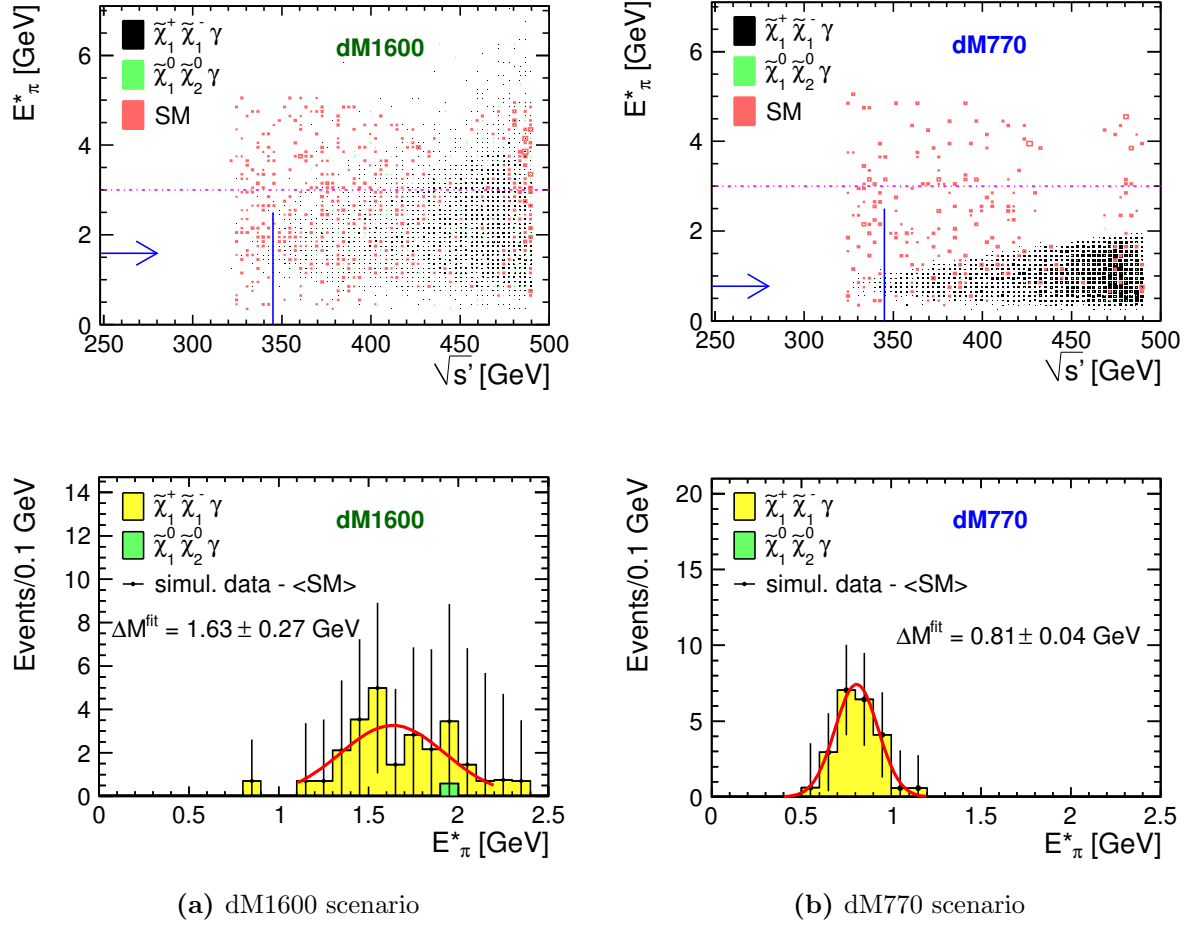**(a)** dM1600 scenario   **(b)** dM770 scenario

Figure 6.13 Measurement of the chargino-LSP mass difference for an integrated luminosity of $\int \mathcal{L}dt = 500\,\mathrm{fb}^{-1}$ with $P(e^+, e^-) = (+30\%, -80\%)$. The upper row shows E_π^* vs. $\sqrt{s'}$. The horizontal dashed line indicates the cut on E_π^*, the vertical line the cut on $\sqrt{s'}$. The arrow indicates the input value of the chargino-LSP mass difference. The lower row shows the E_π^* after cutting on $\sqrt{s'}$.

mass difference reconstruction reduces the signal significance to 2σ [1]. Following the subtraction of the SM background, the remaining signal events are smeared over the neighbour bins since they do not have enough statistics which cause empty bins and a distribution which is not smooth. This could be improved by considering additional decay channel in the selection of the charginos. The obtained E_π^* distribution given in the lower row of the Figure 6.13 is fitted with a Gaussian function to reconstruct the mass difference. The mean value of the fit gives reconstructed mass differences for a centre-of-mass energy of $\sqrt{s} = 500\,\mathrm{GeV}$, and an integrated

---

[1]The significance is calculated as $S = \frac{N_{sig}}{\sqrt{N_{sig} + N_{bkg}}}$.

luminosity of $\int \mathcal{L} dt = 500 \, \text{fb}^{-1}$ with polarisation combination of $P(e^+, e^-) = (+30\%, -80\%)$:

$$\text{dM1600} \quad : \quad \Delta M^{\text{rec}}_{\tilde{\chi}^{\pm}_1 - \tilde{\chi}^0_1} = 1630 \pm 270 \, \text{MeV} \quad (\Delta M^{\text{true}}_{\tilde{\chi}^{\pm}_1 - \tilde{\chi}^0_1} = 1600 \, \text{MeV}), \qquad (6.37)$$

$$\text{dM770} \quad : \quad \Delta M^{\text{rec}}_{\tilde{\chi}^{\pm}_1 - \tilde{\chi}^0_1} = 810 \pm 40 \, \text{MeV} \qquad (\Delta M^{\text{true}}_{\tilde{\chi}^{\pm}_1 - \tilde{\chi}^0_1} = 770 \, \text{MeV}). \qquad (6.38)$$

When the reconstructed mass differences are compered with the true values given in the parentheses in Equations (6.37) and (6.38), it is seen that the obtained values agree with the input value of mass differences within the statistical uncertainity.

6.2.3.1 Determination of a Cut Value on $\sqrt{s'}$

To determine a cut value on $\sqrt{s'}$, several samples with various mass differences, which are 0.57, 0.67, 0.77, and 0.87 GeV, were studied on generator level. Since the peak point of the E^* distribution gives approximately the mass difference, the $E^*_\pi - \Delta M$ difference should peak at around zero as displayed in Figure 6.14. Seven different cut values starting from 330 GeV up to 360 GeV in the interval of 5 GeV were applied on each sample, and the procedure explained in the mass difference reconstruction were applied for each of them separately: The remaining events after application of a $\sqrt{s'}$ cut are projected onto the x-axis, and the mean values are acquired with the help of a Gaussian fit applied on the $E^*_\pi - \Delta M$ distributions. The obtained mean values are plotted in Figure 6.15 for each sample with various mass differences as a function of the applied cut value on $\sqrt{s'}$. There are several points one needs to take into account while choosing the cut value. The cut value should be as high as possible to have enough statistics, while it should stay around zero for $< E^*_\pi - \Delta M >$, and the chosen value shouldn't depend on the model. Figure 6.15 shows that the first two cut values seems to give perfect results, whereas the statistic is not enough to continue the reconstruction. The values higher than $\sqrt{s'} = 345$ look completely off which results in two possible cut values to be chosen. Since $\sqrt{s'} = 345$ has less fluctuation meaning that the choice will be less dependent on the model and it yields higher statistics, it is the most promising value in this case. Therefore, $\sqrt{s'} = 345 \, \text{GeV}$ seems a reasonable choice.

6.2.4 Measurement of the Polarised Chargino Cross Sections

The estimated precision on the polarised cross sections is based on the number of events in the final row of Table 6.5. The formula below, obtained assuming that the background is known precisely, is used to estimate the achievable precision [159]:

$$\frac{\delta \sigma}{\sigma} = \frac{1}{\sqrt{\epsilon \cdot \pi \cdot \sigma \cdot \int \mathcal{L} dt}}. \qquad (6.39)$$

The formula states that the statistical precision on cross section is mainly dependent on efficiency (ϵ) and purity (π) obtained after the event selection. Table 6.8 shows the efficiency, which refers to the total number of the chargino events including all the decay modes, and the purity for
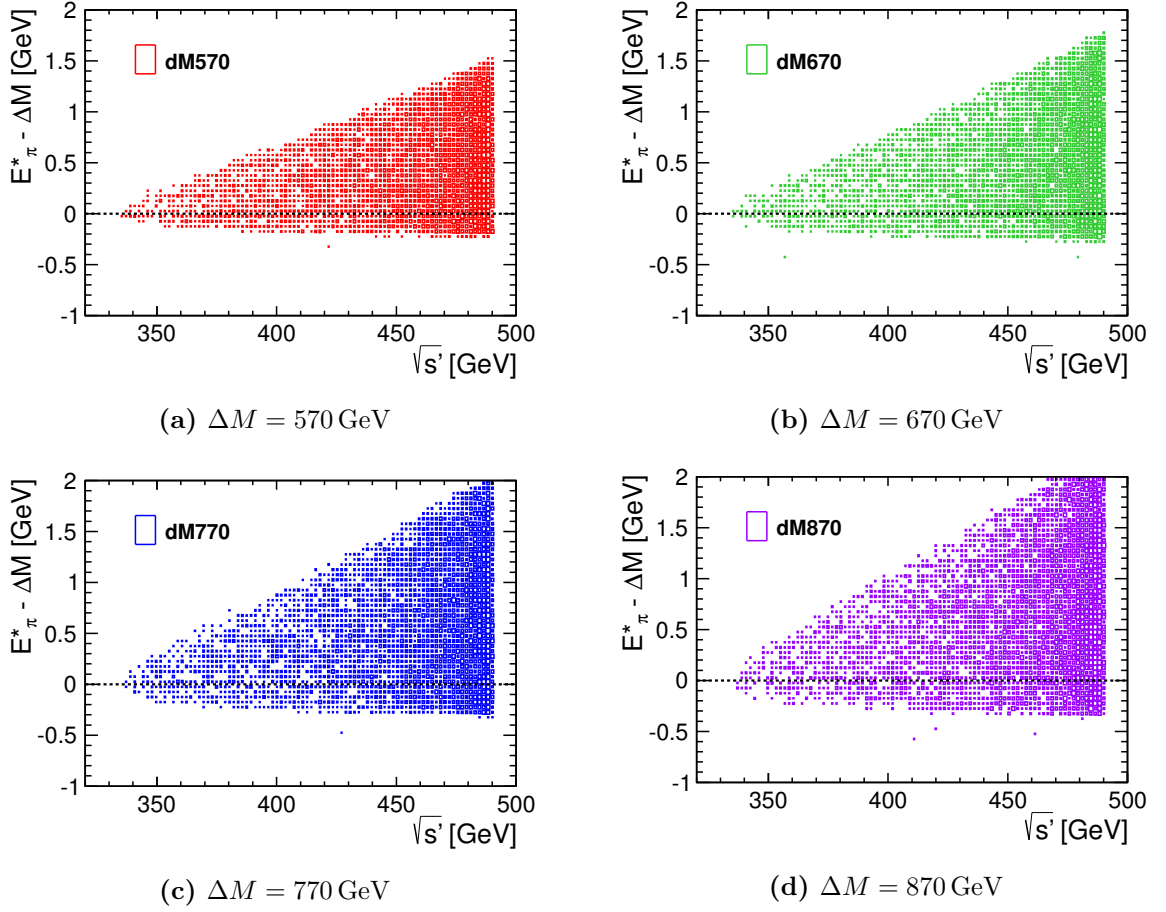
(a) $\Delta M = 570\,\text{GeV}$

(b) $\Delta M = 670\,\text{GeV}$

(c) $\Delta M = 770\,\text{GeV}$

(d) $\Delta M = 870\,\text{GeV}$

Figure 6.14 Difference between the boosted energy of pion and the mass difference calculated in generator level for various mass differences, $\Delta M = 570, 670, 770$, and 870 for the $\sqrt{s} = 500\,\text{GeV}$ centre-of-mass energy, $\int \mathcal{L}dt = 500\,\text{fb}^{-1}$ integrated luminosity, and $P(e^+, e^-) = (+30\%, -80\%)$ polarisation combination.

both polarisation combinations, $P(e^+, e^-) = (+30\%, -80\%)$ and $P(e^+, e^-) = (-30\%, +80\%)$. The efficiency and the purity given in Table 6.8 are calculated as follows:

$$\epsilon = \frac{N_{\text{selected signal events}}}{N_{\text{generated signal events}}} \tag{6.40}$$

$$\pi = \frac{N_{\text{selected signal events}}}{N_{\text{selected signal events}} + N_{\text{selected background events}}} . \tag{6.41}$$

Because the efficiency concerns all the possible decay modes of the chargino events, the branching ratios of selected modes are also displayed in the table in addition to the assumed polarised production cross sections.
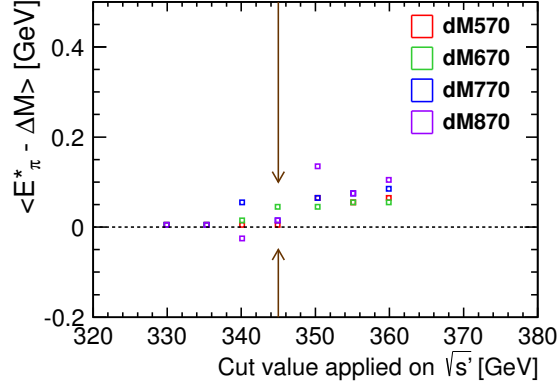
Figure 6.15 Mean values of the fit applied on the $E_\pi^* - \Delta M$ difference projected onto the x-axis after seven different cuts from $330\,\text{GeV}$ to $360\,\text{GeV}$ in the interval of $5\,\text{GeV}$ on $\sqrt{s'}$ for samples with various mass differences at $\sqrt{s} = 500\,\text{GeV}$ and $\int \mathcal{L}dt = 500\,\text{fb}^{-1}$ with $P(e^+, e^-) = (+30\%, -80\%)$.

	$P(e^+, e^-) = (+30\%, -80\%)$		$P(e^+, e^-) = (-30\%, +80\%)$	
	dM1600	dM770	dM1600	dM770
$\int \mathcal{L}dt$	$500\,\text{fb}^{-1}$	$500\,\text{fb}^{-1}$	$500\,\text{fb}^{-1}$	$500\,\text{fb}^{-1}$
σ	$78.7\,\text{fb}$	$77.0\,\text{fb}$	$20.4\,\text{fb}$	$19.9\,\text{fb}$
BR of selected mode(s)	30.5%	34.7%	30.5%	34.7%
efficiency ϵ	9.9%	12.1%	9.5%	12.2%
purity π	70.1%	85.3%	36.4%	56.1%
$\delta\sigma/\sigma$	1.9%	1.6%	5.3%	3.8%

Table 6.8 Efficiency, purity, and relative statistical precision on the visible cross section for charginos. The cross section values given here are higher than those displayed in Fig. 5.3 and 5.4 since in the event generation step no generator level cut on the energy of the ISR photon was applied (cf. Sec. 5.4).

The last row of the table 6.8 shows the achievable statistical precision on the polarised cross sections. For $P(e^+, e^-) = (+30\%, -80\%)$ which causes a higher signal cross sections compared to the other polarisation combination, the polarised cross section can be obtained with 1.9% and 1.6% precision in the dM1600 and dM770 scenarios assuming the branching ratios would be known. For the other combination, the signal cross section is lower, while the dependency of the dominating SM background coming from $\gamma\gamma$ or $e\gamma$ processes on the polarisation is weak. Therefore, the precision is getting worse to 5.3% and 3.8% in the dM1600 and dM770 scenarios, respectively. In general, the dM770 scenario seems to allow for better precision than the dM1600; however, since the chosen decay channels are different, it is difficult to judge this. This could be

interpreted such that the obtained values show the precision only on the chosen semi-leptonic decay channel. Thus, improvement is possible considering more decay modes. To obtain the total uncertainty on the cross section one needs to take into account the uncertainty on the branching ratios of the virtual W and Z boson decays. These branching ratios strongly depend on the available phase space given by the mass differences due to the mass degeneracy. Therefore, the limited knowledge of ΔM implies an additional parametric uncertainties on cross section. This will be discussed further in section 6.4.

6.3 Neutralino Process

6.3.1 Neutralino Selection

The heavier neutralino has two different decay modes as explained in Section 5.1.1. For the selection of neutralino events, the mode where the neutralino decays to the photon and the LSP is chosen since it is the exclusive mode for this signal process. The mode makes up 74% of the neutralino events in the dM770 scenario, while the branching ratio decreases to 24% in the case of dM1600 scenario. Thus, there is very limited Monte Carlo statistic in this case. Even though there are less events in the selected channel, since it is a very clean signal the same mode is chosen for both scenarios contrary to the chargino events. In this decay mode which is the so-called photonic final state, only soft photons around a few GeV due to the mass degeneracy are required in addition to the hard ISR photon. All other particles are vetoed. The required low energy is obtained with the cut of $5\,\mathrm{GeV}$ on the energy of soft particles in the final state apart from the hard ISR photon as listed in Table 6.1 and Table 6.3. If there is more than one soft photon, the one which has the highest transverse momentum is taken. The selection of the photonic final state already reduces most of the SM background events as seen from Table 6.10. A few more cuts can be applied to suppress more of the SM background using the dedicated signal topology. One of them is a cut on polar angle of the soft photons which requires to be in the region fulfilling $|\cos\theta_{\gamma_{\mathrm{soft}}}| < 0.85$, since it is expected to be more central for the signal. This is shown in Figure 6.16 for both scenarios. In analogy to E_π^* in the chargino case, the variable $E_{\gamma_{\mathrm{soft}}}^*$ is introduced for the decay products of the neutralino, namely soft photons:

$$E_{\gamma_{\mathrm{soft}}}^* = \frac{(\sqrt{s} - E_\gamma)E_{\gamma_{\mathrm{soft}}} + \vec{p}_{\gamma_{\mathrm{soft}}} \cdot \vec{p}_\gamma}{\sqrt{s'}}. \tag{6.42}$$

Figure 6.17 indicates the distribution of this variable for both scenarios at $\sqrt{s} = 500\,\mathrm{GeV}$ and $\int \mathcal{L}dt = 500\,\mathrm{fb}^{-1}$ with $P(e^+, e^-) = (+30\%, -80\%)$. Most of the SM background has very small boosted energy of soft photons, while it is large for signal. Therefore, $E_{\gamma_{\mathrm{soft}}}^* > 0.5\,\mathrm{GeV}$ is required at the final selection step. The resulting event counts are summarised in Table 6.10. To represent the performance of the selection one can have a look at p_t distribution of decay products which is shown in Figure 6.18 after all the cuts. As expected the number of remaining neutralino signal events in the dM1600 scenario is much less than the dM770 scenario. However, since it is a unique signature for the neutralino signal it could still help to determine the observables of the neutralinos as will be explained in the next sections.
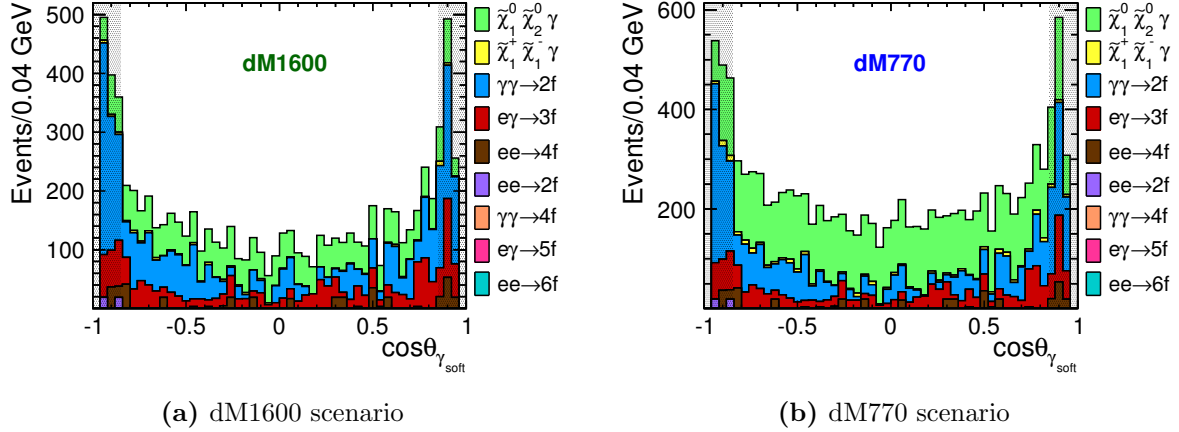
(a) dM1600 scenario

(b) dM770 scenario

Figure 6.16 $\cos\theta_{\gamma_{\mathrm{soft}}}$ distribution after photonic final state selection. Both plots are obtained at $\sqrt{s} = 500\,\mathrm{GeV}$ and $\int \mathcal{L}dt = 500\,\mathrm{fb}^{-1}$ with $P(e^+, e^-) = (+30\%, -80\%)$.
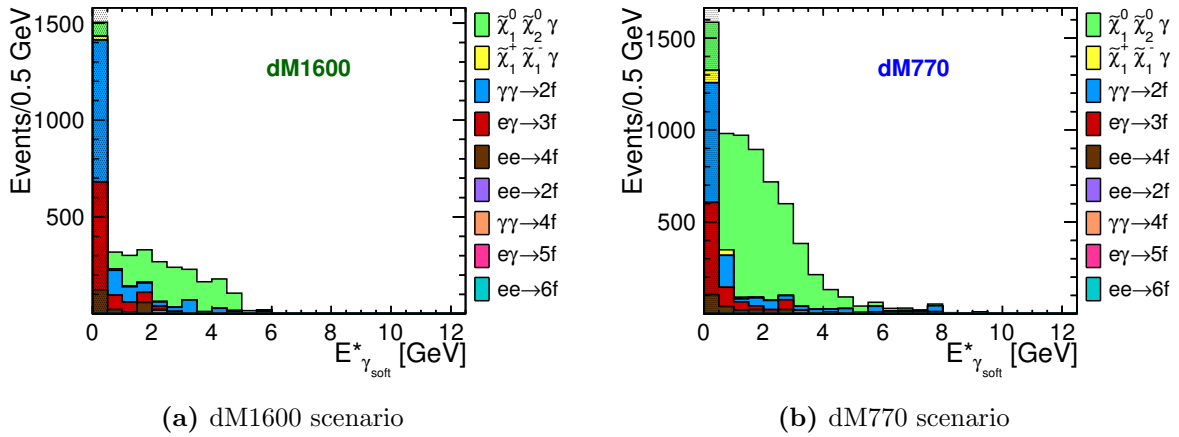

(a) dM1600 scenario

(b) dM770 scenario

Figure 6.17 $E^*_{\gamma_{\mathrm{soft}}}$ distribution after $\cos\theta_{\gamma_{\mathrm{soft}}}$ cut. Both plots are obtained at $\sqrt{s} = 500\,\mathrm{GeV}$ and $\int \mathcal{L}dt = 500\,\mathrm{fb}^{-1}$ with $P(e^+, e^-) = (+30\%, -80\%)$.

6.3.2 Neutralino Mass Reconstruction

The mass of the neutralino $\widetilde{\chi}^0_2$ is reconstructed in the same way as the chargino using the reduced centre-of-mass energy $\sqrt{s'}$ obtained from the recoil against the hard ISR photon. In the definition of $\sqrt{s'}$, the chargino masses were considered equal; however, the neutralinos do not have equal mass. But, because the mass difference is so small and it is even smaller than the resolution of $\sqrt{s'}$, one can use the same formula of the chargino mass reconstruction and correct the obtained result with the applied calibration.

Figure 6.19 shows the distribution of $\sqrt{s'}$ in both scenarios for $P(e^+, e^-) = (+30\%, -80\%)$. The neutralino signal in green is clearly visible on top of the SM background. The same fitting procedure is applied as in the case of the chargino events as explained in Section 6.2.2. First, the

	dM1600		dM770		Standard Model		
	$\widetilde{\chi}_1^+\widetilde{\chi}_1^-\gamma$	$\widetilde{\chi}_1^0\widetilde{\chi}_2^0\gamma$	$\widetilde{\chi}_1^+\widetilde{\chi}_1^-\gamma$	$\widetilde{\chi}_1^0\widetilde{\chi}_2^0\gamma$	$ee \to 2,4,6\mathrm{f}$	$e\gamma \to 3,5\mathrm{f}$	$\gamma\gamma \to 2,4\mathrm{f}$
after preselection	19872	6365	21558	6872	5731	1.1837×10^5	3.3051×10^5
Photon final state	53	1733	155	5224	399	1217	2254
$|\cos\theta_{\gamma_{\mathrm{soft}}}| < 0.85$	38	1467	120	4538	233	800	1145
$E^*_{\gamma_{\mathrm{soft}}} > 0.5\,\mathrm{GeV}$	19	1395	22	4095	109	242	413
$E_{\mathrm{miss}} > 350\,\mathrm{GeV}$	19	1395	22	4095	90	180	384

Table 6.9 Number of events passing the final neutralino selection, following the preselection in Table 6.1, for an integrated luminosity of $\int \mathcal{L}dt = 500\,\mathrm{fb}^{-1}$ and $P(e^+,e^-) = (+30\%, -80\%)$.

	dM1600		dM770		Standard Model		
	$\widetilde{\chi}_1^+\widetilde{\chi}_1^-\gamma$	$\widetilde{\chi}_1^0\widetilde{\chi}_2^0\gamma$	$\widetilde{\chi}_1^+\widetilde{\chi}_1^-\gamma$	$\widetilde{\chi}_1^0\widetilde{\chi}_2^0\gamma$	$ee \to 2,4,6\mathrm{f}$	$e\gamma \to 3,5\mathrm{f}$	$\gamma\gamma \to 2,4\mathrm{f}$
after preselection	5090	5038	5571	5434	4329	1.1284×10^5	3.3051×10^5
Photon final state	11	1414	44	4158	301	1122	2254
$|\cos\theta_{\gamma_{\mathrm{soft}}}| < 0.85$	7	1186	33	3620	227	739	1145
$E^*_{\gamma_{\mathrm{soft}}} > 0.5\,\mathrm{GeV}$	3	1134	3	3230	131	218	413
$E_{\mathrm{miss}} > 350\,\mathrm{GeV}$	3	1134	3	3230	130	169	384

Table 6.10 Number of events passing the final neutralino selection, following the preselection in Table 6.1, for an integrated luminosity of $\int \mathcal{L}dt = 500\,\mathrm{fb}^{-1}$ and $P(e^+,e^-) = (-30\%, +80\%)$.

(a) dM1600 scenario
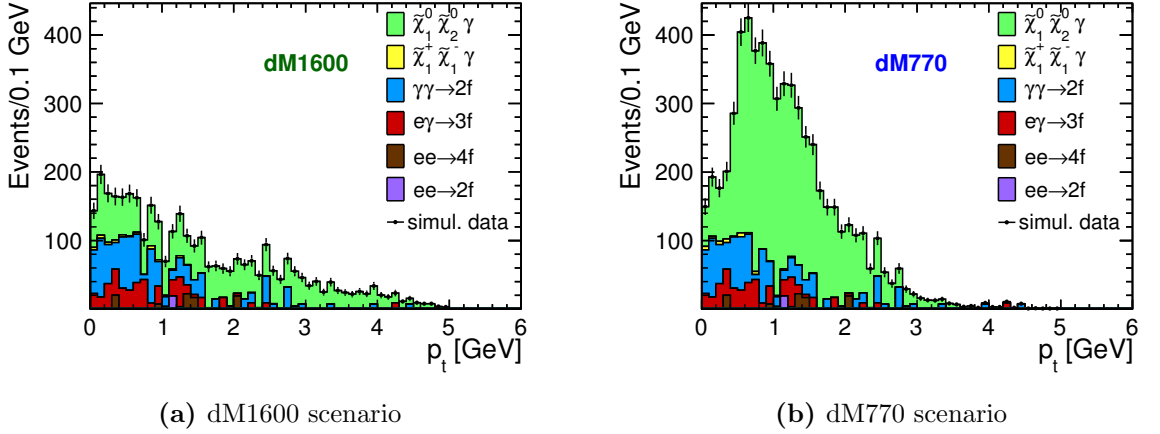
(b) dM770 scenario

Figure 6.18 p_t distribution of the final state particles after the neutralino selections.

SM background is fitted with an exponential function and then a first order polynomial function is added to the SM background fitting function in order to model the signal end point. In this step, the two free parameters of the exponential function are fixed to the values obtained from the
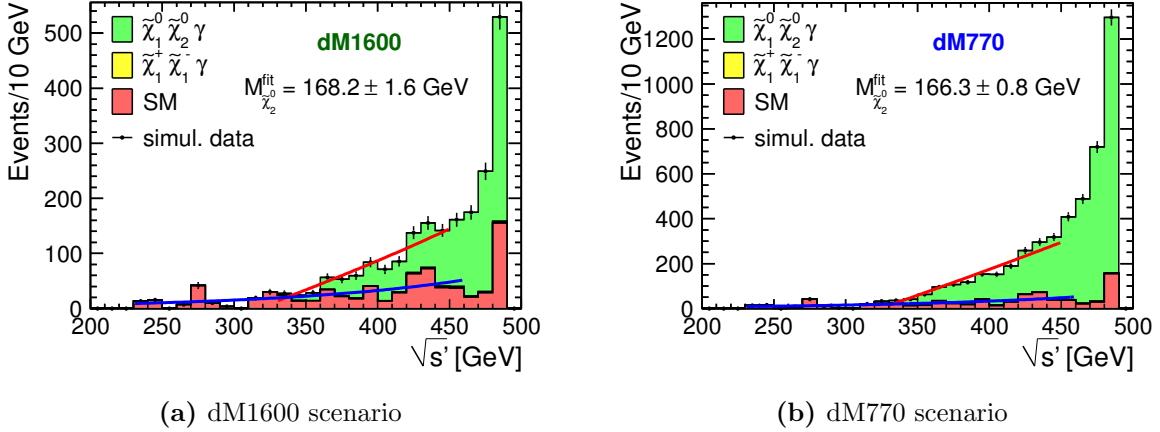
(a) dM1600 scenario

(b) dM770 scenario

Figure 6.19 Distribution of the reduced centre-of-mass energy ($\sqrt{s'}$) of the system recoiling against the hard ISR photon for all events passing the neutralino selection for an integrated luminosity of $\int \mathcal{L}dt = 500\,\mathrm{fb}^{-1}$ with $P(e^+, e^-) = (+30\%, -80\%)$. $M_{\tilde{\chi}_2^0}$ is determined from fitting the sum (red curve) of a straight line for the signal and the background parametrisation (blue curve) to the distribution near the endpoint.

SM only fit. The fitted results, given below for a centre-of-mass energy of $\sqrt{s} = 500\,\mathrm{GeV}$ and an integrated luminosity of $\int \mathcal{L}dt = 500\,\mathrm{fb}^{-1}$ with beam polarisation of $P(e^+, e^-) = (+30\%, -80\%)$, agree within 1 and 1.5 σ with the input mass values.

$$\text{dM1600 scenario:} \qquad M_{\tilde{\chi}_2^0}^{\text{fit}} = 168.2 \pm 1.6 \ \text{GeV} \qquad (6.43)$$

$$\text{dM770 scenario:} \qquad M_{\tilde{\chi}_2^0}^{\text{fit}} = 166.3 \pm 0.8 \ \text{GeV} \qquad (6.44)$$

For the second step of the mass reconstruction, the correlation of the input mass values and fitted masses are investigated as seen in Figure 6.20. In both scenarios, the same decay mode is chosen contrary to the chargino case, therefore one calibration curve should be enough to apply the calibration of the masses in both scenarios. The slope of the calibration curve is 0.5, therefore the statistical uncertainties on the calibrated masses are larger by a factor of 2. The calibrated values for a CM energy of $\sqrt{s} = 500\,\mathrm{GeV}$ and an integrated luminosity of $\int \mathcal{L}dt = 500\,\mathrm{fb}^{-1}$ for polarisation combination $P(e^+, e^-) = (+30\%, -80\%)$ are given as follows:

$$\text{dM1600 scenario:} \qquad M_{\tilde{\chi}_2^0}^{\text{cal}} = 169.6 \pm 3.3 \ \text{GeV} \qquad (M_{\tilde{\chi}_2^0}^{\text{true}} = 166.9 \ \text{GeV}) \qquad (6.45)$$

$$\text{dM770 scenario:} \qquad M_{\tilde{\chi}_2^0}^{\text{cal}} = 165.7 \pm 1.6 \ \text{GeV} \qquad (M_{\tilde{\chi}_2^0}^{\text{true}} = 167.6 \ \text{GeV}) \qquad (6.46)$$

where the results show good agreement with the true mass values almost within the statistical uncertainty.

6.3.3 Measurement of the Polarised Neutralino Cross Sections

The achievable precision on the measurement of the polarised cross section is estimated in the same way of the chargino process. The number in the last line of Table 6.10 is used in the
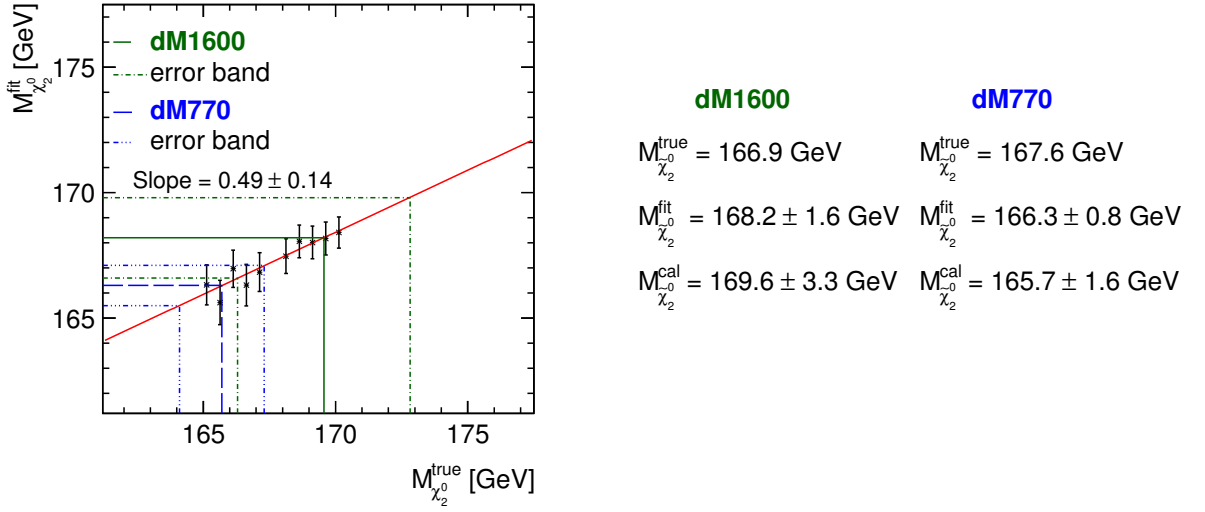
Figure 6.20 Calibration of the $\sqrt{s'}$ method for the neutralino mass determination. Since here the same decay mode is selected for both scenarios, the same calibration curve can be used. The x-axis shows the true mass values of the chargino for different samples obtained by varying the mass of the higgsinos, while the y-axis shows the results of the reconstruction, the so-called fitted mass values. The calibrated $M_{\tilde{\chi}_1^\pm}$ is obtained by projecting the fitted value of the reconstructed mass of the model onto the y-axis. The lines show the central values, and the dashed lines indicate the uncertainties. The green lines refer to the dM1600 scenario, while the blue lines to the dM770 scenario.

calculation. The obtained efficiency and purity of the selection and resulting precision on the cross section are given in Table 6.11 for both polarisation combinations at an CM energy of $\sqrt{s} = 500\,\text{GeV}$ andan integrated luminosity of $\int \mathcal{L} = 500\,\text{fb}^{-1}$. The efficiencies in Table 6.11 refers to the total number of neutralino events regardless of their decay channel. Therefore, the branching ratio of the selection modes are shown in the table, as well as the assumed production cross sections.

The polarised cross sections can be obtained with a precision of 3.2% and 1.7% in the case of dM1600 and dM770 for the $P(e^+, e^-) = (+30\%, -80\%)$, while the precisions are 3.7% and 1.9% respectively for the other combination of polarisation $P(e^+, e^-) = (-30\%, +80\%)$. The numbers show that the polarised cross sections do not depend on the polarisation as much as in the chargino case, which can be deduced from the total cross section dependency on polarisation in Figure 5.4. In the dM770 scenario, the cross section can be determined more precisely than in the case of dM1600. The reason of this is that there are more events due to the higher branching ratio in the case of dM770 scenario. The precision is almost twice worse in the dM1600 scenario. Again these numbers are valid only for specified decay channel. To calculate the precision on total cross sections, the uncertainty on the branching ratios should be taken into account since branching ratios are strongly depend on the mass differences. This will be included in the next chapter.

	$P(e^+, e^-) = (+30\%, -80\%)$		$P(e^+, e^-) = (-30\%, +80\%)$	
	dM1600	dM770	dM1600	dM770
$\int \mathcal{L}dt$	$500\,\text{fb}^{-1}$	$500\,\text{fb}^{-1}$	$500\,\text{fb}^{-1}$	$500\,\text{fb}^{-1}$
σ	$49.0\,\text{fb}$	$48.4\,\text{fb}$	$38.9\,\text{fb}$	$38.4\,\text{fb}$
BR of selected mode	23.6%	74.0%	23.6%	74.0%
efficiency ϵ	5.8%	17.1%	6.0%	17.2%
purity π	67.4%	85.8%	62.3%	82.5%
$\delta\sigma/\sigma$	3.2%	1.7%	3.7%	1.9%

Table 6.11 Efficiency, purity, and relative statistical precision on the visible cross section for associated neutralino production. The cross section values given here are higher than those displayed in Fig. 5.3 and 5.4 since in the event generation step no generator level cut on the energy of the ISR photon was applied (cf. Sec. 5.4).

6.4   Parameter Determination

The parameter determination of the electroweakino parameters, explained in Section 2.2.3, has been performed by K. Rolbiecki [160] in order to investigate how good those can be determined assuming that the observable can be measured with the obtained precisions. The electroweakino parameters defining the chargino and the neutralino sector at tree level are

$$M_1, \quad M_2, \quad \mu, \quad \tan\beta. \tag{6.47}$$

The sign of μ cannot be resolved since it has a negligible impact on the observables because of the large values of M_1 and M_2 as seen in Eqs. (2.118) and (2.119). Therefore, it is fixed to be positive in the study. M_2 is taken as a positive parameter as well while both positive and negative sign of M_1 are considered. These electroweakino parameters can be extracted using the result of the measurements explained in the previous section: the masses of the chargino $M_{\widetilde{\chi}_1^+}$ and the heavier neutralino $M_{\widetilde{\chi}_2^0}$, the mass difference between the chargino and the LSP $\Delta M_{\widetilde{\chi}_1^+ - \widetilde{\chi}_1^0}$, the cross sections of the chargino $\sigma(\widetilde{\chi}_1^+ \widetilde{\chi}_1^- \gamma)$, and the neutralino $\sigma(\widetilde{\chi}_1^0 \widetilde{\chi}_2^0 \gamma)$ processes. All of these observables used in the fit are given in Tables 6.12 and 6.13. The cross section uncertainties obtained in the analysis (cf. Tables 6.8 6.11) did not contain the uncertainty on the branching ratios of the virtual W and Z boson decays. Since the uncertainty on the branching ratios depends on the available phase space given by the mass difference between the chargino and the LSP, the uncertainty on the mass difference measurements has to be taken into account in the cross section uncertainty. This is done by looking at the branching ratios of the corresponding channel for $\Delta M \pm 1\sigma$ values, $BR|_{\Delta M - 1\sigma}, BR|_{\Delta M + 1\sigma}$. It is mainly calculated by taking the average of the differences between these branching ratios and dividing it by the original value of it for a mass difference ΔM. When the mass difference gets a different value within the obtained uncertainty, the branching ratios will change without depending on the polarisation and the centre-of-mass energy of the process. Therefore, this will lead to a correlation between the

changes in the cross section uncertainty for different polarisation combinations and for different energy values. In this analysis, this correlation has been ignored. Table 6.13 gives both the statistical uncertainty obtained from the first part of the study, and the systematic uncertainty stemming from the dependency of the branching ratios on the mass difference. The table shows that in the case of chargino the uncertainty on ΔM dominates the cross section measurement in the dM1600 scenario. These systematic uncertainties amount to 15% for the dM1600 scenario and 2% for the dM770 scenario, while the statistical errors are respectively 5.3% and 3.8% for polarisation combination of $P(e^+, e^-) = (-30\%, +80\%)$. Since the uncertainty on ΔM for the dM1600 scenario is higher than the dM770 scenario, it has a significant effect on the cross section uncertainty.

There are other sources for systematic uncertainties, in addition to the mentioned one. The precision on the measurement of the beam energy, luminosity, and beam polarisation introduces some further uncertainties. It is expected that these machine parameters will be measured at the sub-percent level at the time of the ILC [161, 162, 163]. This indicates that systematic uncertainties coming from them can be neglected in this determination. Therefore, the main source for systematic uncertainty is the efficiencies which represent the reconstruction, identification and selection of the signal and background events. It is assumed that they can be determined to better than 1% based on typical precisions at LEP.

Observable	dM1600	dM770
$M_{\widetilde{\chi}_1^\pm}$ [GeV]	166.2 ± 2.0	167.3 ± 1.5
$M_{\widetilde{\chi}_2^0}$ [GeV]	169.6 ± 3.3	165.7 ± 1.6
$M_{\widetilde{\chi}_1^\pm} - M_{\widetilde{\chi}_1^0}$ [GeV]	1.63 ± 0.27	0.81 ± 0.04

Table 6.12 Observables used in the fit: masses and mass difference between the chargino and the LSP with uncertainties taken from Eqs. (6.22), (6.23), (6.37), (6.38), (6.45), (6.46).

6.4.1 Extrapolation to $\sqrt{s} = 350 \, \text{GeV}$ Centre-of-Mass Energy

In addition to cross section uncertainty at $\sqrt{s} = 500 \, \text{GeV}$, the precision on cross section for $\sqrt{s} = 350 \, \text{GeV}$ is also considered in the fit. The reason to choose $\sqrt{s} = 350 \, \text{GeV}$ is that it has a unique property to be the threshold value for the dM770 scenario (cf. Figure 5.3). According to the available phase space the curves determining the dependency of the polarised cross sections on the centre-of-mass energy will be shifted to the right or left. It is important to determine the curve as precise as possible to have an accurate mass determination. In that sense, the threshold value has a huge effect, since the cross section values change strongly. Even though the error is getting larger at low energies as will be explained in the following, the possibility of the error to include other possible curves, which corresponds to various scenarios with different masses, is getting lower. Therefore, it is important to be able to have results on the threshold value, and it can improve the mass determination of the produced higgsinos.

	δ_{stat}		δ_{sys}	
Observable	dM1600	dM770	dM1600	dM770
$\delta\sigma/\sigma(\widetilde{\chi}_1^+ \widetilde{\chi}_1^- \gamma)^{500}_{(-0.3,0.8)}$	5.3%	3.8%	15.1%	2.0%
$\delta\sigma/\sigma(\widetilde{\chi}_1^+ \widetilde{\chi}_1^- \gamma)^{500}_{(0.3,-0.8)}$	1.9%	1.6%	14.9%	2.0%
$\delta\sigma/\sigma(\widetilde{\chi}_1^0 \widetilde{\chi}_2^0 \gamma)^{500}_{(-0.3,0.8)}$	3.7%	1.9%	1.5%	1.5%
$\delta\sigma/\sigma(\widetilde{\chi}_1^0 \widetilde{\chi}_2^0 \gamma)^{500}_{(0.3,-0.8)}$	3.2%	1.7%	1.4%	1.6%

Table 6.13 Observables used in the fit: relative cross sections statistical uncertainties from Tabs. 6.8 and 6.11 and total uncertainties including systematic uncertainty due to branching ratios as discussed in text. The subscript on $\delta\sigma/\sigma$ denotes the beam polarisation $P(e^+, e^-)$ and the superscript the centre-of-mass energy in GeV.

	$P(e^+, e^-) = (+30\%, -80\%)$		$P(e^+, e^-) = (-30\%, +80\%)$	
E_{CM}	$\sqrt{s} = 500\,\text{GeV}$	$350\,\text{GeV}$	$\sqrt{s} = 500\,\text{GeV}$	$350\,\text{GeV}$
$\int \mathcal{L}dt$	$500\,\text{fb}^{-1}$	$350\,\text{fb}^{-1}$	$500\,\text{fb}^{-1}$	$350\,\text{fb}^{-1}$
$\sigma(\widetilde{\chi}_1^+ \widetilde{\chi}_1^- \gamma)$	20.56 fb	0.67 fb	5.20 fb	0.17 fb
$\sigma(\widetilde{\chi}_1^0 \widetilde{\chi}_2^0 \gamma)$	6.45 fb	0.24 fb	5.11 fb	0.19 fb

Table 6.14 Polarised production cross section values with a generator level cut on the energy of the ISR photon requiring $E_{ISR} > 10\,\text{GeV}$.

Because the analysis has not been performed at $\sqrt{s} = 350\,\text{GeV}$ centre-of-mass energy, the production cross sections were checked requiring a hard ISR photon with $E_\gamma > 10\,\text{GeV}$ on the generator level both for $\sqrt{s} = 500\,\text{GeV}$ at $\int \mathcal{L}dt = 500\,\text{fb}^{-1}$ and for $\sqrt{s} = 350\,\text{GeV}$ at $\int \mathcal{L}dt = 350\,\text{fb}^{-1}$. The results are shown in Table 6.14. As seen from the table the cross sections at $\sqrt{s} = 500\,\text{GeV}$ are approximately 30 times larger than the case of $\sqrt{s} = 350\,\text{GeV}$. Therefore the uncertainties were obtained by scaling the obtained error for $\sqrt{s} = 500\,\text{GeV}$ by $\sqrt{30}$. Another point to keep in mind for $\sqrt{s} = 350\,\text{GeV}$ is that the contribution from the SM background are expected to be smaller which results in lower uncertainties than our current estimate.

6.4.2   Electroweakino Parameter Determination

Determination of the unknown electroweakino parameters consists of several steps [160]. In the first step one needs to obtain the input parameters from the simulation as it is done in the previous part. In the simulation, one loop corrected masses calculated by `SOFTSUSY` were used, which are given in Table 5.1. Then the electroweakino parameters M_1, M_2, μ and $\tan\beta$ are calculated using the tree level relation with the experimental observables obtained by diagonal-

| | δ_{stat} | | δ_{sys} | |
Observable	dM1600	dM770	dM1600	dM770
$\delta\sigma/\sigma(\widetilde{\chi}_1^+\widetilde{\chi}_1^-\gamma)_{(-0.3,0.8)}^{350}$	29%	20.8%	15.1%	2.0%
$\delta\sigma/\sigma(\widetilde{\chi}_1^+\widetilde{\chi}_1^-\gamma)_{(0.3,-0.8)}^{350}$	10%	8.8%	14.9%	2.0%
$\delta\sigma/\sigma(\widetilde{\chi}_1^0\widetilde{\chi}_2^0\gamma)_{(-0.3,0.8)}^{350}$	20%	10%	1.5%	1.5%
$\delta\sigma/\sigma(\widetilde{\chi}_1^0\widetilde{\chi}_2^0\gamma)_{(0.3,-0.8)}^{350}$	17.5%	9.3%	1.4%	1.6%

Table 6.15 Observable used in the fit: relative cross sections statistical uncertainties from Tabs. 6.8 and 6.11 and total uncertainties including systematic uncertainty due to branching ratios as discussed in text. The subscript on $\delta\sigma/\sigma$ denotes the beam polarisation $P(e^+, e^-)$ and the superscript the centre-of-mass energy in GeV.

ising the mass matrices. The calculated M_1, M_2, μ and $\tan\beta$ are varied around their central values and for each set of parameters the theoretical values of $M_{\widetilde{\chi}_1^\pm}$, $M_{\widetilde{\chi}_2^0}$, $\Delta M_{\widetilde{\chi}_1^\pm - \widetilde{\chi}_1^0}$, $\delta\sigma/\sigma$ are calculated. As a next step, the calculated theoretical values are compared with the simulated results by minimising the χ^2 function as defined below, using `Minuit` [164]

$$\chi^2 = \sum_i \left| \frac{\mathcal{O}_i - \bar{\mathcal{O}}_i}{\delta\mathcal{O}_i} \right|^2 . \tag{6.48}$$

Here, $\mathcal{O}_i$ shows the experimental input variables, whereas $\delta\mathcal{O}_i$ gives the corresponding uncertainties. The $\bar{\mathcal{O}}_i$ represents the theoretical values of the experimental observables which are calculated from the electroweakino parameters. Since in the simulation one loop values are considered, while in the calculation tree level relations are used, the difference between tree level and one loop level needs to be taken into account in the fit. This is done by adding correction term as explained in Refs. [165, 166, 167].

However, since the variation of the electroweakino parameters are calculated at the tree level, the fit is to be understood as a tree level fit.

The minimum χ^2 is the best fit point and the values of M_1, M_2, μ, and $\tan\beta$ corresponding the minimum value of the fit give the lower limits on these parameters. To find the maximum values or the allowed region of these parameters a numerical calculation has been performed using $\chi^2_{min} + \Delta\chi^2$. Here $\Delta\chi^2$ depends on the number of the parameters estimated simultaneously. If the estimation is done only for one parameter, it should be $\Delta\chi^2 = 1$, but if the number of parameters is 2, then it is $\Delta\chi^2 = 2.3$ in order to be within one standard deviation. Hence, to obtain the 1 σ contours of M_1 and M_2 values, we considered the region of $\chi^2 + 2.3$.

In this model since it is a higgsino-like model, the mixing between higgsinos and gauginos is very small. The charginos and the neutralinos consist dominantly of higgsinos. This reduces the

effects of $\tan\beta$ on the observables as can be seen indirectly from Eqs. (2.118) and (2.119). The chargino and neutralino masses depend only on $\sin 2\beta$. Since $\sin 2\beta \to 2/\tan\beta$ at the limit of large $\tan\beta$, the masses have weak dependency on the $\tan\beta$, especially due to large M_1 and M_2. This shows that the value of $\tan\beta$ cannot be determined using the experimental input variables given in Tables 6.12, 6.13, 6.15. Because of that $\tan\beta$ is fixed to three different values in the range of $[1, 60]$. The considered values are chosen checking whether the fit has a solution for different values of $\tan\beta$ or not. This is done in three different region within the given range; such as, low, moderate and large $\tan\beta$. After fixing the $\tan\beta$, fitting is applied for the other three parameters of Eq (6.47).

The μ parameter is determined using the mass measurements of the higgsinos $M_{\widetilde{\chi}_1^\pm}$, $M_{\widetilde{\chi}_2^0}$ (cf. Eqs. (2.118) and (2.119)), while M_1 and M_2 depend on the mass difference between chargino and LSP $\Delta M_{\widetilde{\chi}_1^\pm - \widetilde{\chi}_1^0}$ (cf. Eqs. (2.122) - (2.124)). All the defined mass parameters M_1, M_2 and μ depend on the cross section measurements in a general case [43]; however, in the higgsino-like SUSY models, the cross section measurement has a significant effect only on the μ parameter. Therefore, the cross section measurements improve the determination of the μ parameter. If the sneutrino and selectron masses were lighter to the order of electroweak scale, t-channel production would be also possible. In this case, the cross section will be also dependent on the mass of these particles. But, since they are assumed to be heavy and their coupling to the higgsinos is very small, there is no dependency on these parameters in the considered higgsino scenarios.

The fitting has been firstly performed at $\sqrt{s} = 500\,\text{GeV}$ with an integrated luminosity of $\int \mathcal{L}dt = 500\,\text{fb}^{-1}$. And then, the high luminosity case of $\int \mathcal{L}dt = 2\,\text{ab}^{-1}$ has been also considered to see how much improvements can be obtained. The experimental errors are assumed to be reduced by a factor of 2 with the increased luminosity. In addition to the measurements considered before, the measurements of the mass difference between the second lightest neutralino and the first one, $M_{\widetilde{\chi}_2^0} - M_{\widetilde{\chi}_1^0}$ is included by considering that it can be measured with the same precision of the chargino mass difference. In reality, this would not be the case, since the neutralinos are reconstructed from photons which requires calorimeter information, while the tracking information is required for the charginos, which has a better resolution compared to the calorimeter.

The results of the fits are shown in Tables 6.16 and 6.17 and in Figures 6.21 and 6.22 for dM1600 and dM770 scenarios, respectively. The upper row of the tables and the upper plot of the figures show the result for $\int \mathcal{L}dt = 500\,\text{fb}^{-1}$, while the lower row and the lower plot are for $\int \mathcal{L}dt = 2\,\text{ab}^{-1}$. In the following part, first the low luminosity results and then high luminosity results will be discussed.

From the tables one could conclude that only lower limits for M_1 and M_2 can be determined. However, as seen from Figures 6.21 and 6.22, the M_1 and M_2 parameters are dependent each other. The plots show the 1-σ contours with different colours/styles showing different values of $\tan\beta$. The seen correlation between M_1 and M_2 allows a narrow region in the $M_1 - M_2$ parameter space. For the low values of either M_1 or M_2, the allowed region for the other parameter extends to high values, therefore it cannot be constrained. However, if one of them

			$\sqrt{s} = 500\,\mathrm{GeV}$		$\sqrt{s} = 350\,\&\,500\,\mathrm{GeV}$	
		input	lower	upper	lower	upper
500/fb	$\lvert M_1\rvert$ [TeV]	1.7	$\sim 0.8\ (0.4)$	no	$\sim 0.8\ (0.4)$	no
	M_2 [TeV]	4.36	$\sim 1.5\ (1.0)$	no	$\sim 1.5\ (1.0)$	no
	μ [GeV]	165.66	165.2	172.5	165.4	170.2
2/ab	$\lvert M_1\rvert$ [TeV]	1.7	$\sim 1.0\ (0.4)$	$\sim 6.0\ (0.6)$	$\sim 1.0\ (0.4)$	$\sim 6.0\ (0.6)$
	M_2 [TeV]	4.36	$\sim 2.5\ (3.5)$	$\sim 8.5\ (\mathrm{no})$	$\sim 2.5\ (3.5)$	$\sim 8.5\ (\mathrm{no})$
	μ [GeV]	165.66	166.2	170.1	166.4	170.0

Table 6.16 The 1-σ allowed ranges for the parameter fit in scenario dM1600. $\tan\beta$ is allowed to vary in the range $[1, 60]$. Values in parentheses are for $M_1 < 0$. Determination of the parameters for integrated luminosities of $\int \mathcal{L}\,dt = 500$ fb^{-1} and 2 ab^{-1} per polarisation configuration is shown. The high-luminosity fit also includes the mass difference between neutralinos, $M_{\widetilde{\chi}_2^0} - M_{\widetilde{\chi}_1^0}$. For an exact shape of the allowed M_1–M_2 region, see Fig. 6.21. The input values, see Table 5.1, are also shown.

			$\sqrt{s} = 500\,\mathrm{GeV}$		$\sqrt{s} = 350\,\&\,500\,\mathrm{GeV}$	
		input	lower	upper	lower	upper
500/fb	$\lvert M_1\rvert$ [TeV]	5.3	$\sim 2\ (0.3)$	no	$\sim 2\ (0.3)$	no
	M_2 [TeV]	9.51	$\sim 3\ (1.2)$	no	$\sim 3\ (1.2)$	no
	μ [GeV]	167.22	164.8	167.8	165.2	167.7
2/ab	$\lvert M_1\rvert$ [TeV]	5.3	~ 3	no	~ 3	no
	M_2 [TeV]	9.51	~ 7	~ 15	~ 7	~ 15
	μ [GeV]	167.22	165.2	167.4	165.3	167.4

Table 6.17 The 1-σ allowed ranges for the parameter fit in scenario dM770. $\tan\beta$ is allowed to vary in the range $[1, 60]$. Values in parentheses are for $M_1 < 0$ if solutions exist. Determination of the parameters for integrated luminosities of $\int \mathcal{L}\,dt = 500$ fb^{-1} and 2 ab^{-1} per polarisation configuration is shown. The high-luminosity fit also includes the mass difference between neutralinos, $M_{\widetilde{\chi}_2^0} - M_{\widetilde{\chi}_1^0}$. For an exact shape of the allowed M_1–M_2 region, see Fig. 6.22. The input values, see Table 5.1, are also shown.

is higher than 10 TeV, one could estimate an allowed region for the other parameter within 1-2 TeV range. The allowed regions have also a dependency on $\tan\beta$, especially in the case of small mass difference, the dM770 scenario. The allowed regions are changed with the different values of $\tan\beta$, whereas they stay almost in the same region in the case of dM1600, but the allowed regions are getting narrower for small values of $\tan\beta$. For the negative values of M_1, the
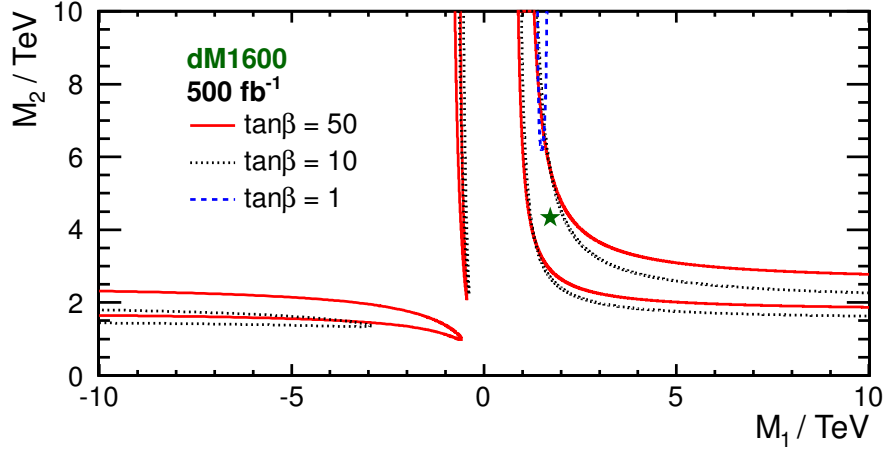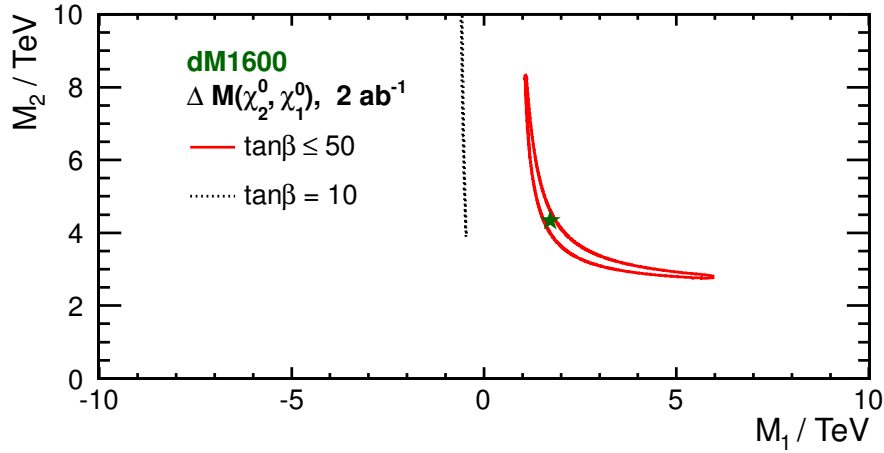
(a) dM1600 scenario, for $\int \mathcal{L} dt = 500 \, \text{fb}^{-1}$

(b) dM1600 scenario, for $\int \mathcal{L} dt = 2 \, \text{ab}^{-1}$

Figure 6.21 The 1-σ contours for determination of M_1 and M_2 in scenario dM1600. The input values of M_1 and M_2 are indicated by the star, and $(\tan \beta)_{\text{true}} = 44$. **Top:** The fit using input values listed in Tabs. 6.12, 6.13 and 6.15 for three different values of $\tan \beta$. **Bottom:** Projected fit results after a high luminosity run, $\int \mathcal{L} dt = 2 \, \text{ab}^{-1}$, with experimental errors improved by factor 2 and with the mass difference $M_{\tilde{\chi}_2^0} - M_{\tilde{\chi}_1^0}$ measurement included for a fixed $\tan \beta = 50$ and $\tan \beta = 10$. For $M_1 > 0$, other values of $\tan \beta$ do not further extend allowed regions and the respective contours are inside the one for $\tan \beta = 50$. For $M_1 < 0$, solutions exist only for $8 \leq \tan \beta \leq 16$ near $M_1 \sim -0.5$ TeV.

minimum values of M_1 and M_2 are smaller and there are two different possibilities seen in two separate contours. The one which has an large absolute value of M_1 shows a similar behaviour to the scenarios considered in this thesis. The other one with $M_1 > -800 \, \text{GeV}$ could have an additional third lightest neutralino with a mass around the value of $|M_1|$. A direct production of it $\tilde{\chi}_3^0$ could be possible at the ILC if the centre-of-mass energy is increased to 1 TeV. It can

be produced via $\widetilde{\chi}_3^0$ pair production or mixed production with either $\widetilde{\chi}_1^0$ or $\widetilde{\chi}_2^0$. In principle, the mixed production could be observable at the LHC, since there is enough mass difference between $\widetilde{\chi}_3^0$ and lighter neutralinos.

For $M_1 < 0$, it is seen that low $\tan\beta$ values are excluded, since they cause an inverted mass hierarchy between the light chargino and the lightest neutralino, $M_{\widetilde{\chi}_1^\pm} < M_{\widetilde{\chi}_1^0}$.

The determined minimum and maximum values of the μ parameter are given in Tables 6.16 and 6.17. To find the uncertainty of this parameter the difference between the input value and the obtained min. and max. values are calculated and the biggest one are counted as an uncertainity. Following this procedure, the μ parameter can be determined with an uncertainty $\sim$2.5 GeV and $\sim$6.8 GeV in the dM770 and dM1600 scenario, respectively. The inclusion of the cross section measurements at $\sqrt{s} = 350$ GeV affects only the μ parameter as explained before. The errors of the lower cross section is larger by a factor of 5.5 due to the low statistics; however, being close to the production threshold turns this drawback into an advantage and it helps to improve the determination. Even though $\sqrt{s} = 350$ GeV centre-of-mass energy provides a better μ parameter determination, since the mass and mass difference measurements requires large statistics, the analysis has been performed at a higher energy, at $\sqrt{s} = 500$ GeV. Another important effect on the error of the μ parameter determination is the variation of $\tan\beta$ within the specified region. For large value of $\tan\beta$ the μ parameter gets its minimum value due to the cancellation of the second term in Equation (2.119), while it gets the maximum value when $\tan\beta = 1$. Therefore, the variation between the smallest and the largest value of $\tan\beta$ shifts the values of μ by nearly ~ 1 GeV.

The results for the high luminosity are given in Tables 6.16 and 6.17 and in the corresponding plot of Figures 6.21 and 6.22. We observed that the increased luminosity, which improves both the mass measurements of the higgsinos and the precision on the cross sections, narrows the allowed region for μ parameter by 2 - 3.5 GeV. Even though the mass difference measurement got improved with the increased luminosity, the crucial effect on the determination of M_1 and M_2 comes from the inclusion of the neutralino mass difference measurement. Since the neutralino mass difference (Eq. (2.124)) has a different dependency on the fundamental parameters compared to the chargino mass difference (Eq. (2.122)), it provides a significant information for the fit. Especially in the low values of $\tan\beta$, where the changes of $\tan\beta$ have an important effect on the other parameters, addition of this parameter, which is independent from $\tan\beta$, helps to constrain M_1, M_2, and hence it breaks the dependency of the M_1 and M_2 on $\tan\beta$. As a result, it increases the lower limits on both M_1 and M_2, and also puts upper limits for most of the masses as seen from the tables. The allowed regions are $2.5 < M_2 < 8.5$ TeV and $1 < M_1 < 6$ TeV for positive values of M_1 in the dM1600 scenario. If $M_1 < 0$, its allowed region is getting smaller, $-700 \lesssim M_1 \lesssim -400$ GeV for only moderate $\tan\beta$ values, $8 \leq \tan\beta \leq 16$, which corresponds a scenario with extra neutralino in the region of M_1. In the dM770 scenario, one could see a clear improvement from the plot which shows the valid solutions existing only for positive values of M_1. In this region, M_2 is constrained in the 7 - 15 TeV region, while the lower limit for M_1 is increased by 1 TeV. As a result of the weak dependency of the model parameters on $\tan\beta$, the smaller values of $\tan\beta$ have been covered with the shown contour and therefore those are not shown separately.

The parameter determination has indicated that the precisions of the key observables are good enough to determine the electroweakino parameters in a percent level. However, the determination could be enhanced by the measurement of the neutralino mass difference, and the measurements of the cross section at a centre-of-mass energy of $\sqrt{s} = 350\,\text{GeV}$, as well as by the high luminosity.
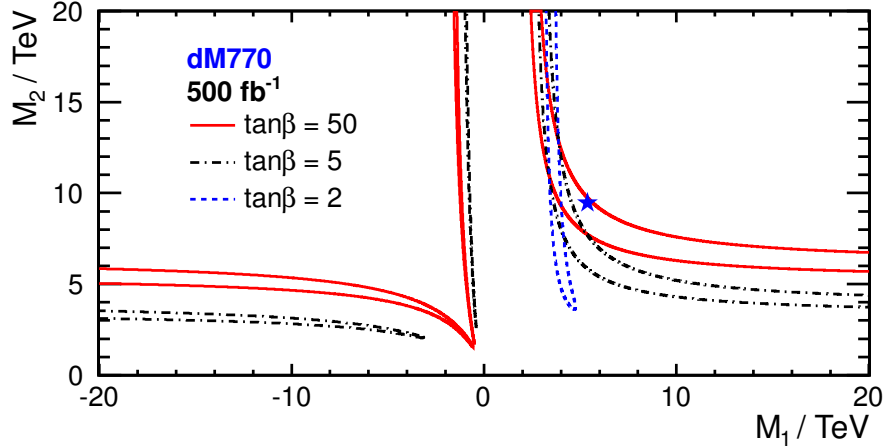
(a) dM770 scenario, for $\int \mathcal{L}dt = 500\,\text{fb}^{-1}$
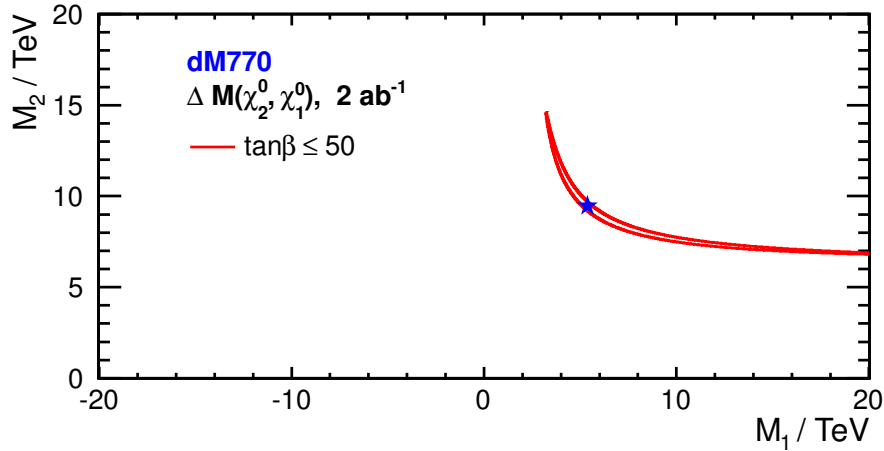
(b) dM770 scenario, for $\int \mathcal{L}dt = 2\,\text{ab}^{-1}$

Figure 6.22 The 1-σ contours for determination of M_1 and M_2 in scenario dM770. The input values of M_1 and M_2 are indicated by the star, and $(\tan \beta)_{\text{true}} = 48$. **Top:** The fit using input values listed in Tabs. 6.12, 6.13, and 6.15 for three different values of $\tan \beta$. **Bottom:** Projected fit results after a high luminosity run, $\int \mathcal{L}\,dt = 2\,\text{ab}^{-1}$, with experimental errors improved by factor 2 and with the mass difference $M_{\tilde{\chi}_2^0} - M_{\tilde{\chi}_1^0}$ measurement included for fixed $\tan \beta = 50$. Other values of $\tan \beta$ do not further extend allowed regions and the respective contours are inside the shown one.

Chapter 7

A Road from SGV to More Realism

The analysis and results explained in the previous chapter are based on a study performed using a fast detector simulation, Simulation à Grande Vitesse (SGV). In the fast simulation analysis, there are some simplifications which are listed in the following, and will be discussed in more detail in this chapter.

Simplifications in SGV are itemised as follows:

- Perfect particle identification is assumed.

- Pair background, which is one of the backgrounds stemming from the beam-beam interactions (cf. Section 3.5.1), is considered partially. The efficiency of tagging high energetic electrons or photons in the BeamCal are acquired by utilising the simulated pair background events (cf. Section 5.5.3). In addition, the tracking efficiency from the full simulation in the presence of pair background is implemented into SGV as explained in Section 5.5.3. However, one of the main consequences of this background, which is the additional real and fake background tracks, is not considered.

- Low p_t $\gamma\gamma$ overlay, which is another important background arising from beam-beam interactions as explained in Section 3.5.2, is not taken into account. Since these events are dominant in the low momentum region, this type of background events play an important role in the higgsino analysis.

Due to the signal topology, these simplifications of SGV could be of high relevance in the higgsino case. In order to investigate whether the higgsino analysis can be performed in a real experiment and which specific requirements would be needed on the detector, the analysis has been conducted in full simulation. The signal topology of the higgsino samples explained in Chapter 6 requires the following analysis steps in the higgsino analysis which might be affected by the realism of full simulation:

- presence of one hard ISR photon with $E_{\mathrm{ISR}} > 10\,\mathrm{GeV}$, $|\cos\theta_{\mathrm{ISR}}| < 0.993$,
- requirement of low multiplicity events, $N_{RP} < 15$,
- constraints on the missing four-momentum, $E_{\mathrm{miss}} > 300\,\mathrm{GeV}$, $|\cos\theta_{\mathrm{miss}}| < 0.992$,

- reconstruction of the soft final state particle with $E_{\text{soft}} < 5\,\text{GeV}$, $|\cos\theta_{\text{soft}}| < 0.9397$
- identification of the final state particles
- selection of the higgsino decay products: semi-leptonic for the chargino process, and photonic for the neutralino process.

In this chapter, the impact of simplifications on the key observables will be discussed. In Section 7.1, first ILD reconstruction procedure applied in full simulation will be explained. Then, the investigation of each analysis steps will be described in Section 7.2. During the study, some challenges, which make the full simulation analysis of the higgsinos impossible, have been observed. Therefore, they need to be studied carefully. Two of them will be discussed in this chapter. One of them is the tracking of low momentum particles which will be discussed in Section 7.3. The second one is the identification of low momentum μ and π which will be the focus of this thesis. The method, which was developed to overcome this challenge, will be explained in detail in Section 7.4. The estimation of the impact of the method on the higgsino events will be explained in Section 7.5.

7.1 ILD Reconstruction

The reconstruction of the particle flow objects is based on Pandora Particle Flow Algorithm (`PandoraPFA`) which is explained in [117] in detail. The main idea behind this concept is given in Section 4.2. `PandoraPFA`, which is implemented to the `Marlin` reconstruction framework, takes a list of the reconstructed tracks and a list of digitised calorimeter hits in order to create particle flow objects (PFO). The conducted track and PFO reconstruction as well as particle identification in full simulation will be explained in the following.

7.1.1 Track Reconstruction Pattern Recognition Algorithms

The reconstruction of tracks consists of several standalone track finding algorithms for different tracking system of the ILD detector; TPC, VTX and SIT, and FTD. The pattern recognition algorithms corresponding to these tracking systems are called `Clupatra`, `SiliconTracking`, and `ForwardTracking`, which are followed by `FullLDCTracking` to merge the standalone track segments [168].

The `SiliconTracking` algorithm is used to find tracks in the VTX and SIT tracking systems. These sub-detectors are divided into regions with fixed solid angle, and three hits are searched for within these regions starting from outermost layer in order to create track seeds (see for details [168, 169]). The acquired track seeds are then combined with the other hits in the inner layers using a helical χ^2-fit. After determining the hits of a track, they are refitted with the Kalman filter [170, 171], which takes into account the material effects such as multiple scattering and energy loss due to ionisation, in order to determine the track parameters at the IP. The importance of this tracking algorithm for low momentum particles will be explained in Section 7.3.

In order to find tracks in the TPC, the `Clupatra` algorithm [172] is used. The algorithm is applied from outside pads to inner pads by using a nearest neighbour clustering algorithm. The

track seeds are searched for in a certain number of pad rows. Then if the created seeds are sufficiently separated from each other, they are fitted with Kalman filter and extrapolated to the inner rows in order to create full TPC tracks. To find the tracks in the forward region and with low-momentum, this procedure is repeated by starting from the consecutive inner pad rows. The details about the algorithm can be found in [168].

The `ForwardTracking` algorithm, which is important for forward tracks and low momentum particles, is based on Cellular Automatons and Hopfield neural networks [173, 168]. The FTD consists of two pixel and five strip discs (cf. Section 4.3.1.2). The hits on one of the discs are combined with the closeby hits on the next disc to create track segments. Then the angle between two adjacent track segments is required to be less than a certain angle. The segments fulfilling the angle criteria are used to create the tracks and the others are removed. With the usage of the remaining hits, the procedure is repeated for segments created with three nearby hits on the three adjacent discs. The obtained tracks are then fitted with Kalman filter and track parameters are determined. Before saving the tracks, they are checked for any hits shared with other tracks using the Hopfield neural network explained in [173].

After these standalone tracking findings, the tracks are combined by checking the consistency of these individual tracks with the help of `FullLDCTracking` processor, and then they are refitted with the Kalman filter and stored [168].

7.1.2 Pandora PFO Reconstruction Algorithms

The obtained track information is transmitted to `PandoraPFA` to create reconstructed objects. The reconstruction of PFOs are done by `PandoraPFA` in several steps, which will be briefly explained in the following. In general, `PandoraPFA` first creates clusters using various algorithms, and then merge the clusters with the tracks by following specialised algorithms.

Track Selection: In the first step, tracks reconstructed with the tracking pattern recognition algorithms are projected onto the front face of the ECAL using a helical fit to the last 50 hits. Then the tracks are classified depending on their likely origin, such as displayed vertices or kinks (cf. Ref. [117]). The track parameters obtained from track reconstruction and the classification information are stored in an object to be used in the event reconstruction.

Calorimeter hit selection: For each digitised hit given as an input to the PandoraPFA, the position (x, y, z), the energy deposition, and the physical layer in the ECAL or HCAL are defined and stored in an object.

Clustering: The clustering algorithm of `PandoraPFA` is a cone-based forward projective method starting from the innermost layer and expanding up to the outermost layer [117]. The determination of the track direction from the tracks projected onto the front face of the ECAL forms the first step of the clustering algorithm. After that, each hit within the defined cone is looped over and the hits in layer k are compared with the hits in the previous layer $k-1$ which was already clustered. If the hit does not find any other hits to associate, then the association of the hits is searched for in layer $k-2$ and $k-3$ in turn. If the hit is still not associated to any

cluster, the same layer can be searched for any hit which is sufficiently close to the considered hit. After these searches, if it is still unassociated then it is used to start a new cluster seeding. In this step fast photon identification is also applied [117] and the clusters creating photons are removed before the cluster merging. The clustering algorithm splits the clusters in order to avoid the merging of clusters from several particles, and then they are merged in the following step using some topological rules.

Topological cluster merging: In the clustering algorithm, it is more likely to acquire splitting clusters into the charged one associated with tracks and the neutral one where there is no association made. In these cases, the distance between two clusters is checked and the clusters are merged if they fulfil the requirement to be sufficiently close to each other. For the details of main topological rules for cluster merging see [117].

Re-Clustering: The defined algorithm might fail especially at higher energies than about $50\,\text{GeV}$ due to confusion as explained in Section 4.2. To improve the performance, the clustering algorithm is modified by choosing a different cone geometry (a smaller radius for example) and checking for the correct clustering. If better clustering is found, then it is used. If not the original clustering is kept.

Photon identification and recovery: After the reconstruction of the clusters, a photon identification algorithm based on the longitudinal shower profile as explained in [117] is applied to identify clusters as photons. Photons may merge with the cluster of charged particles. In order to identify these photon clusters from hadronic showers, the compact feature of EM showers is utilised. The hits associated to the identified photons then removed from the hadronic cluster. After removing the hits, if the remaining energy of the hadronic cluster is inconsistent with the momentum of the associated track, the clusters are vetoed.

Fragment Removal: Apart from the photon clusters, there might be a significant amount of neutral clusters which are fragments of the charged clusters. These fragments are removed by merging them with the parent charged cluster. The merging is done by following the procedure explained in [117].

Formation of particle flow objects: In this final stage, the tracks are merged with the clusters using the closest distance approach, and the reconstructed particles, Pandora PFOs, are created with associated four momenta.

The reconstruction algorithms of the PFOs are mainly optimised for the jet energy resolution [117]. The reconstruction in case of the soft decay products of the higgsinos will be discussed in Section 7.2.1 for the ISR photon, in Section 7.2.2 for missing energy and in Section 7.2.4 for both tracks and PFOs.

7.1.3   Particle Identification

In DBD version of the reconstruction, a simple particle identification (PID) is provided by `PandoraPFA`. The identification of clusters for neutral and charged particles are considered separately. In order to create a neutral PFO, the following criteria are used. Firstly, the number of

hits of a cluster is checked; if it is less than $N_{\text{hit,min}} = 5$, then the cluster is not considered. If it is not, then the neutral particles are classified as either photon or non-photon with the help of fast photon identification explained in [117], which is based on EM shower structure of photons. Then, the non-photon clusters are vetoed if their energy is below a hadronic energy threshold, which is $E_{\text{hadron,min}} = 0.25\,\text{GeV}$, and if they are occupying a single layer ($N_{\text{layer,min}} = 2$). These cuts, especially the energy cut, could cause problems in the case of low momentum particles as the higgsino case. The effect of these cuts will be discussed in Section 7.4.

For the charged PFOs, the identification is more complex. There are some quality cuts applied in order to create PFOs as explained in [174]. In general, for muon reconstruction there is an algorithm which identifies the hits both in the muon system and in the tracking sub-systems, and then matches them by extrapolating the inner detector tracks to the muon system. The details of the algorithm can be found in [175]. This algorithm is performed for muons with energy larger than 7 GeV in order to have sufficient quality MIP tracks in the muon system (muons must have at least 4 GeV momentum to reach the muon system as explained in Section 4.3.3). However, the muons which cannot reach the muon system can be identified using their specific MIP signature. Electrons are identified by the properties of their electromagnetic shower. All other charged clusters associated to tracks apart from those identified as electrons or muons are labelled as pions. The low momentum particles may be less likely than the high momentum particles to be identified as e or μ. The situation in the higgsino case containing low momentum final state particles will be investigated in the following section.

7.2 The Feasibility of the Analysis in a Real Experiment

In order to check the feasibility of the analysis in full simulation, the chargino sample of the dM770 scenario introduced in Section 5.1.1 was chosen with the polarisation combination of $P(e^+, e^-) = (-100\%, +100\%)$. For the reconstruction and analysis of the higgsino samples in full simulation, the Detailed Baseline Design (DBD) version of the `ILCSoft` framework (cf. Section 5.6), `v01_16_02`, was utilised. The samples were generated with the ILC set-up of `Whizard 1.95` at $\sqrt{s} = 500\,\text{GeV}$ as it was explained in Section 5.4. They were simulated with the DBD version of `Mokka`, `00_00_03`, for the ILD detector of `ILD_o1_v05` (see Section 5.6.1). Then, they were passed through the reconstruction using the DBD version `v01_06` of the `Marlin` framework. The full simulation samples were produced both with low p_t $\gamma\gamma$ overlay and without. In the overlay of the $\gamma\gamma$ background, the updated estimation of $\langle N \rangle = 1.2$ events per bunch crossing (BX) (cf. Section 3.5.2) was used, not the standard overlay of $\langle N \rangle = 1.7$ events per BX which was used in the SM samples. The pair background was not taken into account in this step. The impact of the pair background will be explained in Section 7.3.

7.2.1 Reconstruction of ISR Photon

The reconstruction of the highest energetic photon, considered as an ISR photon, is shown in Figure 7.1 for three cases: fast simulation (the blue line), full simulation without $\gamma\gamma$ overlay (the red line) and full simulation with $\gamma\gamma$ overlay of $\langle N \rangle = 1.2$ events per BX (the green line). The figure displays the energy and $\cos\theta$ distribution of the photons with the highest reconstructed

energy within the tracking acceptance region $|\cos\theta| < 0.9397$. This region corresponds to $7°$ which is required to be able to separate the electron and photon (cf. Section 6.1). It is seen that both full simulation cases either with $\gamma\gamma$ overlay background or without show very good agreement with SGV.
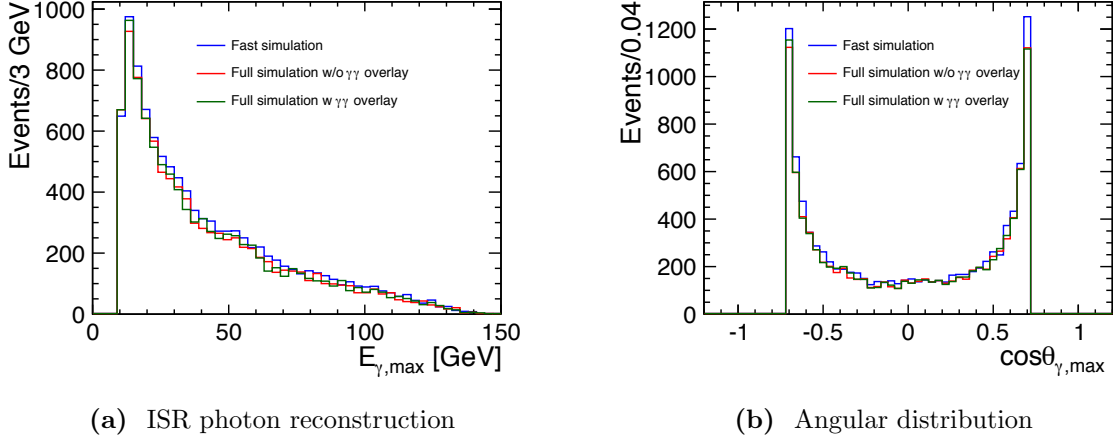

(a) ISR photon reconstruction   **(b)** Angular distribution

Figure 7.1 (a) Energy distribution of highest energetic photons within $7°$ polar angle for $E_{ISR} > 10\,\text{GeV}$ (b) $\cos\theta$ distribution of these photons (chargino sample of dM770 scenario chosen as an example). The blue line indicates the case of SGV, the red line shows the case in full simulation without $\gamma\gamma$ overlay, and the green line is for full simulation with an overlay of 1.2 events per BX.

As a result, one can conclude that the reconstruction of the ISR photon would work well in a real experiment. Since the reconstruction of the chargino and the second lightest neutralino masses are determined from the recoil mass of the ISR photon as explained in Section 6.2.2, $M_{\widetilde{\chi}_1^\pm}$ and $M_{\widetilde{\chi}_2^0}$ would be reconstructed efficiently, if the particles could be identified correctly.

7.2.2 Reconstruction of the Missing Four-Momentum

Figure 7.2 depicts the missing energy and polar angle distribution of the missing energy in terms of $\cos\theta$ within $|\cos\theta| < 0.992$ corresponding to the forward tracking region of the detector ($\theta \sim 7°$), for the three cases. As seen from Figure 7.2a, the reconstruction for the missing energy of the full simulation without $\gamma\gamma$ overlay agrees well with the SGV, whereas the energy distribution of the missing particles in full simulation with $\gamma\gamma$ overlay background of 1.2 events per BX is shifted towards lower energies. Nevertheless, the angular distribution of the missing energy is almost the same in all three cases shown in Figure 7.2b. Since the $\gamma\gamma$ interactions produce visible particles in addition to the signal final state particles, the expected missing energy would be less. When these overlay particles are suppressed with the proper methods, which will be explained in Section 7.2.3.1, there will be no shift on the reconstruction of the missing energy. On the other hand, this parameter does not play a role in the reconstruction of the key observables, it is used as a cut in the analysis to reduce the SM background. The events
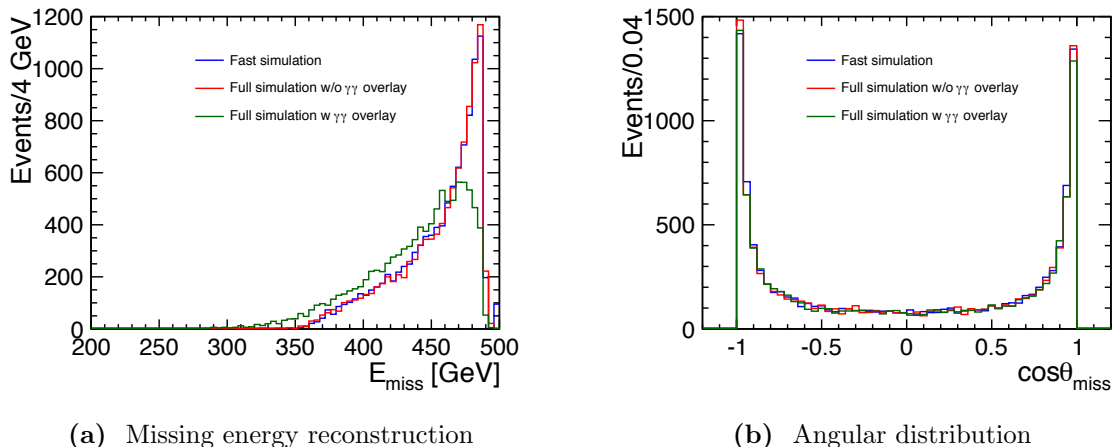
(a) Missing energy reconstruction

(b) Angular distribution

Figure 7.2 (a) Energy distribution of the missing energy within $|\cos\theta| < 0.992$ (the applied cut in fast simulation is $E_\mathrm{miss} < 300\,\mathrm{GeV}$ for $M_{\widetilde{\chi}_1^\pm}$, $M_{\widetilde{\chi}_2^0}$ and $\Delta M_{\widetilde{\chi}_1^\pm - \widetilde{\chi}_1^0}$, and $E_\mathrm{miss} < 350\,\mathrm{GeV}$ for the estimation of the precision on cross section) (b) $\cos\theta$ distribution of the missing energy (the applied cut in fast simulation is $|\cos\theta| < 0.992$). The blue line indicates the case of SGV, the red line shows the case in full simulation without $\gamma\gamma$ overlay, and the green line is for full simulation with recently estimated overlay of 1.2 events per BX.

which have a missing energy larger than $E_\mathrm{miss} > 300\,\mathrm{GeV}$ are considered for the reconstruction of key observables. But, for the estimation of the precision on cross section, the cut on the missing energy is tighten to $E_\mathrm{miss} > 350\,\mathrm{GeV}$. Therefore, the shift is not relevant to the reconstruction of $M_{\widetilde{\chi}_1^\pm}$, $M_{\widetilde{\chi}_2^0}$ and $\Delta M_{\widetilde{\chi}_1^\pm - \widetilde{\chi}_1^0}$, but the estimation of $\delta\sigma/\sigma$. If one assumes that the $\gamma\gamma$ overlay particles are suppressed to a reasonable level, it can be concluded that the reconstruction of the missing four-momentum in full simulation works well.

7.2.3 Number of Reconstructed Particles

The higgsino samples contain low multiplicity events, therefore the number of reconstructed particles are required to be less than $N_{RP} < 15$ in the fast simulation analysis. In a real experiment, additional particles arise due to the background of $\gamma\gamma \rightarrow$hadrons and pair background which are stemming from the beam-beam interactions as explained in Section 3.5. These additional tracks mainly constitute two of the simplifications considered in fast simulation. The effects of these on the analysis, which will be performed in a real experiment, will be discussed in the following.

7.2.3.1 Impact of $\gamma\gamma$ Overlay on Analysis and Its Suppression

The effect of the low p_t $\gamma\gamma$ overlay decaying hadronically (cf. Section 3.5.2) is shown in Figure 7.3. It displays the transverse momentum distribution of stable charged true particles and the cosine distribution of their polar angle for three different cases. The blue and red lines show the cases in fast simulation and in full simulation without $\gamma\gamma$ overlay, respectively. The lines indicate a good agreement between these two cases. The figure also shows that the implementation of the

145

tracking efficiency into SGV works fine. The green line indicates the case in full simulation when the $\gamma\gamma$ overlay is taken into account. The figure shows explicitly that the $\gamma\gamma$ overlay background particles are in the same p_t region with the signal particles and they are mostly going towards the forward region. In general, the $\gamma\gamma$ overlay particles are suppressed by applying an exclusive jet algorithm [176]. The algorithm reconstructs these objects going to the forward region into two additional jets, and then excludes them. However, since the higgsino events do not contain any jet in the final state, applying a jet clustering algorithm would ruin the signature of the events. Therefore, this usual procedure does not work in the higgsino case. Another way would be to veto the particles with transverse momentum below $p_t < 1\,\mathrm{GeV}$. With a cut on $p_t = 1\,\mathrm{GeV}$, the number of reconstruction particles would be sufficiently small for the required cut in SGV. However, because of the similarity of the signal and $\gamma\gamma$ background events, the usual procedures cannot be applicable to the higgsino analysis. Therefore alternative ways, which will be explained in the following, need to be taken into account in the higgsino case to suppress these large amount of background.

(a) Effect of $\gamma\gamma$ overlay

(b) Angular distribution
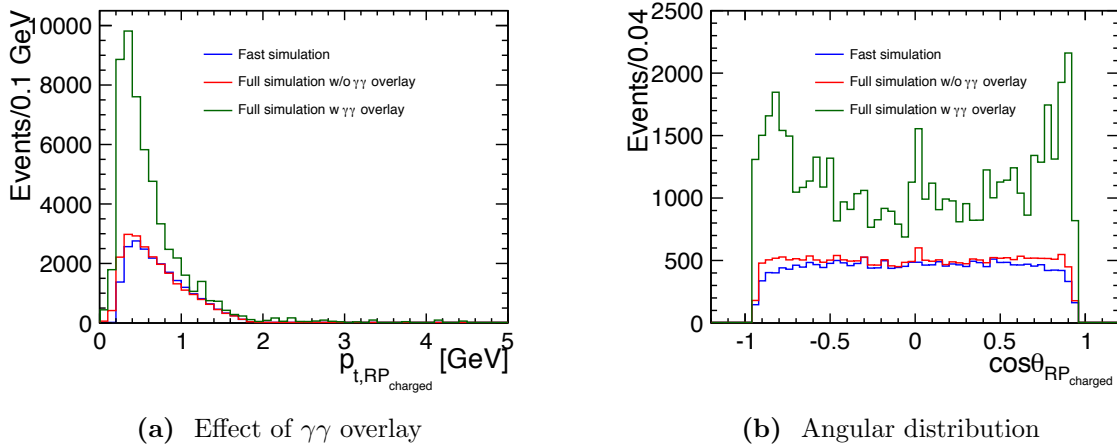
Figure 7.3 (a) p_t distribution of charged reconstructed particles (b) $\cos\theta$ distribution of charged reconstructed particles (chargino sample of dM770 scenario chosen as an example). The blue line indicates the case in fast simulation SGV, the red line shows the case in full simulation without $\gamma\gamma$ overlay, and the green line is for full simulation with the recently estimated overlay of 1.2 events per BX.

Since higgsinos have a non-zero lifetime as mentioned in Section 5.1.1, their decay products will have a displaced decay vertex in the transverse direction, while the vertices of the overlay particles are displaced along the length of the bunch. Therefore, determination of the vertex position would be very useful in order to suppress the $\gamma\gamma$ overlay background particles.

The $\gamma\gamma \rightarrow$ hadrons background dominantly arises from a vector boson dominance processes where photons oscillate into neutral ρ vector mesons, $\gamma\gamma \rightarrow \rho^0\rho^0$ [116] (cf. Section 3.5.2). Then the neutral vector mesons convert to charged ones with the exchange of a charged π. The created charged vector mesons decay to pion-pairs, $\rho^\pm \rightarrow \pi^\pm\pi^0$ with a branching ratio of 100%. This property of $\gamma\gamma$ overlays provides another way to suppress the overlay particles. The way

to implement this signature would be to search for one charged π and one neutral π which decays to 2 photons, and to exclude the events having the invariant mass of these pions in the same order with the ρ meson mass. This would suppress the $\gamma\gamma$ overlay particles. However, a preliminary investigation showed that the simulation of the $\gamma\gamma$ events used in the DBD is not quite representing the state of the art, in particular using a description older than the results of LEP/HERA [177, 178]. Therefore, the detailed investigation of the suppression of the $\gamma\gamma$ overlay was beyond the scope of this thesis.

7.2.3.2 Impact of Pair Background on Analysis

The production of pair background is explained in Section 3.5.1. As it is explained, the pair background produces additional real tracks in VTX detector, TPC, and especially in forward region detectors, such as BeamCal. In addition, the backscattering tracks from the endcap can also increase the amount of the background tracks. Not only real tracks, but also ghost tracks play a role in the creation of additional tracks. In the higgsino-like chargino events, the presence of pair background gives rise to nearly 21.6 background tracks per event. The created background tracks per event in the chargino sample using the DBD tracking are shown as a function of transverse momentum in Figure 7.4. The right plot of the figure shows the zoomed version into the low p_t region, as most of the background tracks are situated in this region. Since the low p_t region is of high interest for the higgsino events, the background tracks cannot be reduced by considering tracks with a certain p_t (e.g. $p_t > 1\,\text{GeV}$), thus they would affect the low multiplicity signature of the signal events. Because of that, they need to be suppressed in the analysis. In order to do this, one can investigate the variables that give different distributions for the background tracks and signal tracks, such as momentum or angular distribution, or χ^2 distribution of track reconstruction.

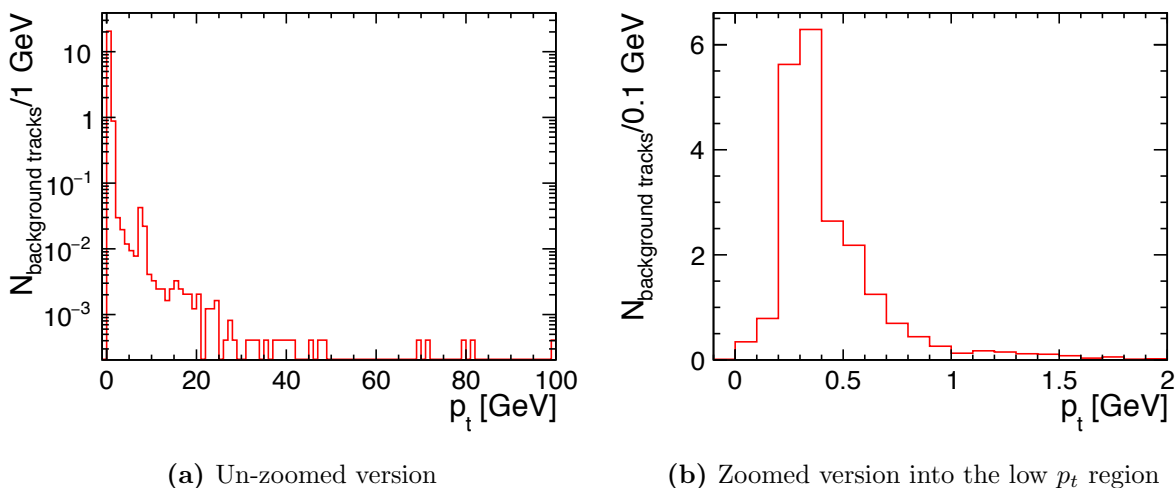(a) Un-zoomed version   (b) Zoomed version into the low p_t region

Figure 7.4 Number of the background tracks of the higgsino-like chargino process per event in the presence of pair background using the DBD tracking. There is approximately 21.6 background tracks per event. Figure is adapted from Ref. [179].

Due to the impact of these additional backgrounds both from $\gamma\gamma$ overlay and pair background, one needs to apply the proposed suppression methods to be able to perform the analysis in a real experiment. But, after the suppression of these backgrounds, it would be fine to use the low multiplicity of the higgsino events as a feature of the signal events.

7.2.4   Reconstruction of Soft Particles

The reconstruction of stable and charged soft particles was studied under the reconstruction of both tracks (cf. Section 7.1.1) and Pandora Particle Flow Objects (PFO) (cf. Section 4.2 and Section 7.1.2). The reconstruction efficiencies of tracks and Pandora PFOs for the three compared cases are indicated in Figure 7.5 for the stable charged particles within $|\cos\theta| < 0.9397$ ($20°$). It is seen that the tracks can be reconstructed almost completely down to $0.3\,\text{GeV}$ for all cases. The tracking efficiencies of both full simulation cases with the $\gamma\gamma$ overlay and without

(a)   Track reconstruction

(b)   PFO reconstruction
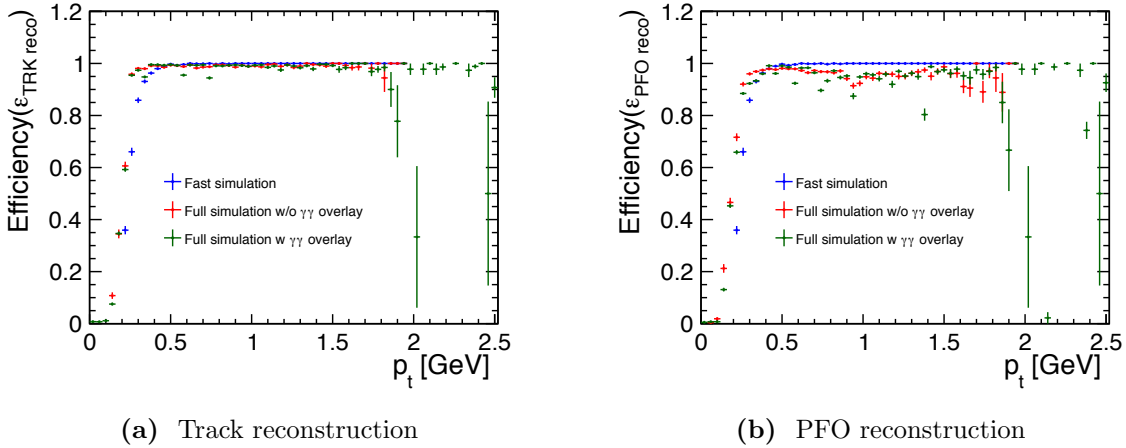
Figure 7.5   (a) Tracking efficiency of stable charged true particles as a function of transverse momentum of these true particles within $20°$ polar angle (b) Particle Flow Object reconstruction efficiency of stable charged true particles against their p_t (chargino sample of dM770 scenario chosen as an example). The blue line indicates the case of SGV, the red line shows the case in full simulation without $\gamma\gamma$ overlay, and the green line is for full simulation with estimated overlay of 1.2 events per BX.

agree well with the SGV tracking efficiency. It is seen that the implementation of the tracking efficiency from the full simulation including pair background (cf. Section 5.5.3) looks compatible with the full simulation tracking efficiency. It can be concluded that the tracking of the DBD would be fine for a study in a real experiment, but there is still room for improvement.

The efficiency of Pandora PFO reconstruction is not as good as the track reconstruction for both full simulation cases. In particular for $p_t \approx 1\,\text{GeV}$, there is a visible drop on the PFO reconstruction efficiency, while the efficiency is closer to one between $0.3 < p_t < 0.9$ and $p_t > 1\,\text{GeV}$ with larger statistical error bars due to the smaller number of particles at around $2\,\text{GeV}$ as can be seen from Figure 5.7. This reduction of the reconstruction efficiency of the PFOs

indicates that some of the particles with momentum below $2\,\mathrm{GeV}$ cannot fulfil the required cuts to create a charged PFO (for details of the algorithm see Ref. [117, 174]). The observed fluctuations require improvements in the reconstruction algorithm in order to tune the algorithm for low momentum particles.

7.2.5 Particle Identification of Soft Particles

The identification of particles is one of the simplification made in SGV, which plays a crucial role in any kind of analysis. The resulting identification efficiencies of the related decay products of the higgsino events, which are π, μ and e as described in Section 6.2.1, are shown in Figure 7.6 as a function of the transverse momentum of true particles. Figure 7.6a shows the π identification

(a) Pion Identification   (b) Muon Identification   (c) Electron Identification
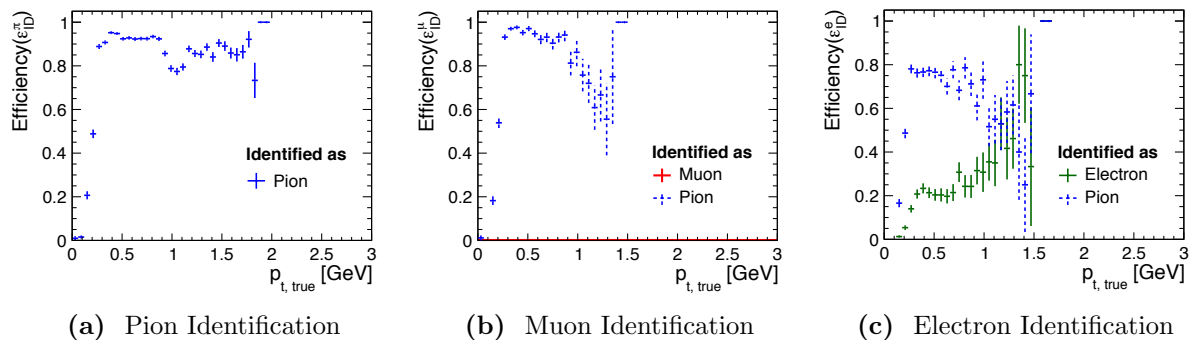
Figure 7.6 Identification efficiency of particles in the higgsino signal samples generated with the full simulation. The blue histograms show the efficiency of pion identification either correctly or not. The green histogram shows the electron identification efficiency. The red histogram, which is shown in (b) with "zero" value, indicates the muon identification efficiency.

efficiency. Pions down to $300\,\mathrm{MeV}$ can be correctly identified with $\sim 90\,\%$ efficiency. The same structure as in the PFO reconstruction, having a drop around $p_t \approx 1\,\mathrm{GeV}$, is seen in the identification efficiency of pions as well. Figure 7.6b indicates the μ identification efficiency if they are identified as μ with the red line, and π with the blue dashed line. It is seen that there is no muon identified correctly. Most of them are identified as pions which makes the separation of the low momentum π and μ a key ingredient of the full simulation analysis. A suitable method has been developed in the context of this thesis as will be explained in Section 7.4. Figure 7.6c displays that the identification efficiency of electrons, shown with the green histogram, is also not sufficient for proceeding with the analysis without any further identification, since also most of the electrons are identified as pions.

According to the results of Figure 7.6, it can be concluded that the current particle identification cannot be used as it is, it needs improvements for both e and μ identification in order to be able to separate them from π. Even the particles are very soft, the identification of them can be done by using dE/dx and cluster shape information respectively for e and μ identification, which will be explained in the following.

7.2.5.1 e and π Identification

While a development of an electron identification was beyond the scope of this thesis, the ionisation energy loss of a single particle per length dE/dx, which is measured by the TPC, offers an efficient particle identification method especially for low momentum particles. Since the value of dE/dx depends on the mass of the particles, it is an efficient method only for particles with different masses, therefore it works well for the separation of e and π. However, the information about dE/dx was not available at the time of the analysis. The reconstruction of dE/dx was not implemented in the DBD reconstruction and is only currently being developed.

As an example, the dE/dx distribution of the particles as a function of momentum is shown in Figure 7.7 [180, 181]. It can be seen that electrons and pions are separated very well in the momentum region relevant for the higgsino analysis. Therefore, it can be assumed that the electrons would be identified efficiently using this method.
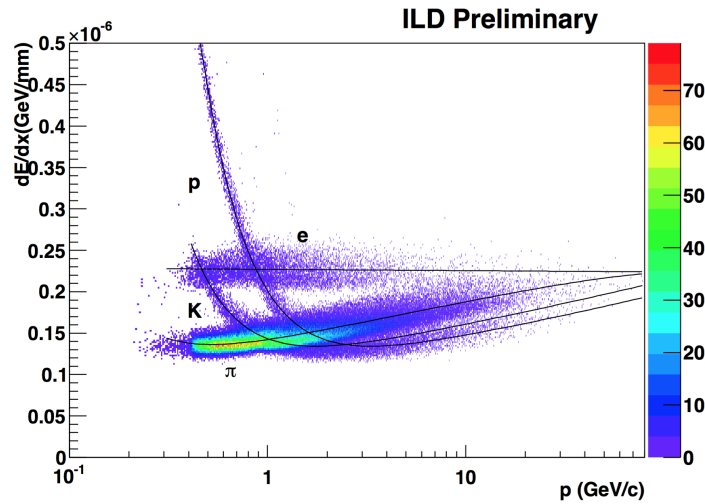
Figure 7.7 An example for the distribution of dE/dx for different particles as a function of their momentum. Figure taken from Ref. [181].

7.2.5.2 μ and π Identification

While dE/dx works very well for the identification of e and π in the low momentum region, it cannot be used for μ and π identification since their masses are close to each other. But, μ and π can be separated using the cluster shape differences, since muons leave the signature of a minimum ionising particle (MIP), while pions deposit their energy as a hadronic shower (cf. Section 4.1).

As explained in Section 4.1, at sufficiently high energies, a π showers mostly in the hadronic calorimeter, while a muon, which goes through the calorimeters, is detected by the help of the muon detector. However, if the muons do not have enough energy to reach the muon detector

(cf. Section 4.3.3), they will stop in the HCAL or the ECAL depending on their energies. If a pion has low momentum, it may start showering already in the ECAL and may deposit most of its energy in that calorimeter. In that sense, the place where they are detected will be the same and it will be challenging to identify low energetic μ and π properly. The separation of low momentum μ and π has been studied in detail using the cluster shape information in the context of this thesis (see Section 7.4).

7.2.6 Selection of Higgsino Decay Products

The higgsinos can be produced in two different processes at the ILC: chargino and neutralino processes (cf. Section 5.1.2). These two processes can be separated from each other by selecting the proper decay modes (cf. Section 5.1.3). The selection procedure of these processes are explained in Sections 6.2.1 and 6.3.1. The selection of the higgsino decay products in case of real experiment can be affected by several issues explained in the previous sections concerning the analysis steps of the higgsino samples.

The major issue is the particle identification which can be improved by the dE/dx (cf. Section 7.2.5.1) and cluster shapes (cf. Section 7.2.5.2). Therefore, the decay products of the higgsinos should have sufficient momentum to reach the TPC and calorimeters to be able to use the mentioned methods for particle identification.

The other issue is the $\gamma\gamma$ overlay which can be suppressed using the vertex information (cf. Section 7.2.3.1). The $\gamma\gamma$ overlay has a significant influence on the number of the particles in the final state, therefore the suppression of this background particles is important as well for the selection of higgsino decay products. Thus, the tracking of vertex detector should be taken into account in the selection of the tracks. However, in the DBD software versions, the VTX information, the so-called silicon hits have not been considered as a criterion in the selection of the tracks. The investigation of the tracking in the DBD software and possible updates with the inclusion of silicon hits will be discussed in the next section.

7.3 Tracking of Low Momentum Particles

7.3.1 Tracking in DBD

The tracking efficiencies of the DBD versions shown in Figures 4.11 and 5.14, were obtained considering the tracks stemming from a region of $R_{\text{trk,vtx}} < 10\,\text{cm}$ around the IP, within a polar angle of $\cos\theta < 0.99$, and with a transverse momentum of $p_t > 100\,\text{MeV}$. While assigning a track as found, 90% of the hits are required to belong to the same true particles. The resulting efficiency is shown in Figure 7.8 as a function of p_t and $\cos\theta$ with blue markers. The figure shows that the DBD efficiency works well even for low momentum particles. But, the VTX tracking is needed as well for the higgsino analysis as explained in Section 7.2.6. Because of that the criteria of the DBD tracking have been updated including the VTX/silicon hits.

The updated DBD tracking algorithm is shown in Figure 7.8 with red markers. In this criterion, the p_t cut is removed and the region around the IP is reduced to $R_{\text{trk,vtx}} < 10\,\text{mm}$, which still

covers the vertex of the higgsino-like charginos. This is important in order to distinguish the signal events and $\gamma\gamma$ overlay events. The tracks with 75% purity and having at least three silicon hits $N_{\text{SiHit}} \geq 3$ are assigned as found. The updated criteria, especially the requirement of the silicon hits, reduces the tracking efficiency for low momentum particles by a significant amount.
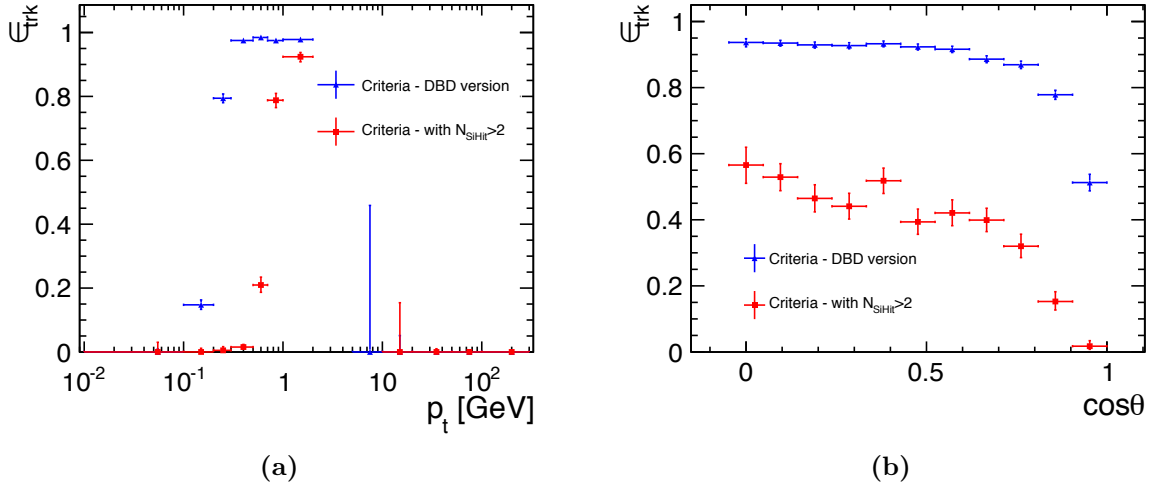

(a)   (b)

Figure 7.8 Tracking efficiency comparison between the criteria used at the time of Technical Design Report and the criteria used in the updated version as a function of (a) p_t and (b) $\cos\theta$. The blue markers show the tracking efficiency using DBD criteria, while the red markers indicate the tracking efficiency using new criteria including $N_{\text{SiHit}} > 2$,which is used in the following figures. Figure is adapted from Ref. [179].

To understand the reason behind the reduction of the tracking efficiency for low momentum particles, the explanation of the applied algorithm would be instructive. In the DBD ILD standard tracking, the whole VTX and SIT are divided into 80 small regions with $4.5°$ as seen in Figure 7.9a. To create track seeds, there should be 3 hits within the determined region. When there are 3 hits, they are combined to create track seeds as long as a simple helical fitting succeeds (cf. Section 7.1.1). And then they are extrapolated and combined to generate a so-called silicon track [169]. One of the disadvantages of this method for low p_t tracks is that since the tracks with low p_t curl, the determined region is too narrow to have 3 hits (for details see Ref. [169]), which reduces the tracking efficiency for low p_t tracks.

Because of that, there are ongoing studies to improve the tracking efficiency of low momentum particles. The ongoing studies and their effects on the number of background tracks are explained in the following.

7.3.2   Alternative Methods for Tracking of Low p_t Particles

The standard DBD tracking method gives unsatisfactory results for the low p_t tracks as explained above. Therefore, the performance of vertex tracking needs to be optimised for low momentum tracks. In order to optimise the vertex tracking performance, two alternative methods are being

investigating under the ILD optimisation studies. These are FPCCD track finder [169] and Cellular Automaton (CA) tracking algorithm using Mini-Vectors [121].

FPCCD track finder is one of the alternative approaches to overcome this disadvantage. In this method, firstly the hits on the outer layer are determined shown with a red circle in Figure 7.9b, and the region for track seeding is optimised for tracks with $p_t > 0.18\,\text{GeV}$, indicated with dotted lines [169]. Then tracks are searched for within this window, which provides a reconstruction of low p_t tracks down to $180\,\text{MeV}$.

(a) DBD ILD Tracking

(b) FPCCD Track Finder
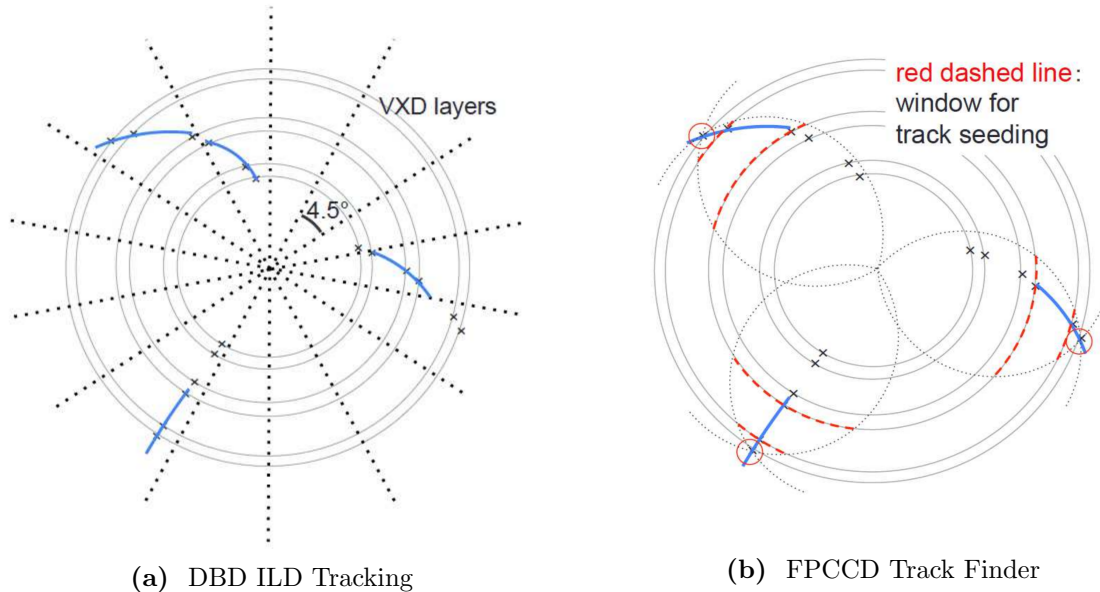
Figure 7.9 (a) DBD ILD Tracking Method (b) FPCCD Track Finder Method. Figure taken from Ref. [169].

The mini-vector tracking method is based on CMOS technology of VTX detectors with double sided layers which provide two hits per layer as described in Section 4.3.1.1. Instead of considering each point as separate hit, they can be combined in order to create the so-called mini-vectors. Then, the tracks are constructed by connecting the mini-vectors using a Cellular Automaton algorithm [121] which is also used for FTD tracks as explained in Section 7.1.1. The algorithm connects mini-vectors if the angle between them is smaller than 10° [182]. The details about construction of mini-vectors and the track creation from them are presented in [121].

7.3.3 Tracking Efficiency and Background Tracks

The layers of the DBD vertex detector have different time resolutions as represented in Table 7.1, since the sides of the first layer are optimised for high spatial resolution and fast readout while the other layers are optimised for power consumption as explained in 4.3.1.1. The longer readout time will store many hits on the sides of the layers which will increase the number of possible mini vectors such that determination of a real track will be difficult. Therefore, the Cellular Automaton tracking algorithm requires fast readout for at least one side of the layers

compared to the DBD VTX detector. Because of that, a new VTX detector with fast readout is considered in the studies related with the mini-vector tracking as indicated in Table 7.1. The table shows the spatial and time resolution of the layers for both DBD VTX and Fast CMOS VTX as well as the ideal VTX detector with 1 BX time resolution of 0.6 ns for each layer. For the spatial resolution of an ideal vertex detector, the DBD resolutions are considered since the spatial resolutions for those time resolutions have not been studied yet. All mentioned three tracking

VTXD types	DBD VTX		Fast CMOS VTX		Ideal VTX (1 BX)	
Layers	$\sigma_{spatial}(\mu m)$	$\sigma_{time}(\mu s)$	$\sigma_{spatial}(\mu m)$	$\sigma_{time}(\mu s)$	$\sigma_{spatial}(\mu m)$	$\sigma_{time}(\mu s)$
Layer 1	3/6	50/10	3/6	50/2	3/6	0.6/0.6
Layer 2	4	100/100	4/10	100/7	4	0.6/0.6
Layer 3	4	100/100	4/10	100/7	4	0.6/0.6

Table 7.1 Vertex detector types considered in the optimisation of tracking including a comparison with the one used in the DBD. The last columns shows the case where only 1BX of pair background is overlaid at each layer. For the spatial resolution of an ideal vertex detector with 1 BX time resolution, the DBD spatial resolutions are considered.

algorithms, DBD, CA and FPCCD, are studied for one of the higgsino samples by taking 1000 events from the chargino signal of dM770 scenario. The tracking efficiency comparison of these algorithms for the higgsino sample including pair background for fast CMOS VTX detector are shown in Figure 7.10. The plots in the figure were created considering the criteria described in the beginning of this section, which can be called as the updated criteria: for selection; $|\cos\theta| < 0.99$, $R_{trk,vtx} < 10\,mm$, and for assigning them as found $N_{SiHit} \geq 3$, $\pi > 75\%$. Those which are not fulfilling the second set of the criteria are considered as background tracks, which will be explained in the following.

Figure 7.10 shows the tracking efficiencies obtained after following these criteria as a function of transverse momentum and $\cos\theta$ for the chargino sample. As explained before, the figure indicates that the DBD tracking does not have a high efficiency for low p_t tracks. However, the alternative tracking methods the CA and FPCCD tracking give much better results than the standard DBD tracking method. In particular, the CA tracking method provides the highest efficiency. The CA tracking is able to reconstruct tracks with $\sim 90\%$ for an angular region $|\cos\theta| < 0.8$, while the efficiency within the same region is higher than 80% for FPCCD tracking. One should note that, even though tracking algorithms seem to be able to reconstruct tracks below $\sim 0.1\,GeV$ momentum, those tracks can not reach the TPC and calorimeters, which are necessary for the particle identification.

In the presence of pair background, tracks arising from e^+e^--pairs need to be taken into account. These background tracks can stem from either back scattering hits, fake tracks, or real tracks from pair background. Figure 7.11a presents the background tracks per event from all sources as a function of momentum for different tracking algorithms using fast CMOS VTX detector. As seen from the figure, the DBD tracking algorithm produces on average $N_{trk,bkg} \approx 20$ background tracks in the low p_t region where the signal events lie, which is prohibitive for the higgsino analysis expecting a few tracks in the final state. The new CA algorithm which gives very nice results
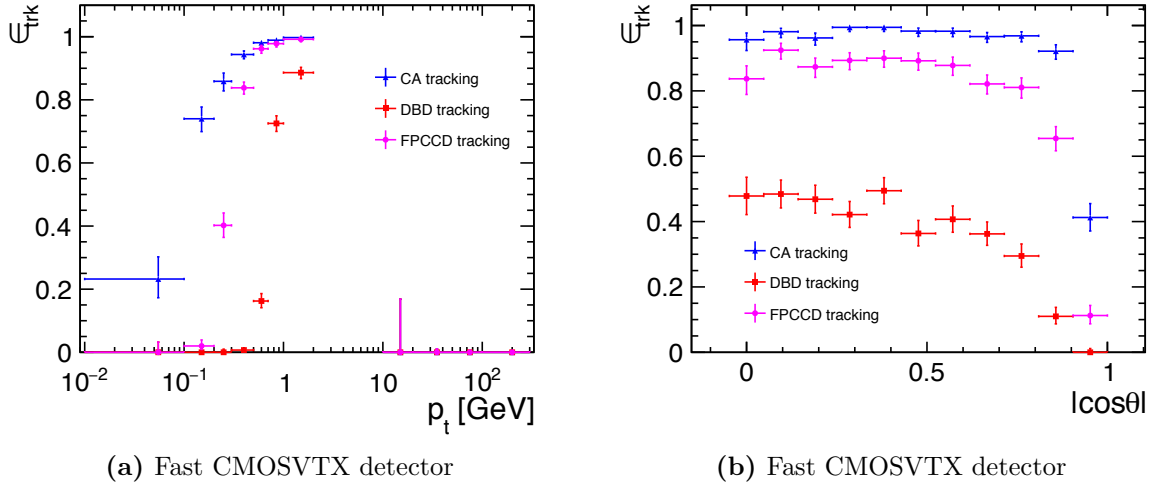
(a) Fast CMOSVTX detector   **(b)** Fast CMOSVTX detector

Figure 7.10 Tracking efficiency of low p_t tracks of a higgsino sample for three different silicon tracking algorithms using fast CMOS vertex detector with time resolution of $50/2\,\mu$s for the first layer and $100/7\,\mu$s for the others. Considered algorithms are Cellular Automaton (CA) using mini-vectors (blue), Standard DBD algorithm (red), and FPCCD algorithm (pink). Tracking efficiency is shown (a) as a function of transverse momentum of charged particles, and (b) as a function of $\cos\theta$. 1000 events from the chargino sample of dM770 scenario are studied as an example. Figure adapted from Ref. [179].

for the tracking efficiency of low $p_t(\,<1\,\mathrm{GeV})$ tracks produces even more background tracks, but in the very low p_t region. Considering the current p_t cut of the tracks of $0.2\,\mathrm{GeV}$, the DBD and CA algorithms give almost same number of background tracks, which is also nearly same with the FPCCD tracking algorithm.

In order to investigate whether the number of the background tracks could be reduced, in addition to optimisation of the tracking algorithm, different time resolution options per layer are studied as well [179]. In Figure 7.11b, the number of background tracks per layer for an ideal VTX detector with a time resolution of 1 BX is shown. As seen from the figure, the number of background tracks in very low p_t region produced with the CA tracking algorithm are reduced significantly, while the number of the background tracks does not change dramatically for other algorithms. The reason is the different approaches followed in the pattern recognition process. The DBD and FPCCD tracking require SIT hits only from the outer layer of the vertex detector, which is less occupied by the pair background hits. However, the CA algorithm based on a different approach, where the hits from the highly occupied inner layers of the vertex detectors are taken into account. Therefore, the CA algorithm gives rise to more pair background tracks compared to the DBD and FPCCD tracking in the case of fast CMOS VTX detector. When one considers the ideal case with 1 BX, since the number of the background hits on the VTX detector layers is significantly less, most of the background tracks stem from the TPC tracks [179].

With the comparison of three tracking algorithms, and two vertex detector options, a few conclu-
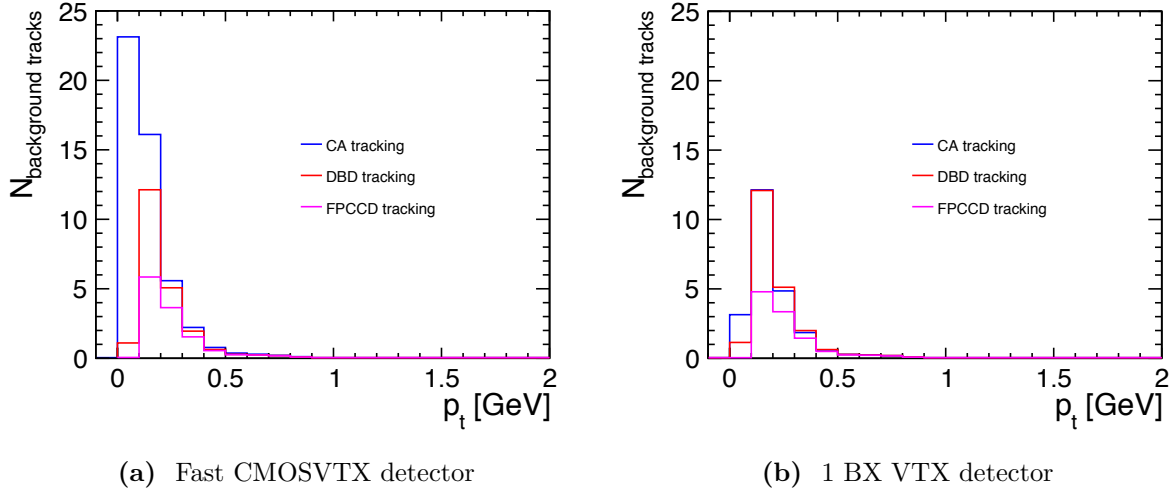
(a) Fast CMOSVTX detector

(b) 1 BX VTX detector

Figure 7.11   Background tracks per event arising mainly from overlaid events for different tracking algorithms. (a) Using fast CMOS VTX detector with time resolution of $50/2\,\mu$s for the first layer and $100/7\,\mu$s for the others, (b) Using an ideal VTX detector with 1 BX time resolution. Figure adapted from Ref. [179].

sions can be drawn. One of the conclusions is that the usage of CA algorithm with mini-vector would save most of the tracks and give the best tracking efficiency. This algorithm causes high background rate per event ($N_{\mathrm{trk,bkg}} \sim 20$) at very low p_t; however they can be suppressed by improving the vertex detector time resolution as seen from Figure 7.11b, or applying a cut on $p_t < 0.2\,\mathrm{GeV}$. In order to make this option feasible, either vertex detectors with 1 BX time resolution needs to be build, or one should live with the cut on $p_t < 0.2\,\mathrm{GeV}$, which might reduce the amount of signal events in the higgsino case. On the other hand, to be able perform the required particle identification for low momentum particles, the particles should have a certain momentum. Therefore, cutting the events including final state particles with $p_t < 0.2\,\mathrm{GeV}$ away would be fine. The second main conclusion is the usage of less efficient FPCCD tracking algorithm resulting in almost two times less background tracks ($N_{\mathrm{trk,bkg}} \sim 10$) even with the fast CMOS VTX detector having time resolutions of $50/2\,\mu$s for the first layer and $100/7\,\mu$s for the others. In both options, even with 1 BX VTX detector, there is a significant number of background tracks, that should be suppressed in the analysis. These can be suppressed as explained in Section 7.2.3.

7.4 μ and π Identification Using Cluster Shape Variables

In Section 7.2.5.2, it has been introduced that the separation of the reconstructed low momentum μ and π can be done using their different cluster shapes. Before investigating the cluster shapes in detail, the information about the position of the clusters would be instructive. Figure 7.12 indicates the cluster position of the reconstructed particles identified as pions in terms of radius versus z position of the cluster centre of gravity. The blue boxes show the pions if they are correctly identified, while the red boxes for the pions which actually should have been identified
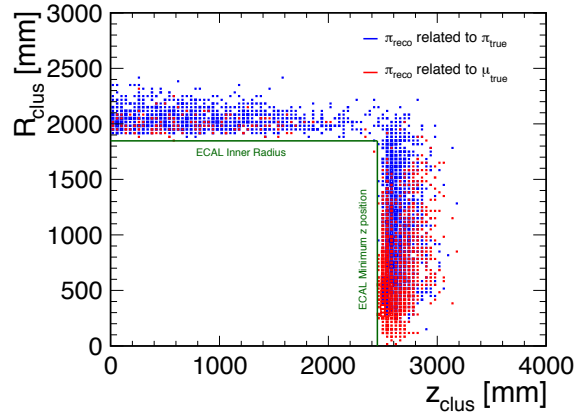
Figure 7.12 A histogram of the radius of the cluster centre of gravity versus the z position of the cluster centre of gravity, which indicates the direction of the reconstructed pions of the chargino sample, which are coming from either true pions or true muons. The blue boxes represent the identified pions which are originally pions, while the red boxes show the identified pions which are originally muons. The green lines show the ECAL inner radius, and minimum z position of the ECAL. The z-axis of the histogram is fixed to the maximum value of the muon distribution.

as muons. The green lines denote the inner radius and minimum z position of the ECAL used in the geometry design of the DBD reconstruction. It can be seen that both μ and π deposit their energy in the same area and mostly in the endcap region, especially muons as can be seen from the redness of the plot in that region.

In order to investigate the behaviour of low momentum μ and π, event displays can be helpful. Figure 7.13 shows event displays of an event with $\widetilde{\chi}_1^+ \widetilde{\chi}_1^- \gamma \rightarrow \mu\nu_\mu\pi\gamma$. Figure 7.13a indicates four particles in total: one π, one μ and two photons (one of them is a hard ISR photon, while the other one is a soft photon). The charged particles are presented with both the Marlin track and the Pandora cluster information. The Marlin tracks includes the actual hits shown with points, and the fit shown with a white line. The seen two curling tracks correspond to μ and π from left to right. The hard ISR photon is displayed in front of the tracks including just Pandora cluster information. The Pandora cluster also shows the centre of gravity of the cluster and the associated errors. The remaining soft photon is clustered in the very forward region close to the muon (left). The event display indicates that the low momentum μ and π curl due to the magnetic field, travel along the magnetic field, and hit the endcap region of the detector. This is a typical behaviour for such low energetic charged particles.

In the second row of the figure, the zoomed in versions of muon and pion signatures show the expected difference on the shapes of the corresponding clusters. The μ leaves a signature as MIP track, while the π leaves a signature as hadronic shower. The shapes of the μ and π clusters are illustrated in Figure 7.14.

To investigate the differences in detail, pure μ and π samples were generated using the particle gun feature of `Mokka` (cf. Section 5.6). Since the structure of the cluster shapes changes with
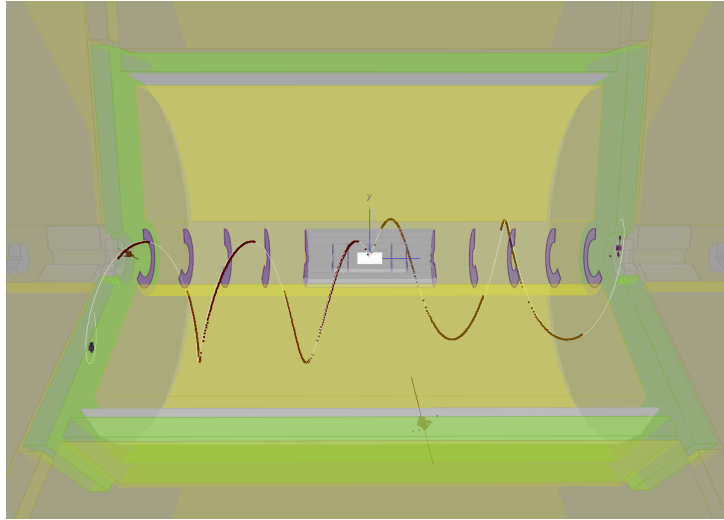
(a) An event including both a low momentum muon and pion ($\widetilde{\chi}_1^+ \widetilde{\chi}_1^- \gamma \to \mu\nu_\mu\pi\gamma$). The curling track on the left corresponds to a muon, and the right one corresponds to a pion. The clustered hits without track seen in front of the tracks and in the middle side of the sketch corresponds to the ISR photon.
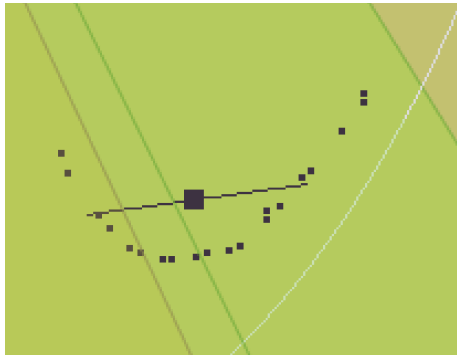
(b) A muon cluster: a MIP track.
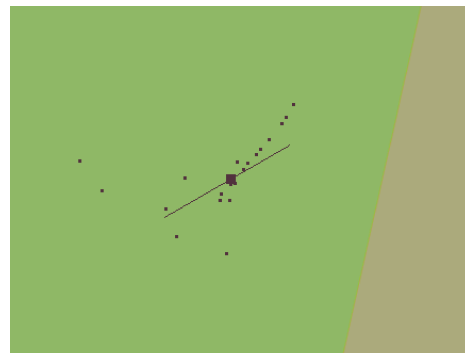
(c) A pion cluster: a shower

Figure 7.13 (a) An event display of an event including both a muon and a pion which have low momentum ($\widetilde{\chi}_1^+ \widetilde{\chi}_1^- \gamma \to \mu\nu_\mu\pi\gamma$). In the figure, the Marlin tracks and the Pandora cluster are displayed. Marlin tracks include both the actual hits represented with points, and the fit results presented with white lines. Pandora clusters indicate the centre of gravity and the associated errors. (b) Zoomed into a pure muon cluster. (c) Zoomed into a pure pion cluster.

the momentum, in particular for the low momentum region, 10000 μ and 10000 π events were generated for 19 different momenta starting from $0.2\,\mathrm{GeV}$ up to $2\,\mathrm{GeV}$ with an interval of $0.1\,\mathrm{GeV}$ using the same versions of the softwares as the full simulation described in Section 7.2, which are `v01_16_02` of `ILCSoft`, `00_00_03` version of `Mokka` for the ILD detector of `ILD_o1_v05` .

One important point in the separation of the π and μ signature is that the pions can also decay to muons before they reach the detector. In order to avoid this complication arising due to decaying of particles, the particle gun samples are shot directly to the ECAL. Therefore, the
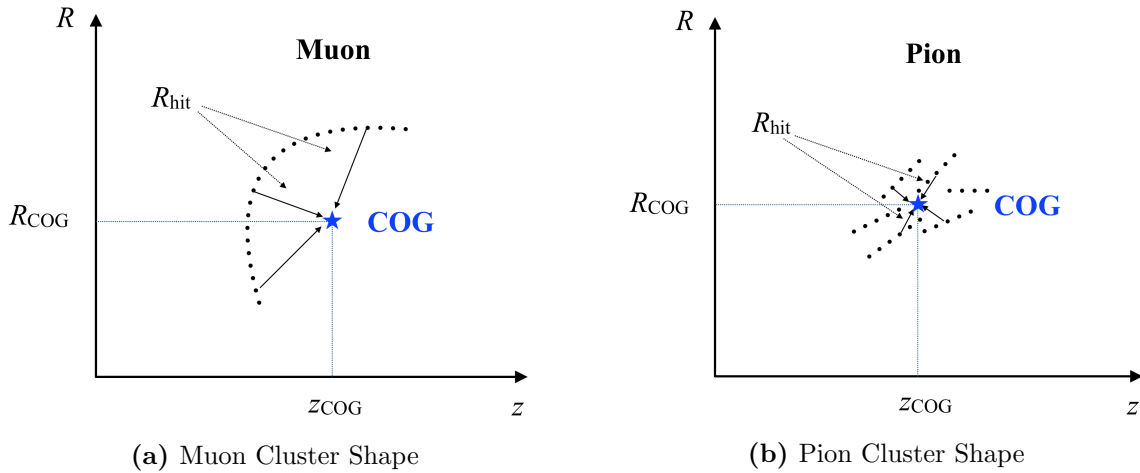
(a) Muon Cluster Shape   **(b)** Pion Cluster Shape

Figure 7.14 Sketch of the cluster shapes of low momentum muon and pion, and demonstration of the radius of the hits.

tracking information is ignored in this investigation. The other key point is the position where the muon particles hit the calorimeter. The low momentum muons as shown in Figure 7.12 goes mostly towards the endcap. Because of that, the particle gun particles are shot towards to the endcap of the ECAL.

The procedure followed in the generation of pure μ and π samples is illustrated in Figure 7.15 and can be explained as follows: the particles were shot directly to the ECAL endcap by keeping the z position of the gun fixed. The x and y positions of the gun were simultaneously changed by a certain step size. The scanned values of x and y are shown in Figure 7.16a. The shooting direction of the gun was uniformly smeared over the polar and azimuthal angles by $90°$ and $180°$, respectively. This is displayed in Figure 7.16b. The polar angle θ is determined to cover the shown octant of the detector in Figure 7.15, corresponding to only positive values of x, y and z positions of the gun. However, due to the uniform smearing of the azimuthal angle, the particle can be shot in the direction of negative x values which results in negative ϕ angle in a range $\phi = [-90, \; 0]$.

The reconstruction efficiency of the particle gun particles is depicted in Figure 7.17 as a function of true momentum of the particles from $0.2\,\text{GeV}$ to $2\,\text{GeV}$. The reconstruction efficiency calculated using the following formula:

$$\epsilon^{\pi/\mu} = \frac{\text{Number of true } \pi/\mu \text{ reconstructed at all}}{\text{Number of true } \pi/\mu} \; . \tag{7.1}$$

The figure shows that the efficiency to reconstruct PFOs using `PandoraPFA` is decreasing as the momentum decreases. Especially in the very low momentum region it goes down to 30-40%, which is not sufficient. The obtained efficiency seems worse than the one shown in Figure 7.5b for the Pandora PFOs. The difference between two cases is that in Figure 7.17 tracks are not taken into account. Therefore, the particles are reconstructed only if they have any cluster. However, the `PandoraPFA` reconstructs the particles when they do not have any cluster as well,

if there is any track. The possibility to reconstruct the particles using their track could explain the seen difference between Figures 7.5b and 7.17. In order to compensate for the effect of this lack of reconstructed particles in the separation, more than 10000 μ and π are generated such that 10000 reconstructed π clusters and 10000 reconstructed μ clusters were used in this step of the analysis.

7.4.1   Discriminating Variables

After the generation of the pure μ and π samples, as a next step four discriminative variables were determined as will be explained below. The distribution of the input variables are shown in Figure 7.19 for the lowest $(0.2\,\mathrm{GeV})$, middle $(1.0\,\mathrm{GeV})$ and highest $(2.0\,\mathrm{GeV})$ momenta (for all momenta see Appendix D). The input variables were plotted using the information of the hits which form the Pandora PFOs for 10000 reconstructed π clusters and 10000 reconstructed μ clusters as described above. In the low momentum region, the number of reconstructed particles, if there are any, is mostly equal to one, whereas the reconstructed number of particles increases when the momentum of the true particle goes up. To take this into account, the highest energetic cluster was considered as a reconstructed particle corresponding to a true particle. In the following, the definition and interpretation of the input variables will be explained in detail.

Energy of a cluster over momentum of a track: This variable is the most important one which shows the key properties of the low momentum μ, π behaviour. It presents a ratio of the energy of a cluster and the momentum of a track associated to the cluster.

$$\mathrm{E_{clus}/p_{trk}} \quad = \quad \frac{\text{Energy of a cluster}}{\text{Momentum of a track associated to the cluster}} \tag{7.2}$$
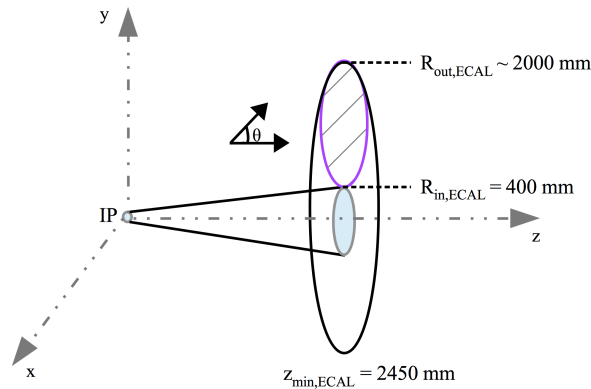

Figure 7.15 Demonstration of a place of the detector where the particle gun was shot. The purple circle shows the region of a detector shot. z position of the gun was fixed to the minimum z position of the ECAL endcap: $z = z_{\mathrm{min,ECAL}} = 2450\,\mathrm{mm}$, while x & y positions were scanned starting from the inner radius of the ECAL endcap: $400\,\mathrm{mm} < x_{\mathrm{ECAL}} \& y_{\mathrm{ECAL}} < 1200\,\mathrm{mm}$, with a defined step size according to number of events. The angles were uniformly smeared by $\theta = 90°$ and $\phi = 180°$.
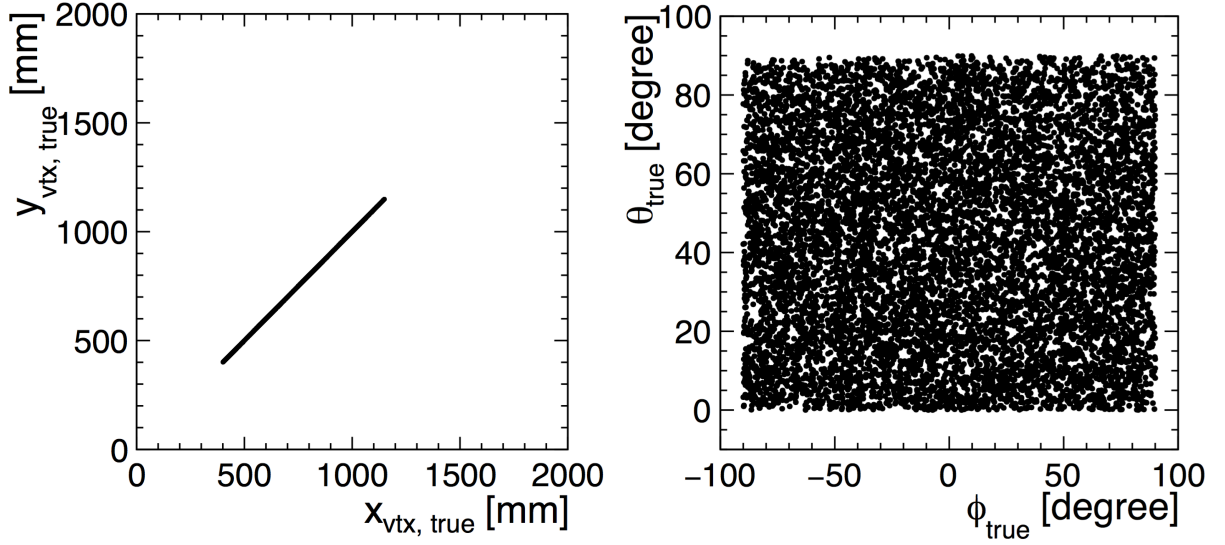
160

(a) The x and y positions of the particle gun

(b) θ versus ϕ distribution of true particles

Figure 7.16 The position and angular distribution of the 10000 true particles produced by particle gun (muon sample for $p = 1\,\text{GeV}$ is shown as an example). Half of them are used for training and the rest for testing. (a) The scanned x and y positions of the particle gun corresponding to the production vertex position of the true particles. It shows that the x and y positions are scanned between ~ 400 and ~ 1200 mm simultaneously. (b) The scanned region of the θ and ϕ angles. θ is scanned from $0°$ to $90°$, while ϕ is scanned over $0° \leqq \phi \leqq 90$ and $270° \leqq \phi \leqq 360$ shown in the figure from $-90°$ to $0°$ uniformly.
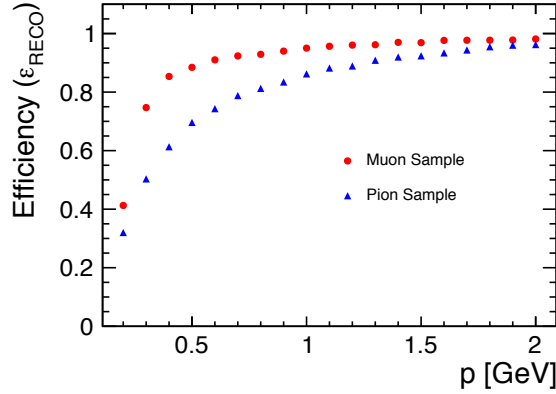
Figure 7.17 Reconstruction efficiency of Pandora PFOs for the generated 10000 μ and 1000 π events. The red points show the muon reconstruction, while the blue triangles show the pion reconstruction.

where the momentum of true particles p_{true} is used instead of the track momentum in case of the particle gun samples due to lack of tracking information.

The value of this variable is expected to be nearly equal to one for electrons and hadrons, while it is lower than one for muons since only small fraction of their energies are deposited on the calorimeter system. Hence, this variable is used as a discriminating variable for high momentum particles. Although it is a useful variable for high momentum μ and π separation, in the case of low momentum the expected value of the variable changes depending on where the particles deposit their energies mostly. As explained before, the low momentum particles may be stopped in either ECAL or HCAL. The responses of the electromagnetic and hadronic calorimeters for an incoming particle with the same energy are different due to the properties of the active materials of the calorimeters. The energy response of the ECAL for a hadron is less than it actually is, while the HCAL's response for a lepton corresponds to higher energy than its actual energy. Because, the ECAL and the HCAL are calibrated to respectively electromagnetic and hadronic response. Therefore, if the low momentum pions deposit most or all of their energies in the ECAL, the measured energy will be less than expected, while the low momentum muons deposited most of their energies in the HCAL will have higher energies than actually it is. This is the reason why muons with sufficient momentum to reach the HCAL have a value of $E_{\text{clus}}/P_{\text{trk}}$ larger than 1 as seen in Figures 7.19b and 7.19c. Due to the low momentum of the pions, the significant amount of their energy is deposited in the ECAL, therefore the value of $E_{\text{clus}}/P_{\text{trk}}$ for pions is less than one in all three momenta.

Depth of a cluster: This variable is a momentum-dependent variable which can be useful only for low momentum particles which go through the endcap. The definition of the depth of a cluster is

$$D_{\text{clus}} \quad = \quad \frac{z_{COG} - z_{\text{start}}}{\cos \alpha} \tag{7.3}$$

where z_{COG} and z_{start} are the z position of the centre of gravity (COG) and starting point of a cluster, respectively. α is the incident angle of the particle. The usage of the depth variable takes into account the particles in the same z position but having different incident angles. The $\cos \alpha$ is calculated by

$$\cos \alpha \quad = \quad \frac{z_{\text{COG}} - z_{\text{start}}}{\sqrt{(x_{\text{COG}} - x_{\text{start}})^2 + (y_{\text{COG}} - y_{\text{start}})^2 + (z_{\text{COG}} - z_{\text{start}})^2}} \, . \tag{7.4}$$

where "COG" denotes the centre of gravity, and "start" represents the starting position of the cluster. In the current study, it is obtained from the production vertex information of the Monte Carlo particles, since the tracking information is ignored. The production vertex shows the point where the true particles are created. In the case when the gun is shot directly to the calorimeter, it shows the starting point of the cluster. In a real experiment, it can be calculated using the tracking information by determining the end position of the tracks.

Considering the equations of D_{clus} and $\cos \alpha$, it is seen that the depth parameter can be calculated using a simple distance formula between starting point of a cluster and centre of gravity of the cluster. A sketch of the depth of a cluster is displayed in Figure 7.18.

At any energy, the muons will travel longer distances compared to the pions since they lose only minimum energy as they travel through the detector. This property of the muons can be seen clearly from the plot of the variable especially in Figures 7.19b and 7.19c.
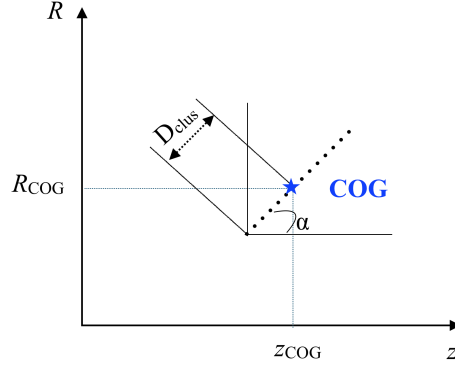
Figure 7.18 A sketch showing the depth of a cluster: distance between the centre of gravity of a cluster and the starting point of a cluster.

Mean value of the radius of the hits: Another important variable which determines the shape of the clusters is the radius of the hits with respect to the COG of the cluster. The variable is calculated with the following formula:

$$R_{\mathrm{hit}_i} = \sqrt{(x_{\mathrm{hit}_i} - x_{\mathrm{COG}})^2 + (y_{\mathrm{hit}_i} - y_{\mathrm{COG}})^2} \tag{7.5}$$

where x_{hit_i}, y_{hit_i} denotes the x and y position of the hit$_i$, while x_{COG}, y_{COG} denotes the x and y position of the centre of gravity of a cluster. The radius of the hits is demonstrated in Figure 7.14, which shows the difference between the distribution of the radius for μ and π. As can be seen from the figure, the value of the radius is larger for muons. However, instead of this variable the mean and RMS values of the distributions were chosen as discriminative parameters since they change per cluster. The mean value of it is:

$$\langle R_{\mathrm{hit}} \rangle = \frac{\sum_{i=0}^{N_{\mathrm{hits}}} R_{\mathrm{hit}_i}}{N_{\mathrm{hits}}} \, . \tag{7.6}$$

Due to feature of the cluster shapes depicted in Figure 7.14, the mean value of the radius of the hits is expected to be large. This can be seen from the related plot of Figures 7.19b and 7.19c.

RMS value of the radius of the hits: The root mean square (RMS) of the radius of the hits is the last discriminative variable which can be calculated as follows:

$$R_{\mathrm{hit,RMS}} = \sqrt{\frac{\sum_{i=0}^{N_{\mathrm{hits}}} R_{\mathrm{hit}_i}^2}{N_{\mathrm{hits}}}}. \tag{7.7}$$

The value of the variable of muons is expected to be larger than the value of pions as in the case of mean value because of the behaviour of the cluster shapes. This is shown in Figure 7.19 for $1\,\mathrm{GeV}$ and $2\,\mathrm{GeV}$ momenta cases.

In this case, between the $\langle R_{\mathrm{hit}} \rangle$ and $R_{\mathrm{hit,RMS}}$ variables, there is a large correlation as can be seen from the similar distribution of the variables in Figure 7.19. This is mainly because of the

considered formula for the RMS value of the hit radius; however, it could be improved if it is calculated with respect to mean value of the distribution as follows:
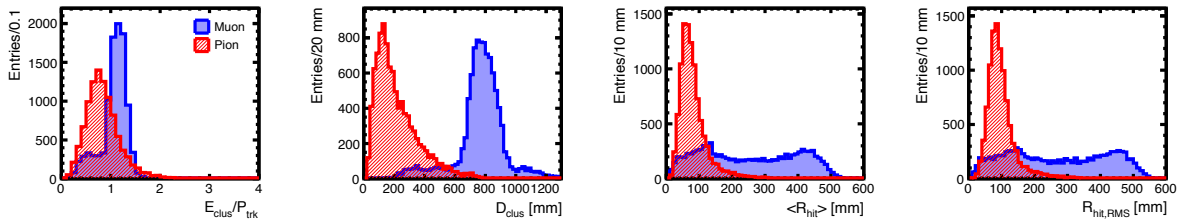
$$R_{\mathrm{hit,RMS}} = \sqrt{\frac{\sum R_{\mathrm{hit}_i}^2}{N_{\mathrm{hits}}} - \left(\frac{\sum R_{\mathrm{hit}_i}}{N_{\mathrm{hits}}}\right)^2}. \tag{7.8}$$
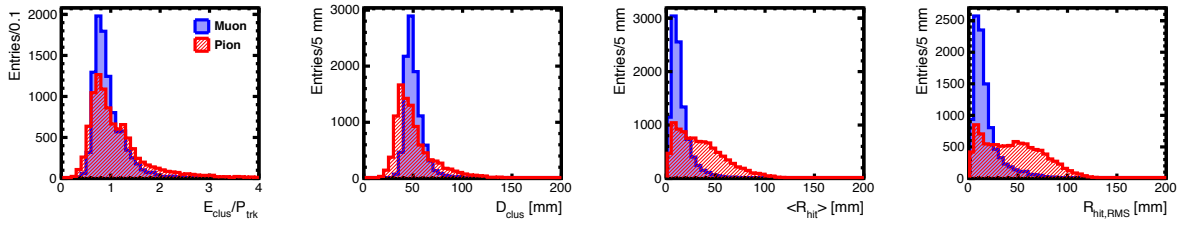
(a) 0.2 GeV Momentum – please take note for different ranges of x-axis from others
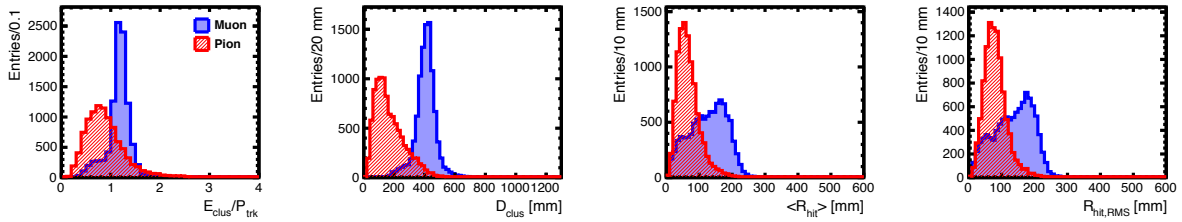
(b) 1.0 GeV Momentum

(c) 2.0 GeV Momentum

Figure 7.19 Input variables for the hits of the Pandora PFO clusters of reconstructed 10000 μ and 10000 π particle gun samples for (a) 0.2 GeV momentum, (b) 1.0 GeV momentum, and (c) 2.0 GeV momentum. The blue histogram shows the signal (muon) distribution, while the red histogram shows the distribution of background (pion).

From Figure 7.19, one can see that the distribution of the variables for both signal (μ) and background (π) nicely differ from each other at higher momenta, however even at 0.2 GeV momentum there are some differences which would allow the separation of the μ and π. One should also note that the discriminating variables strongly depend on the momentum.

7.4.2 Determination of the Multivariate Method

The separation analysis has been performed using the Toolkit for MultiVariate Analysis (TMVA) [183]. TMVA offers a feature to perform different multivariate analysis methods, which helps to choose the best method depending on the analysis. The comparison of the available methods is shown in Figure 7.20 for three different momenta, $0.2\,\text{GeV}$, $1.0\,\text{GeV}$, and $2.0\,\text{GeV}$. It shows background rejection as a function of signal efficiency, where both should get the highest probable values. Therefore, the upper right corner of the plot indicates the best value. The methods are also listed on the plot starting from the best one.

(a) $0.2\,\text{GeV}$ Momentum **(b)** $1.0\,\text{GeV}$ Momentum **(c)** $2.0\,\text{GeV}$ Momentum
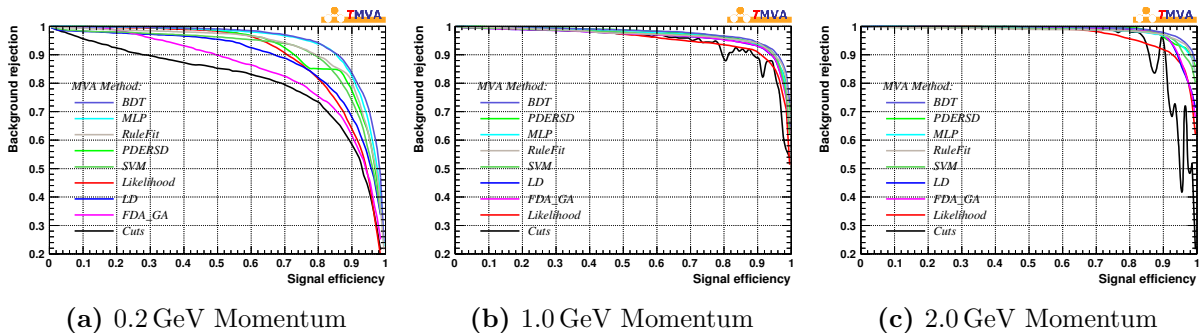
Figure 7.20 Background rejection as a function of signal efficiency for all available multivariate methods in TMVA. The comparison is shown for three different momenta.

As seen from the figure, the Boosted Decision Tree (BDT) method shows the best performance, hence BDT method, which will be explained in the following, is chosen for the separation of the low momentum μ and π.

The Boosted Decision Tree Method

The boosted decision tree method [184, 185, 186] is one of the multivariate analysis (MVA) methods, with a boosting feature of the MVA. Boosting [187, 188] is a common way applied in many MVA methods to enhance the classification by optimally exploiting the available statistics by a reweighting method. A certain MVA method is sequentially applied to reweighted/boosted versions of the existing training data. Then the weighted sum of the samples produced with boosting are taken to obtain the output of the MVA method.

Decision tree (DT) method creates a tree by taking decisions whether the object is signal-like or background-like in each step. A schematic view of a decision tree is shown in Figure 7.21. The existing data constitutes the root node of a tree. Then all the discriminating variables are checked in order to find the best variable denoted by x_i and to determine the cut value which gives the best separation of the signal and background, which is denoted by c1. The events fulfilling the cut condition ($x_i > $ c1) are classified to one node, while the rest of the events are classified to the second node, as can be seen from the first step branches of the tree shown in the figure. In the second step the process of looping over the input variables in order to find the next
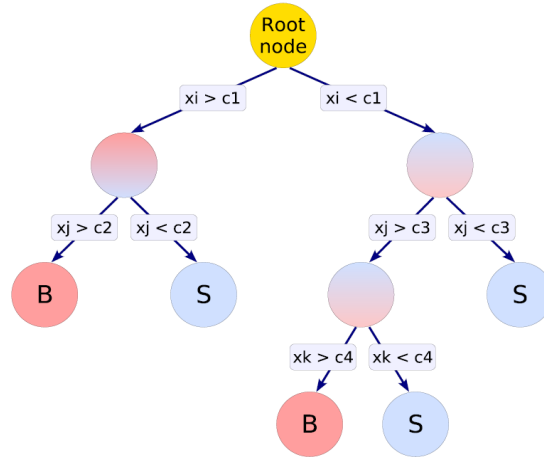
Figure 7.21   A schematic view of a decision tree. Root node represents the sample to be classified. All the discriminative variables, represented by $x_{i,j,k}$, are checked to determine the cut value, shown with $c1, c2, c3, c4$, which gives the best separation of signal and background. This is done until each node reaches a stop criteria. In the final nodes, depending on the majority of the (training) events they are classified as signal events, or as background events. Figure is taken from Ref. [183].

best discriminating variable (x_j) and the cut values (c2, c3) is repeated again. The determined best discriminative variables could be same in the different nodes, while the cut values most probably will be different for each node. For the classified nodes the process is repeated over and over again until each node reaches a stop criterion (minimum number of events required in a final node) [183]. The signal and background events are determined from the final nodes of a tree which are called leaves. The leaves are classified as signal if the majority of the events are signal events, else they are classified as background leaves. This indicates that each leaf has misclassified events as well, i.e. signal events on a background leaf or background events on a signal leaf.

One of the disadvantages of decision trees is that they are sensitive to fluctuations in data. Boosting is a good way to compensate this by creating many trees and taking the weighted average over all trees. In the process of boosting, misclassified events are reweighted and new trees are built using these reweighted events. To explain the process of boosting one of the most common boosting algorithms, the so-called Adaptive Boosting (AdaBoost) [189], will be considered as an example. Let us consider that by means of reweighting the misclassified events, M boosted trees are created. For tree m ($m = 0, 1, .., M$) the weight value α_m is determined by considering the fraction of misclassified events, err;

$$err_m = \frac{\text{sum of weights of the misclassified events}}{\text{sum of weights of all the events}} . \tag{7.9}$$

The weight value of tree m is then calculated by the following formula;

$$\alpha_m = \beta \ln \left(\frac{1 - err_m}{err_m} \right) , \qquad (7.10)$$

where β is the so-called learning rate, which is set to 0.5 as default for Adaboost. Before any reweighting, the events on the original tree, $m = 0$, have weights of $w_i = 1$. Depending on the weight parameter α_m of tree m, each misclassified event in that tree gains a weight of $w_i \rightarrow w_i \times e^{\alpha_m}$, while the correctly classified events have the same weight as before which is $w_i = 1$. The weights of the trees are calculated after the classification of each tree, therefore each tree will have a different weight value.

As a result of the boosting, a given event x might have a different weights in each tree. Therefore, to find the output of the BDT for that event, the output of the event in the mth tree $T_m(x)$, which is $T_m(x) = +1$ if the event is on the signal leaf, or $T_m(x) = -1$ if it is on the background leaf, is multiplied with a weight parameter α_m, and the multiplication is summed over each tree [190]:

$$T(x) = \sum_{m=0}^{M} \alpha_m T_m(x) \qquad (7.11)$$

where $m = 0, 1, ..., M$ is the number of trees, $T_m(x)$ is the output of a decision tree corresponding to tree of m, α_m shows the weight used to create the mth boosted tree, $T(x)$ displays the final output of the BDT for event x.

In general, the weight parameters α_m are determined by the minimisation of the difference between the output of the model $T(x)$ and the true value y obtained from the training sample, which is either $y = +1$ (signal) or $y = -1$ (background) [183, 186]. This difference is represented with a function called loss function $L(T(x), y)$. There are several boosting algorithms with different loss functions. The adaptive boost (AdaBoost) is based on exponential loss $L(T(x), y) = e^{-T(x)y}$. Exponential loss is not robust enough in presence of outliers or mislabelled data points (for instance noisy settings) [183]. A more robust algorithm called Gradient Boost [191] uses a differentiable loss function, the binomial log-likelihood loss, $L(T(x), y) = ln(1 + e^{-2T(x)y})$.

The reweighting algorithm can be differentiated in a straightforward way by applying the minimisation condition to the loss function for AdaBoost [189], but this is not the case for Gradient Boost. In order to minimise the loss function of gradient boosting one has to consider a steepest-descent approach (gradient descent) [186, 191], which is a way to find a local minimum of a function by taking the gradient of the loss function and subtracting it from the output value of the corresponding tree such that after some iterations it will converge to a point where the gradient is zero.

The decision tree method using the second explained boosting algorithm, Gradient Boost, BDTG is used for the particle identification analysis since it gives the best result.

7.4.3   Separation Using Particle Flow Objects

To separate muons and pions, as the first step of the multivariate analysis, input files including the discriminative variables for both signal and background are acquired using the reconstructed 10000 μ and 10000 π events. After that, the samples are trained and tested using the first half of the events for training and the second half of it for testing as default, while creating the weight file of each training. The output values of the applied multivariate method BDTG are shown in Figure 7.22 for three different momenta. The figure shows how many of the events are classified as signal (μ) and how many of them as background (π). The events are separated very well in all three momenta cases, even in 0.2 GeV momentum case.

| (a) 0.2 GeV Momentum | (b) 1.0 GeV Momentum | (c) 2.0 GeV Momentum |
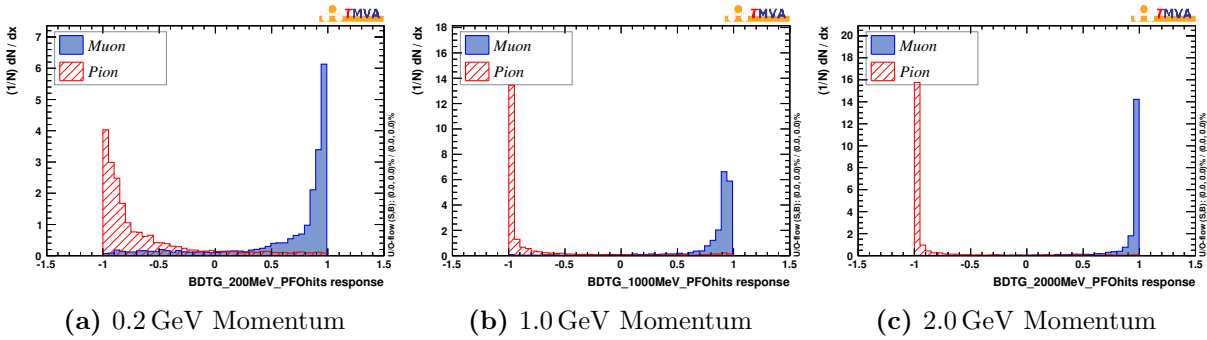
Figure 7.22 BDTG outputs for three different momenta. The blue area displays the distribution of muon (signal) and the red lines show the output values of pion (background).

In the next step, the cut variables were determined using cut efficiency plots shown in Figure 7.23. The default setting of these plots show the cut values for maximum significance $S/\sqrt{S+B}$. However, one can also change the settings to require some fixed signal or background efficiencies. In this step of the analysis, the default settings will be used and cut values which give the maximum significance will be determined for each momentum.

After obtaining the weight files of the training and the cut values, in the application phase of the analysis the existing particle IDs are updated with the new μ and π identification while keeping the others as they are. The performance of the separation is presented by the identification efficiency and misidentification probability defined as follows:

Identification Efficiency of μ:

$$\varepsilon_{\mathrm{ID}}^{\mu} = \frac{\text{Number of true } \mu \text{ reconstructed as } \mu}{\text{Number of true } \mu \text{ reconstructed as either } \pi \text{ or } \mu}, \tag{7.12}$$

Misidentification Probability of π:

$$P_{\mathrm{misID}}^{\pi} = \frac{\text{Number of true } \pi \text{ reconstructed as } \mu}{\text{Number of true } \pi \text{ reconstructed as either } \pi \text{ or } \mu} = 1 - \varepsilon_{ID}^{\pi}. \tag{7.13}$$

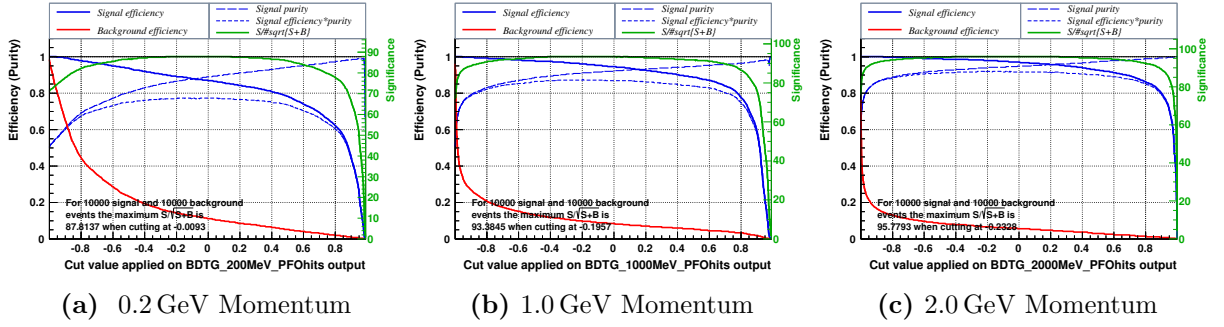**(a)** 0.2 GeV Momentum   **(b)** 1.0 GeV Momentum   **(c)** 2.0 GeV Momentum

Figure 7.23 Cut efficiencies and optimal cut values for three different momenta. It shows the signal and background efficiencies displayed with a blue and red line respectively. The blue dashed lines represent the signal purity and the signal efficiency*purity, while the green line indicates the significance. The cut value shown in the plots are obtained for the maximum significance.

Figure 7.24 depicts these as a function of momentum from 0.2 GeV to 2 GeV including the statistical error calculated with the error propagation of a ratio. For example, the efficiency

(a) ID Efficiency   **(b)** MisID Probability
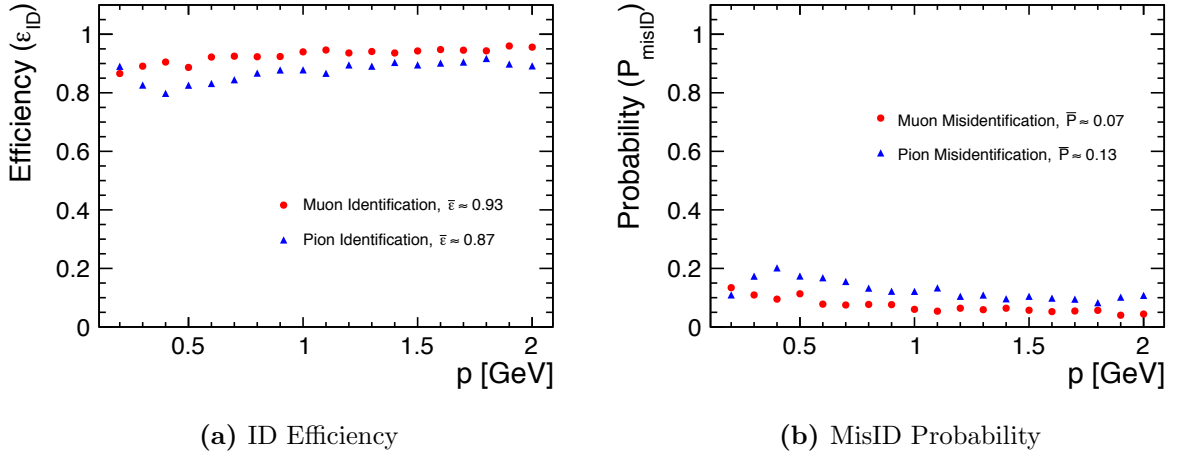
Figure 7.24 (a) Identification efficiencies of μ and π as a function of different momenta, (b) Misidentification probabilities of μ (as a π) and π (as a μ) as a function of different momenta. Red dots shows the muon efficiency, while blue triangles shows the efficiency of pions.

(ε) of muon (signal) identification can be calculated using the number of identified signal and background events as N_{sig}^{ID} and N_{bkg}^{ID}:

$$\varepsilon = \frac{N_{sig}^{ID}}{N_{sig}^{ID} + N_{bkg}^{ID}} \tag{7.14}$$

where $N_{sig}^{ID} + N_{bkg}^{ID} = N_{tot}$. In order to use the error propagation approach for a ratio, the nominator and denominator should be uncorrelated with each other. Thus, the efficiency is

written in terms of uncorrelated parameters:

$$\frac{1}{\varepsilon} = 1 + z \quad \text{with} \quad z = \frac{N_{bkg}}{N_{sig}} . \tag{7.15}$$

This can be differentiated on both sides to give a relationship between the statistical uncertainty on the z ratio and on the efficiency as below:

$$\sigma_\varepsilon = \varepsilon^2 \cdot \sigma_z. \tag{7.16}$$

The statistical precision on z is calculated with a usual error propagation formula for a function depending on two parameters, $z = f(N_{sig}, N_{bkg})$:

$$\sigma_z^2 = \left(\frac{\partial z}{\partial N_{sig}} \right)^2 \cdot \sigma_{N_{sig}}^2 + \left(\frac{\partial z}{\partial N_{bkg}} \right)^2 \cdot \sigma_{N_{bkg}}^2 \tag{7.17}$$

where $\sigma_N = \sqrt{N}$. So, the precision on z is obtained as

$$\sigma_z = z \sqrt{\frac{1}{N_{sig}} + \frac{1}{N_{bkg}}}. \tag{7.18}$$

The resulting statistical uncertainty on the identification efficiency of muons then can be calculated with the following formula:

$$\sigma_\varepsilon = \sqrt{\frac{\varepsilon(1 - \varepsilon)}{N_{tot}}} . \tag{7.19}$$

Even though the errors of the ID efficiencies and misID probabilities are included in the figures, since they are in a few per mille level it is not possible to see them. This means that the variation of the efficiencies with the momentum, in particular a decrease and increase towards to lower momenta around $0.5\,\text{GeV}$ cannot be explained with the statistical error. An explanation would be the transition of the input variables at around $0.5\,\text{GeV}$ as seen in Figure 7.25. It shows the input variables for $0.4\,\text{GeV}$, $0.5\,\text{GeV}$ and $0.6\,\text{GeV}$. Especially for the last two variables it is seen that π and μ have almost the same distribution. The muon distribution moves from the left side of the pion distribution to the right side. Actually, it is expected that μ has large mean and RMS values of radius of hits because of the MIP signature of muons as explained in Section 7.4.1. When one compares the input variables at such low momenta with the ones at higher momenta given in Figure 7.19 for example, one can see that they behave differently which influences the separation of μ and π as seen in the efficiency plots (Figure 7.24).

Nevertheless, it can be assumed that the slight dependency of the efficiencies on the momentum at a negligible level for a first estimate of the impact of the separation. In that sense, the mean value of the distributions can be considered as an overall efficiency to identify particles as μ or π. Figure 7.24 indicates that muons can be identified in average with $\varepsilon_{\text{ID}}^\mu \approx 93\%$ efficiency, while pion identification efficiency is $\varepsilon_{\text{ID}}^\pi \approx 87\%$ in average. The probability of misidentifying a π as a μ is approximately 13%.

(a) 0.4 GeV Momentum

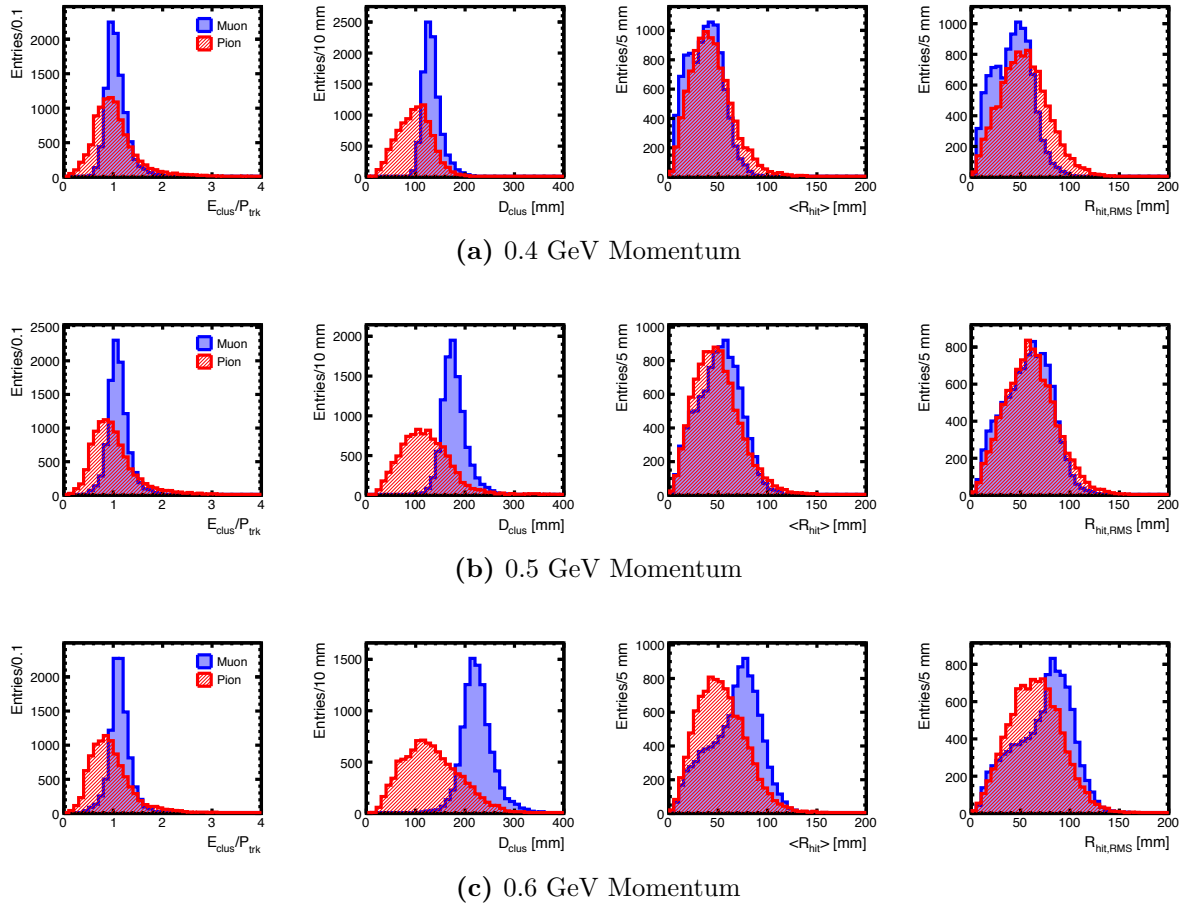**(b)** 0.5 GeV Momentum

(c) 0.6 GeV Momentum

Figure 7.25 Input variables considering hits of the Pandora PFO clusters of reconstructed 10000 μ and 10000 π particle gun samples for (a) 0.4 GeV momentum, (b) 0.5 GeV momentum, and (c) 0.6 GeV momentum. The blue histogram shows the signal distribution which is muon, while the red one shows the background distribution which is pion.

This separation method has been implemented in the existing software under the `PIDTools` package of the reconstruction software of `MarlinReco` in the ILCSoft version of `v01_17_08`. This is the preliminary version, the updated version is currently accessible under the svn head version [192], and will be included in future releases. In the `PIDTools` package there are five algorithms for the particle identification using various methods. The fifth algorithm contains the developed separation method of low momentum μ and π.

7.4.4 An Alternative Reconstruction Approach of Clusters

In Section 7.4.3, it has been presented that the neutral particles cannot be reconstructed with high efficiency using Pandora PFO algorithm, which is optimised for a jet environment. This has already been indicated in Figure 7.17 showing the reconstruction efficiency of the muon and pion

samples using the Pandora PFO algorithm. Since the higgsino samples have low multiplicity events, one can introduce a simplistic approach to investigate what would be achieved with a dedicated low multiplicity clustering. The idea behind this study was to investigate whether these missing reconstructed particles can be saved using this aproach, and what would be the impact of this new approach to the identification. In this approach, instead of using the Pandora PFOs, mainly all the calorimeter hits are utilised. In order to avoid noise hits, a cylindrical region is determined and at least 3 hits were required to be in this region. A crucial point of this approach is that such simplistic approach only works for low multiplicity events like higgsino events; however it will not be possible to apply this approach to high multiplicity events.

Since the particle gun particles are only shot to one of the endcaps of the detector, that region is selected to suppress the noise hits from the other part of the detector. The determination of the region is illustrated in Figure 7.26. The radius of the cylinder $R_{\text{cut,max}}$ is determined from
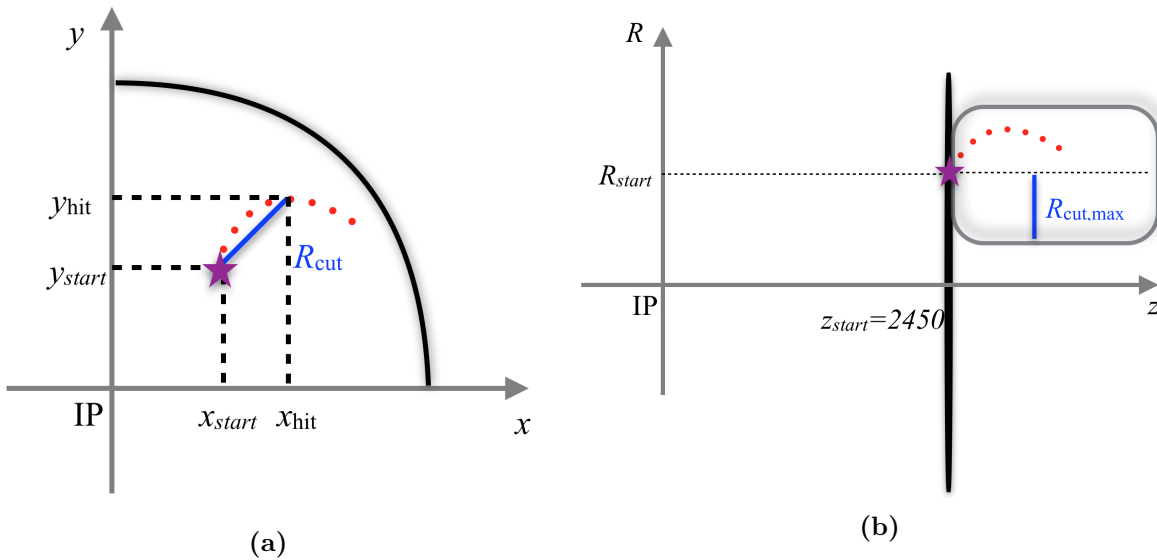

(a)

(b)

Figure 7.26 Sketches illustrating the determination of the region considered around the vertex position of the true particles. The violet star indicates the starting position of the cluster. R_{cut} is the distance between the hit position and the starting point of the cluster in the transverse plane. A cylindrical area is determined around the starting point with a radius of the max value of R_{cut} which is $R_{\text{cut,max}}$. The sketches are not to scale.

the distance between the hit position and the starting point of the cluster (production vertex position of the true particles in this case) in the transverse plane as represented in Figure 7.26a, which is denoted by R_{cut}. The maximum value of this distance is considered as the radius of the chosen cylindrical region as shown in Figure 7.26b. The value of R_{cut} can be calculated with the following formula:

$$R_{\text{cut}_i} = \sqrt{(x_{\text{start}} - x_{\text{hit}_i})^2 + (y_{\text{start}} - y_{\text{hit}_i})^2} \tag{7.20}$$

where x_{start}, and y_{start} are the x and y position of the starting point of the cluster. x_{hit_i} and y_{hit_i} are the x and y position of each hit. The radius of the cluster hits changes depending on

the momentum, hence this value is determined for each momentum separately. However, one should note that the chosen region is very simplistic, it includes almost all the hits which are in the same detector region. To optimise this, one could use the track information to calculate the incident angle, and then determine a cylindrical region around the hits with an angle to the z-axis.

The resulting reconstruction efficiency of a cluster considering all the hits within a determined area including at least three hits is indicated in Figure 7.27. The figure shows much better
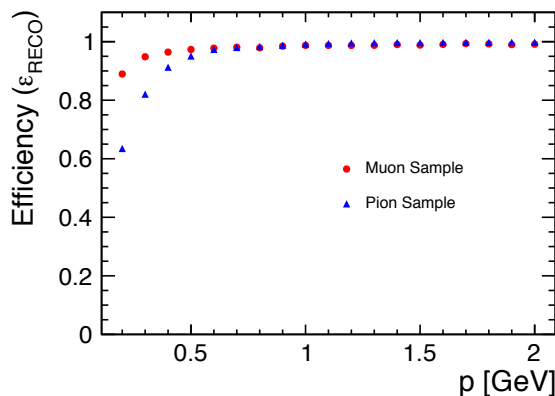
Figure 7.27 Reconstruction efficiency using new approach considering all the hits within a determined region requiring minimum three hits for the generated 10000 μ and 10000 π events. The red points show the muon reconstruction, while the blue triangles show the pion reconstruction.

results compared to the reconstruction efficiency of Pandora PFOs as shown in Figure 7.17.

Contrary to the previous case of considering Pandora PFO clusters, generated 10000 μ and 10000 π events were used since this new approach has a better reconstruction efficiency. Before the calculation of the input variables, the hit selection procedure explained above was executed: the hits remaining outside of the cylinder were ignored, and at least 3 hits were required to be within the selected region. Then the discriminative variables were calculated for those hits, and the obtained input variables are shown in Figure 7.28 for three different momenta, 0.2 GeV (lowest), 1.0 GeV (middle), and 2.0 GeV (highest). In general, the muon distributions look more or less similar to the previous case shown in Figure 7.19, while the pion distributions seem wider towards higher values. For a direct comparison, the input variable distributions are displayed for reconstructed objects created with the `PandoraPFA`, and with the new approach in Figure 7.29 for 1.0 GeV momentum as an example. In this figure both x-axis and y-axis of the input variables obtained for two approaches are set to the same ranges to be able to compare them easily. The figure indicates that the first and second variables $E_{\mathrm{clus}}/p_{\mathrm{trk}}$ and D_{clus} have similar shapes with a slight shift to the right for the pion distributions. The third and fourth variables $\langle R_{\mathrm{hit}} \rangle$ and $R_{\mathrm{hit,RMS}}$ have different shapes, especially for pions. Some of the muon events with small $\langle R_{\mathrm{hit}} \rangle$ and $R_{\mathrm{hit,RMS}}$ have been shifted to higher values as seen from the number of events. The changes in the pion events are more visible; those events with small $\langle R_{\mathrm{hit}} \rangle$ and $R_{\mathrm{hit,RMS}}$ have

(a) 0.2 GeV Momentum

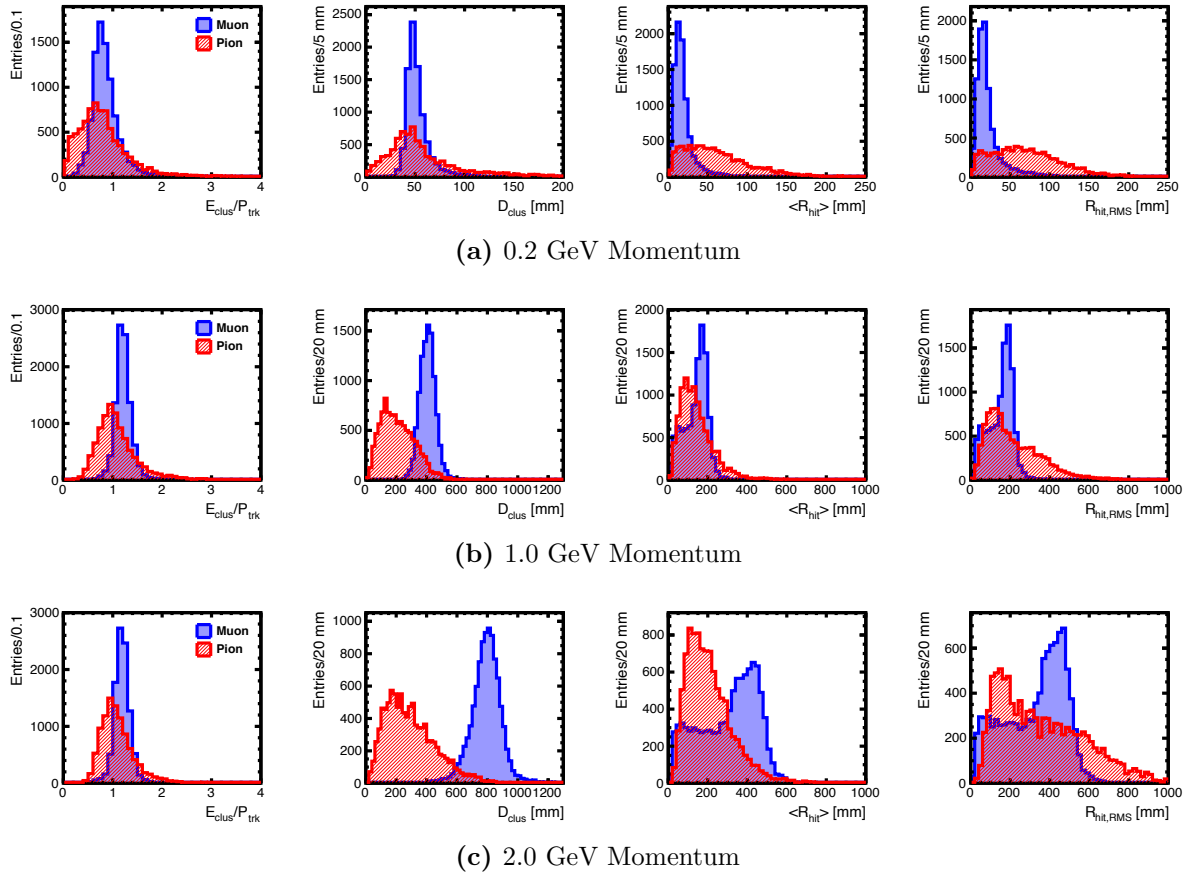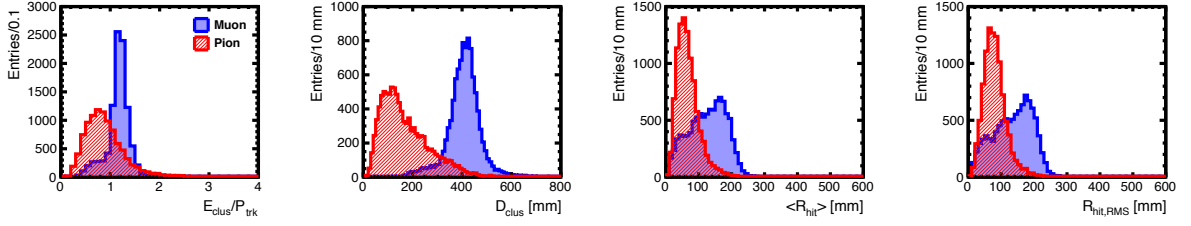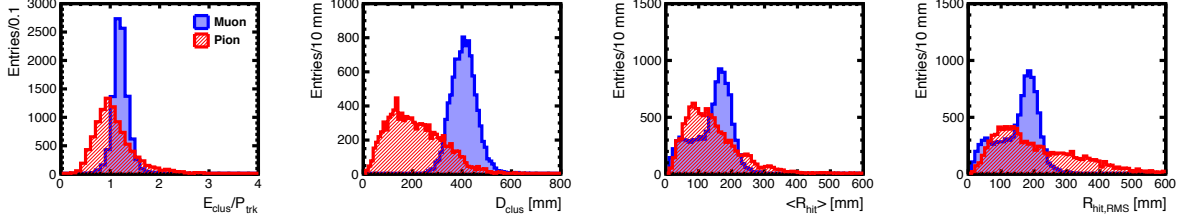**(b)** 1.0 GeV Momentum

(c) 2.0 GeV Momentum

Figure 7.28 Input variables calculated using hits of the reconstructed object created with new approach for (a) 0.2 GeV, (b) 1.0 GeV and (c) 0.2 GeV momentum. The blue histogram shows the muon distribution, while the red histogram represents the pion distribution.

been smeared out towards higher values, especially for the $R_{\text{hit,RMS}}$ variable, which means that they have a wider distribution of the radius of the hits. The distribution of the input variables are directly related with the selected region in order to determine the hits to create an object. Therefore, using the usual approach to determine the cylindrical region as explained above would change the behaviour of the input variable as well, which might improve the separation.

After acquiring the input variables, the procedure of the multivariate analysis is repeated as explained in the previous section for the statistically independent events from the ones used in the training. The cut values on the BDTG output are determined for the maximum significance. The resulting performance of the separation is seen in Figure 7.30, which gives the similar or slightly better results than before. The same feature at very low momentum is also seen in this new reconstruction approach due to the transition of the input variables as explained before. Since there is only a slight dependency on the momentum like in the PFO case, the same idea of considering the mean value of efficiency distributions as an overall efficiency was applied as well for a first estimate of its impact. In this case muon identification efficiency is $\varepsilon_{ID}^{\mu} \approx 96\,\%$,

(a) Hits of the reconstructed object with Pandora PFA

(b) Hits of the reconstructed object with new approach

Figure 7.29 Comparison of input variables of two methods at $1.0\,\mathrm{GeV}$ momentum. (a) Input variables using hits of the reconstructed object with Pandora PFA. (b) Input variables using all hits up to $R_{\mathrm{cut,max}}$. The blue histogram shows the muon distribution, while the red histogram represents the pion distribution.
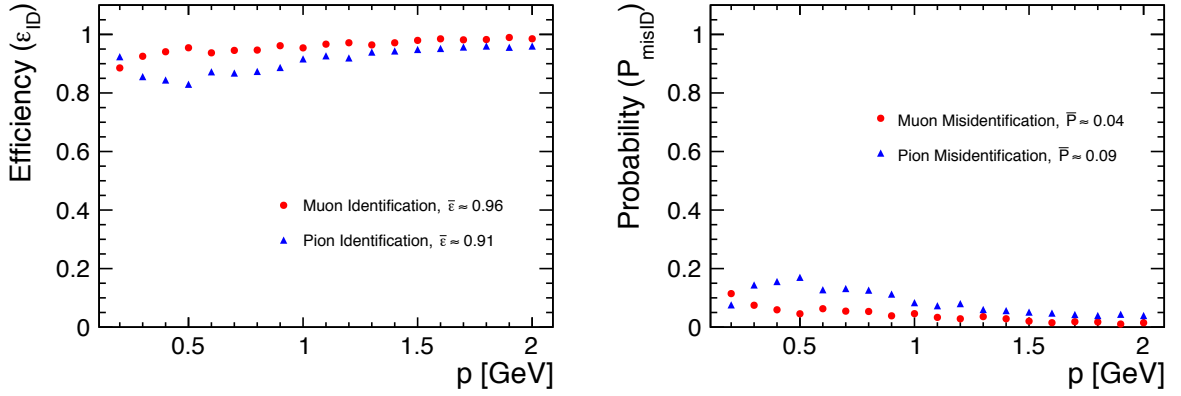
(a) ID efficiency

(b) MisID Probability

Figure 7.30 Identification efficiency results of new approach within a determined region with minimum three hits for the generated 5000 μ and 5000 π events. The cut values are determined with the maximum significance. The red points show the muon reconstruction, while the blue triangles show the pion reconstruction.

while pions can be identified with an efficiency of $\varepsilon_{ID}^{\pi} \approx 91\,\%$ which gives a $9\,\%$ probability to identify a pion as a muon.

Although the identification of μ and π has quite a high efficiency, in order to justify the separation of μ from π in terms of purity, the probability to misidentify a background particle π as a signal particle μ should be as low as possible, which provides high purity muons. Especially in the analysis of higgsinos, this situation is important due to the majority of pions in the final state compared to the muons because of high branching ratio of the charginos to a single pion. For a general example to judge the required misidentification probability of an identification, one can see from [193] that the misidentification probability of π is below 2% for momenta larger than 2 GeV. For the low momentum particles such low probability may not be possible, but it could be still considered as a reference value. To be able to achieve such low misidentification probabilities, at least as close as possible, and to acquire high purity muon events, the separation can be optimised by choosing another criteria to determine the cut values applied on the BDTG output.

7.4.5 Optimisation of the Separation

The results obtained with the new reconstruction approach correspond to the case when the cut values on the BDTG output were determined for the maximum significance. Figure 7.23, showing the background rejection as a function of the signal efficiency, indicates that the maximum significance does not give the minimum rejection of the background. Therefore instead of using the value at the maximum significance, the BDTG output values which give a signal efficiency of 80 % are determined as cut values for the optimisation of the separation. The resulting efficiencies are displayed in Figure 7.31.
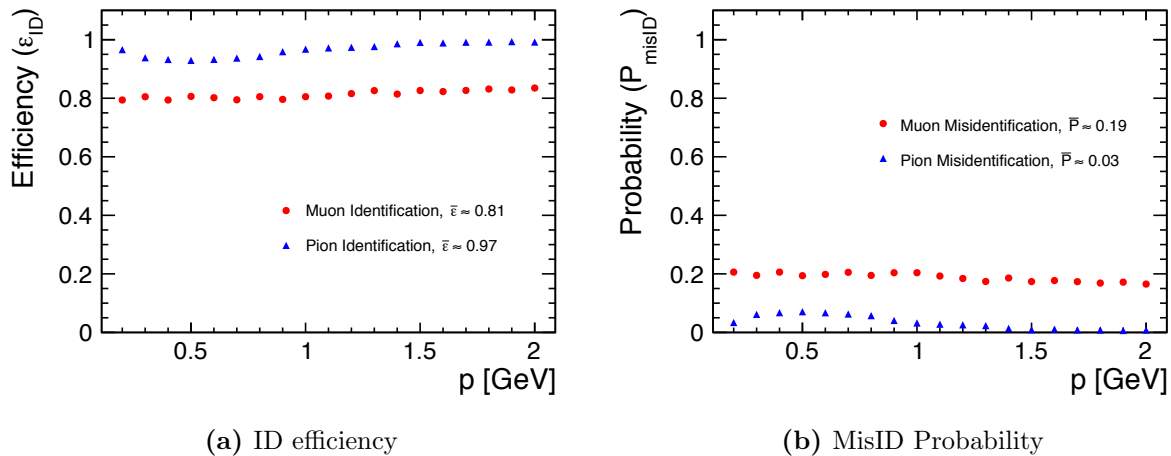

(a) ID efficiency   **(b)** MisID Probability

Figure 7.31 Optimised identification efficiency results of the new reconstruction approach within a determined region with minimum three hits for the generated 5000 μ and 5000 π events. The cut values are determined by choosing 80% signal efficiency. The red points show the muon reconstruction, while the blue triangles show the pion reconstruction.

With the optimisation, the misidentification probability of a π (background) goes down to 3% which results in highly pure muon samples with an efficiency at approximately 80%. The effect

of the mentioned feature of the input variable transition in the very low momentum region (0.4 - 0.6 GeV) can be seen for pion case. Assuming the slight fluctuations are negligible, one can again consider the mean value of the efficiencies as an overall identification efficiency. This property of the separation provides a nice feature in order to estimate the effect of the separation on higgsino samples.

7.5 Estimated Impact on Higgsino Events

In the SGV analysis of higgsino events, semi-leptonic final states have been chosen to be able to distinguish the chargino and neutralino samples from each other as explained in Section 6.2.1. Since the decay products of the higgsinos consist of π and μ in addition to a hard ISR photon, the identification of low momentum μ and π will influence the results acquired with the SGV analysis (cf. Chapter 6).

In order to estimate the impact of the μ and π separation on higgsino samples, the identification efficiency and miss identification probability distributions shown as a function of momentum in the previous section are considered as constant. The mean values of the distributions are taken as overall ID efficiency to identify μ and π correctly, and overall probability to identify a μ as a π or vice versa. The efficiencies are given as follows:

$$\varepsilon_{ID}^{\mu} = 81\% \qquad \varepsilon_{ID}^{\pi} = 97\% \qquad P_{misID}^{\mu} = 19\% \qquad P_{misID}^{\pi} = 3\%\,. \tag{7.21}$$

While the obtained efficiencies reduce the number of events selected as $\pi\mu$ semi-leptonic decay channel, they will give rise to additional backgrounds as well due to misidentification of $\pi\pi$ and $\mu\mu$ final states which are suppressed in the chargino selection of the SGV case. Both the reduction in the signal events and the increase in the background events raise the statistical precision of the cross section measurement. In order to estimate this effect, an efficiency matrix consisting of all possible combinations of π and μ final states is built up as below:

$$\mathcal{E}^{ID} = \begin{array}{c} \pi\pi^{\text{reco}} \\ \pi\mu^{\text{reco}} \\ \mu\mu^{\text{reco}} \end{array} \begin{pmatrix} \overset{\pi\pi^{\text{true}}}{94.1\%} & \overset{\pi\mu^{\text{true}}}{18.4\%} & \overset{\mu\mu^{\text{true}}}{3.6\%} \\ 5.8\% & 79.1\% & 30.8\% \\ 0.1\% & 2.4\% & 65.6\% \end{pmatrix}\,.$$

The element of the efficiency matrix can be represented as $(\mathcal{E}^{ID})_{ij}$, where i indicates the reconstructed final states of $\pi\pi$, $\pi\mu$, and $\mu\mu$, while j represents the true origin of those reconstructed final states. According to obtained efficiency matrix, true $\pi\mu$ final states can be reconstructed correctly as $\pi\mu$ final states with an efficiency of 79.1%, while they are reconstructed to a $\pi\pi$ final states with approximately 18% efficiency.

In the application of the identification to the higgsino samples, the chargino sample of the dM770 scenario with the polarisation combination of $P(e^+, e^-) = (+30\%, -80\%)$ has been considered as signal. The effect on the precision of the polarised cross section of the given process has been investigated as follows. The events which survive the preselection of SGV are classified

into three groups which contain only $\pi\pi$, $\pi\mu$ and $\mu\mu$ particles. This provides an ability to apply the efficiency matrix on the higgsino sample. Since $\pi\mu$ semi-leptonic final states are targeted in the analysis, only the second row of the efficiency matrix which is highlighted with red will be used in the calculations. The number of events under these three classes for both signal and background samples are given as a matrix in the following:

$$
\mathcal{N}^{SGV} = \begin{array}{c} \pi\pi^{\mathrm{true}} \\ \pi\mu^{\mathrm{true}} \\ \mu\mu^{\mathrm{true}} \end{array} \overset{\begin{array}{ccccc} \widetilde{\chi}_1^+\widetilde{\chi}_1^- & \widetilde{\chi}_1^0\widetilde{\chi}_2^0 & ee(4f) & e\gamma(3f) & \gamma\gamma(2f) \end{array}}{\left(\begin{array}{ccccc} 6470 & 110 & 0 & 512 & 1651 \\ \mathbf{3554} & 36 & 1 & 1240 & 3624 \\ 464 & 61 & 246 & 2252 & 1240 \end{array} \right)},
$$

where the elements of the matrix $(\mathcal{N}^{SGV})_{jk}$ correspond to the number of events assigned to classes of $\pi\pi$, $\pi\mu$, and $\mu\mu$ represented by j for each sample k. The first column ($k = 1$) shows the number of events for the chargino signal, while the second one corresponds to the neutralino sample considered as a SUSY background when the chargino sample is the signal. The remaining columns show the number of events for SM background classes ee, $e\gamma$, and $\gamma\gamma$. In the SGV case since the reconstruction is considered as perfect, the efficiency matrix $\mathcal{E}^{ID}$ is the identity matrix which suppresses all other contributions to the reconstructed $\pi\mu$ final state, and only true $\pi\mu$ events are reconstructed in this case as shown in the second row of $\mathcal{N}^{SGV}$ matrix.

The impact of the identification on the reconstructed number of events can be obtained by multiplying the efficiency matrix with the number matrix of the SGV final states $\mathcal{N}^{SGV}$, which can be considered as true final states since the identification is assumed to be perfect.

$$
(\mathcal{N}^{FS})_{jk} = (\mathcal{E}^{ID})_{ij|_{i=2}} \cdot (\mathcal{N}^{SGV})_{jk}, \tag{7.22}
$$

where only the second row of the efficiency matrix corresponding to the case when $i = 2$ is considered. The number matrix $\mathcal{N}^{FS}$, obtained as a result of this multiplication, shows the estimated number of events contributing to the reconstructed semi-leptonic final states of $\pi\mu$ in full simulation studies. The acquired number of reconstructed events as $\pi\mu$ is given in the following by indicating from which true class they are stemming:

$$
\mathcal{N}^{FS} = \begin{array}{c} \pi\pi^{\mathrm{true}} \\ \pi\mu^{\mathrm{true}} \\ \mu\mu^{\mathrm{true}} \end{array} \overset{\begin{array}{ccccc} \widetilde{\chi}_1^+\widetilde{\chi}_1^- & \widetilde{\chi}_1^0\widetilde{\chi}_2^0 & ee(4f) & e\gamma(3f) & \gamma\gamma(2f) \end{array}}{\left(\begin{array}{ccccc} 377 & 6 & 0 & 30 & 96 \\ \mathbf{2813} & 29 & 1 & 982 & 2868 \\ 143 & 19 & 76 & 693 & 382 \end{array} \right)}\Bigg|_{\pi\mu^{reco}}.
$$

This matrix provides an important input for estimating the effect of the identification on the final result of the SGV, explained in Chapter 6, by comparing the statistical precision of the SGV and Full Simulation estimations. The estimated cross section precision is determined with the following formula as already explained in Section 6.2.4:

$$
\frac{\delta\sigma}{\sigma} = \frac{1}{\sqrt{\epsilon \cdot \pi \cdot \sigma \cdot \int \mathcal{L}dt}}. \tag{7.23}
$$

The efficiency and purity of the selection can be formulated as follows:

$$\text{Efficiency:} \quad \varepsilon = \frac{(\mathcal{N})_{jk|_{j=2,k=1}}}{N^{all}_{\widetilde{\chi}_1^+ \widetilde{\chi}_1^-}} \,, \qquad \text{Purity:} \quad \pi = \frac{(\mathcal{N})_{jk|_{j=2,k=1}}}{\sum_{j,k}(\mathcal{N}_{\pi\mu^{reco}})_{jk}} \,. \tag{7.24}$$

where $(\mathcal{N})_{jk|_{j=2,k=1}}$ shows the number of signal events written in bold in both number matrices of SGV and Full Simulation cases, and $N^{all}_{\widetilde{\chi}_1^+ \widetilde{\chi}_1^-} = 38130$ is the total weighted number of events before any cut applied on the event selection of the analysis as can be seen in Table 6.1. The denominator of the purity calculation is different for the SGV and Full Simulation cases:

- $\sum_{j,k}(\mathcal{N}_{\pi\mu^{reco}})_{jk} = \sum_{k=1}^{5} (\mathcal{N}^{SGV})_{jk|_{j=2}}$ in SGV

- $\sum_{j,k}(\mathcal{N}_{\pi\mu^{reco}})_{jk} = \sum_{k=1}^{5}\sum_{j=1}^{3} (\mathcal{N}^{FS})_{jk}$ in Full Simulation.

The reason for this is that the contribution to the reconstructed $\pi\mu$ events comes only from the second row of $\mathcal{N}^{SGV}$ matrix, while all the elements of $\mathcal{N}^{FS}$ contribute to the reconstructed events of the $\pi\mu$ final state.

Following the explained steps, the efficiency and purity of the selection for the SGV and Full Simulation can be obtained as $\varepsilon_{SGV} = 9.32\%$, $\pi_{SGV} = 42.03\%$, and $\varepsilon_{FS} = 7.38\%$ $\pi_{FS} = 33.04\%$. These correspond to an estimation on the cross section precision of 2.58% in SGV, and 3.26% in Full Simulation for an integrated luminosity of $\int \mathcal{L}dt = 500\,\text{fb}^{-1}$ and polarised cross section of $\sigma_{pol} = 76.997\,\text{fb}$ for $P(e^+, e^-) = (+30\%, -80\%)$ in the dM700 scenario. These results are acquired considering only $\mu\pi$ channel, however in the SGV analysis other possible semi-leptonic decay channel $e\pi$ is included as well. To extrapolate the obtained result, a scaling parameter can be obtained from the ratio of the precisions of FS to SGV, which results in $f_s = 1.26$.

Assuming that not only $e - \pi$ identification can be done with the same efficiency, but also other challenges can be compensated by keeping the decrease on efficiency and purity as small as possible, the obtained precision on the polarised cross section from SGV analysis decreases from $\delta\sigma/\sigma = 1.63\%$ to $\delta\sigma/\sigma = 2.05\%$ in full simulation

$$\left.\frac{\delta\sigma}{\sigma}\right|_{SGV} = 1.63\% \qquad \left.\frac{\delta\sigma}{\sigma}\right|_{FS} = 2.05\% \,. \tag{7.25}$$

The SGV precision on the polarised cross section was obtained for a centre-of-mass energy of $\sqrt{s} = 500\,\text{GeV}$ and an integrated luminosity of $\int \mathcal{L}dt = 500\,\text{fb}^{-1}$. In order achieve a precision of 1.63% with full simulation, less than two times more luminosity is necessary (see Equation (7.23)). This necessity of the scenario fits perfectly with one of the planned operating scenarios of the ILC explained in Section 3.4.1. One can conclude that assuming the same identification efficiency of electron as muons, and suppression of the $\gamma\gamma$ overlay, the such Natural SUSY scenarios including light and almost mass degenerate higgsinos could be observable at the ILC with the achieved precisions from fast simulation analysis by taking data at 500 GeV for an integrated luminosity of $\int \mathcal{L}dt \approx 1000\,\text{fb}^{-1}$. This could be achieved with the high luminosity upgrade run of the preferred operating scenario H-20 of the ILC [95].

7.6   Summary

The Natural SUSY scenarios play a crucial role in new physics searches. The scenarios including light higgsinos which are almost degenerate in mass are extremely challenging for both the LHC and the ILC. In Chapter 6, the results of a fast simulation study has been interpreted. They indicated that such analysis can be performed at the ILC. In order to investigate further how realistic the results are, and which improvements could be necessary to be able to perform the analysis in a real experiment, a full simulation analysis has been performed.

The key observables of the analysis are $M_{\widetilde{\chi}_1^\pm}$, $M_{\widetilde{\chi}_2^0}$, $\Delta M_{\widetilde{\chi}_1^\pm - \widetilde{\chi}_1^0}$, and the estimation of $\delta\sigma/\sigma$. The reconstruction of $M_{\widetilde{\chi}_1^\pm}$, and $M_{\widetilde{\chi}_2^0}$ depends on the reconstruction of the ISR photon and initial centre-of-mass energy, since they are calculated from the recoil mass of the ISR photon as it is described in Sections 6.2.2 and 6.3.2. The mass difference $\Delta M_{\widetilde{\chi}_1^\pm - \widetilde{\chi}_1^0}$ is reconstructed from the energy of the chargino decay products which are boosted into the rest frame of the charginos as explained in Section 6.2.3, therefore it is based on the reconstruction and identification of the higgsino decay products. The precision on the polarised cross section is also dependent on the reconstruction and identification of the decay products, since it can be estimated from the purity and efficiency of the selection of the required higgsino decay products (cf. Section 6.2.4).

In this chapter, all steps of the analysis have been investigated step by step. It has been indicated that both the reconstruction of the ISR photon and the missing four-momentum works well in full simulation, even in the presence of the $\gamma\gamma$ overlay. Some of the simplification made in the SGV, which are the $\gamma\gamma$ overlay and pair background, give rise to additional background particles which will increase the number of the reconstructed particles. On the other hand, the particles from $\gamma\gamma$ overlay can be suppressed using the VTX information, while the pair background can be suppressed during the analysis by adding cuts which are discriminative between signal and pair background particles as explained in Section 7.2.3. The studies showed that the decay products of the higgsinos can be reconstructed efficiently in terms of their tracks, but not for their PFOs. The Pandora PFO reconstruction in full simulation requires improvements to be tuned for low momentum particles. The remaining simplification made in the SGV is the particle identification. The studied efficiencies indicated that the analysis cannot be done in a real experiment without any further investigation, especially for e and μ identification to prevent them to be identified as π (cf. Section 7.2.5). It has been explained that these particles can be identified by using dE/dx and cluster shape information (cf. Section 7.2.5). The μ identification has been investigated in detail in the context of this thesis as explained in Section 7.4.

Even though the tracks can be reconstructed efficiently, the DBD version of the tracking efficiency used in the analysis does not require any hit to be detected in the VTX detector. Currently, it only contains hits from the TPC, which are also necessary to apply dE/dx information for the separation of $e - \pi$. However, this existing version of the tracking is not sufficient for the analysis of the higgsinos in a real experiment due to lack of VTX hits. In the time of this analysis, the DBD tracking has been updated by including the silicon hits (VTX information), and concluded that the inclusion of the silicon hits reduces the tracking efficiency of low momentum particles in a significant amount as shown in Figure 7.8 [179]. Because of this, alternative tracking algorithms as described in Section 7.3.2 has been studied [179]. It has been concluded

that the CA algorithm, which uses mini-vectors, compensates the reduction on efficiency due to the inclusion of silicon hits, and provides high tracking efficiency almost in the same level with the DBD. One of the outcome of the CA algorithm is the high number of background tracks, but fortunately in the very low momentum region below $0.2\,\mathrm{GeV}$. Since, the particles have to reach the calorimeters to be able to identify μ, the particles with $p < 0.2\,\mathrm{GeV}$ are out of the interested region for this analysis, and they can be safely vetoed. This concludes that CA algorithm provides a high tracking efficiency in the presence of silicon hits, while keeping the number of background tracks from the pair background in the same level with the DBD. So, it would be a good tracking method in the study of this analysis in a real experiment.

Finally, the obtained results from the developed method for the $\mu - \pi$ separation have been used to estimate the impact of this on the higgsino events in terms of the precision on the polarised cross section. The results from the $\mu - \pi$ channel, has been extrapolated to the semi-leptonic channel considered in SGV by including $e - \pi$ channel presuming the identification of them can be done with the same efficiency. Assuming not only the $e - \pi$ identification, but also all the required optimisations can be done with the same reduction on the efficiency and purity of the selection of the higgsino decay products, one can conclude that the obtained results from the SGV analysis can be achieved in a real experiment by taking data almost two times longer than the time necessary for the integrated luminosity of $\int \mathcal{L}dt = 500\,\mathrm{fb}^{-1}$ at $\sqrt{s} = 500\,\mathrm{GeV}$.

Chapter 8

Charge Transfer Measurements in the Amplification Region of a TPC

The Time Projection Chamber is the central tracking system of the ILD detector. As explained in Section 4.3.1.3, it is based on the idea of ionisation of gas atoms due to the passage of charged particles. However, this primary ionisation does not provide a sufficient number of signal electrons to be measured by the readout system. Therefore, the electrons produced by the primary ionisation are amplified using different technologies which will be explained in Section 8.2. One of the technology uses Gas Electron Multiplier (GEM) in order to amplify electrons. In this chapter a study based on the measurements of charge transfer coefficients in a triple GEM stack with three commonly used gases will be explained.

The gases, which are investigated to be used in the TPC, consist of a mixture of several gases chosen according to their properties as given in the following: The "T2K" gas includes a mixture of Argon, Tetrafluoromethane and Isobutane ($Ar(95\%)$, $CF_4(3\%)$, $C_4H_{10}(2\%)$), while the "P5" gas contains only Argon and Methane gases ($Ar(95\%)$, $CH_4(5\%)$), and the "TDR" gas is composed of Carbon dioxide in addition to Argon and Methane ($Ar(93\%)$, $CH_4(5\%)$, $CO_2(2\%)$).

There have been already existing past studies which measured the charge transfer coefficients using either P5 gas or TDR gas, or both gases [194, 195, 196, 197]. One recent study [198] used T2K gas, which is the proposed gas for the TPC of the ILD detector. In the measurements with the T2K gas, it has been observed that the T2K gas behaves differently when it is compared with the past measurements [194, 195, 196, 197]. In addition, T2K gas does not follow the electrostatic prediction proposed in [199], while the prediction shows good agreement in the case of P5 and TDR gases. These observed discrepancies constitute the main motivations to understand the influence of the T2K, P5 and TDR gases on the movement of the charged particles in the amplification region by investigating all three gases in the same setup.

In the following sections, the fundamentals of charge transfer will be explained in Section 8.1. Following that, the gas properties influencing the behaviour of the particles will be compared. In Section 8.4 the parameters determining the charge transfer will be explained. Moreover, the

183

setup will be explained and the results of the measurement will be shown in Section 8.7. Finally, the procedure and the results for the charge up effects will be discussed.

8.1   Fundamentals of the Charge Transfer within the TPC

A charged particle, which goes through a gaseous volume, interacts with the atoms of the gas and loses its energy by ionising the atoms. The ionisation energy loss of the charged particle per length is determined by the Bethe-Bloch equation as explained in Section 4.1. The electron and ion pairs created by means of the primary ionisation, the so-called charge carriers, experience both drift because of the electromagnetic field, and diffusion due to the collisions between the charge carriers and gas atoms. In addition, the attachment, causing the absorption of the electrons, has an effect on the amount of primary signal electrons reaching the anode. These effects and the existing latest technologies used in the amplification of the signal will be explained in this section.

8.1.1   Drift and Diffusion of Charge Carriers

The electron and ion pairs produced by the primary ionisation lose their energies by interacting with the gas atoms in the absence of electric and magnetic field. Due to the kinetic theory of the gases, the charge carriers will acquire a thermal kinetic energy of $E = 3/2kT = 1/2mv^2$, where k is the Boltzmann constant, T is the temperature of the gas, m and v are the mass and a mean instantaneous velocity of the particles, respectively. The multiple collisions of the charge carriers with the atoms of the gas result in a diffusion which is isotropic in the absence of external fields.

When an electric field is applied, charge carriers drift parallel (ion) and antiparallel (electron) to the electric field, $\vec{E}$. Their drift directions are determined by both electric and magnetic field in the presence of magnetic field. Since the charge carriers experience the Lorentz force in this case, they move in a circular direction while they are travelling towards to the anode or cathode of the TPC. The motion of the charge carriers under these fields can be explained by the equation of motion:

$$m\frac{d\vec{v}_{\mathrm{D}}}{dt} = e\vec{E} + e[\vec{v}_{\mathrm{D}} \times \vec{B}] - K\vec{v}_{\mathrm{D}} \tag{8.1}$$

where m, e and $\vec{v}_{\mathrm{D}}$ are the mass, electric charge and drift velocity of the related charged carrier, respectively. K corresponds to the friction force caused by the interaction of the charge carrier with the gas, which can be related to the time between two collisions denoted by τ as $\tau = m/K$. Considering the steady state solution of Eq.(8.1) with $t \gg \tau$ condition, *the drift velocity* can be written as a function of the electric and magnetic field as follows [200, 201]:

$$\vec{v}_{\mathrm{D}} = \frac{e}{m}\frac{\tau}{(1 + \omega^2\tau^2)}\left(\vec{E}_{\mathrm{D}} + \frac{\omega\tau}{B}(\vec{E}_{\mathrm{D}} \times \vec{B}) + \frac{\omega^2\tau^2}{B^2}(\vec{E}_{\mathrm{D}} \cdot \vec{B})\vec{B}\right) \tag{8.2}$$

where τ is the time between two collisions which depends on the electric field, and ω is the cyclotron frequency of the charge carriers stemming from the effect of the magnetic field which is defined by $\omega = eB/m$.

Since the mass of the ions is large, the value of $\omega\tau$ is very low, of the order of 10^{-4}. Therefore, the influence of the magnetic field on the drift velocity is negligible [202], and the drift velocity is approximated to the following simple form:

$$\vec{v}_{\mathrm{D}} \approx \mu \vec{E}_{\mathrm{D}} \qquad \text{with} \qquad \mu = \frac{e}{m}\tau \tag{8.3}$$

where μ, the so-called mobility, defined as the ratio of drift velocity to electric field in the absence of magnetic field. In principle, μ is not constant since τ depends on the electric field. However, due to the high mass of ions the value of mobility stays constant up to high electric fields [202]. Therefore, the drift velocity of the ions increases with the electric field linearly up to high electric fields.

For electrons, the effect of the magnetic field depends on $\omega\tau$. When $\omega\tau = 0$ (B=0), the drift velocity is directed along $\vec{E}_{\mathrm{D}}$ as explained above and it takes the simple form as in the case of ions. The mobility of electrons changes significantly depending on the electric field because of their low mass. If $\omega\tau$ is large, the drift field tends to be directed along the magnetic field, but if $\vec{E}_{\mathrm{D}} \cdot \vec{B} = 0$, then for large $\omega\tau$ the drift velocity will be directed in the direction of $\vec{E}_{\mathrm{D}} \times \vec{B}$.

In the case in a TPC when the electric field is parallel to the magnetic field $\vec{E} \parallel \vec{B}$ in the z direction ($\vec{E} \times \vec{B} = 0$), the drift velocity won't be affected by the magnetic field and will be directed along the electric field. However, any slight shift in the direction of the magnetic field, will cause distortions stemming from $\vec{E} \times \vec{B}$ term of Equation (8.2).

Drift velocities are dependent on the components of the gas as well, in addition to the electromagnetic field, and type of the particle. The effects of the gas enter via the microscopic picture of the motion of the charge carriers, which is explained in [201]. According to this picture the drift velocity of a charged particle mainly depends on fractional energy loss of the particle per collision denoted by λ and a collision cross section per molecule σ [201]:

$$v_{\mathrm{D}}^2 = \frac{e\vec{E}}{mN\sigma}\sqrt{\frac{\lambda}{2}} \tag{8.4}$$

where N denotes the number density of gas atoms. Figure 8.1 shows the dependence of fractional energy loss (left) and collision cross section on the gas type for Argon (Ar) and Methane (CH_4). Figure 8.1a indicates that both gases have a clear dip which is the so-called Ramsauer minimum [203] stemming form the quantum mechanical processes in the scattering. Because of the relation between $\vec{v}_{\mathrm{D}}$ and σ as seen from Equation (8.4), this minimum will cause a maximum on the drift velocity of the particles which will be seen in Figure 8.3. Figure 8.1b shows that the argon atoms have a higher threshold energy for their excitation compared to the methane atoms. This significant different behaviour between gases shows clearly the dependency of the drift velocity on the gas mixture.

The diffusion of the created electrons or ions, which stems from the collision of the electrons or ions with the atoms of the gas, also affects the transfer of charge carriers. Since the electrons are lighter than ions, they scatter more when they experience any collision. Because of that, the effect of the diffusion on the electrons is larger than the effect on the ions. Considering the
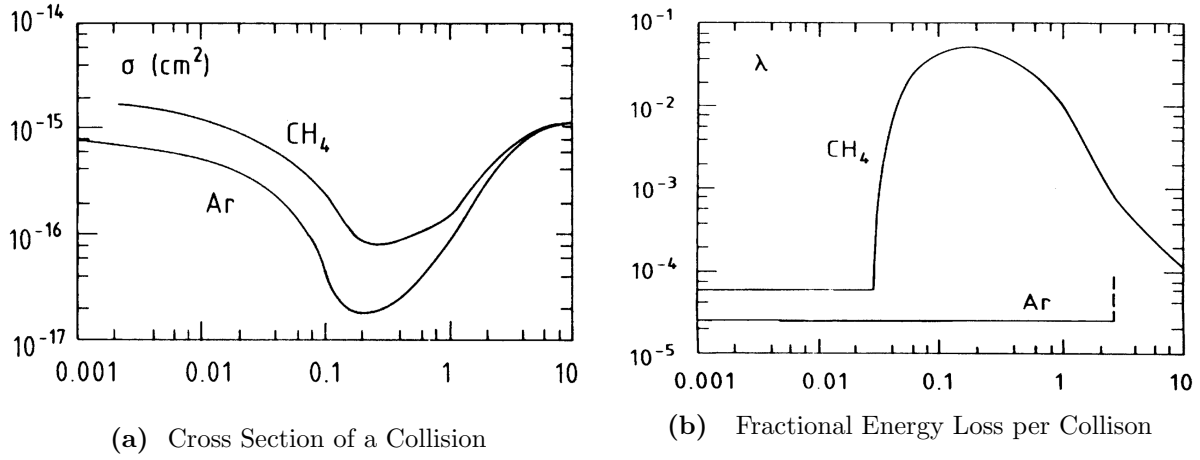
(a)   Cross Section of a Collision

(b)   Fractional Energy Loss per Collison

Figure 8.1   (a) Cross section of a collision as a function of the total energy [eV] of the drifting electrons for Argon and Methane. (b) Fractional energy loss per collision as a function of the total energy [eV] of the drifting electron for Argon and Methane. Figure is taken from Ref. [201].

simplest case where the diffusion is same in all direction (isotropic), the diffusion coefficient D is given by [201];

$$D = \mu \frac{kT}{e} \tag{8.5}$$

where μ is the mobility, k is the Boltzman's constant, and T is the temperature. The minimum diffusion width for an electron cloud which has drifted a distance L in an electric field parallel to the z direction [201, 202] for only one direction denoted by x is given by:

$$\sigma_x = (2Dt)^{1/2} \quad \text{with} \quad t = \frac{L}{v_{\mathrm{D}}} \tag{8.6}$$

which results in:

$$\sigma_{x,\mathrm{min}} = \left(\frac{2kTL}{e|\overrightarrow{E_{\mathrm{D}}}|} \right)^{1/2} . \tag{8.7}$$

Equation 8.7 shows that in order to have a small diffusion, either the temperature of the particles should be low or the electric field should be high. This simplest isotropic case is valid for ions in all conditions apart from very high electric fields, while it is valid for electrons only for electric fields lower than 100 V/cm [202]. At high electric fields, electrons follow an anisotropic diffusion [204] in an electric field E_{D} which is parallel to z [202]:

$$\sigma_x = (2D_T t)^{1/2} \tag{8.8}$$
$$\sigma_t = v_{\mathrm{D}}^{-1}\sigma_z = v_{\mathrm{D}}^{-1}(2D_L t)^{1/2}. \tag{8.9}$$

where σ_x and σ_t denotes the transverse diffusion in one direction of x, and a spread of arrival times, respectively. D_T and D_L are the diffusion coefficients of the transverse and longitudinal

186

components of the diffusion which are different in the presence of magnetic field. The transverse diffusion of electrons has a significant effect on the spatial resolution, thus it needs to be as small as possible. The transverse diffusion coefficient D_T decreases in the presence of magnetic field, while it does not change the longitudinal coefficient of the diffusion, D_L [202]:

$$
\begin{aligned}
D_T(B) &= D_T(B=0)\frac{1}{1+\omega^2\tau^2} & (8.10)\\
D_L(B) &= D_L(B=0). & (8.11)
\end{aligned}
$$

Like in the case of drift velocity, diffusion has also a dependency on the gas mixture via the definition of the τ, which is the mean time between two collision. Therefore, minimising the diffusion also plays a role in the choice of the gas.

8.1.2 Attachment of Electrons

Along the way of the electrons towards the anode they can experience *the attachment*. In this process, the electrons are absorbed by electronegative components or impurities in the gas. Especially halogenides and oxygen have the largest electron affinity, which means that the possibility of an electron to bind to the atom is largest in these elements. Therefore, the contamination of the TPC gas with one of these including air and water should be kept as small as possible. The rate of an attachment for a two body process $e^- + M \rightarrow M^-$ or $e^- + M \rightarrow A^- + B + ...$ is given as follows [201]:

$$
R = v\sigma N \tag{8.12}
$$

where v is the electron velocity, σ is the cross section of the attachment, and N is the number density of the attaching atoms. Since it reduces the amount of the primary signal electrons, the attachment of a chosen gas itself should be small. In addition, one needs to be sure that the gas will stay as pure as possible during the operation of the TPC.

8.1.3 High Electric Fields and Stability

As explained in Section 4.3.1.3, in order to have sufficient signal, the primary electrons from the ionisation are needed to be amplified. The ILC TPC is designed to use GEMs in the endplate to perform the amplification. The amplification takes place by the subsequent electron-pair productions as long as electrons have enough energy to ionise the gas atoms. This results in a drop-like shape of an avalanche of charge carriers because of the difference in the drift velocity of the electrons and ions. Since electrons have higher drift velocity, all electrons are placed in the front part of the drop-like distribution of charges, while the ions are distributed on the rest part of the avalanche. This process is limited by the so-called spark breakdown, caused by the photon emission of gas atoms which generates an avalanche spread over the gas volume. Therefore it may reduce the spatial resolution, and remove the possibility to obtain any signal or even destroy the GEMs [205]. The emission of photon is a common inelastic phenomena for nobel gases; however, weakly-bound polyatomic molecules have radiationless transitions of a rotational and vibrational nature. Therefore, these type of gases, the so-called quenchers, are added to gas mixture to acquire high gain and stable setup.

8.2   Gas Amplification with Micro Pattern Gaseous Detectors

Gas amplification is a necessary process to have sufficiently high signal to be measured by the readout system. This is done by applying a high electric field which makes the electrons acquire enough kinetic energy between collisions to ionise further atoms. In this way, an avalanche of electrons is created, and the signal from primary ionisation is amplified before it reaches the readout. For amplification, Micro-Pattern Gas Detectors (MPGDs) [206], introduced in the late 1980's, are preferred compared to Multi-Wire Proportional Chambers (MWPCs) [207]. Due to relatively large distances between two wires ($d > 1 - 2\,\mathrm{mm}$), the MWPC results in large transverse diffusion which reduces the spatial resolution [208]. Using a large magnetic field this disadvantage can be compensated, however it will still suffer from the large $E \times B$ effect because of the distance of two wires. Therefore, it can not be used for ILD TPC. However, in the MPGDs the distance between two holes are in a few hundred micrometer ($d \approx \mu$m) level, thus the MPGDs provide an excellent spatial resolution of approximately $30\,\mu$m, and a high rate capability of larger than $10^6\,\mathrm{Hz/mm}^2$ [201]. There are different types of MPGDs, two of them are Gas Electron Multipliers (GEM) [209], and Micro-Mesh Gaseous Detectors (MicroMegas) [210]. The studies performed within the context of this thesis use GEM technology in order to amplify the signal, therefore this technology will be explained in the following.

An image of a GEM from a scanning electron microscope is displayed in Figure 8.2a [211]. A GEM consists of a thin $50\,\mu$m kapton foil covered from both sides by 5 μm copper layers. The holes have conical shape with outer and inner diameters of $70\,\mu$m and $50\,\mu$m, respectively. The distance between two holes is $140\,\mu$m. These are values for the main characteristics for the GEM type produced at CERN, which is used in the measurements. A high electric field in the order of $50 - 70\,\mathrm{kV/cm}$ is applied between the copper layers of a GEM to multiply the signal electrons. A schematic of the generated electric field lines is seen in Figure 8.2b. Since the field strength is higher within the hole, the lines are compressed in the transition from the low drift field region to the hole, while they are spreading out in the process of leaving the hole. This feature of the electric fields helps to collect more electron within the GEM holes where the amplification takes place. It also determines the behaviour of the charge transfer coefficients which will be explained in Section 8.4.1. To achieve a more stable setup, the high field is divided into several GEMs, such that the required amplification can be achieved in several steps.

8.3   Gas Properties

Concerning the choice of the gas, the main aim is to provide a high spatial resolution and fast readout, which is affected from important properties explained in the previous section; the drift velocity and the transverse diffusion. In addition, the attachment rate has an important effect on the amount of the signal depending on the type of gas.

- *The drift velocity* of the gas (v_D), which is a measure of the time needed to read out the signal after the primary ionisation, should be high to fulfil the requirement of high spatial resolution. Since the drift velocity changes depending on the electric field, the field on the
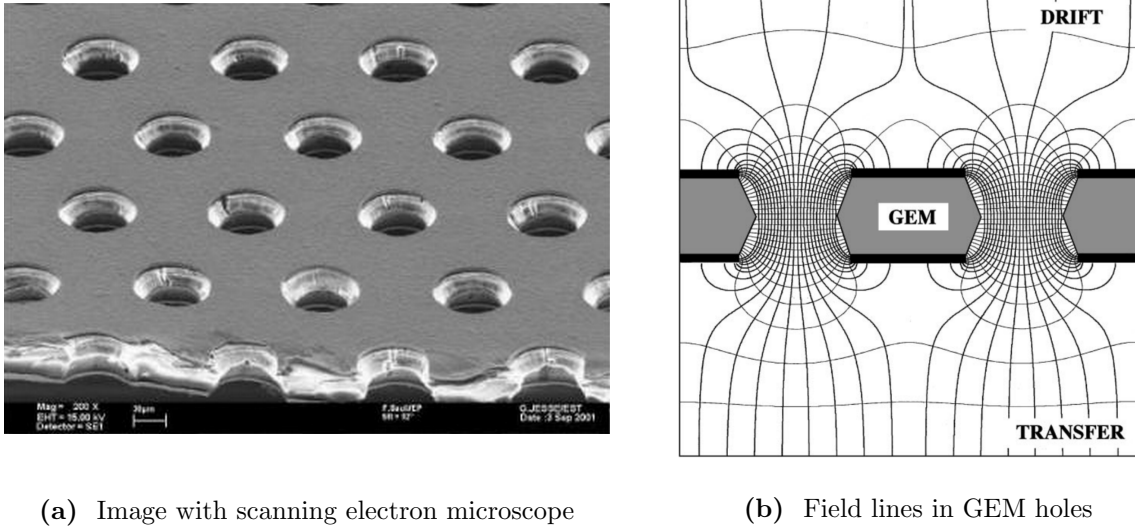
(a) Image with scanning electron microscope

(b) Field lines in GEM holes

Figure 8.2 Gas Electron Multipliers (GEM): (a) An image of the GEM surface and cross section using scanning electron microscope, it is taken from Ref. [211]. (b) Demonstration of electric field lines in the GEM holes, it is taken from Ref. [206].

drift region is determined considering the maximum value of the drift velocity which gives the highest spatial resolution.

- *The transverse diffusion* reduces the spatial resolution when it acquires large values, therefore it needs to be small.

- *The attachment rate* reduces the amount of the primary ionised electrons, and decreasing the signal arriving to the readout. Therefore, it should be kept as small as possible.

The comparison of these properties for three commonly used gases T2K, P5 and TDR will be given in the following.

The drift velocity as a function of the electric field in the drift region, often referred to as drift field (E_{D}) is given in Figure 8.3a for these all three gases. The P5 gas has maximum drift velocity at $E_{\mathrm{D}} \approx 90\,\mathrm{V/cm}$, while T2K and TDR gases have maximum drift velocity at $E_{\mathrm{D}} \approx 200\,\mathrm{V/cm}$ and $E_{\mathrm{D}} \approx 250\,\mathrm{V/cm}$, respectively. In the comparison of the gases, the one which gives the highest maximum drift velocity can be considered as a best choice, since it provides faster readout of the signal.

In Figure 8.3b, the transverse diffusion is shown as a function of the drift field below $E_{\mathrm{D}} < 300\,\mathrm{V/cm}$. The displayed drift field region is chosen because the maximum drift velocities are acquired in that region. The figure indicates that the values of the transverse diffusion for each gas stay almost constant within the given region of the drift fields when $E_{\mathrm{D}} > 100\,\mathrm{V/cm}$. The absolute values of the transverse diffusions are different for each gas; T2K has the smallest transverse diffusion, while P5 has the highest value. As a consequence of this, the signal can be obtained more focused with a better spatial resolution in the case of T2K compared to others.

189

(a) Drift Velocity

(b) Transverse Diffusion
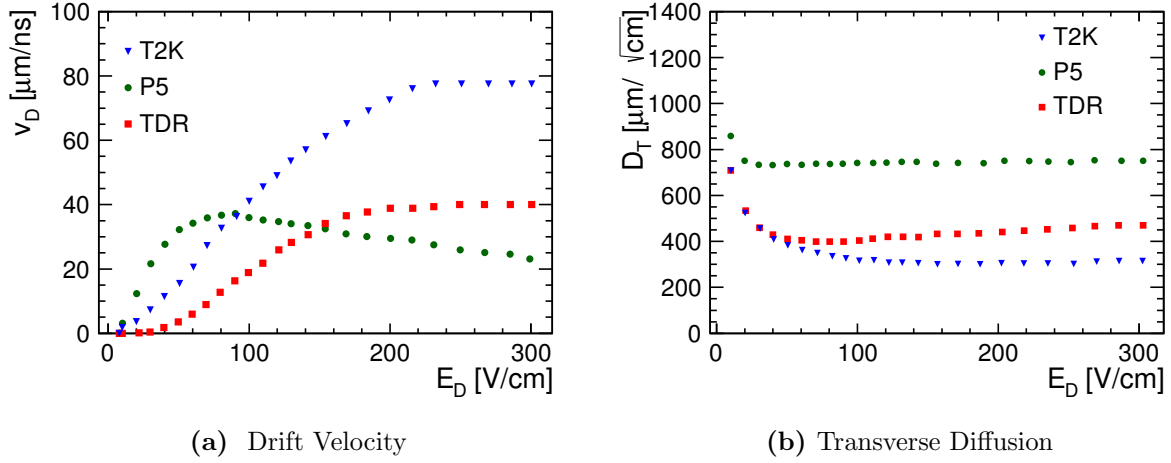
Figure 8.3 Comparison of the drift velocity and the transverse diffusion for P5, TDR and T2K gases at $B = 0\,\text{T}$. Figure is adapted from Ref. [212].
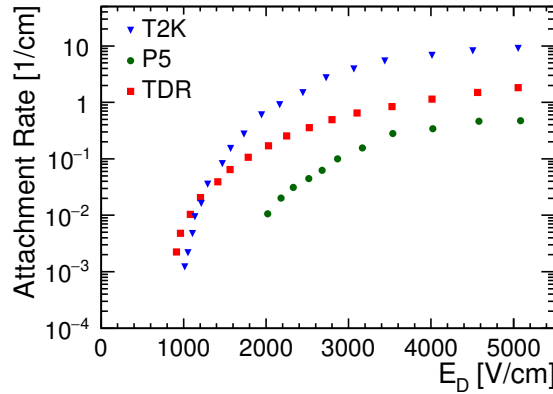

Figure 8.4 Comparison of the attachment rates for P5, TDR and T2K gases at $B = 0\,\text{T}$. Figure is adapted from Ref. [212].

The attachment rate of the gases is shown in Figure 8.4. The rate indicates the amount of electrons attached to the gas atoms in the drift region. As seen in the figure, the attachment rate is getting significant for the high drift velocities, therefore it was not studied for the drift fields smaller than approximately $1000\,\text{V/cm}$. At high electric field region, the P5 and TDR gases have small attachment rates compared to the T2K gas. The upper limits of the attachment rate are respectively almost $0.5\,\text{cm}^{-1}$ and $2\,\text{cm}^{-1}$ for P5 and TDR gases at around $5000\,\text{V/cm}$, while it is almost $10\,\text{cm}^{-1}$ for T2K gas at the same drift field. Therefore, it is expected that the number of the primary electrons would be much smaller for T2K gas since it has high attachment rate resulting in less signal, while it is more or less comparable for P5 and TDR. Even though the attachment has no influence on the results in the interested region which is below $E_\text{D} < 500\,\text{V/cm}$, since high electric fields up to $5000\,\text{V/cm}$ are used in the measurements,

it has a visible impact on the measurements, which will be explained in Section 8.4.1.

8.4   Parameters Related with the Charge Transfer

As explained in the previous chapters when a charge particle passes through the TPC, it ionises the gas atoms and produces electron-ion pairs which travel towards the electrodes due to the voltage difference applied between them. Since this primary ionisation is not sufficient for the readout, the produced electrons are amplified using GEM stacks. The amplification is mainly done by creating a high electric field between the surfaces of each GEM. Figure 8.5 shows the naming convention of GEM voltages, electric fields and output currents on each surface of a triple GEM stack.

Because of the difference between the electric fields outside and inside GEMs, the electric field lines will be compressed or spread out while they are entering or exiting the hole respectively as displayed in Figure 8.2b. In this process, some of the field lines will end up on the surfaces of GEMs due to the geometrical structure of GEMs. Therefore, neither all the electrons produced in the primary ionisation will enter a GEM hole nor all the electrons amplified within the hole will leave the GEM without any loss as will be illustrated in Figure 8.6. The same situation is valid for the ions as well. In order to determine this charge transfer, several coefficients are defined such as collection and extraction efficiencies as well as the gain of a single GEM. They will be explained in the next section.
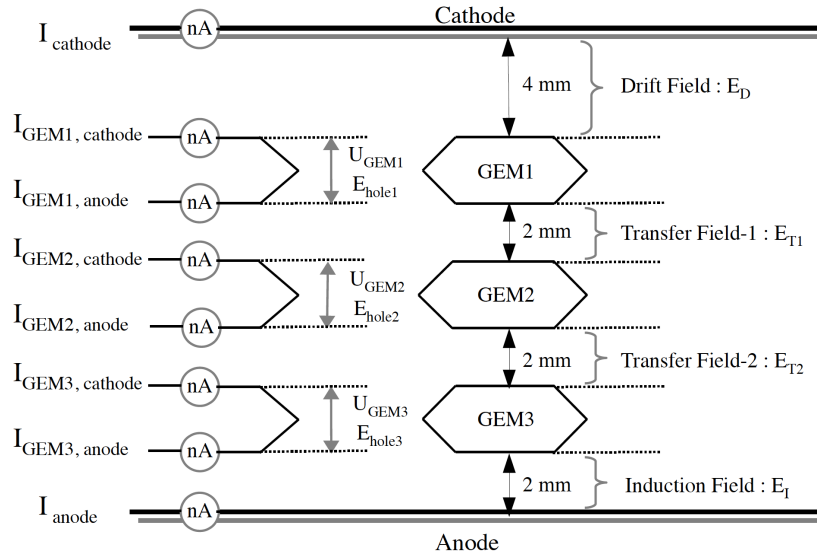
Figure 8.5 Chamber parameters indicating the voltages on each surface and produced electric fields between the surfaces, as well as the acquired currents on each surface.

The electric field created inside the GEM hole due to the voltage applied on the GEM surfaces, the so-called hole field is parametrised in [199] as following:

$$E_{\text{hole}_i} = a.U_{\text{GEM}i} + b.(E_{\text{top}} + E_{\text{bottom}}) \tag{8.13}$$

where E_{top} and E_{bottom} shows the electric fields on the top and bottom side of the corresponding GEM (see Figure 8.5). The hole field depends on the fields outside the GEM and the GEM geometry which determines the parameters of a and b. For the standard CERN GEM, these are $a = 142.87$ cm^{-1} and $b = 0.0623$ [195]. This produced hole field influences the transfer of the charge carriers through the hole of the GEMs, and it affects the coefficients determining the transfer of the charge carriers. Therefore, it is important to take into account its impact. Due to this reason, a ratio of the external field (E_{ext}), which can be any of the fields: either the drift field, one of the transfer fields or the induction field displayed in Figure 8.5 depending on the GEM, and the hole field (E_{hole}) of the corresponding GEM, which is called x, is defined as follows:

$$x = \frac{E_{\text{ext}}}{E_{\text{hole}}} \,. \tag{8.14}$$

It reduces the dependency of the measured coefficients on the GEM voltages. Hence, the coefficients of charge transfer have been studied as a function of the x variable instead of the field itself (see Section 8.7.1).

The output currents as labeled in Figure 8.5 give the number of charge carriers collected on the electrodes or on the GEM surfaces. Thus, the currents can be used to determine the charge transfer parameters. Depending on the type of the charge carriers, they can be either positive or negative in the case of electron and ion in turn. In the following section, the charge transfer parameter will be defined in terms of the output currents al well, and these definitions will be used while discussing the results of the measurements in Section 8.7.1.

8.4.1 Charge Transfer Coefficients

The main charge transfer coefficients are the collection and the extraction efficiencies for the electrons and ions, and the gain of a single GEM. The total gain of a GEM stack and the ion back flow are the others coefficient parameters determining the performance of the amplification. Since a current gives the number of particles on the corresponding surface, the definition of the parameters in terms of currents will be also explained in this section. In the case of having more than one GEM, the hole field of a GEM will have a contribution to the current on the other GEM surfaces which results in overlaps of the currents. Therefore, one can calculate the parameters only at a certain GEM which is less influenced by the other GEMs. The definitions of the parameters are based on [195].

8.4.1.1 Collection Efficiency

The collection efficiency describes how many electrons or ions are collected into a GEM hole as shown in the left sketch of Figure 8.6 [99]. In the figure, three of the field lines out of four are collected into the hole by resulting 75% collection efficiency. In general, it can be calculated [195] as follows:

$$C^{\pm} = \frac{N_{(e^-, I^+) \text{ collected into hole}}}{N_{(e^-, I^+) \text{ in front of GEM}}} \,. \tag{8.15}$$
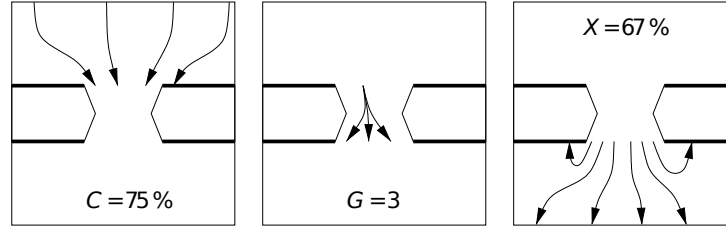
Figure 8.6 Charge transfer coefficients; (left) collection efficiency into a GEM, (middle) gain in a GEM, (right) extraction efficiency from a GEM. Figure is taken from Ref. [99].

The dependency of the parameter on the place of GEMs differs for the electrons and ions. The idea behind it will be explained in the following.

Electron Collection Efficiency : Since the electrons that reach the GEM hole are amplified, it is not possible to determine the collection efficiency and the gain separately. Hence, different drift field values are considered to determine the collection efficiency, and the maximum anode current is assumed as a value giving maximum efficiency and the efficiency curve is normalised according to this.

$$C^-_{(\text{GEM1})}(E_{\text{D}}) = \frac{I_{\text{anode}}}{I_{\text{anode,max}}} \tag{8.16}$$

The changes made on the drift field will affect the amount of particles which are collected into the GEM1 hole and the amplification within the GEM1 will be influenced as well. Therefore, it will directly affect the current measured on the anode. This dependency is taken into account when the collection efficiency parameter is measured as a function of the x parameter, where x=$E_{\text{D}}/E_{\text{hole1}}$, instead of the drift field.

Ion Collection Efficiency: This parameter can be calculated for GEM2 considering the currents in the case of GEM3 is switched off and on. To determine the fraction of extracted GEM3 ions to be collected into the GEM2 hole, one can calculate the ratio of how many of them end up on the GEM2 anode and then subtract it from one as given by

$$C^+_{(\text{GEM2})}(E_{\text{T2}}) = 1 - \frac{I_{\text{GEM2,anode}} - I^0_{\text{GEM2,anode}}}{-(I_{\text{GEM3,anode}} + I_{\text{anode}}) + I_{\text{GEM3,cathode}}}. \tag{8.17}$$

$I^0_{\text{GEM2,anode}}$ is the current when GEM3 is switched off, which gives the number of the electrons ending up on the GEM2 anode. When it is subtracted from the current while GEM3 is switched on, it gives the number of ions collected on the GEM2 anode meaning that they are not collected in the GEM2 hole. The denominator is the total number of ions in front of GEM2. -($I_{\text{GEM3,anode}} + I_{\text{anode}}$) is the negative sign of the total number of electrons produced by GEM3 which composes a big part of the number of ions created in GEM3. The rest can be obtained adding the current on GEM3 cathode that is the number of ions which end up on the electrode of the GEM3. Since the parameter is calculated based on GEM2 and using the relation with GEM3, the transfer field-2 (E_{T2}) is scanned over a range.

193

8.4.1.2   Extraction Efficiency

The extraction efficiency is a measure of the number of the extracted particles from a GEM compared to the particles inside the GEM hole as shown in the third sketch of Figure 8.6 [99]. The figure shows an extraction efficiency of 67%.The efficiency is calculated with the following formula [195]:

$$X^{\pm} = \frac{N_{(e^-, I^+)} \text{ extracted from GEM}}{N_{(e^-, I^+)} \text{ in GEM hole}} \, . \tag{8.18}$$

It is a valid parameter for both electrons and ions, however for ions it has one additional definition depending on the place where they are extracted from. If they are extracted from a GEM in which they are produced, it is called *primary extraction efficiency.* This is similar to the extraction efficiency of electrons. If they are extracted from a different GEM, then the situation becomes different and it is called *secondary extraction efficiency* as shown in Figure 8.7. In this case the collected ions mainly stay in the centre, because diffusion is negligible and only the field lines in the centre of the previous GEM can reach the other GEM passing through the centre of the GEM. Since in the former case the ions close to the corners will end up on the electrodes, the secondary extraction efficiency is larger than the primary extraction efficiency.
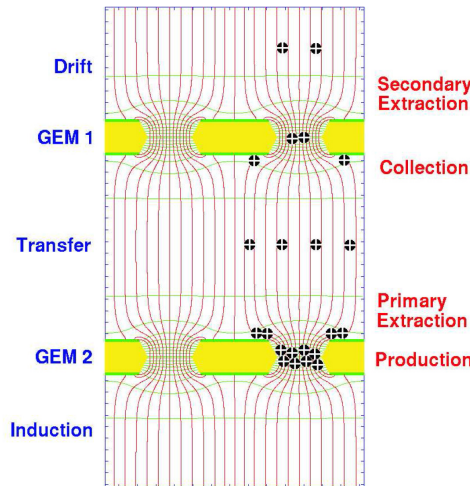
Figure 8.7 Primary and secondary extraction efficiency of ions. Figure is taken from Ref. [195].

Electron Extraction Efficiency: The electron extraction efficiency is calculated with GEM3, because both the anode and GEM3 anode have no effect from ions going back or the electrons created in other GEMs. The number of extracted electrons from GEM3 are equal to the anode current, while the created number of electrons are calculated with the sum of the extracted number of electrons and the number of electrons ending up on GEM3 anode. In this case the value of the currents are obtained after a scan of the induction field (E_{I}), and the efficiency is calculated as follows [195]:

$$X^-_{(\text{GEM3})}(E_{\text{I}}) = \frac{I_{\text{anode}}}{I_{\text{anode}} + I_{\text{GEM3,anode}}} \, . \tag{8.19}$$

Ion Extraction Efficiency: The primary extraction efficiency of the ions also depends on GEM3, while the secondary extraction efficiency depends on GEM1. For the former efficiency, one needs to scan the value of transfer field-2 (E_{T2}), while the drift field E_D needs to be scanned for the latter efficiency.

The primary extraction efficiency can be defined with the following formula:

$$X^+_{\text{prim,(GEM3)}}(E_{T2}) = \frac{I_{\text{GEM3,anode}} + I_{\text{anode}} + I_{\text{GEM3,cathode}}}{I_{\text{GEM3,anode}} + I_{\text{anode}}} \tag{8.20}$$

where the sum of the GEM3 anode and the anode currents gives the number of electrons created in the GEM3 hole, and the negative sign of it is a measure of the number of ions. $I_{\text{GEM3,cathode}}$ is the number of ions which are not extracted from GEM3.

The secondary extraction efficiency calculation for GEM1 is a bit more clear, since there is no effect from electrons. The number of extracted ions can be divided by the sum of the extracted ions and the ions which end up on GEM1 cathode:

$$X^+_{\text{sec,(GEM1)}}(E_D) = \frac{I_{\text{cathode}}}{I_{\text{cathode}} + I_{\text{GEM1,cathode}}} \,. \tag{8.21}$$

8.4.1.3 Gain of a Single GEM

The gain of a single GEM can only be calculated for electrons, since only the electrons are amplified. The gain of a GEM shows how efficient the amplification is, and it is calculated by dividing the number of electrons created in a GEM hole by the number of collected electrons into the hole [195] as follows:

$$G = \frac{N_{(e^-)\text{ in a GEM hole}}}{N_{(e^-)\text{ collected into hole}}} \tag{8.22}$$

This can be seen from the second sketch of Figure 8.6 as well [99]. To avoid the effect of other GEMs and ions, generally it is calculated based on GEM3. For this, first of all the current on the cathode of GEM3 is measured when no voltage applied on the electrodes of GEM3. This current corresponds to the number of electrons arriving in front of GEM3. Then the measurement is repeated after the voltage on GEM3 is switched on. Considering the collection efficiency of electrons into GEM3 hole is 100%, the sum of the currents on the anode and the GEM3 anode correspond to the number of electrons after amplification. So the gain can be calculated in terms of currents as below [195] :

$$G_{\text{(GEM3)}} = \frac{I_{\text{anode}} + I_{\text{GEM3,anode}}}{I_{\text{GEM3,cathode}(U_{GEM3}=0)}} \,. \tag{8.23}$$

8.4.2 Total Gain and Ion Back Flow

The total gain of a GEM stack is proportional to the current on anode, since it shows the amount of electrons which successfully reaches the anode after amplification. So it can be represented by

$$G_{\text{total}} \propto I_{\text{anode}} \,. \tag{8.24}$$

The ion back flow effect of the TPC is a significant issue which needs to be addressed (cf. Section 4.3.1.3). As explained in Section 4.3.1.3, the ions produced in the primary ionisation, but especially in the amplification phase cause shift of the electrons transverse direction which can be seen in Figure 4.9. Therefore, the amount of the ions, which drift back, should be kept as low as possible. This amount can be calculated by the following ratio in terms of the number of electrons and ions [195]:

$$I_{bf}^{+} = \frac{N_{(I^{+}) \text{ drifting back}}}{N_{(e^{-}) \text{ on anode}}} \, . \tag{8.25}$$

One can convert this as a ratio of cathode and anode currents for the number of ions drifting back and the number of ions created in total which is equal to the number electrons on the anode:

$$I_{bf}^{+} = \frac{I_{\text{cathode}}}{I_{\text{anode}}} \, . \tag{8.26}$$

8.5   Experimental Setup with a Triple GEM

The setup consists of a small gas filled chamber which contains a GEM stack with three GEMs, an anode and a cathode. Each layer, meaning each surface of the GEMs and the electrodes, is connected to a high voltage (HV) power supply via current monitors called CUMOs to read out the currents. A radioactive source ^{55}Fe is used to produce ionisation. A detailed explanation of the setup is given in [195, 198]. It will be briefly summarised in the following.

The chamber and the whole setup are shown in Figure 8.8. As seen in the detailed view of the setup, the bottom part of the chamber consists of a copper plate which is the anode, then three GEMs are placed on top in spacing of 2 mm. As a top most part of the stack the cathode is mounted 4mm away from the first GEM. The cathode is made of an aluminised mylar foil with $8\,\mu$m thickness. To cover the gas volume, another thin mylar foil is glued to the composite frame. Such a thin foil is chosen for both the cathode and the cover, because the photons coming from the radioactive source need to go through the cover and the cathode to reach the drift region.

The current monitor CUMO is a nano ampere meter which has a reading accuracy of 0.01 nA in the smallest measurement range of $\pm$ 20 nA. The highest range is the $\pm$ 20 μA. It is working with the automatic range selection, if the currents exceed the percentage of the corresponding range, then the range of the CUMOs is set to high. Both the HV power supply and the CUMOs are connected to a PC. With the help of a software, called `xtc`, connection between the parameters can be easily made. `xtc` stands for X Window System Test Chamber. It has a multi-functional interface which is represented in Figure 8.9. In the left part of the interface, it is seen that the voltages applied to the GEMs and the electric fields between layers can be set, and they can be controlled with the *HV* buttons below. In the right part, the output currents and their errors for all the channels can be read out. Range information of the currents, which shows the level of the uncertainity on the measurments, is given with the coloured spectrum. In addition to HV buttons, there are more helpful choices, such as *Zero Offsets* which makes zero offset by considering the leakage currents and CUMO offsets by closing the shutter to eliminate charge creation by the source. Using *Interval* button, one can set the requested interval for a measurement, and the *Read* button can be used to read out the currents once or with regular
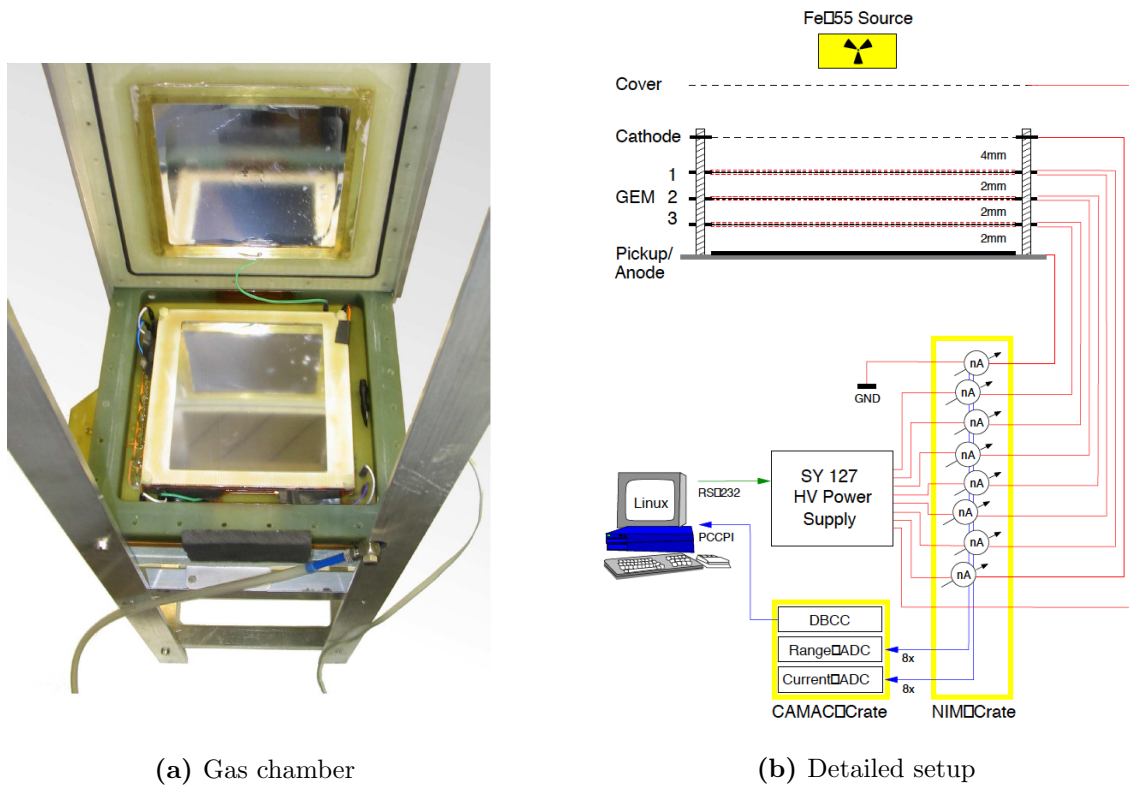
(a) Gas chamber   **(b)** Detailed setup

Figure 8.8 (a) A photograph of the gas chamber, (b) A sketch of the detailed setup including chamber layout, radioactive source, and connections to high voltage and current monitors. Figure is taken from Ref. [195].

intervals. In addition to these two ways to read out the result, one can also execute a script to run more measurements in one go. The software can monitor magnetic field and temperature information as seen on the right bottom part of its interface.

Throughout the studies, in addition to the measurements done for charge transfer coefficients, temperature sensors were added to the system in order to monitor temperature changes. Temperature differences of the order of one degree has been observed which does not influence the results.

8.6 Measurement Settings

This study is based on mainly comparison of three gases with standard settings that are given in Table 8.1. In the standard settings, GEM voltages and transfer fields are kept the same for each gas. The induction field is generally higher than the transfer fields to get more signal strength by increasing the extraction efficiency of electrons as explained in the next section. In the case of drift field, more focused distribution of the field lines are preferred to ensure more primary particles go into the GEM holes. Therefore the difference between GEM1 voltage U_{GEM1} and

Figure 8.9 A screen shot of the user interface of the `xtc` software. The field values are shown on the left, while the output currents on each surface can be read from the right panel. Figure is taken from Ref. [195].

drift field E_D is kept small. In the table, the values labelled with a star (*) are reduced to 1500 V/cm to be able to reach the maximum high voltage limited by the power supply.

Parameters		E_D [V/cm]	U_{GEM1} [V]	E_{T1} [V/cm]	U_{GEM2} [V]	E_{T2} [V/cm]	U_{GEM3} [V]	E_I [V/cm]
T2K	STD	250	270	1500	270	1500	270	3000*
P5	STD	200	315	2500	315	2500	315	5000*
TDR	STD	250	310	2500*	310	2500*	310	5000*

Table 8.1 Settings for T2K, P5 and TDR gases for $B = 0$. The given settings are used in all scans apart from the scan of the drift field E_D. The values labelled with star are reduced to the value of 1500 V/cm in the scan of E_D. The setting for T2K, P5 and TDR gases are respectively taken and adapted (if necessary) from Refs. [198, 194, 195].

Although the settings given in Table 8.1 are used as standard settings (STD), measurements with various GEM voltages are performed as well. They are used in some cases to demonstrate

Parameter	U_{GEMi} [V]		
T2K	260	270	280
P5	310	315	320
TDR	310	315	-

Table 8.2 GEM voltages for T2K, P5 and TDR gases, where i=1,2,3, and refer to the three GEMs composing the stack.

the dependency on GEM voltages. For T2K and P5 gases the measurements are done with three

different GEM voltages, while for TDR two different GEM voltages are considered as listed in Table 8.2.

In Section 8.4.1, the dependency of the charge transfer coefficients on the fields are explained. Due to these dependencies, the measurements are done by scanning the corresponding electric fields. The parameters and their scanned ranges with the step sizes are represented in Table 8.3.

Parameters	E_D [V/cm]	E_T2 [V/cm]	E_I [V/cm]	U_GEM3 [V]
Range	100 - 3800	100 - 5000	0 - 5000	0 - U_GEM
Step	20	20	20	5

Table 8.3 Scanned ranges and steps of the related variables.

Using the STD settings the measurements are done for all three gases, T2K, P5 and TDR, and the results will be shown in the next section. Before the comparison of T2K, P5 and TDR gases, the measurements with the STD settings using various GEM voltages are compared with the past measurements for each gas [198, 194, 195] by using the collection efficiency of electrons. The settings used in the past measurements are given in Table 8.4.

Parameters	E_D [V/cm]	U_GEM1 [V]	E_T1 [V/cm]	U_GEM2 [V]	E_T2 [V/cm]	U_GEM3 [V]	E_I [V/cm]
T2K @ DESY, 2014	250	280	1500	280	1500	280	3000
P5 @ Aachen, 2003	200	320	2500	320	2500	320	5000
TDR @ Aachen, 2006	600	320	2500	315	2500	315	0

Table 8.4 Settings used in the past studies. TDR measurements were done with a magnetic field of $B = 4\,\mathrm{T}$. Settings for T2K, P5 and TDR gases are respectively taken from Refs. [198, 194, 195].

In addition to the STD settings, another setting which reduces the ion back flow (IBF) is considered as well for T2K and P5 gases. The main idea for the reduced ion back flow setting

Parameters		E_D [V/cm]	U_GEM1 [V]	E_T1 [V/cm]	U_GEM2 [V]	E_T2 [V/cm]	U_GEM3 [V]	E_I [V/cm]
T2K	IBF	250	230	2500	260	290	290	4500*#
P5	IBF	200	285	3500	315	700	320	6500*+

Table 8.5 Ion back flow settings in order to reduce the amount of ions drifting back for T2K and P5 gases. Labels *, #, and + mean that E_I is reduced to $1500\,\mathrm{V/cm}$ for E_D scan, $3000\,\mathrm{V/cm}$ for U_GEM3 scan, and $5000\,\mathrm{Vcm}$ for U_GEM3 scan, respectively. The settings for T2K gas are taken from Ref. [198].

is to have less ions drifting back in the TPC volume, while keeping the number of electrons the same. To be able to do this, settings are arranged as shown in Table 8.5. U_{GEM1} is reduced to produce less electron-ion pairs in the first GEM while keeping other GEM voltages high to produce more electron-ion pairs in the others. The ions created in the first GEM go directly to the cathode, so it is important to produce less ions in this step; however, the ions created in the other GEMs can be collected during their way to the cathode. E_{T1} is increased to extract more electrons from GEM1 hole, and E_{T2} is decreased to collect more ions on the GEM3 cathode.

The IBF settings will only be displayed in terms of the total gain of a GEM stack and the ion back flow. In this step the measurements done with the STD settings using different GEM voltages will be also used in order to show the dependency of the total gain and ion back flow on the GEM voltages.

8.7   Measurement Results

The main aim of this study is to compare the behaviour of the charge transfer coefficients using three commonly investigated gases which are the T2K, P5 and TDR, in the same setup, in order to enhance the understanding of the dependency of the charge transfers on the gas mixtures. To do this, as a first step, the currents on each surface are measured after applying high voltages on each GEM surface and electrode, and the definition of the coefficients in terms of output currents described in Section 8.4 are used.

During the measurements, after the desired settings given in Section 8.6 are achieved, currents are internally read 100 times, which produces a Gaussian distribution. The mean and error of the distribution correspond to the value of the current, and its statistical error. Table 8.6 displays the measured currents acquired using the standard settings (see Table 8.1). The table

Currents [nA]	T2K	P5	TDR
I_{cathode}	-5.589 ± 0.003	-0.776 ± 0.002	-0.661 ± 0.002
$I_{\text{GEM1,cathode}}$	-37.747 ± 0.049	-9.133 ± 0.006	-5.958 ± 0.006
$I_{\text{GEM1,anode}}$	-0.010 ± 0.005	-0.594 ± 0.008	-0.566 ± 0.006
$I_{\text{GEM2,cathode}}$	-17.070 ± 0.006	-2.404 ± 0.006	-1.852 ± 0.003
$I_{\text{GEM2,anode}}$	6.274 ± 0.005	0.303 ± 0.007	-0.144 ± 0.004
$I_{\text{GEM3,cathode}}$	-295.278 ± 0.806	-15.575 ± 0.009	-11.660 ± 0.006
$I_{\text{GEM3,anode}}$	197.516 ± 0.227	14.976 ± 0.007	10.786 ± 0.005
I_{anode}	145.506 ± 0.179	12.813 ± 0.006	9.750 ± 0.004

Table 8.6 The measured currents on the electrodes and each surface of the GEMs using the STD settings given in Table 8.1. The negative currents are caused by the ions, while the positive currents stemming from the electrons.

shows that for the given standard settings, the T2K gas produces much more electrons compared to the P5 and TDR, which is seen by the current on anode. It is seen that the currents can be

measured with a reasonably small uncertainty. In Table 8.7, one can see the measured currents on anode obtained with the standard settings but using different GEM voltages as listed in Table 8.2. It indicates that changing the GEM voltages by 5 to 10 V changes the current on anode drastically for T2K, and moderately for both P5 and TDR. This provides a high gain by increasing the GEM voltages in the case of T2K gas.

	Current on Anode [nA]		
Settings	T2K	P5	TDR
STD$|_{U_{GEM}=U_{std}}$	145.506 ± 0.179	12.813 ± 0.006	9.750 ± 0.004
STD$|_{U_{GEM}<U_{std}}$	70.056 ± 0.094	8.694 ± 0.004	$-$
STD$|_{U_{GEM}>U_{std}}$	294.483 ± 1.070	18.888 ± 0.006	14.632 ± 0.005

Table 8.7 The measured currents on anode using the STD settings, but with different GEM voltages given in Tables 8.1 and 8.2. The first row corresponds the STD settings (T2K$|_{U_{std}=270}$, P5$|_{U_{std}=315}$, and TDR$|_{U_{std}=310}$), while the second row corresponds to the standard settings if the GEM voltages are smaller than the one in STD setting (T2K$|_{U_{GEM}=260}$, P5$|_{U_{GEM}=310}$, and $-$). The third row shows the case when the GEM voltages are higher than the one used in STD setting (T2K$|_{U_{GEM}=280}$, P5$|_{U_{GEM}=315}$, and TDR$|_{U_{GEM}=315}$).

Finally, Table 8.8 indicates the anode currents and the ion back flow for both standard settings and optimised settings for ion back flow. The table shows that the chosen IBF settings do not provide amplification in the same level as the STD settings, but they reduce the ion back flow for both P5 and T2K gases. The given values of the currents in Tables 8.6 and 8.7 correspond

	Anode Current [nA]		Ion Back Flow	
Settings	T2K	P5	T2K	P5
STD Setting	145.506	12.813	0.038	0.061
IBF Setting	16.396	5.154	0.021	0.024

Table 8.8 The measured currents on the anode and ion back flow using the STD and IBF settings given in Tables 8.1 and 8.5.

to one working point. In order to determine the behaviour of the charge transfer coefficients, the field values have been varied as shown in Table 8.3, and the current values for each point are repeated and the results are stored. In the following, first of all, the results of the charge transfer coefficients will be compared with the past measurements, and then the results of the measurement of the charge transfer coefficients will be presented and explained in order to compare the behaviour of the different gas mixtures. After that the investigation of the charge up effect will be described and discussed in Section 8.7.2.

8.7.1   Charge Transfer Coefficients

Since the motivation of this study was to investigate the discrepancy between the T2K gas measurements [198] and the electrostatic parametrisation [199] which agreed well for P5 [194] and TDR gases [195], as a first step the past results were reproduced. The comparison between past measurements and parametrisation is shown in Figure 8.10. The dots show the measurement results, while the lines show the parametrisation [199]. As seen from the figure, the P5 and TDR results agree very well with the parametrisation, whereas the T2K gas does not agree. To investigate this discrepancy, the collection efficiency of electrons have been measured for all three gases in the same setup, and the results will be displayed in the following section. Following that, the comparison of three gases will be presented for each charge transfer coefficient.
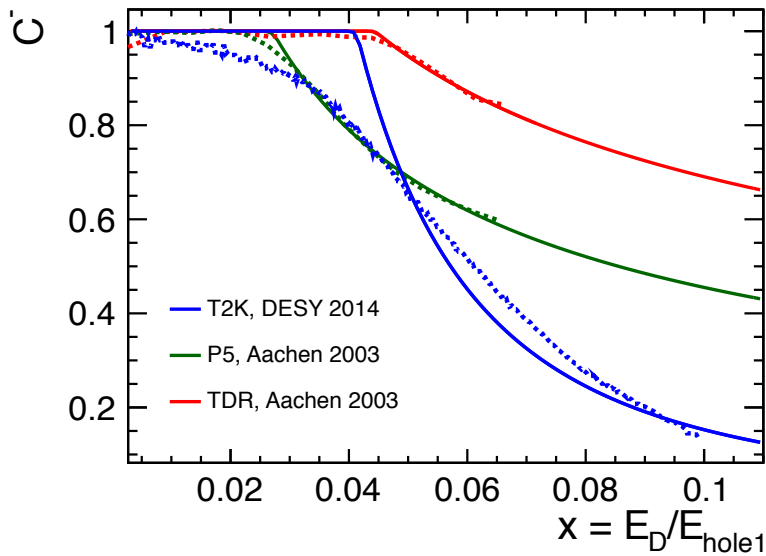
Figure 8.10 The charge collection efficiencies of electrons as a function of $x = E_\mathrm{D}/E_\mathrm{hole1}$ for the past measurements [198, 194, 195] and their compatibility with the parametrisation [199] for T2K, P5 and TDR gases. The dots show the measurement results, while the lines show the parametrisation. Figure is adapted from Ref. [213].

Collection Efficiency

Figure 8.11 shows the collection efficiency of electrons as a function of the field ratio, $x = E_\mathrm{D}/E_\mathrm{hole1}$ for the new and past measurements for each gas separately. It is displayed for different GEM voltages as well to show how the parameter changes depending on the GEM voltages. In terms of GEM voltages, it is clear that the dependency is negligible, especially for P5 and TDR gases, while there is a slight dependency for T2K gas. The results show a good agreement with the past measurement results. For P5 gas, the shape of the efficiency curve fits well, but the past measurement gives slightly higher values.

(a) P5 gas

(b) TDR gas

(c) T2K gas
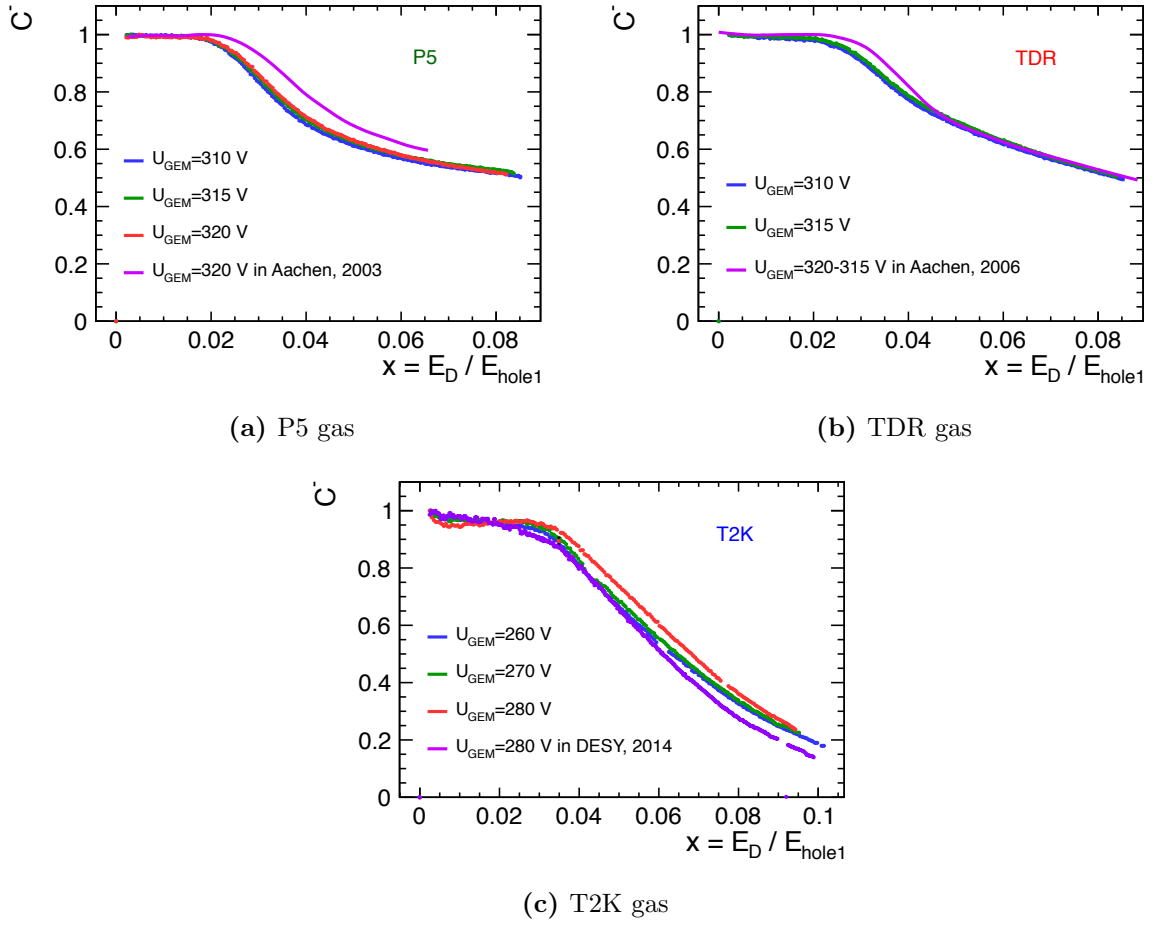
Figure 8.11 The measurement results for the charge collection efficiencies of electrons for three gases including different GEM voltages and comparison with the past measurements [198, 194, 195] is shown. In general, the blue, green and red lines show the results for various GEM voltages, while the violet line represents the result from past studies.

In order to compare the T2K, P5 and TDR gases, the collection efficiency of electrons and ions are represented as a function of x in Figure 8.12. Figure 8.12a shows the electron collection efficiency for all gases. In general, it shows that the P5 and TDR gases have a similar behaviour, while T2K behaves differently, especially in the high drift field region. In the low field region, all gases have almost constant and maximum efficiency. As the drift field increases, the electric field lines start to end up on the GEM surfaces which reduces the collection efficiency of electrons. However, the decrease is not the same for all gases. The collection efficiency decreases more at high drift field regions for T2K gas. The explanation to this could be the different attachment rates of the gases, which are approximately 0.2, 0.8, and 4 at the 3000 V/cm corresponding to $x \approx 0.08$ for respectively P5, TDR and T2K gas, as seen in Figure 8.4. This means that in the case of T2K, more primary electrons attach to the gas in the drift region which makes the signal strength smaller in the high drift field compared to other gases. This is an important feature

(a) Electron Collection Efficiency

(b) Ion Collection Efficiency
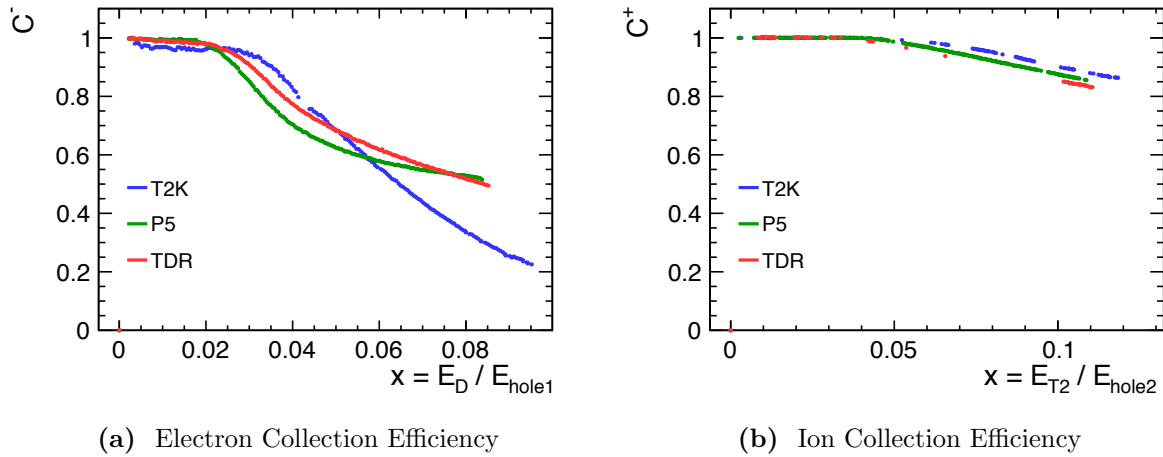
Figure 8.12 The measurement results for the collection efficiency for three gases as a function of corresponding field ratio for (a) electrons and (b) ions. Blue points show the result for T2K gas, while green and red points represent the P5 gas and TDR gas respectively.

of the T2K gas which makes it different than the other gases, and explain the discrepancy with the electrostatic parametrisation.

The collection efficiency of ions is indicated in Figure 8.12b, which shows that the gas type does not affect the collection efficiency of ions, since all gases show a similar behaviour. As seen from the plot, some points are missing due to the fluctuation of the field values during the scan. If the fluctuation on the measured value is larger than the expected value, the points are not considered. The situation has been updated after this study, and it can be seen in [198]. The dependency of the collection efficiency on the field ratio is not as strong as the electron's. However, it still gets lower at higher ratios almost in the same level for all gases.

Gain of a Single GEM

The gain of a single GEM calculated using the third GEM is given as a function of GEM3 voltage in Figure 8.13a. It shows that GEM3 has similar gain curve for P5 and TDR gases. The curve starts to increase after approximately 200 V for P5 and TDR gases, while this value is 150 V for T2K gas. It means that the amplification starts at lower GEM voltages for T2K gas. The increase on the gain of T2K gas as a function of GEM voltages is larger, so the final gain for a single GEM becomes higher than when using the other gases.

Extraction Efficiency

The extraction efficiency of electrons depends almost linearly on the field ratio $x = E_I/E_{hole3}$ as seen in Figure 8.13b. The curves of the different gases are comparable with each other. From this distribution one can deduce that to extract electrons from GEMs more effectively, higher induction fields should be chosen.

(a) Gain of a single GEM

(b) Extraction efficiency of electrons
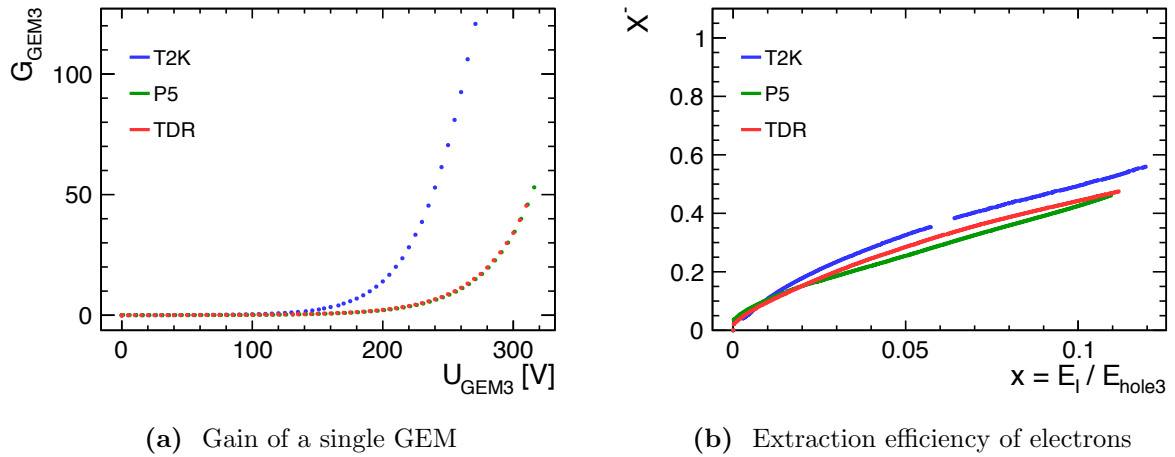
Figure 8.13 The measurement results for (a) the gain of a Single GEM as a function of GEM3 voltage, (b) the extraction efficiency of electrons as a function of x parameter for all gases.

The primary and secondary extraction efficiencies of ions are presented in Figure 8.14. As expected the secondary extraction efficiency is higher than the primary one by definition as explained before. The primary extraction efficiency looks almost the same for P5 and TDR gas, while it is lower for T2K gas. The secondary extraction efficiency gets higher values for TDR gas for $x < 0.05$. However, in higher x values, T2K is getting closer to the TDR curve, while P5 stays always lower than the other two gases.

(a) Primary Extraction Efficiency

(b) Secondary Extraction Efficiency
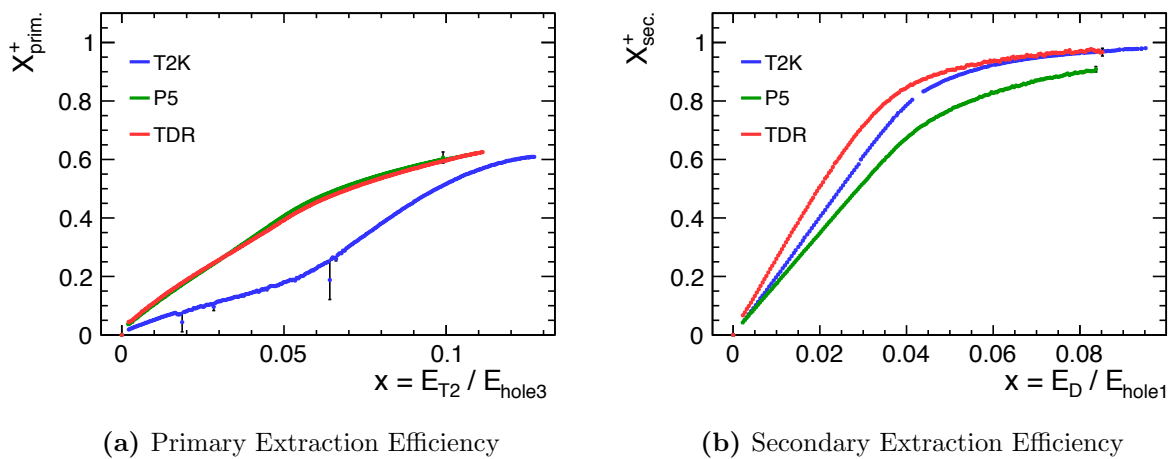
Figure 8.14 The measurement results for (a) the primary extraction efficiency, (b) the secondary extraction efficiency of ions for all gases

Total Gain and Ion Back Flow

Figure 8.15 shows the current on anode for T2K and P5 gases. In the figure, the STD settings with various GEM voltages as well as the IBF settings are compared. Higher GEM voltages yield higher gain in both gases, while the IBF settings give lower gain compared to the STD settings. Concerning the gases, the achieved gain for T2K gas is nearly 10 times higher than the P5 gas.

(a) T2K gas
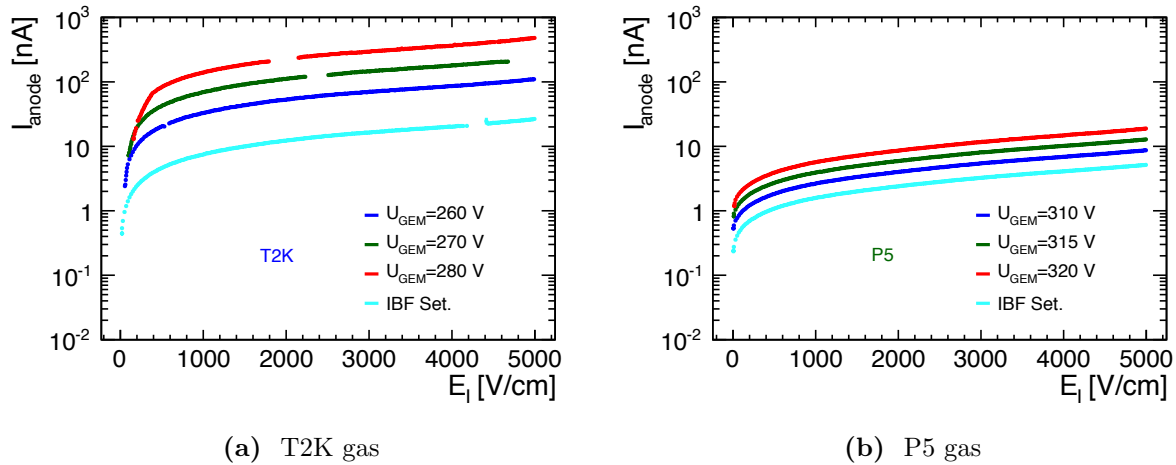
(b) P5 gas

Figure 8.15 The measurement results for the current on anode, which is proportional to the gain, using the STD setting with various GEM voltages, and the IBF settings for (a) T2K and (b) P5 gases.

The ion back flow is indicated using the same settings with the total gain in Figure 8.16. The different behaviour of T2K gas can be seen in this figure as well. The ion back flow changes depending on the total gain or GEM voltages, whereas this is not visible in the case of P5 gas. For T2K gas, the ion back flow is reduced as the GEM voltages are increased. The IBF settings help to reduce it even further. For P5 gas, the gain does not influence the amount of the ions drifting back; however the IBF settings reduce the ion back flow in a significant level.

However, one shouldn't forget that the gain is lower in minimal ion back flow setting compared to the standard settings as shown in Figure 8.13a. Therefore, the amount of the reduction would be affected when the gain is the same in both settings. Moreover, the settings used in the analysis are not optimised for the minimum ion back flow, but they are sufficient to show the dependency on the gas type.

8.7.2   Investigation of Charging Up Effects on the Measurements

In the beginning of the amplification stage, some of the produced electrons are accumulated on the dielectric kapton layer of the GEM [214, 215]. This process is known as the charging up process, and it affects the gain of the GEMs. It not only reduces the number of electrons

(a) T2K gas   **(b)** P5 gas
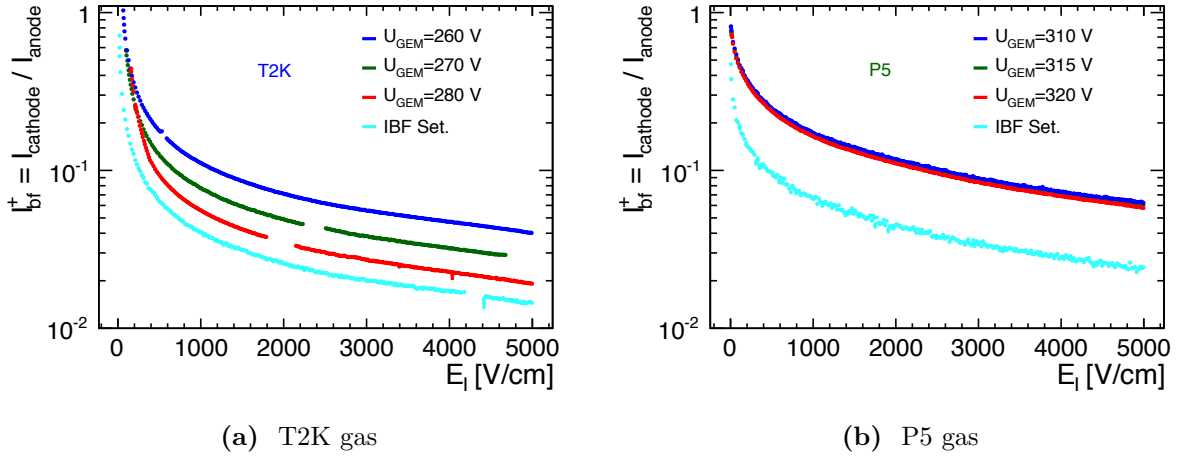
Figure 8.16 The measurement results for the ion back flow using the STD setting with various GEM voltages, and the IBF settings for (a) T2K and (b) P5 gases.

reaching the anode, but also affects the field in the GEM hole due to the field created by the collected charges on the kapton layer. After some time the layers are getting fully charged, and they don't accept any other charges so that the current on the anode has its maximum value. Thus, if the measurements are done before charging up the GEMs, the result might be affected from this situation. One of the aim of this study was to examine this charging up effect on measurements.

This study has been mainly performed by considering one of the charge transfer coefficient parameter, the electron collection efficiency of electrons, which is determined by the first GEM (GEM1). Since the charging up process is faster for other two GEMs due to the large amount of the charges involved in the amplification, the effect of those can be neglected. The collection efficiency was measured when the system is uncharged, and after charging up the system as shown in Figure 8.17. It is seen that the charging up system influences the results, in particular for low field ratio values. The obtained electron collection efficiency is lower in the case of uncharged system. For high x values, the electron collection efficiency is higher for uncharged system, but the behaviour of the curve is similar to the one with charged system. Therefore, the main impact of the uncharged system is experienced in the low drift field region.

To investigate this, measurements using the standard settings without any scanning were done with an interval of 5 seconds during 4 hours after opening the shutter. Figure 8.17b shows the anode current behaviour while the system is charging up for different cases including the measurements with uncharged GEMs and with several discharging time options. The red curve shows the situation with the uncharged GEMs, while the other curves are obtained after waiting a given time interval to discharge the charged GEMs. The plot is normalised considering the max current on anode. The figure provides information on the time needed to have a completely charged GEMs, and on the necessary time to discharge the GEMs. The former case corresponds to the case when the current on anodes becomes constant as a function of time, which is approximately three hours. For the latter, the part where the currents are increasing is important.

It is clear that the GEMs are still charged after discharging them two hours. Even after five hours discharging, the curve is not fully consistent with the one describing the uncharged GEM. It is however very compatible. Therefore, it can be considered as uncharged GEMs. Since the minimum values of current for three, four or five hours discharging are more or less in the same level, it can be concluded that minimum three hours would be enough to discharge the GEMs down to a reasonable level.
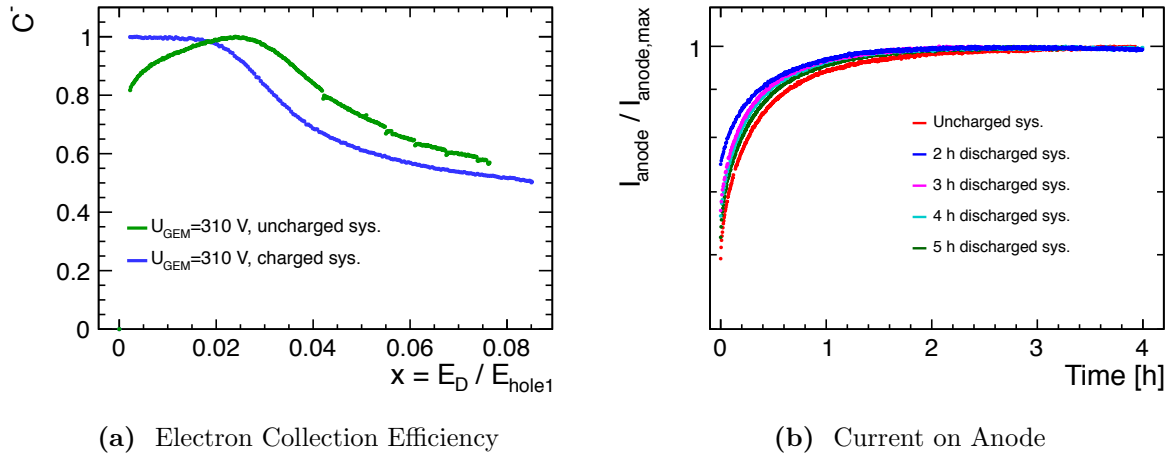

(a) Electron Collection Efficiency

(b) Current on Anode

Figure 8.17 The measurement results for (a) the collection efficiency of electrons using the uncharged and charged GEMs quoted as system in the figure, (b) the current on anode in the charging up process of the GEMs for P5 gas.

8.8 Summary

The gas type is one of the most important points which needs to be studied in detail before making a decision about the type of gas that will be used in the TPC. There are three commonly studied gases by the ILD TPC collaboration, which are T2K, P5 and TDR gas. T2K gas is foreseen as a TPC gas nowadays, however a discrepancy has been observed between the measurements of T2K gas and the electrostatic parametrisation of the charge transfer coefficients [198]. In order to understand the behaviour of T2K gas, an investigation by studying all these gases under the same conditions and comparing them in terms of charge transfer coefficients, such as collection and extraction efficiencies for both electron and ions, as well as gain in a GEM hole, has been performed in the context of this thesis.

In addition, the charge up effects, that affect the gain of GEMs, has been studied as well. It has been showed that in order to avoid the observed charging up effect of the GEMs, one needs to wait at least three hours before starting to take data after allowing the passage of the particles, ionisation and amplification for the studied setup. In the case of ILD, waiting times could differ, but the charging up of a GEM would influence the measurements, therefore it should be taken into account in a long scale experiment as well.

In the first part of the study, as a first step, the results of the measurements have been compared with past studies [194, 195, 198] in order to check the compatibility of the measurements, and it has been acquired that the results are in good agreement. In the next step, the charge transfer coefficients of three gas mixtures have been compared for a given standard setting. As a result of those studies, it has been observed that the gas type has a crucial impact on some of the charge transfer coefficients, in particular collection efficiency of electrons. The P5 and TDR gas provide similar efficiency, while T2K has low efficiency at the high drift field region. The main reason for this is the high attachment rate of T2K gas. It has been concluded that this is a feature of the gas which explains the seen discrepancy. As a consequence, a new parametrisation including the effect of the attachment rate has been introduced in [198].

Even though, T2K gas gives lower collection efficiency at high drift field, this shortcoming can be compensated easily by the advantages of the gas. One of the advantages is the high gain which can be obtained with T2K gas. In addition, T2K gas has a high drift velocity and low transverse diffusion in contrary to others, which would increase the spatial resolution. Another important point is that the working point of the drift field, chosen as the value giving highest drift velocity, is relatively small such that the result will not be affected by the decrease on the collection efficiency of electrons at high drift fields ($E_D \approx 250\,\mathrm{V/cm}$ ($x \approx 0.005$) for T2K gas). Because of these, one would consider T2K gas as a good candidate for being used in the TPC of ILD.

Chapter 9

Conclusion

The discovery of the Higgs boson at the LHC enlightens the origin of the fermion and gauge boson masses, but also raises the question how the mass of the Higgs boson can be stabilised to its measured value in spite of quadratic divergences caused by large loop contributions. Supersymmetry is one of the proposed theories that can explain the mass of the Higgs boson by cancelling the quadratic divergences. To avoid the regeneration of any divergences on the mass of either the Higgs boson or Z boson, it is required that the scalar top quarks and superpartners of gluons should not be very heavy, and the masses of the higgsinos should be of the same order as the Z boson mass. These scenarios are referred to as Natural SUSY. Since the LHC experiments have not found any sign of supersymmetric particles, the scenarios with a rather heavy coloured SUSY sector and a light electroweak SUSY sector require more attention, in particular scenarios with light higgsinos. One of these scenarios has been studied in this thesis. The considered scenario includes three light higgsino-like charginos and neutralinos, $\widetilde{\chi}_1^{\pm}$, $\widetilde{\chi}_1^0$ and $\widetilde{\chi}_2^0$, with mass splittings of a few GeV or even sub-GeV, while all other supersymmetric particles are in the multi-TeV region. One should note that this is an extreme case which puts a maximum challenge to current and future experiments.

In order to research the feasibility of searching for such Natural SUSY scenarios at the International Linear Collider (ILC), in the first part of the thesis, the analysis of the scenario has been conducted using fast detector simulation at a centre-of-mass energy of $\sqrt{s} = 500\,\mathrm{GeV}$ and an integrated luminosity of $\int \mathcal{L}dt = 500\,\mathrm{fb}^{-1}$ for polarisation combinations $P(e^+, e^-) = (\pm 30\%, \mp 80\%)$. The exclusive decay channels of the light higgsinos, produced via $e^+e^- \rightarrow \widetilde{\chi}_1^+\widetilde{\chi}_1^-\gamma$ and $e^+e^- \rightarrow \widetilde{\chi}_1^0\widetilde{\chi}_2^0\gamma$ are considered in order to disentangle the two signal processes. The hard initial state radiation (ISR) photon is required to suppress one of the dominant Standard Model background arising from the beam-beam interactions. The potential of the ILC has been studied in two different benchmark scenarios depending on the mass difference between $\widetilde{\chi}_1^{\pm}$ and $\widetilde{\chi}_1^0$. The considered mass differences are 1.6 GeV (dM1600) and 0.77 GeV (dM770). It has been shown that the masses of the $\widetilde{\chi}_1^{\pm}$ and $\widetilde{\chi}_2^0$ can be reconstructed from the reduced centre-of-mass energy recoiling against the hard ISR photon. The mass of the $\widetilde{\chi}_1^{\pm}$ can be reconstructed with a precision of 2.0 GeV for the dM1600 scenario and 1.5 GeV for the dM770 scenario, while the precisions on

the mass of the $\widetilde{\chi}_2^0$ are 3.3 GeV (dM1600) and 1.6 GeV (dM770) for the polarisation combination of $P(e^+, e^-) = (+30\%, -80\%)$, which enhances the signal. The mass difference between the chargino and the LSP can be estimated from the energy of the decay products of the charginos, boosted into the rest frame of the chargino production, with 270 MeV (dM1600) and 40 MeV (dM770) precision using the same polarisation combination.

The impact of the polarisation can be seen in the precision of the determination of the polarised cross sections. The cross section of the chargino process can be determined with an accuracy of 1.9% (dM1600) and 1.6% (dM770) with the favoured beam polarisations, while the determination can be done with 5.3% (dM1600) and 3.8% (dM770) precisions with the other beam polarisations. The polarised cross section of the neutralino processes can be estimated with 3.2% (dM1600) and 1.7% (dM770) precision for the preferential polarisations, and with a precision of 3.7% (dM1600) and 1.9% (dM770) for the other combination. Due to the effect of the interference between the Z boson and γ exchange in the s-channel production of the charginos, the cross section of the charginos depends more strongly on the polarisation compared to the neutralino case. Because of that, the obtained precisions for determining the cross sections are different. This strong dependency can be used to provide an improvement on the measurement of the observables by using the proper beam polarisations. Moreover, the measurements of the cross sections with both polarisation combinations are important for understanding the nature of the processes and for enhancing the determination of the electroweakino parameters.

The obtained precisions from the experimental observables have been used by K. Rolbiecki [2] to investigate how well the electroweakino mass parameters M_1, M_2, μ and $\tan\beta$ can be extracted. The parameter determination has been performed for both an integrated luminosity of $\int \mathcal{L}dt = 500\,\text{fb}^{-1}$ and $\int \mathcal{L}dt = 2\,\text{ab}^{-1}$. For the high integrated luminosity, assuming that the statistical uncertainty dominates the systematic uncertainty, the measurement uncertainties on the cross section are reduced by a factor of 2. In this study it has been shown that the μ parameter can be determined with an uncertainty of approximately 6.8 GeV (dM1600) and 2.5 GeV (dM770) for $\int \mathcal{L}dt = 500\,\text{fb}^{-1}$, while the uncertainty of the μ parameter is reduced to nearly 4.5 GeV and 2 GeV with the increased luminosity. It has been concluded that the lower limits for the bino and wino mass parameters M_1 and M_2 can be set around a few TeV, and the allowed region within a 1-σ contour can be determined up to a narrow band depending on $\tan\beta$. It has been shown that if one assumes the same precision of the neutralino mass difference as the chargino mass difference, the high luminosity case puts extra constraints on the allowed region of the parameter space of $M_1 - M_2$, and reduces the dependence on $\tan\beta$. Even though the fast simulation results are good enough to determine the electroweakino parameters, it has been shown that the determination of the higgsino mass parameter could be enhanced by taking data at $\sqrt{s} = 350\,\text{GeV}$, which is a threshold value for the production of higgsinos.

Considering all this, the results from the fast simulation show that such scenarios could be well observable at the ILC. However, one should note that the fast simulation study includes some simplifications such as assuming perfect particle identification, not taking into account the low p_t $\gamma\gamma$ overlay background as well as pair background which both stem from the beam-beam interaction. In order to address these simplifications and to investigate the feasibility in a more realistic way, the analysis has been extended to a full detector simulation, which constitutes

the second part of the thesis. As expected, the full simulation results have shown that the reconstruction and identification algorithms work well for high momentum particles, however, dedicated algorithms are needed to be developed for low momentum particles ($p < 2(5)\,\mathrm{GeV}$) in order to be able to perform this analysis in full simulation.

In the context of this thesis, an identification algorithm for muons with momentum less than $2\,\mathrm{GeV}$ has been developed. It has been shown that the high granularity of the particle flow calorimeters of ILD enable the separation of muons and pions using the calorimeter cluster shape differences, even at such low momentum. The developed method indicated that the muons can be identified with 80% efficiency, whereas the probability to misidentify pions as muons is 3%, but it could be improved in further studies. This indicates that the low momentum muon and pion separation should be considered as a detector design benchmark in addition to the jet energy resolution.

The ionisation energy loss measurements dE/dx, which can be used in order to identify the low momentum electrons, are provided by the Time Projection Chamber (TPC). Therefore, the dE/dx resolution and so the tracking in the TPC is important for the analysis of light higgsinos. In the third part of the thesis, the charge transfer coefficients have been measured for three different gas mixtures, which are commonly studied by the ILD TPC collaboration. This study provided a good understanding of the dependence of the charge transfer on the gas mixture. The T2K gas has been concluded to be the best, since its properties enable high spatial resolution. This provides a better precision on the dE/dx measurements, which is necessary for the electron and pion separation of the higgsino decay products.

It has been discussed that the reconstruction of the tracks needs to be tuned in order to take into account the vertex hits, especially in the presence of pair background. The vertex hits are crucial for the analysis to suppress the low p_t $\gamma\gamma$ overlay particles. However, the inclusion of the vertex hits requires an adequate pattern recognition algorithm and fast timing in order to reduce the large number of hits and fake tracks from backscattered e^+e^- pair background.

As a result of this thesis, it has been indicated that the analysis of Natural SUSY scenarios including light higgsinos puts extra detector requirements which have not been taken into account before. It has been shown that ILD has already a promising design to fulfil these requirements, but they need to be studied in more detail. Assuming that electrons can be identified with the same efficiency and purity as the muons, and tracks can be reconstructed after the inclusion of vertex hits with the same efficiency as before, the obtained results from the fast simulation analysis can be achieved in a real experiment by taking data at a centre-of-mass energy of $\sqrt{s} = 500\,\mathrm{GeV}$ with an integrated luminosity of $\int \mathcal{L}dt = 1000\,\mathrm{fb}^{-1}$. This concludes that the considered Natural SUSY scenarios, that could play a significant role in the searches for new physics and are extremely challenging for the LHC, could be well observable at the ILC in the scenario H-20, which is proposed for the first 20 years of running.

Bibliography

[1] H. Sert, "Nailing Natural SUSY: Higgsino Parameter Determination at the ILC," *PoS* **EPS-HEP2013** (2013) 032.

[2] M. Berggren, F. Brmmer, J. List, G. Moortgat-Pick, T. Robens, K. Rolbiecki, and H. Sert, "Tackling light higgsinos at the ILC," *Eur. Phys. J.* **C73** no. 12, (2013) 2660, `arXiv:1307.3566 [hep-ph]`.

[3] S. L. Glashow, "Partial Symmetries of Weak Interactions," *Nucl. Phys.* **22** (1961) 579–588.

[4] S. Weinberg, "A Model of Leptons," *Phys. Rev. Lett.* **19** (1967) 1264–1266.

[5] A. Salam and J. C. Ward, "Weak and electromagnetic interactions," *Nuovo Cim.* **11** (1959) 568–577.

[6] M. Thomson, *Modern particle physics*. Cambridge University Press, New York, 2013. `http://www-spires.fnal.gov/spires/find/books/www?cl=QC793.2.T46::2013`.

[7] **Super-Kamiokande** Collaboration, Y. Fukuda *et al.*, "Evidence for oscillation of atmospheric neutrinos," *Phys. Rev. Lett.* **81** (1998) 1562–1567, `arXiv:hep-ex/9807003 [hep-ex]`.

[8] P. A. M. Dirac, "Quantized Singularities in the Electromagnetic Field," *Proc. Roy. Soc. Lond.* **A133** (1931) 60–72.

[9] D. H. Perkins, *Introduction to high energy physics*. 1982.

[10] T. Nakano and K. Nishijima, "Charge Independence for V-particles," *Prog. Theor. Phys.* **10** (1953) 581–582.

[11] M. Gell-Mann, "The interpretation of the new particles as displaced charge multiplets," *Nuovo Cim.* **4** no. S2, (1956) 848–866.

[12] E. Noether, "Invariant Variation Problems," *Gott. Nachr.* **1918** (1918) 235–257, `arXiv:physics/0503066 [physics]`. [Transp. Theory Statist. Phys.1,186(1971)].

[13] F. Halzen and A. D. Martin, *Quarks and Leptons: An introductory course in modern particle physics* . 1984.

[14] C.-N. Yang and R. L. Mills, "Conservation of Isotopic Spin and Isotopic Gauge Invariance," *Phys. Rev.* **96** (1954) 191–195.

[15] **Particle Data Group** Collaboration, K. A. Olive *et al.*, "Review of Particle Physics," *Chin. Phys.* **C38** (2014) 090001.

[16] P. W. Higgs, "Broken Symmetries and the Masses of Gauge Bosons," *Phys. Rev. Lett.* **13** (1964) 508–509.

[17] F. Englert and R. Brout, "Broken Symmetry and the Mass of Gauge Vector Mesons," *Phys. Rev. Lett.* **13** (1964) 321–323.

[18] G. S. Guralnik, C. R. Hagen, and T. W. B. Kibble, "Global Conservation Laws and Massless Particles," *Phys. Rev. Lett.* **13** (1964) 585–587.

[19] Y. Nambu, "Quasiparticles and Gauge Invariance in the Theory of Superconductivity," *Phys. Rev.* **117** (1960) 648–663.

[20] J. Goldstone, A. Salam, and S. Weinberg, "Broken Symmetries," *Phys. Rev.* **127** (1962) 965–970.

[21] G. 't Hooft, "Renormalization of Massless Yang-Mills Fields," *Nucl. Phys.* **B33** (1971) 173–199.

[22] C. Bouchiat, J. Iliopoulos, and P. Meyer, "An Anomaly Free Version of Weinberg's Model," *Phys. Lett.* **B38** (1972) 519–523.

[23] H. Georgi and S. L. Glashow, "Unity of All Elementary Particle Forces," *Phys. Rev. Lett.* **32** (1974) 438–441.

[24] D. J. Gross and R. Jackiw, "Effect of anomalies on quasi-renormalizable theories," *Phys. Rev.* **D6** (1972) 477–493.

[25] T. Morii, C. S. Lim, and S. N. Mukherjee, *The physics of the standard model and beyond.* 2004.

[26] G. Bertone, D. Hooper, and J. Silk, "Particle dark matter: Evidence, candidates and constraints," *Phys. Rept.* **405** (2005) 279–390, arXiv:hep-ph/0404175 [hep-ph].

[27] S. M. Kent, "Dark matter in spiral galaxies. II - Galaxies with H I rotation curves," *Astron. J.* **93** (1987) 816–832.

[28] K. G. Begeman, A. H. Broeils, and R. H. Sanders, "Extended rotation curves of spiral galaxies: Dark haloes and modified dynamics," *Mon. Not. Roy. Astron. Soc.* **249** (1991) 523.

[29] D. Clowe, M. Bradac, A. H. Gonzalez, M. Markevitch, S. W. Randall, C. Jones, and D. Zaritsky, "A direct empirical proof of the existence of dark matter," *Astrophys. J.* **648** (2006) L109–L113, arXiv:astro-ph/0608407 [astro-ph].

[30] K. N. Abazajian *et al.*, "Cosmological and Astrophysical Neutrino Mass Measurements," *Astropart. Phys.* **35** (2011) 177–184, `arXiv:1103.5083 [astro-ph.CO]`.

[31] S. P. Martin, "A Supersymmetry primer," `arXiv:hep-ph/9709356 [hep-ph]`. [Adv. Ser. Direct. High Energy Phys.18,1(1998)].

[32] **ATLAS, CMS** Collaboration, G. Aad *et al.*, "Combined Measurement of the Higgs Boson Mass in pp Collisions at $\sqrt{s} = 7$ and 8 TeV with the ATLAS and CMS Experiments," *Phys. Rev. Lett.* **114** (2015) 191803, `arXiv:1503.07589 [hep-ex]`.

[33] P. Langacker, "Introduction to the Standard Model and Electroweak Physics," in *Proceedings of Theoretical Advanced Study Institute in Elementary Particle Physics on The dawn of the LHC era (TASI 2008)*, pp. 3–48. 2010. `arXiv:0901.0241 [hep-ph]`. `http://inspirehep.net/record/810197/files/arXiv:0901.0241.pdf`.

[34] J. Ellis, "Outstanding questions: Physics beyond the Standard Model," *Phil. Trans. Roy. Soc. Lond.* **A370** (2012) 818–830.

[35] S. R. Coleman and J. Mandula, "All Possible Symmetries of the S Matrix," *Phys. Rev.* **159** (1967) 1251–1256.

[36] I. J. R. Aitchison, *Supersymmetry in Particle Physics. An Elementary Introduction.* 2007. `http://www-public.slac.stanford.edu/sciDoc/docMeta.aspx?slacPubNumber=slac-r-865`.

[37] Y. Okada, M. Yamaguchi, and T. Yanagida, "Upper bound of the lightest Higgs boson mass in the minimal supersymmetric standard model," *Prog. Theor. Phys.* **85** (1991) 1–6.

[38] J. R. Ellis, G. Ridolfi, and F. Zwirner, "Radiative corrections to the masses of supersymmetric Higgs bosons," *Phys. Lett.* **B257** (1991) 83–91.

[39] A. Arbey, M. Battaglia, A. Djouadi, F. Mahmoudi, and J. Quevillon, "Implications of a 125 GeV Higgs for supersymmetric models," *Phys. Lett.* **B708** (2012) 162–169, `arXiv:1112.3028 [hep-ph]`.

[40] H. E. Haber and G. L. Kane, "The Search for Supersymmetry: Probing Physics Beyond the Standard Model," *Phys. Rept.* **117** (1985) 75–263.

[41] J. F. Gunion and H. E. Haber, "Two-body Decays of Neutralinos and Charginos," *Phys. Rev.* **D37** (1988) 2515.

[42] P. Binetruy, *Supersymmetry: Theory, experiment and cosmology.* 2006.

[43] K. Desch, J. Kalinowski, G. A. Moortgat-Pick, M. M. Nojiri, and G. Polesello, "SUSY parameter determination in combined analyses at LHC / LC," *JHEP* **02** (2004) 035, `arXiv:hep-ph/0312069 [hep-ph]`.

[44] T. Han, S. Padhi, and S. Su, "Electroweakinos in the Light of the Higgs Boson," *Phys. Rev.* **D88** no. 11, (2013) 115010, `arXiv:1309.5966 [hep-ph]`.

[45] S. Heinemeyer, W. Hollik, and G. Weiglein, "Electroweak precision observables in the minimal supersymmetric standard model," *Phys. Rept.* **425** (2006) 265–368, `arXiv:hep-ph/0412214 [hep-ph]`.

[46] G. J. Gounaris, C. Le Mouel, and P. I. Porfyriadis, "A description of the neutralino observables in terms of projectors," *Phys. Rev.* **D65** (2002) 035002, `arXiv:hep-ph/0107249 [hep-ph]`.

[47] K. A. Olive, "Phases in the MSSM," in *Supersymmetry and unification of fundamental interactions. Proceedings, International Workshop, SUSY 95, Palaiseau, France, May 15-19, 1995.* 1995. `arXiv:hep-ph/9508413 [hep-ph]`.

[48] H. Baer, V. Barger, P. Huang, and X. Tata, "Natural Supersymmetry: LHC, dark matter and ILC searches," *JHEP* **05** (2012) 109, `arXiv:1203.5539 [hep-ph]`.

[49] M. Papucci, J. T. Ruderman, and A. Weiler, "Natural SUSY Endures," *JHEP* **09** (2012) 035, `arXiv:1110.6926 [hep-ph]`.

[50] J. L. Feng, "Naturalness and the Status of Supersymmetry," *Ann. Rev. Nucl. Part. Sci.* **63** (2013) 351–382, `arXiv:1302.6587 [hep-ph]`.

[51] A. Djouadi, "Implications of the Higgs discovery for the MSSM," *Eur. Phys. J.* **C74** (2014) 2704, `arXiv:1311.0720 [hep-ph]`.

[52] **MSSM Working Group** Collaboration, A. Djouadi *et al.*, "The Minimal supersymmetric standard model: Group summary report," in *GDR (Groupement De Recherche) - Supersymetrie Montpellier, France, April 15-17, 1998.* `arXiv:hep-ph/9901246 [hep-ph]`.

[53] P. Bechtle, T. Plehn, and C. Sander, "The Status of Supersymmetry after the LHC Run 1," in *The Large Hadron Collider: Harvest of Run 1*, T. Schrner-Sadenius, ed., pp. 421–462. 2015. `arXiv:1506.03091 [hep-ex]`.

[54] A. Djouadi, "The Anatomy of electro-weak symmetry breaking. I: The Higgs boson in the standard model," *Phys. Rept.* **457** (2008) 1–216, `arXiv:hep-ph/0503172 [hep-ph]`.

[55] F. Brummer and W. Buchmuller, "Light Higgsinos as Heralds of Higher-Dimensional Unification," *JHEP* **07** (2011) 010, `arXiv:1105.0802 [hep-ph]`.

[56] F. Brummer and W. Buchmuller, "The Fermi scale as a focus point of high-scale gauge mediation," *JHEP* **05** (2012) 006, `arXiv:1201.4338 [hep-ph]`.

[57] **ATLAS** Collaboration, G. Aad *et al.*, "Search for squarks and gluinos with the ATLAS detector in final states with jets and missing transverse momentum using $\sqrt{s} = 8$ TeV proton–proton collision data," *JHEP* **09** (2014) 176, `arXiv:1405.7875 [hep-ex]`.

[58] **ATLAS** Collaboration, G. Aad *et al.*, "Search for supersymmetry at $\sqrt{s}=8$ TeV in final states with jets and two same-sign leptons or three leptons with the ATLAS detector," *JHEP* **06** (2014) 035, `arXiv:1404.2500 [hep-ex]`.

[59] **CMS** Collaboration, S. Chatrchyan *et al.*, "Search for new physics in the multijet and missing transverse momentum final state in proton-proton collisions at $\sqrt{s}$= 8 TeV," *JHEP* **06** (2014) 055, `arXiv:1402.4770` `[hep-ex]`.

[60] **ATLAS** Collaboration, G. Aad *et al.*, "Search for squarks and gluinos in events with isolated leptons, jets and missing transverse momentum at $\sqrt{s} = 8$ TeV with the ATLAS detector," *JHEP* **04** (2015) 116, `arXiv:1501.03555` `[hep-ex]`.

[61] **CMS** Collaboration, S. Chatrchyan *et al.*, "Search for top squark and higgsino production using diphoton Higgs boson decays," *Phys. Rev. Lett.* **112** (2014) 161802, `arXiv:1312.3310` `[hep-ex]`.

[62] **ATLAS** Collaboration, G. Aad *et al.*, "Search for top squark pair production in final states with one isolated lepton, jets, and missing transverse momentum in $\sqrt{s}$ =8 TeV *pp* collisions with the ATLAS detector," *JHEP* **11** (2014) 118, `arXiv:1407.0583` `[hep-ex]`.

[63] **ATLAS** Collaboration, G. Aad *et al.*, "Search for direct top-squark pair production in final states with two leptons in pp collisions at $\sqrt{s} = 8$TeV with the ATLAS detector," *JHEP* **06** (2014) 124, `arXiv:1403.4853` `[hep-ex]`.

[64] **CMS** Collaboration, S. Chatrchyan *et al.*, "Search for top-squark pair production in the single-lepton final state in pp collisions at $\sqrt{s} = 8$ TeV," *Eur. Phys. J.* **C73** no. 12, (2013) 2677, `arXiv:1308.1586` `[hep-ex]`.

[65] **ATLAS** Collaboration, G. Aad *et al.*, "Search for direct third-generation squark pair production in final states with missing transverse momentum and two *b*-jets in $\sqrt{s} = 8$ TeV *pp* collisions with the ATLAS detector," *JHEP* **10** (2013) 189, `arXiv:1308.2631` `[hep-ex]`.

[66] **ATLAS** Collaboration, G. Aad *et al.*, "Search for direct top squark pair production in events with a Z boson, b-jets and missing transverse momentum in sqrt(s)=8 TeV pp collisions with the ATLAS detector," *Eur. Phys. J.* **C74** no. 6, (2014) 2883, `arXiv:1403.5222` `[hep-ex]`.

[67] **ATLAS** Collaboration, G. Aad *et al.*, "Search for direct pair production of the top squark in all-hadronic final states in proton-proton collisions at $\sqrt{s} = 8$ TeV with the ATLAS detector," *JHEP* **09** (2014) 015, `arXiv:1406.1122` `[hep-ex]`.

[68] **ATLAS** Collaboration, G. Aad *et al.*, "Search for pair-produced third-generation squarks decaying via charm quarks or in compressed supersymmetric scenarios in *pp* collisions at $\sqrt{s} = 8$ TeV with the ATLAS detector," *Phys. Rev.* **D90** no. 5, (2014) 052008, `arXiv:1407.0608` `[hep-ex]`.

[69] **CMS** Collaboration, V. Khachatryan *et al.*, "Searches for third-generation squark production in fully hadronic final states in proton-proton collisions at $\sqrt{s} = 8$ TeV," *JHEP* **06** (2015) 116, `arXiv:1503.08037` `[hep-ex]`.

[70] **ATLAS** Collaboration, G. Aad *et al.*, "Search for a supersymmetric partner to the top quark in final states with jets and missing transverse momentum at $\sqrt{s} = 7$ TeV with the ATLAS detector," *Phys. Rev. Lett.* **109** (2012) 211802, `arXiv:1208.1447` `[hep-ex]`.

[71] **ATLAS** Collaboration, G. Aad *et al.*, "Search for direct top squark pair production in final states with one isolated lepton, jets, and missing transverse momentum in $\sqrt{s} = 7$ TeV *pp* collisions using $4.7\ fb^{-1}$ of ATLAS data," *Phys. Rev. Lett.* **109** (2012) 211803, `arXiv:1208.2590 [hep-ex]`.

[72] **ATLAS** Collaboration, G. Aad *et al.*, "Search for a heavy top-quark partner in final states with two leptons with the ATLAS detector at the LHC," *JHEP* **11** (2012) 094, `arXiv:1209.4186 [hep-ex]`.

[73] **ATLAS** Collaboration, G. Aad *et al.*, "Search for direct production of charginos and neutralinos in events with three leptons and missing transverse momentum in $\sqrt{s} = 8$TeV *pp* collisions with the ATLAS detector," *JHEP* **04** (2014) 169, `arXiv:1402.7029 [hep-ex]`.

[74] **ATLAS** Collaboration, G. Aad *et al.*, "Search for the direct production of charginos, neutralinos and staus in final states with at least two hadronically decaying taus and missing transverse momentum in *pp* collisions at $\sqrt{s} = 8$ TeV with the ATLAS detector," *JHEP* **10** (2014) 96, `arXiv:1407.0350 [hep-ex]`.

[75] **ATLAS** Collaboration, G. Aad *et al.*, "Search for supersymmetry in events with four or more leptons in $\sqrt{s} = 8$ TeV pp collisions with the ATLAS detector," *Phys. Rev.* **D90** no. 5, (2014) 052001, `arXiv:1405.5086 [hep-ex]`.

[76] **ATLAS** Collaboration, G. Aad *et al.*, "Search for direct production of charginos, neutralinos and sleptons in final states with two leptons and missing transverse momentum in *pp* collisions at $\sqrt{s} = 8$ TeV with the ATLAS detector," *JHEP* **05** (2014) 071, `arXiv:1403.5294 [hep-ex]`.

[77] **CMS** Collaboration, V. Khachatryan *et al.*, "Searches for electroweak neutralino and chargino production in channels with Higgs, Z, and W bosons in pp collisions at 8 TeV," *Phys. Rev.* **D90** no. 9, (2014) 092007, `arXiv:1409.3168 [hep-ex]`.

[78] **CMS** Collaboration, V. Khachatryan *et al.*, "Searches for electroweak production of charginos, neutralinos, and sleptons decaying to leptons and W, Z, and Higgs bosons in pp collisions at 8 TeV," *Eur. Phys. J.* **C74** no. 9, (2014) 3036, `arXiv:1405.7570 [hep-ex]`.

[79] M. Berggren, T. Han, J. List, S. Padhi, S. Su, and T. Tanabe, "Electroweakino Searches: A Comparative Study for LHC and ILC (A Snowmass White Paper)," in *Community Summer Study 2013: Snowmass on the Mississippi (CSS2013) Minneapolis, MN, USA, July 29-August 6, 2013.* 2013. `arXiv:1309.7342 [hep-ph]`. `http://inspirehep.net/record/1255853/files/arXiv:1309.7342.pdf`.

[80] **ATLAS** Collaboration, "Physics at a High-Luminosity LHC with ATLAS," in *Community Summer Study 2013: Snowmass on the Mississippi (CSS2013) Minneapolis, MN, USA, July 29-August 6, 2013.* 2013. `arXiv:1307.7292 [hep-ex]`. `http://inspirehep.net/record/1245017/files/arXiv:1307.7292.pdf`.

[81] **CMS** Collaboration, "Projected Performance of an Upgraded CMS Detector at the LHC and HL-LHC: Contribution to the Snowmass Process," in *Community Summer Study 2013: Snowmass on the Mississippi (CSS2013) Minneapolis, MN, USA, July 29-August 6, 2013.* 2013. `arXiv:1307.7135`. `http://inspirehep.net/record/1244669/files/arXiv:1307.7135.pdf`.

[82] C. H. Chen, M. Drees, and J. F. Gunion, "Searching for invisible and almost invisible particles at e+ e- colliders," *Phys. Rev. Lett.* **76** (1996) 2002–2005, `arXiv:hep-ph/9512230 [hep-ph]`.

[83] H. Baer, V. Barger, and P. Huang, "Hidden SUSY at the LHC: the light higgsino-world scenario and the role of a lepton collider," *JHEP* **11** (2011) 031, `arXiv:1107.5581 [hep-ph]`.

[84] T. Behnke, J. E. Brau, B. Foster, J. Fuster, M. Harrison, J. M. Paterson, M. Peskin, M. Stanitzki, N. Walker, and H. Yamamoto, "The International Linear Collider Technical Design Report - Volume 1: Executive Summary," `arXiv:1306.6327 [physics.acc-ph]`.

[85] C. Adolphsen, M. Barone, B. Barish, K. Buesser, P. Burrows, J. Carwardine, J. Clark, H. M. Durand, G. Dugan, E. Elsen, *et al.*, "The International Linear Collider Technical Design Report - Volume 3.II: Accelerator Baseline Design," `arXiv:1306.6328 [physics.acc-ph]`.

[86] T. Behnke, J. E. Brau, P. N. Burrows, J. Fuster, M. Peskin, *et al.*, "The International Linear Collider Technical Design Report - Volume 4: Detectors," `arXiv:1306.6329 [physics.ins-det]`.

[87] H. Baer, T. Barklow, K. Fujii, Y. Gao, A. Hoang, S. Kanemura, J. List, H. E. Logan, A. Nomerotski, M. Perelstein, *et al.*, "The International Linear Collider Technical Design Report - Volume 2: Physics," `arXiv:1306.6352 [hep-ph]`.

[88] G. Moortgat-Picka *et al.*, "Physics at the e+ e- Linear Collider," `arXiv:1504.01726 [hep-ph]`.

[89] K. Fujii *et al.*, "Physics Case for the International Linear Collider," `arXiv:1506.05992 [hep-ex]`.

[90] K. J. Bae, H. Baer, N. Nagata, and H. Serce, "Prospects for Higgs coupling measurements in SUSY with radiatively-driven naturalness," *Phys. Rev.* **D92** no. 3, (2015) 035006, `arXiv:1505.03541 [hep-ph]`.

[91] **Top Quark Working Group** Collaboration, K. Agashe *et al.*, "Working Group Report: Top Quark," in *Community Summer Study 2013: Snowmass on the Mississippi (CSS2013) Minneapolis, MN, USA, July 29-August 6, 2013.* 2013. `arXiv:1311.2028 [hep-ph]`.

[92] Y. J. Chae and M. Perelstein, "Dark Matter Search at a Linear Collider: Effective Operator Approach," *JHEP* **05** (2013) 138, `arXiv:1211.4008 [hep-ph]`.

[93] M. Berggren, A. Cakir, D. Krcker, J. List, A. Lobanov, and I. A. Melzer-Pellmann, "Non-Simplified SUSY: stau-Coannihilation at LHC and ILC," in *Community Summer Study 2013: Snowmass on the Mississippi (CSS2013) Minneapolis, MN, USA, July 29-August 6, 2013*. 2013. `arXiv:1307.8076 [hep-ph]`.

[94] **LHC/LC Study Group** Collaboration, G. Weiglein *et al.*, "Physics interplay of the LHC and the ILC," *Phys. Rept.* **426** (2006) 47–358, `arXiv:hep-ph/0410364 [hep-ph]`.

[95] T. Barklow, J. Brau, K. Fujii, J. Gao, J. List, N. Walker, and K. Yokoya, "ILC Operating Scenarios," `arXiv:1506.07830 [hep-ex]`.

[96] P. Chen, "An Introduction to Beamstrahlung and Disruption," *Lect. Notes Phys.* **296** (1988) 495.

[97] K. Buesser, "The International Linear Collider," *PoS* **Corfu2012** (2013) 013.

[98] D. V. Schroeder, *Beamstrahlung and QED backgrounds at future linear colliders*. PhD thesis, SLAC, 1990. `http://www.slac.stanford.edu/cgi-wrap/pubpage?slac-r-371`.

[99] A. Vogel, "Beam-induced backgrounds in detectors at the ILC,". DESY-THESIS-2008-036.

[100] D. Schulte, *Study of Electromagnetic and Hadronic Background in the Interaction Region of the TESLA Collider*. PhD thesis, Hamburg U., 1997. `https://inspirehep.net/record/888433/files/shulte.pdf`.

[101] G. Moortgat-Pick *et al.*, "The Role of polarized positrons and electrons in revealing fundamental interactions at the linear collider," *Phys. Rept.* **460** (2008) 131–243, `arXiv:hep-ph/0507011 [hep-ph]`.

[102] I. Boovi Jelisavi, S. Luki, G. Milutinovi Dumbelovi, M. Pandurovi, and I. Smiljani, "Luminosity measurement at ILC," *JINST* **8** (2013) P08012, `arXiv:1304.4082 [physics.acc-ph]`.

[103] B. Vormwald, "Polarisation and Beam Energy Measurement at a Linear e^+e^- Collider," *JINST* **9** (2014) C08012, `arXiv:1406.3636 [physics.ins-det]`.

[104] H. Abramowicz, A. Abusleme, K. Afanaciev, J. Aguilar, P. Ambalathankandy, *et al.*, "Forward Instrumentation for ILC Detectors," *JINST* **5** (2010) P12002, `arXiv:1009.2433 [physics.ins-det]`.

[105] A. Hinze and K. Monig, "Measuring the beam energy with radiative return events," *eConf* **C050318** (2005) 1109, `arXiv:physics/0506115 [physics]`.

[106] M. Beckmann, *Spin Transport at the International Linear Collider and its Impact on the Measurement of Polarization*. PhD thesis, Hamburg U., 2013. `http://www-library.desy.de/cgi-bin/showprep.pl?thesis13-053`.

[107] P. Chen, "Disruption, Beamstrahlung and Beamstrahlung Pair Creation," *eConf* **C8806271** (1988) 673. SLAC-PUB-4822.

[108] M. Zolotorev, E. Kuraev, and V. Serbo, "Estimates Of Electromagnetic Background Processes For The Vlepp Project,". SLAC-TRANS-0227.

[109] K. Yokoya and P. Chen, "Beam-beam phenomena in linear colliders," *Lect.Notes Phys.* **400** (1992) 415–445.

[110] C. Rimbault, P. Bambade, K. Monig, and D. Schulte, "Incoherent pair generation in a beam-beam interaction simulation," *Phys.Rev.ST Accel.Beams* **9** (2006) 034402.

[111] E. Avetisyan, "Study of the anti-DID magnetic Fields' Effects on the Beam-induced Pair Backgrounds in ILD," 2013. `http://flc.desy.de/lcnotes/notes/localfsExplorer_read?currentPath=/afs/desy.de/group/flc/lcnotes/LC-REP-2013-002.pdf`.

[112] C. Hensel, "Beam induced background at a TESLA detector,". In *2nd ECFA/DESY Study 1998-2001* 396-430.

[113] O. Markin, "Backgrounds at future linear colliders," `arXiv:1402.2515 [physics.ins-det]`.

[114] T. Sjostrand, S. Mrenna, and P. Z. Skands, "PYTHIA 6.4 Physics and Manual," *JHEP* **05** (2006) 026, `arXiv:hep-ph/0603175 [hep-ph]`.

[115] D. Schulte, "Beam-beam simulations with GUINEA-PIG,". CERN-PS-99-014-LP, CERN-CLIC-NOTE-387.

[116] P. Chen, T. L. Barklow, and M. E. Peskin, "Hadron production in gamma gamma collisions as a background for e+ e- linear colliders," *Phys. Rev.* **D49** (1994) 3209–3227, `arXiv:hep-ph/9305247 [hep-ph]`.

[117] M. Thomson, "Particle Flow Calorimetry and the PandoraPFA Algorithm," *Nucl.Instrum.Meth.* **A611** (2009) 25–40, `arXiv:0907.3577 [physics.ins-det]`.

[118] J. Marshall and M. Thomson, "Pandora Particle Flow Algorithm," `arXiv:1308.4537 [physics.ins-det]`.

[119] I. G. Knowles and G. D. Lafferty, "Hadronization in Z^0 decay," *J. Phys.* **G23** (1997) 731–789, `arXiv:hep-ph/9705217 [hep-ph]`.

[120] ILD web site, http://www.ilcild.org/.

[121] **ILD, SiD groups** Collaboration, G. G. Voutsinas, "Vertexing Software and Methods for the ILC," *PoS* **Vertex2014** (2015) 040. `https://inspirehep.net/record/1373028`.

[122] I. Valin *et al.*, "A reticle size CMOS pixel sensor dedicated to the STAR HFT," *JINST* **7** (2012) C01102.

[123] Y. Sugimoto, "Fine Pixel CCD Option for the ILC Vertex Detector," *eConf* **C050318** (2005) 0804.

[124] J. J. Velthuis *et al.*, "DEPFET, a monolithic active pixel sensor for the ILC," *Nucl. Instrum. Meth.* **A579** (2007) 685–689.

[125] O. Schäfer, "Ein Monitorsystem für Gasbasierte Detektoren am International Linear Collider (ILC)," Master thesis, Universität Rostock, 2006.

[126] D. C. Arogancia *et al.*, "Study in a beam test of the resolution of a Micromegas TPC with standard readout pads," *Nucl. Instrum. Meth.* **A602** (2009) 403–414, `arXiv:0705.2210 [physics.ins-det]`.

[127] K. o. Ackermann, "Results from a TPC Prototype for the Linear Collider Tracker with the MWPC and GEM Endplate Technologies,".

[128] M. S. Dixit, J. Dubeau, J. P. Martin, and K. Sachs, "Position sensing from charge dispersion in micropattern gas detectors with a resistive anode," *Nucl. Instrum. Meth.* **A518** (2004) 721–727, `arXiv:physics/0307152 [physics]`.

[129] **Linear Collider ILD Concept Group -** Collaboration, T. Abe *et al.*, "The International Large Detector: Letter of Intent," `arXiv:1006.3396 [hep-ex]`.

[130] B. C. Allanach, "SOFTSUSY: a program for calculating supersymmetric spectra," *Comput. Phys. Commun.* **143** (2002) 305–331, `arXiv:hep-ph/0104145 [hep-ph]`.

[131] H. Baer and J. List, "Post LHC8 SUSY benchmark points for ILC physics," *Phys. Rev.* **D88** (2013) 055004, `arXiv:1307.0782 [hep-ph]`.

[132] **OPAL** Collaboration, K. Ackerstaff *et al.*, "Search for stable and longlived massive charged particles in e+ e- collisions at $\sqrt{s} = 130$-GeV - 183-GeV," *Phys. Lett.* **B433** (1998) 195–208, `arXiv:hep-ex/9803026 [hep-ex]`.

[133] **OPAL** Collaboration, G. Abbiendi *et al.*, "Search for stable and longlived massive charged particles in e+ e- collisions at $\sqrt{s} = 130$-GeV to 209-GeV," *Phys. Lett.* **B572** (2003) 8–20, `arXiv:hep-ex/0305031 [hep-ex]`.

[134] **ALEPH** Collaboration, A. Heister *et al.*, "Search for charginos nearly mass degenerate with the lightest neutralino in e^+e^- collisions at centre-of-mass energies up to 209-GeV," *Phys. Lett.* **B533** (2002) 223–236, `arXiv:hep-ex/0203020 [hep-ex]`.

[135] **DELPHI** Collaboration, J. Abdallah *et al.*, "Searches for supersymmetric particles in e^+e^- collisions up to 208 GeV and interpretation of the results within the MSSM," *Eur. Phys. J.* **C31** (2003) 421–479, `arXiv:hep-ex/0311019 [hep-ex]`.

[136] **L3** Collaboration, "Searches for supersymmetry in e^+e^- interactions at $\sqrt{s} = 202$ - 208 GeV,". L3 note 2707.

[137] **OPAL** Collaboration, "New Particle Searches in e^+e^- Collisions at $\sqrt{s} = 200$ - 209 GeV,". OPAL note PN470.

[138] LEP2 SUSY Working Group, "Combined LEP Chargino Results, up to 208 GeV for low DM,". LEPSUSYWG/02-04.1.

[139] W. Kilian, T. Ohl, and J. Reuter, "WHIZARD: Simulating Multi-Particle Processes at LHC and ILC," *Eur. Phys. J.* **C71** (2011) 1742, `arXiv:0708.4233 [hep-ph]`.

[140] H. E. Haber and D. Wyler, "Radiative Neutralino Decay," *Nucl. Phys.* **B323** (1989) 267.

[141] ILC Generator Group. `http://ilcsoft.desy.de/dbd/generated/`. Monte Carlo Samples for the DBD benchmarks.

[142] C. Hensel, *Search for nearly mass degenerate charginos and neutralinos in e+ e-collisions*. PhD thesis, Hamburg U., 2002.
`http://www-library.desy.de/cgi-bin/showprep.pl?thesis02-047`.

[143] P. Z. Skands *et al.*, "SUSY Les Houches accord: Interfacing SUSY spectrum calculators, decay packages, and event generators," *JHEP* **07** (2004) 036, `arXiv:hep-ph/0311123` `[hep-ph]`.

[144] M. Moretti, T. Ohl, and J. Reuter, "O'Mega: An Optimizing matrix element generator," `arXiv:hep-ph/0102195 [hep-ph]`.

[145] L. Garren. `http://cepa.fnal.gov/psm/stdhep/`. StdHep Manual, 2016, Home Page.

[146] M. Bahr *et al.*, "Herwig++ Physics and Manual," *Eur. Phys. J.* **C58** (2008) 639–707, `arXiv:0803.0883 [hep-ph]`.

[147] D. Grellscheid and P. Richardson, "Simulation of Tau Decays in the Herwig++ Event Generator," `arXiv:0710.1951 [hep-ph]`.

[148] M. Berggren, "SGV 3.0 - a fast detector simulation," in *International Workshop on Future Linear Colliders (LCWS11) Granada, Spain, September 26-30, 2011.* 2012. `arXiv:1203.0217 [physics.ins-det]`.

[149] T. Kraemer, "Track Parameters in LCIO (2006),". LC-DET-2006-004.

[150] P. Billoir, "Track Fitting With Multiple Scattering: A New Method," *Nucl. Instrum. Meth.* **A225** (1984) 352–366.

[151] F. Gaede, "Marlin and LCCD: Software tools for the ILC," *Nucl. Instrum. Meth.* **A559** (2006) 177–180.

[152] ILCSoft Home Page. `http://ilcsoft.desy.de/portal`.

[153] S. Aplin, J. Engels, F. Gaede, N. A. Graf, T. Johnson, and J. McCormick, "LCIO: A Persistency Framework and Event Data Model for HEP," in *Proceedings, 2012 IEEE Nuclear Science Symposium and Medical Imaging Conference (NSS/MIC 2012): Anaheim, California, USA, October 29-November 3, 2012*, pp. 2075–2079. 2012.

[154] H. V. P. Mora de Freitas. Detector simulation with MOKKA/GEANT4: present and future. LC-TOOL-2003-010.

[155] Mokka Home Page. `https://llrforge.in2p3.fr/trac/Mokka/`.

[156] **GEANT4** Collaboration, S. Agostinelli *et al.*, "GEANT4: A Simulation toolkit," *Nucl. Instrum. Meth.* **A506** (2003) 250–303.

[157] J. Allison *et al.*, "Geant4 developments and applications," *IEEE Trans. Nucl. Sci.* **53** (2006) 270.

[158] **Particle Data Group** Collaboration, S. Eidelman *et al.*, "Review of particle physics. Particle Data Group," *Phys. Lett.* **B592** (2004) 1–1109.

[159] B. List, "Why and when to optimise efficiency times purity,". `https://www.desy.de/~blist/notes/whyeffpur.ps.gz`. ETH Zurich internal note (2002).

[160] K. Rolbiecki. Private Communication, 2015.

[161] C. Rimbault, P. Bambade, K. Monig, and D. Schulte, "Impact of beam-beam effects on precision luminosity measurements at the ILC," *JINST* **2** (2007) P09001.

[162] A. Rosca, "Measurement of the beam polarisation at the ILC using $e^+e^- \to W^+W^- \to qql\nu$ data,". `http://www-flc.desy.de/lcnotes/notes/LC-REP-2013-009.pdf`. LC-REP-2013-009.

[163] S. Poss and A. Sailer, "Luminosity Spectrum Reconstruction at Linear Colliders," *Eur. Phys. J.* **C74** no. 4, (2014) 2833, `arXiv:1309.0372 [physics.ins-det]`.

[164] F. James and M. Roos, "Minuit: A System for Function Minimization and Analysis of the Parameter Errors and Correlations," *Comput. Phys. Commun.* **10** (1975) 343–367.

[165] A. Bharucha, A. Fowler, G. Moortgat-Pick, and G. Weiglein, "Consistent on shell renormalisation of electroweakinos in the complex MSSM: LHC and LC predictions," *JHEP* **05** (2013) 053, `arXiv:1211.3134 [hep-ph]`.

[166] T. Fritzsche and W. Hollik, "Complete one loop corrections to the mass spectrum of charginos and neutralinos in the MSSM," *Eur. Phys. J.* **C24** (2002) 619–629, `arXiv:hep-ph/0203159 [hep-ph]`.

[167] A. C. Fowler, *Higher order and CP-violating effects in the neutralino and Higgs boson sectors of the MSSM*. PhD thesis, Durham U., 2010. `http://etheses.dur.ac.uk/449/`.

[168] F. Gaede, S. Aplin, R. Glattauer, C. Rosemann, and G. Voutsinas, "Track reconstruction at the ILC: the ILD tracking software," *J. Phys. Conf. Ser.* **513** (2014) 022011.

[169] T. Mori, D. Kamai, A. Miyamoto, Y. Sugimoto, A. Ishikawa, T. Suehara, E. Kato, and H. Yamamoto, "Study of Tracking and Flavor Tagging with FPCCD Vertex Detector," in *International Workshop on Future Linear Colliders (LCWS13) Tokyo, Japan, November 11-15, 2013*. 2014. `arXiv:1403.5659 [physics.ins-det]`.

[170] KalTest, "KalTest: A ROOT-based Kalman Filter Package website." `http://www-jlc.kek.jp/subg/offl/kaltest/`.

[171] K. Fuji, "Extended Kalman Filter." `http://www-jlc.kek.jp/subg/offl/kaltest/doc/ReferenceManual.pdf`.

226

[172] F. Gaede, "Pattern recognition in a TPC," AIDA Work Package-2 Meeting, CERN, 2011. `http://indico.cern.ch/event/159340/`.

[173] R. Glattauer, R. Fruhwirth, J. Lettenbichler, and W. Mitaroff, "Forward Tracking in the ILD Detector," `arXiv:1202.2761 [physics.data-an]`.

[174] B. Xu, "Track selection in Pandora," High Level Reconstruction Workshop, DESY, 2015. `https://agenda.linearcollider.org/event/6787/timetable/#20150708.detailed`.

[175] E. van der Kraaij and J. Marshall, "Development of the PANDORAPFANEW muon reconstruction algorithm,". `http://cds.cern.ch/record/1443539`.

[176] M. Cacciari, G. P. Salam, and G. Soyez, "FastJet User Manual," *Eur. Phys. J.* **C72** (2012) 1896, `arXiv:1111.6097 [hep-ph]`.

[177] S. Sasikumar. Private Communication, 2015.

[178] **L3** Collaboration, M. Acciarri *et al.*, "Total cross-section in $\gamma\gamma$ collisions at LEP," *Phys. Lett.* **B519** (2001) 33–45, `arXiv:hep-ex/0102025 [hep-ex]`.

[179] G. G. Voutsinas. Private Communication, 2015.

[180] M. Kurata, "High Level Reconstruction Tools,". `https://agenda.linearcollider.org/event/6557/session/10/contribution/44/material/slides/0.pdf`.

[181] M. Kurata. Private Communication, 2015.

[182] R. Glattauer, *Track Reconstruction in the Forward Region of the Detector ILD at the Electron-Positron Linear Collider ILC.* PhD thesis, TU Vienna, 2012. `http://www.hephy.at/fileadmin/user_upload/Publikationen/DiplomaThesis.pdf`.

[183] A. Hocker *et al.*, "TMVA - Toolkit for Multivariate Data Analysis," *PoS* **ACAT** (2007) 040, `arXiv:physics/0703039 [PHYSICS]`.

[184] Y. Freund and R. E. Schapire, "Experiments with a New Boosting Algorithm," in *In Proceedings of the thirteenth international conference on machine learning*, pp. 148–156. Morgan Kaufmann, 1996.

[185] J. Friedman, T. Hastie, and R. Tibshirani, "Additive logistic regression: a statistical view of boosting (With discussion and a rejoinder by the authors)," *Ann. Statist.* **28** no. 2, (04, 2000) 337–407. `http://dx.doi.org/10.1214/aos/1016218223`.

[186] T. Hastie, R. Tibshirani, and J. Friedman, *The Elements of Statistical Learning.* Springer Series in Statistics. Springer New York Inc., New York, NY, USA, 2001.

[187] R. E. Schapire, "The Strength of Weak Learnability," *Mach. Learn.* **5** no. 2, (July, 1990) 197–227. `http://dx.doi.org/10.1023/A:1022648800760`.

[188] Y. Freund, "Boosting a Weak Learning Algorithm by Majority," *Information and Computation* **121** no. 2, (1995) 256 – 285.

[189] Y. Freund and R. E. Schapire, "A Decision-Theoretic Generalization of On-Line Learning and an Application to Boosting," *J. Comput. Syst. Sci.* **55** no. 1, (1997) 119–139.

[190] B. P. Roe, H.-J. Yang, J. Zhu, Y. Liu, I. Stancu, and G. McGregor, "Boosted decision trees as an alternative to artificial neural networks for particle identification," *Nuclear Instruments and Methods in Physics Research A* **543** (May, 2005) 577–584, `physics/0408124`.

[191] J. H. Friedman, "Stochastic gradient boosting," *Comput. Stat. Data Anal.* **38** (2002) 367–378.

[192] MarlinReco svn repository, `https://svnsrv.desy.de/viewvc/marlinreco/`, PIDTools package of MarlinReco: `svn repository for PIDTools`.

[193] **ALEPH** Collaboration, D. Decamp *et al.*, "Measurement of tau branching ratios," *Z. Phys.* **C54** (1992) 211–228.

[194] A. Münnich, "Experimentelle Untersuchung von GEM-Auslesestrukturen für eine TPC," Diploma Thesis, Aachen, 2003. `http://web.physik.rwth-aachen.de/~tpcmgr/en/papers.html`.

[195] S. Lotze, *Ion Backdrift Minimisation in a GEM-Based TPC Readout*. PhD thesis, Aachen, 2006. `http://web.physik.rwth-aachen.de/~tpcmgr/en/papers.html`.

[196] C. Krieger, "Messung von Transferkoeffizienten einer GEM-Auslesestruktur.," Beachelor Thesis, Bonn, 2009. `http://www.lhc-ilc.physik.uni-bonn.de/research-groups/experimental-physics/prof.-k.-desch/results/theses`.

[197] R. Menzen, "Charakterisierung von GEMs.," Beachelor Thesis, Bonn, 2010. `http://www.lhc-ilc.physik.uni-bonn.de/research-groups/experimental-physics/prof.-k.-desch/results/theses`.

[198] K. Zenker, *Studies of field distortions in a Time Projection Chamber for the International Linear Collider*. PhD thesis, U. Hamburg, Dept. Phys., 2014. `http://www-library.desy.de/cgi-bin/showprep.pl?thesis14-044`.

[199] B. Sobloher, "Simulationsstudien zu GEM-Folien für die Auslese einer TPC.," Diploma Thesis, Aachen, 2002. `http://web.physik.rwth-aachen.de/~tpcmgr/en/papers.html`.

[200] P. D. Group, "Particle Detectors at Accelerators, 2011,". `http://pdg.lbl.gov/2011/reviews/rpp2011-rev-particle-detectors-accel.pdf`.

[201] W. Blum, W. Riegler, and L. Rolandi, *Particle Detection with Drift Chambers*. Springer, Verlag Berlin Heidelberg, 2008.

[202] H. J. Hilke, "Time projection chambers," *Rept. Prog. Phys.* **73** (2010) 116201.

[203] C. Ramsauer, "Über den Wirkungsquerschnitt der Gasmoleküle gegenüber langsamen Elektronen," *Annalen der Physik* **369** no. 6, (1921) 513–540. `http://dx.doi.org/10.1002/andp.19213690603`.

[204] E. B. Wagner, F. J. Davis, and G. S. Hurst, "Time of Flight Investigations of Electron Transport in Some Atomic and Molecular Gases," *The Journal of Chemical Physics* **47** no. 9, (1967) 3138–3147.
http://scitation.aip.org/content/aip/journal/jcp/47/9/10.1063/1.1712365.

[205] F. Sauli, "Principles of Operation of Multiwire Proportional and Drift Chambers,".

[206] F. Sauli and A. Sharma, "Micropattern gaseous detectors," *Ann. Rev. Nucl. Part. Sci.* **49** (1999) 341–388.

[207] G. Charpak, R. Bouclier, T. Bressani, J. Favier, and C. Zupancic, "The use of multiwire proportional counters to select and localize charged particles," *Nucl. Instrum. Meth.* **62** (1968) 262–268.

[208] V. Lepeltier, "Review on TPC's," *J. Phys. Conf. Ser.* **65** (2007) 012001.

[209] F. Sauli, "GEM: A new concept for electron amplification in gas detectors," *Nucl. Instrum. Meth.* **A386** (1997) 531–534.

[210] Y. Giomataris, P. Rebourgeard, J. P. Robert, and G. Charpak, "MICROMEGAS: A High granularity position sensitive gaseous detector for high particle flux environments," *Nucl. Instrum. Meth.* **A376** (1996) 29–35.

[211] P. D. Group, "CERN Gas Detectors Development group (GDD)."
http://gdd.web.cern.ch/GDD/.

[212] A. Ishikawa, "Gas Properties."
http://www-hep.phys.saga-u.ac.jp/ILC-TPC/gas/index.html.

[213] K. Zenker. Private Communication, 2014.

[214] V. Tikhonov and R. Veenhof, "GEM simulation methods development," *Nucl. Instrum. Meth.* **A478** (2002) 452–459.

[215] M. Alfonsi, G. Croci, S. D. Pinto, E. Rocco, L. Ropelewski, F. Sauli, R. Veenhof, and M. Villa, "Simulation of the dielectric charging-up effect in a {GEM} detector," *Nuclear Instruments and Methods in Physics Research Section A: Accelerators, Spectrometers, Detectors and Associated Equipment* **671** (2012) 6 – 9.
http://www.sciencedirect.com/science/article/pii/S0168900211022789.

Appendix A

Representations

A.1 Pauli Matrices

The Pauli matrices are

$$\sigma^0 = \bar\sigma^0 = \begin{pmatrix} 1 & 0 \\ 0 & 1 \end{pmatrix} \qquad \sigma^1 = -\bar\sigma^1 = \begin{pmatrix} 0 & 1 \\ 1 & 0 \end{pmatrix} \tag{A.1}$$

$$\sigma^2 = -\bar\sigma^2 = \begin{pmatrix} 0 & -i \\ i & 0 \end{pmatrix} \qquad \sigma^3 = -\bar\sigma^3 = \begin{pmatrix} 1 & 0 \\ 0 & -1 \end{pmatrix} \tag{A.2}$$

A.2 Gamma Matrices

In Dirac-Pauli representation, the gamma matrices are given by

$$\gamma^0 = \begin{pmatrix} I & 0 \\ 0 & I \end{pmatrix} \quad \text{and} \quad \gamma^i = \begin{pmatrix} 0 & \sigma^i \\ -\sigma^i & 0 \end{pmatrix} \quad \text{and} \quad \gamma_5 = \begin{pmatrix} -I & 0 \\ 0 & -I \end{pmatrix} \tag{A.3}$$

where σ^i denotes the Pauli matrices for $i = 1, 2, 3$. γ_5 matrix is obtained by the multiplication of other γ matrices $\gamma_5 = i\gamma^0\gamma^1\gamma^2\gamma^3$ and I denotes the identity matrix:

$$I = \begin{pmatrix} 1 & 0 \\ 0 & 1 \end{pmatrix} \tag{A.4}$$

Appendix B

Les Houches Files

B.1 dM1600 Scenario

SOFTSUSY3.1.7
Block SPINFO # Program information
1 SOFTSUSY # spectrum calculator
2 3.1.7 # version number

Block MODSEL   # Select model
        1   0   # gutscGMSB

Block SMINPUTS   # Standard Model inputs
        1   1.279250000000000e+02   # alpha_em$^{(-1)}$(MZ) SM MSbar
        2   1.166367000000000e-05   # G_Fermi
        3   1.176000000000000e-01   # alpha_s(MZ)MSbar
        4   9.118760000000000e+01   # MZ(pole)
        5   4.200000000000000e+00   # mb(mb)
        6   1.733000000000000e+02   # Mtop(pole)
        7   1.776990000000000e+00   # Mtau(pole)

Block MINPAR   # SUSY breaking input parameters
        3   4.460000000000000e+01   # tanb
        1   1.900000000000000e+02   # M_soft
        4   2.000000000000000e+01   # n1
        5   2.800000000000000e+01   # n2
        6   1.100000000000000e+01   # n3

Low energy data in SOFTSUSY: MIXING=0 TOLERANCE=1.000000000000000e-03
mgut=9.631622368025226e+15 GeV

Block MASS   # Mass spectrum
PDG code   mass   particle

24	8.038995351487011e+01	# MW
25	1.240792012544481e+02	# h0
35	2.157529685177313e+03	# H0
36	2.160010329137058e+03	# A0
37	2.161799938926020e+03	# H+
1000021	4.375353274501803e+03	# ~g
1000022	1.641754367668350e+02	# ~neutralino(1)
1000023	-1.668743162572481e+02	# ~neutralino(2)
1000024	1.657656701146739e+02	# ~chargino(1)
1000025	1.698639278355411e+03	# ~neutralino(3)
1000035	4.362852386174281e+03	# ~neutralino(4)
1000037	4.362959118506908e+03	# ~chargino(2)
1000001	5.150717470966018e+03	# ~d_L
1000002	5.150266007945411e+03	# ~u_L
1000003	5.150586842657014e+03	# ~s_L
1000004	5.150135364599209e+03	# ~c_L
1000005	3.116345646815519e+03	# ~b_1
1000006	2.570433305852961e+03	# ~t_1
1000011	3.652578200233719e+03	# ~e_L
1000012	3.651405680014416e+03	# ~nue_L
1000013	3.651653789892482e+03	# ~mu_L
1000014	3.650866714296213e+03	# ~numu_L
1000015	5.883284690838435e+02	# ~stau_1
1000016	3.477847108317418e+03	# ~nu_tau_L
2000001	3.822099260422164e+03	# ~d_R
2000002	3.934369693975646e+03	# ~u_R
2000003	3.821749335508991e+03	# ~s_R
2000004	3.934350763798861e+03	# ~c_R
2000005	4.452831606868757e+03	# ~b_2
2000006	4.457624481297771e+03	# ~t_2
2000011	1.684506421979879e+03	# ~e_R
2000013	1.682117344249424e+03	# ~mu_R
2000015	3.479067100777233e+03	# ~stau_2

Higgs mixing
 Block alpha   # Effective Higgs mixing parameter
          -2.298990200733434e-02   # alpha

 Block nmix   # neutralino mixing matrix

1 1	2.109795297087265e-02	# N_{1,1}
1 2	-1.341804973443344e-02	# N_{1,2}
1 3	7.099036517753522e-01	# N_{1,3}
1 4	-7.038548412263586e-01	# N_{1,4}
2 1	-1.670310034163906e-02	# N_{2,1}

2 2	1.200707865604216e-02	# N_{2,2}
2 3	7.042906526638455e-01	# N_{2,3}
2 4	7.096136364751311e-01	# N_{2,4}
3 1	9.996378023365021e-01	# N_{3,1}
3 2	8.672533086886662e-04	# N_{3,2}
3 3	-3.214429718482804e-03	# N_{3,3}
3 4	2.670541992052949e-02	# N_{3,4}
4 1	-3.833526630827694e-04	# N_{4,1}
4 2	9.998375037350672e-01	# N_{4,2}
4 3	1.072011165546804e-03	# N_{4,3}
4 4	-1.799082982038890e-02	# N_{4,4}
Block Umix	# chargino U mixing matrix	
1 1	-1.622672147660392e-03	# U_{1,1}
1 2	9.999986834666840e-01	# U_{1,2}
2 1	-9.999986834666840e-01	# U_{2,1}
2 2	-1.622672147660392e-03	# U_{2,2}
Block Vmix	# chargino V mixing matrix	
1 1	-2.512429369479947e-02	# V_{1,1}
1 2	9.996843351110076e-01	# V_{1,2}
2 1	-9.996843351110076e-01	# V_{2,1}
2 2	-2.512429369479947e-02	# V_{2,2}
Block stopmix	# stop mixing matrix	
1 1	4.309868642578436e-02	# F_{11}
1 2	9.990708199263814e-01	# F_{12}
2 1	9.990708199263814e-01	# F_{21}
2 2	-4.309868642578436e-02	# F_{22}
Block sbotmix	# sbottom mixing matrix	
1 1	2.722282285694315e-03	# F_{11}
1 2	9.999962945827134e-01	# F_{12}
2 1	9.999962945827134e-01	# F_{21}
2 2	-2.722282285694315e-03	# F_{22}
Block staumix	# stau mixing matrix	
1 1	1.358002459931011e-03	# F_{11}
1 2	9.999990779142343e-01	# F_{12}
2 1	9.999990779142343e-01	# F_{21}
2 2	-1.358002459931011e-03	# F_{22}
Block gauge	Q= 3.308030806810062e+03	
1	3.656827954478413e-01	# g'(Q)MSSM DRbar
2	6.356208810601692e-01	# g(Q)MSSM DRbar
3	9.966844914128874e-01	# g3(Q)MSSM DRbar
Block yu	Q= 3.308030806810062e+03	
3 3	8.127325565041706e-01	# Yt(Q)MSSM DRbar
Block yd	Q= 3.308030806810062e+03	
3 3	5.855575384704830e-01	# Yb(Q)MSSM DRbar
Block ye	Q= 3.308030806810062e+03	
3 3	4.559713961942305e-01	# Ytau(Q)MSSM DRbar

Block hmix	Q= 3.308030806810062e+03	# Higgs mixing parameters
1	1.600000124181774e+02	# mu(Q)MSSM DRbar
2	4.380986380939400e+01	# tan beta(Q)MSSM DRbar
3	2.431068039014293e+02	# higgs vev(Q)MSSM DRbar
4	4.898342778559063e+06	# mA^2(Q)MSSM DRbar
Block msoft	Q= 3.308030806810062e+03	# MSSM DRbar SUSY breaking parameters
1	1.718570684065487e+03	# M_1(Q)
2	4.334671096220062e+03	# M_2(Q)
3	4.199770060680284e+03	# M_3(Q)
21	4.756081646814502e+06	# mH1^2(Q)
22	9.359595368473956e+04	# mH2^2(Q)
31	3.627321801285055e+03	# meL(Q)
32	3.626781689413113e+03	# mmuL(Q)
33	3.461479077073161e+03	# mtauL(Q)
34	1.664426668575963e+03	# meR(Q)
35	1.662010316246173e+03	# mmuR(Q)
36	5.873993666229258e+02	# mtauR(Q)
41	5.048375173419354e+03	# mqL1(Q)
42	5.048240531565893e+03	# mqL2(Q)
43	4.378030716320443e+03	# mqL3(Q)
44	3.822095954229407e+03	# muR(Q)
45	3.822076728423227e+03	# mcR(Q)
46	2.497170326815858e+03	# mtR(Q)
47	3.704926918485583e+03	# mdR(Q)
48	3.704571624427103e+03	# msR(Q)
49	3.017539425896394e+03	# mbR(Q)
Block au	Q= 3.308030806810062e+03	
1 1	-5.274829597307795e+03	# Au(Q)MSSM DRbar
2 2	-5.274708717617984e+03	# Ac(Q)MSSM DRbar
3 3	-3.928950588567513e+03	# At(Q)MSSM DRbar
Block ad	Q= 3.308030806810062e+03	
1 1	-5.654207875509367e+03	# Ad(Q)MSSM DRbar
2 2	-5.653889220164242e+03	# As(Q)MSSM DRbar
3 3	-4.680761245115323e+03	# Ab(Q)MSSM DRbar
Block ae	Q= 3.308030806810062e+03	
1 1	-2.104323446834111e+03	# Ae(Q)MSSM DRbar
2 2	-2.103423315912323e+03	# Amu(Q)MSSM DRbar
3 3	-1.827213096266639e+03	# Atau(Q)MSSM DRbar

```
# PDG Width
DECAY          1000024                 8.52561E-12    # chargino1+ decays
# BR          NDA      ID1    ID2   ID3    ID4
0.164899         2   1000022   211                   # BR(~chi_1+ → pi+ ~chi_10 )
0.173099         3   1000022   -11     12             # BR(~chi_1+ → e+ nu_e ~chi_10 )
0.165876         3   1000022   -13     14             # BR(~chi_1+ → mu+ nu_mu ~chi_10 )
0.285071         3   1000022   211    111             # BR(~chi_1+ → pi+ pi0 ~chi_10 )
0.0115362        2   1000022   321                   # BR(~chi_1+ → K+ ~chi_10 )
0.075293         4   1000022   211    111    111     # BR(~chi_1+ → pi+ pi0 pi0 ~chi_10 )
0.009565         3   1000022   311    211             # BR(~chi_1+ → k0 pi+ ~chi_10 )
0.0709278        4   1000022   211   -211    211     # BR(~chi_1+ → Pi+ pi+ pi- ~chi_10 )
0.00476588       3   1000022   321    111             # BR(~chi_1+ → K+ pi0 ~chi_10 )
0.00226211       4   1000022   311    211    111     # BR(~chi_1+ → k0 pi+ pi0 ~chi_10 )
0.00191119       4   1000022   321    211   -211     # BR(~chi_1+ → K+ pi+ pi- ~chi_10 )
0.00110102       4   1000022   211    111     22     # BR(~chi_1+ → k0 pi+ pi0 ~chi_10 )
0.0010642        3   1000022   321   -311             # BR(~chi_1+ → K+ kbar0 ~chi_10 )
0.000528265      4   1000022   221    211    111     # BR(~chi_1+ → eta pi+ pi0 ~chi_10 )
0.000386307      4   1000022   321   -311    111     # BR(~chi_1+ → K+ kbar0 pi0 ~chi_10 )
0.00037974       4   1000022   321   -321    211     # BR(~chi_1+ → K+ K- pi+ ~chi_10 )
0.000269485      4   1000022   310    211    130     # BR(~chi_1+ → K_S0 pi+ K_L0 ~chi_10 )
```

```
# BR          NDA      ID1    ID2   ID3    ID4    ID5    ID6
0.0240564        5   1000022   211    211   -211    111
                             # BR(~chi_1+ → pi+ pi+ pi- pi0 ~chi_10 )

0.00519408       5   1000022   211    111    111    111
                             # BR(~chi_1+ → pi+ pi0 pi0 pi0 ~chi_10 )

0.000337135      6   1000022   211    111    111    111    111
                             # BR(~chi_1+ → pi+ pi0 pi0 pi0 pi0 ~chi_10 )

0.00027021       6   1000022   211    211    211   -211   -211
                             # BR(~chi_1+ → pi+ pi+ pi+ pi- pi- ~chi_10 )

0.00120662       6   1000022   211    211   -211    111    111
                             # BR(~chi_1+ → pi+ pi+ pi- pi0 pi0 ~chi_10 )
```

# BR	NDA	ID1	ID2			
DECAY	1000023			9.9995582E-11		# neutralino2 decays
# BR	NDA	ID1	ID2			
0.236011	2	1000022	22			# BR($\sim$chi_20 $\to$ $\sim$chi_10 gamma)

# BR	NDA	ID1	ID2	ID3	ID4	
0.162566	3	1000022	1	-1		# BR($\sim$chi_20 $\to$ $\sim$chi_10 d dbar)
0.160917	3	1000022	3	-3		# BR($\sim$chi_20 $\to$ $\sim$chi_10 s sbar)
0.12607	3	1000022	2	-2		# BR($\sim$chi_20 $\to$ $\sim$chi_10 u ubar)
0.0733764	3	1000022	12	-12		# BR($\sim$chi_20 $\to$ $\sim$chi_10 nu_e nuebar)
0.0733764	3	1000022	14	-14		# BR($\sim$chi_20 $\to$ $\sim$chi_10 nu_mu numubar)
0.0733764	3	1000022	16	-16		# BR($\sim$chi_20 $\to$ $\sim$chi_10 nu_tau nutaubar)
0.0368783	3	1000022	11	-11		# BR($\sim$chi_20 $\to$ $\sim$chi_10 e- e+)
0.0365894	3	1000022	13	-13		# BR($\sim$chi_20 $\to$ $\sim$chi_10 mu- mu+)
0.00339368	2	-1000024	211			# BR($\sim$chi_20 $\to$ $\sim$chi_1- pi+)
0.00339368	2	1000024	-211			# BR($\sim$chi_20 $\to$ $\sim$chi_1+ pi-)
0.00308268	3	-1000024	211	111		# BR($\sim$chi_20 $\to$ $\sim$chi_1- pi+ pi0)
0.0030244	3	1000024	-211	111		# BR($\sim$chi_20 $\to$ $\sim$chi_1+ pi- pi0)
0.00171972	3	1000024	-12	11		# BR($\sim$chi_20 $\to$ $\sim$chi_1+ nu_ebar e-)
0.00172496	3	-1000024	12	-11		# BR($\sim$chi_20 $\to$ $\sim$chi_1- nu_e e+)
0.00163516	3	-1000024	14	-13		# BR($\sim$chi_20 $\to$ $\sim$chi_1- nu_mu mu+)
0.00165659	3	1000024	-14	13		# BR($\sim$chi_20 $\to$ $\sim$chi_1+ nu_mubar mu-)
0.000224553	2	-1000024	321			# BR($\sim$chi_20 $\to$ $\sim$chi_1- K+)
0.000224553	2	1000024	-321			# BR($\sim$chi_20 $\to$ $\sim$chi_1+ K-)
0.000134472	4	1000024	-211	111	111	# BR($\sim$chi_20 $\to$ $\sim$chi_1+ pi- pi0 pi0)
0.000130201	4	-1000024	211	211	-211	# BR($\sim$chi_20 $\to$ $\sim$chi_1- pi+ pi+ pi-)
0.000130026	4	-1000024	211	111	111	# BR($\sim$chi_20 $\to$ $\sim$chi_1- pi+ pi0 pi0)
0.00012728	4	1000024	211	-211	-211	# BR($\sim$chi_20 $\to$ $\sim$chi_1+ pi+ pi- pi-)
7.24262e-05	3	-1000024	311	211		# BR($\sim$chi_20 $\to$ $\sim$chi_1- k0 pi+)
7.07683e-05	3	1000024	-311	-211		# BR($\sim$chi_20 $\to$ $\sim$chi_1+ k0bar pi-)
3.54953e-05	3	-1000024	321	111		# BR($\sim$chi_20 $\to$ $\sim$chi_1- K+ pi0)
3.55376e-05	3	1000024	-321	111		# BR($\sim$chi_20 $\to$ $\sim$chi_1+ K- pi0)

# BR	NDA	ID1	ID2	ID3	ID4	ID5
1.02295e-05	5	-1000024	211	211	-211	111
						# BR($\sim$chi_20 $\to$ $\sim$chi_1- pi+ pi+ pi- pi0)
9.84374e-06	5	1000024	211	-211	-211	111
						# BR($\sim$chi_20 $\to$ $\sim$chi_1+ pi+ pi- pi- pi0)
2.07547e-06	5	-1000024	211	111	111	111
						# BR($\sim$chi_20 $\to$ $\sim$chi_1- pi+ pi0 pi0 pi0)
2.02297e-06	5	1000024	-211	111	111	111
						# BR($\sim$chi_20 $\to$ $\sim$chi_1+ pi- pi0 pi0 pi0)

B.2 dM770 Scenario

Block MODSEL		# Select model
1	0	# gutscGMSB
Block SMINPUTS		# Standard Model inputs
1	1.279250000000000e+02	# alpha_em$^{(-1)}$(MZ) SM MSbar
2	1.166367000000000e-05	# G_Fermi
3	1.176000000000000e-01	# alpha_s(MZ)MSbar
4	9.118760000000000e+01	# MZ(pole)
5	4.200000000000000e+00	# mb(mb)
6	1.733000000000000e+02	# Mtop(pole)
7	1.776990000000000e+00	# Mtau(pole)
Block MINPAR		# SUSY breaking input parameters
3	4.766000000000000e+01	# tanb
1	2.500000000000000e+02	# M_soft
4	4.600000000000000e+01	# n1
5	4.600000000000000e+01	# n2
6	2.000000000000000e+01	# n3
Block MASS		# Mass spectrum
# PDG code	mass	particle
24	8.038852268424102e+01	# MW
25	1.269973759244983e+02	# h0
35	4.041078362985608e+03	# H0
36	4.049990617878873e+03	# A0
37	4.051034966388102e+03	# H+
1000021	9.908105002350812e+03	# ~g
1000022	1.665921908565798e+02	# ~neutralino(1)
1000023	-1.676313411594621e+02	# ~neutralino(2)
1000024	1.673635026917621e+02	# ~chargino(1)
1000025	5.299320106026587e+03	# ~neutralino(3)
1000035	9.514961078578568e+03	# ~neutralino(4)
1000037	9.515096108917543e+03	# ~chargino(2)
1000001	1.108065458846898e+04	# ~d_L
1000002	1.108052526871690e+04	# ~u_L
1000003	1.108035136066556e+04	# ~s_L
1000004	1.108022203313569e+04	# ~c_L
1000005	6.903260181093013e+03	# ~b_1
1000006	6.253214828750123e+03	# ~t_1
1000011	7.730101856559096e+03	# ~e_L
1000012	7.729380057786821e+03	# ~nue_L
1000013	7.728453972181693e+03	# ~mu_L
1000014	7.728042125868656e+03	# ~numu_L
1000015	2.873479532294004e+03	# ~stau_1
1000016	7.302883929166065e+03	# ~nu_tau_L

2000001	8.485631648070146e+03	# ~d_R
2000002	8.870610772687267e+03	# ~u_R
2000003	8.484839214661504e+03	# ~s_R
2000004	8.870573103343546e+03	# ~c_R
2000005	9.565863347803010e+03	# ~b_2
2000006	9.568332238927018e+03	# ~t_2
2000011	4.597193231805299e+03	# ~e_R
2000013	4.592606182305874e+03	# ~mu_R
2000015	7.303631661311701e+03	# ~stau_2

Higgs mixing
Block alpha   # Effective Higgs mixing parameter
-2.143076683602239e-02   # alpha
Block nmix   # neutralino mixing matrix

1 1	6.304208740837269e-03	# N_{1,1}
1 2	-6.005384788587952e-03	# N_{1,2}
1 3	7.081899368527649e-01	# N_{1,3}
1 4	-7.059682752405876e-01	# N_{1,4}
2 1	-5.689386079410201e-03	# N_{2,1}
2 2	5.581054925020143e-03	# N_{2,2}
2 3	7.060217525683175e-01	# N_{2,3}
2 4	7.081453012004844e-01	# N_{2,4}
3 1	9.999639210465828e-01	# N_{3,1}
3 2	2.804308795643170e-04	# N_{3,2}
3 3	-4.476970805159438e-04	# N_{3,3}
3 4	8.478061747216501e-03	# N_{3,4}
4 1	-2.108158796102425e-04	# N_{4,1}
4 2	9.999663537029567e-01	# N_{4,2}
4 3	3.127429655926822e-04	# N_{4,3}
4 4	-8.194462185871922e-03	# N_{4,4}

Block Umix   # chargino U mixing matrix

1 1	-5.021739964176188e-04	# U_{1,1}
1 2	9.999998739106307e-01	# U_{1,2}
2 1	-9.999998739106307e-01	# U_{2,1}
2 2	-5.021739964176188e-04	# U_{2,2}

Block Vmix   # chargino V mixing matrix

1 1	-1.140884328045350e-02	# V_{1,1}
1 2	9.999349170296045e-01	# V_{1,2}
2 1	-9.999349170296045e-01	# V_{2,1}
2 2	-1.140884328045350e-02	# V_{2,2}

Block stopmix   # stop mixing matrix

1 1	2.335775832661234e-02	# F_{11}
1 2	9.997271703449675e-01	# F_{12}
2 1	9.997271703449675e-01	# F_{21}
2 2	-2.335775832661234e-02	# F_{22}

Block sbotmix		# sbottom mixing matrix
1 1	9.115412743554137e-04	# F_{11}
1 2	9.999995845461662e-01	# F_{12}
2 1	9.999995845461662e-01	# F_{21}
2 2	-9.115412743554137e-04	# F_{22}
Block staumix		# stau mixing matrix
1 1	4.545516916546355e-04	# F_{11}
1 2	9.999998966913745e-01	# F_{12}
2 1	9.999998966913745e-01	# F_{21}
2 2	-4.545516916546355e-04	# F_{22}
Block gauge	Q= 7.574994022369382e+03	
1	3.674553025082697e-01	# g'(Q)MSSM DRbar
2	6.328310427221140e-01	# g(Q)MSSM DRbar
3	9.624449400932055e-01	# g3(Q)MSSM DRbar
Block yu	Q= 7.574994022369382e+03	
3 3	7.895723672110101e-01	# Yt(Q)MSSM DRbar
Block yd	Q= 7.574994022369382e+03	
3 3	6.101792334320755e-01	# Yb(Q)MSSM DRbar
Block ye	Q= 7.574994022369382e+03	
3 3	4.832005286858336e-01	# Ytau(Q)MSSM DRbar
Block hmix	Q= 7.574994022369382e+03	# Higgs mixing parameters
1	1.599994307568483e+02	# mu(Q)MSSM DRbar
2	4.692822443859787e+01	# tan beta(Q)MSSM DRbar
3	2.425904614723263e+02	# higgs vev(Q)MSSM DRbar
4	1.694683172509626e+07	# mA^2(Q)MSSM DRbar
Block msoft	Q= 7.574994022369382e+03	# MSSM DRbar SUSY breaking parameters
1	5.367941591972743e+03	# M_1(Q)
2	9.465616145256212e+03	# M_2(Q)
3	9.572634373448629e+03	# M_3(Q)
21	1.707571275129889e+07	# mH1^2(Q)
22	6.887501685078413e+05	# mH2^2(Q)
31	7.667712223543844e+03	# meL(Q)
32	7.666369935343277e+03	# mmuL(Q)
33	7.262581015135343e+03	# mtauL(Q)
34	4.556312871234635e+03	# meR(Q)
35	4.551693400604479e+03	# mmuR(Q)
36	2.885091662687066e+03	# mtauR(Q)
41	1.084083216836577e+04	# mqL1(Q)
42	1.084051903479280e+04	# mqL2(Q)
43	9.398978903575768e+03	# mqL3(Q)
44	8.625471665510639e+03	# muR(Q)
45	8.625433428368329e+03	# mcR(Q)
46	6.103223754640188e+03	# mtR(Q)
47	8.232308141643025e+03	# mdR(Q)
48	8.231504722344704e+03	# msR(Q)
49	6.706418145394591e+03	# mbR(Q)

```
Block au    Q= 7.574994022369382e+03
    1 1          -1.151741337127809e+04      # Au(Q)MSSM DRbar
    2 2          -1.15173044583208e+04       # Ac(Q)MSSM DRbar
    3 3          -8.677153777444082e+03      # At(Q)MSSM DRbar
Block ad    Q= 7.574994022369382e+03
    1 1          -1.198191693705103e+04      # Ad(Q)MSSM DRbar
    2 2          -1.198115911343399e+04      # As(Q)MSSM DRbar
    3 3          -9.797045832528309e+03      # Ab(Q)MSSM DRbar
Block ae    Q= 7.574994022369382e+03
    1 1          -4.622508841021669e+03      # Ae(Q)MSSM DRbar
    2 2          -4.620259839460072e+03      # Amu(Q)MSSM DRbar
    3 3          -3.94174132793781e+03       # Atau(Q)MSSM DRbar
```

```
# PDG             Width
DECAY          1000024        2.64052E-13      # chargino1+ decays
# BR      NDA       ID1    ID2    ID3   ID4
0.604464        2   1000022    211                  # BR(~chi_1+ → pi+ ~chi_10 )
0.149744        3   1000022    -11     12           # BR(~chi_1+ → e+ nu_e ~chi_10 )
0.137396        3   1000022    -13     14           # BR(~chi_1+ → mu+ nu_mu ~chi_10 )
0.0727573       3   1000022    211    111           # BR(~chi_1+ → pi+ pi0 ~chi_10 )
0.0346195       2   1000022    321                  # BR(~chi_1+ → K+ ~chi_10 )
0.000296946     4   1000022    211    111   111     # BR(~chi_1+ → pi+ pi0 pi0 ~chi_10 )
0.00029652      3   1000022    311    211           # BR(~chi_1+ → k0 pi+ ~chi_10 )
0.000267824     4   1000022    211   -211   211     # BR(~chi_1+ → Pi+ pi+ pi- ~chi_10 )
0.000158295     3   1000022    321    111           # BR(~chi_1+ → K+ pi0 ~chi_10 )
```

```
# PDG             Width
DECAY          1000023        6.9578013E-13    # neutralino2 decays
# BR      NDA       ID1    ID2
0.740221        2   1000022    22                   # BR(~chi_20 → ~chi_10 gam)
# BR      NDA       ID1    ID2    ID3   ID4
0.0714966       3   1000022     1     -1            # BR(~chi_20 → ~chi_10 d dbar )
0.0554493       3   1000022    -2      2            # BR(~chi_20 → ~chi_10 ubar u )
0.0322734       3   1000022    12    -12            # BR(~chi_20 → ~chi_10 nu_e nuebar )
0.0322734       3   1000022    14    -14            # BR(~chi_20 → ~chi_10 nu_mu numubar )
0.0322734       3   1000022    16    -16            # BR(~chi_20 → ~chi_10 nu_tau nutaubar )
0.0162203       3   1000022    11    -11            # BR(~chi_20 → ~chi_10 e- e+ )
0.0153303       3   1000022    13    -13            # BR(~chi_20 → ~chi_10 mu- mu+ )
0.00212304      2  -1000024    211                  # BR(~chi_20 → ~chi_1- pi+ )
0.00212304      2   1000024   -211                  # BR(~chi_20 → ~chi_1+ pi- )
7.39365e-05     3   1000024    -12     11           # BR(~chi_20 → ~chi_1+ nu_ebar e- )
7.3071e-05      3  -1000024     12    -11           # BR(~chi_20 → ~chi_1- nu_e e+ )
3.45984e-05     3  -1000024     14    -13           # BR(~chi_20 → ~chi_1- nu_mu mu+ )
3.44846e-05     3   1000024    -14     13           # BR(~chi_20 → ~chi_1+ nu_mubar mu- )
```

Appendix C

Data Samples

The samples used in the analysis are given in the following for both signal and background samples. The polarisation of the beam electron and positron is denoted with P_{e+} and P_{e-}. The production cross sections and the generated number of events with the corresponding integrated luminosity are indicated in Tables for $\sqrt{s} = 500\,\text{GeV}$ centre-of-mass energy. Number of events shows the values before any weighting.

C.1 Signal Samples

Signal					
Process	P_{e+}	P_{e-}	N_{events}	σ [fb]	$\int \mathcal{L}dt$ [fb^{-1}]
dM1600 scenario					
$e^+e^- \to \widetilde{\chi}_1^+ \widetilde{\chi}_1^-$	+1.0	−1.0	54637	132.97	500
$e^+e^- \to \widetilde{\chi}_1^+ \widetilde{\chi}_1^-$	−1.0	+1.0	10988	26.83	500
$e^+e^- \to \widetilde{\chi}_1^0 \widetilde{\chi}_2^0$	+1.0	−1.0	39970	80.11	500
$e^+e^- \to \widetilde{\chi}_1^0 \widetilde{\chi}_2^0$	−1.0	+1.0	30765	61.66	500
dM770 scenario					
$e^+e^- \to \widetilde{\chi}_1^+ \widetilde{\chi}_1^-$	+1.0	−1.0	64989	130.05	500
$e^+e^- \to \widetilde{\chi}_1^+ \widetilde{\chi}_1^-$	−1.0	+1.0	13134	26.28	500
$e^+e^- \to \widetilde{\chi}_1^0 \widetilde{\chi}_2^0$	+1.0	−1.0	39424	79.16	500
$e^+e^- \to \widetilde{\chi}_1^0 \widetilde{\chi}_2^0$	−1.0	+1.0	30334	60.92	500

Table C.1 Signal samples with fully polarised beams at $\sqrt{s} = 500\,\text{GeV}$ for both dM1600 and dM770 scenarios.

C.2   e⁺e⁻ Class

SM Background : $e^+e^- \to 2f$ Class

Process	P_{e^+}	P_{e^-}	N_{events}	σ [fb]	$\int \mathcal{L}dt$ [fb^{-1}]
$e^+e^- \to 2f - Z - bhabhag$	−1.0	−1.0	28139	2962	9.5
$e^+e^- \to 2f - Z - bhabhag$	+1.0	+1.0	28091	2957	9.5
$e^+e^- \to 2f - Z - bhabhag$	−1.0	+1.0	52268	3372	15.5
$e^+e^- \to 2f - Z - bhabhag$	+1.0	−1.0	56500	3645	15.5
$e^+e^- \to 2f - Z - h$	+1.0	−1.0	503294	32470	15.5
$e^+e^- \to 2f - Z - h$	−1.0	+1.0	278918	17995	15.5
$e^+e^- \to 2f - Z - l$	+1.0	−1.0	85988	5548	15.5
$e^+e^- \to 2f - Z - l$	−1.0	+1.0	67345	4345	15.5

Table C.2 $e^+e^- \to 2f$ class of the Standard Model background for fully polarised beams at $\sqrt{s} = 500$ GeV. "Z" in the process name refers to the same flavour fermion pairs in the final state (Z-like). $2f - Z - bhabhag$ subclass shows the events including Radiative Bhabha events in the final state, while $2f - Z - h$ and $2f - Z - l$ subclasses indicate the events with the hadronic and leptonic final states.

SM Background : $e^+e^- \to 4f$ Class

Process	P_{e^+}	P_{e^-}	N_{events}	σ [fb]	$\int \mathcal{L}dt$ [fb^{-1}]
hadronic					
$e^+e^- \to 4f - WW - had$	+1.0	−1.0	119052	7680.7	15.5
	−1.0	+1.0	520	33.5	15.5
$e^+e^- \to 4f - ZZ - had$	+1.0	−1.0	10544	680.2	15.5
	−1.0	+1.0	4214	271.9	15.5
$e^+e^- \to 4f - ZZorWW - had$	+1.0	−1.0	99202	6400.1	15.5
	−1.0	+1.0	1220	78.7	15.5

Table C.3 $e^+e^- \to 4f$ class of the Standard Model background including hadronic final states for fully polarised beams at $\sqrt{s} = 500$ GeV. WW like events contains any combination of $l\nu_l$ type particles and different flavour quarks, while ZZ like (two same flavour particles), WW like (any combination of $l\nu_l$ type particles and different flavour quarks)

Process	P_{e^+}	P_{e^-}	N_{events}	σ [fb]	$\int \mathcal{L}dt$ [fb^{-1}]
leptonic					
$e^+e^- \to 4f - singleW - lep$	+1.0	−1.0	40390	2605.8	15.5
	−1.0	+1.0	130	8.4	16.2
	+1.0	+1.0	2394	252.0	9.5
	−1.0	−1.0	2395	252.1	9.5
$e^+e^- \to 4f - singleZee - lep$	+1.0	−1.0	112496	7257.7	15.5
	−1.0	+1.0	110170	7107.7	15.5
	+1.0	+1.0	66358	6985.0	9.5
	−1.0	−1.0	66415	6991.0	9.5
$e^+e^- \to f - sinZorsinW - lep$	+1.0	−1.0	15669	1011	15.5
	−1.0	+1.0	443	28.6	15.5
	−1.0	−1.0	1489	156.7	9.5
	+1.0	+1.0	1490	156.8	9.5
$e^+e^- \to 4f - singleZ\nu\nu - lep$	+1.0	−1.0	4321	278.8	15.5
	−1.0	+1.0	230	14.8	15.5
$e^+e^- \to 4f - WW - lep$	+1.0	−1.0	12256	790.7	15.5
	−1.0	+1.0	65	4.2	15.5
$e^+e^- \to 4f - ZZ - lep$	+1.0	−1.0	930	60.0	15.5
	−1.0	+1.0	571	36.8	15.5
$e^+e^- \to 4f - ZZorWW - lep$	+1.0	−1.0	12707	819.8	15.5
	−1.0	+1.0	295	19.0	15.5

Table C.4 $e^+e^- \to 4f$ class of the Standard Model background including leptonic final states for fully polarised beams at $\sqrt{s} = 500\,\text{GeV}$. If the final state contains the same flavour leptons as the initial state, they are called single W ($e\bar{\nu}_e + l\bar{\nu}_l/q\bar{q}'$) or single Z ($e^+e^-/\nu_e\bar{\nu} - e + e\bar{e}/l\bar{l}/\nu\bar{\nu}/q\bar{q}'$, $\nu_e\bar{\nu}_e + l\bar{l}/q\bar{q}'$) like events, or mixed single Z and single W like events with a final state of $e\bar{e}\nu\bar{\nu}$.

Process	P_{e^+}	P_{e^-}	N_{events}	σ [fb]	$\int \mathcal{L}dt$ [fb^{-1}]
semi-leptonic					
$e^+e^- \to 4f - singleW - semi\_lep$	$+1.0$	-1.0	120986	7805.5	15.5
	-1.0	$+1.0$	354	22.8	15.5
	$+1.0$	$+1.0$	7126	750.1	9.5
	-1.0	-1.0	7154	753.1	9.5
$e^+e^- \to 4f - singleZee - semi\_lep$	$+1.0$	-1.0	30398	1961.1	15.5
	-1.0	$+1.0$	26762	1726.6	15.5
	$+1.0$	$+1.0$	16891	1778.0	9.5
	-1.0	-1.0	16867	1775.5	9.5
$e^+e^- \to 4f - singleZ\nu\nu - semi\_lep$	$+1.0$	-1.0	14752	951.7	15.5
	-1.0	$+1.0$	914	59.0	15.5
$e^+e^- \to 4f - WW - semi\_lep$	$+1.0$	-1.0	147582	9521.4	15.5
	-1.0	$+1.0$	706	45.6	15.5
$e^+e^- \to 4f - ZZ - semi\_lep$	$+1.0$	-1.0	9433	608.6	15.5
	-1.0	$+1.0$	4470	288.4	15.5

Table C.5 $e^+e^- \to 4f$ class of the Standard Model background including semi-leptonic final states for fully polarised beams at $\sqrt{s} = 500\,\text{GeV}$.

SM Background : $e^+e^- \to 6f$ Class

Process	P_{e^+}	P_{e^-}	N_{events}	σ [fb]	$\int \mathcal{L}dt$ [fb^{-1}]
$e^+e^- \to 6f - had$	$+1.0$	-1.0	147316	946.0	156
$e^+e^- \to 6f - had$	-1.0	$+1.0$	57628	367	157
$e^+e^- \to 6f - semi\_lep$	-1.0	$+1.0$	51855	331	157
$e^+e^- \to 6f - semi\_lep$	$+1.0$	-1.0	135800	873	156

Table C.6 $e^+e^- \to 6f$ class arising from $e^+e^- \to t\bar{t}$ events of the Standard Model background for fully polarised beams at $\sqrt{s} = 500\,\text{GeV}$. The events are classified whether they contain final state with fully hadrons, or semi leptons.

Process	P_{e^+}	P_{e^-}	N_{events}	σ [fb]	$\int \mathcal{L}dt$ [fb^{-1}]
$e^+e^- \to 6f - lep$	-1.0	$+1.0$	113	0.08	1412
$e^+e^- \to 6f - lep$	$+1.0$	-1.0	5	0.03	167
$e^+e^- \to 6f - lep$	-1.0	-1.0	23	0.02	1150
$e^+e^- \to 6f - lep$	$+1.0$	$+1.0$	83	0.06	1383
$e^+e^- \to 6f - semi\_lep$	$+1.0$	$+1.0$	261	7.6	34
$e^+e^- \to 6f - semi\_lep$	-1.0	$+1.0$	322	1.2	268
$e^+e^- \to 6f - semi\_lep$	$+1.0$	-1.0	1375	6.4	215
$e^+e^- \to 6f - semi\_lep$	-1.0	-1.0	51	0.09	567

Table C.7 The remaining $e^+e^- \to 6f$ class of the Standard Model background for fully polarised beams at $\sqrt{s} = 500\,\text{GeV}$. The classification are done depending on the final state particles.

C.3 $\gamma\gamma$ Class

<div align="center">SM Background : $\gamma\gamma \to 2f$ Class</div>

Process	P_{e^+}	P_{e^-}	N_{events}	σ [fb]	$\int \mathcal{L}dt$ [fb^{-1}]
$\gamma\gamma \to 2f - yy$	B	W	4347749	8730.0	498
	W	B	4307563	8740.0	493
	B	B	5263671	27173.8	194
	W	W	1546650	3093.0	500
$\gamma\gamma \to 2f - ll$	B	W	16966164	242784.1	70
	W	B	16968593	242537.5	70
	B	B	16968643	831955.5	20
	W	W	3085280	86485.8	36

Table C.8 $\gamma\gamma \to 2f$ class of the Standard Model background for fully polarised beams at $\sqrt{s} = 500\,\text{GeV}$. B and W indicate if the photon is real which comes from the photon component of the beam, or if it is virtual which is radiated from the incoming leptons. The events including yy final states are weighted in order to take into account the events with xx final state. $\gamma\gamma \to ll$ events are reconstructed after including the tracking efficiency implementation of the full simulation for small momentum region.

<div align="center">SM Background : $\gamma\gamma \to 4f$ Class</div>

| Process	P_{e^+}	P_{e^-}	N_{events}	σ [fb]	$\int \mathcal{L}dt$ [fb^{-1}]
$\gamma\gamma \to 4f - lep(ch\ l)$	0	0	6075	56.0	108
$\gamma\gamma \to 4f - lep(ch\&neu\ l)$	0	0	1347	21.0	64
$\gamma\gamma \to 4f - semi\_lep(ch\ l)$	0	0	2955	22.0	134
$\gamma\gamma \to 4f - semi\_lep(neu\ l)$	0	0	62	0.2	248
$\gamma\gamma \to 4f - semi\_lep(ch\&neu\ l)$	0	0	5313	48.1	110

Table C.9 $\gamma\gamma \to 4f$ class of the Standard Model background for fully polarised beams at $\sqrt{s} = 500\,\text{GeV}$. Both real and virtual photon case are included. The events are classified whether they contain final state with fully hadrons, or semi leptons. The events are classified whether they contain final state with fully charged leptons, both charged and neutral leptons, or semi leptons either with charged leptons or neutral leptons.

C.4 e$^{\pm}\gamma$ Class

SM Background : $e^{\pm}\gamma \to 3f$ Class

| Process	P_{e^+}	P_{e^-}	N_{events}	σ [fb]	$\int \mathcal{L}dt$ [fb^{-1}]
$e^+\gamma \to 3f - lep(ch\ l)$	−1.0	0	4926288	98524	50
$e^+\gamma \to 3f - lep(ch\ l)$	+1.0	0	4946150	98901	50
$e^+\gamma \to 3f - lep(ch\&neu\ l)$	−1.0	0	17159	509	34
$e^+\gamma \to 3f - lep(ch\&neu\ l)$	+1.0	0	165046	3299	50
$e^+\gamma \to 3f - semi\_lep(ch\ l)$	−1.0	0	1358101	27159	50
$e^+\gamma \to 3f - semi\_lep(ch\ l)$	+1.0	0	1424001	28477	50
$e^+\gamma \to 3f - semi\_lep(neu\ l)$	+1.0	0	247711	4954	50

Table C.10 $e^+\gamma \to 3f$ class of the Standard Model background for fully polarised beams at $\sqrt{s} = 500$ GeV. Both real and virtual photon case are included. The events are classified whether they contain final state with fully charged leptons, fully neutral leptons, both charged and neutral leptons, or semi leptons either with charged leptons or neutral leptons.

Process	P_{e^+}	P_{e^-}	N_{events}	σ [fb]	$\int \mathcal{L}dt$ [fb^{-1}]
$\gamma e^- \to 3f - lep(ch\ l)$	0	−1.0	4922698	98808.83	50
$\gamma e^- \to 3f - lep(ch\ l)$	0	+1.0	4940568	98451.04	50
$\gamma e^- \to 3f - lep(ch\&neu\ l)$	0	−1.0	164925	3297.0	50
$\gamma e^- \to 3f - lep(ch\&neu\ l)$	0	+1.0	17137	508.0	34
$\gamma e^- \to 3f - semi\_lep(ch\ l)$	0	−1.0	1422823	28178.9	50
$\gamma e^- \to 3f - semi\_lep(ch\ l)$	0	+1.0	1356532	27129	50
$\gamma e^- \to 3f - semi\_lep(neu\ l)$	0	−1.0	247617	4952.0	50

Table C.11 $\gamma e^- \to 3f$ class of the Standard Model background for fully polarised beams at $\sqrt{s} = 500$ GeV. Both real and virtual photon case are included.

SM Background : $e^{\pm}\gamma \to 5f$ Class

Process	P_{e^+}	P_{e^-}	N_{events}	σ [fb]	$\int \mathcal{L}dt$ [fb^{-1}]
$e^+\gamma \to 5f - atleast1e - lep$	+1.0	0	3459	8.1	427
$e^+\gamma \to 5f - atleast1e - lep$	−1.0	0	2316	5.1	454
$e^+\gamma \to 5f - atleast1e - semi\_lep$	+1.0	0	15318	50.1	306
$e^+\gamma \to 5f - atleast1e - semi\_lep$	−1.0	0	7869	21.2	371
$e^+\gamma \to 5f - noe - lep$	+1.0	0	121	0.06	2017
$e^+\gamma \to 5f - noe - semi\_lep$	+1.0	0	1449	2.2	659

Table C.12 $e^+\gamma \to 5f$ class of the Standard Model background for fully polarised beams at $\sqrt{s} = 500\,$GeV. Both real and virtual photon case are included. For events including at least one electron in the final state, positron can have the both helicity L and R. If there is no electron in the final state then the positron can have only right handed helicity (R). Therefore events are classified according to this.

Process	P_{e^+}	P_{e^-}	N_{events}	σ [fb]	$\int \mathcal{L}dt$ [fb^{-1}]
$\gamma e^- \to 5f - atleast1e - lep$	0	−1.0	3320	8.0	415
$\gamma e^- \to 5f - atleast1e - lep$	0	+1.0	2304	5.1	452
$\gamma e^- \to 5f - atleast1e - semi\_lep$	0	−1.0	15250	52.2	292
$\gamma e^- \to 5f - atleast1e - semi\_lep$	0	+1.0	7852	21.2	370
$\gamma e^- \to 5f - noe - lep$	0	−1.0	119	0.06	1983
$\gamma e^- \to 5f - noe - semi\_lep$	0	−1.0	1433	2.2	651

Table C.13 $e^+\gamma \to 5f$ class of the Standard Model background for fully polarised beams at $\sqrt{s} = 500\,$GeV. Both real and virtual photon case are included. For events including at least one electron in the final state, electron can have the both helicity L and R. If there is no electron in the final state then the electron can have only left handed helicity (L).

Appendix D

Low Momentum Muon Pion Separation Input Variables
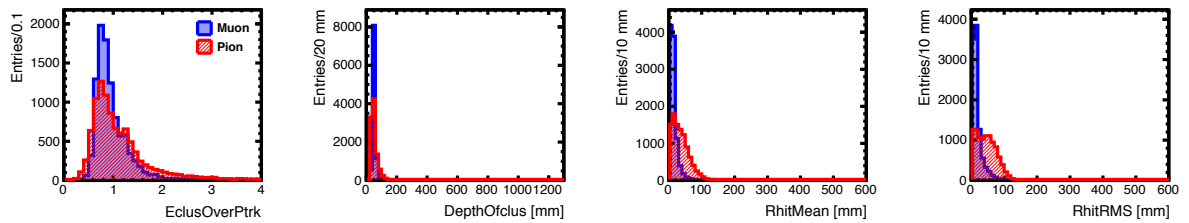
(a) 0.2 GeV P
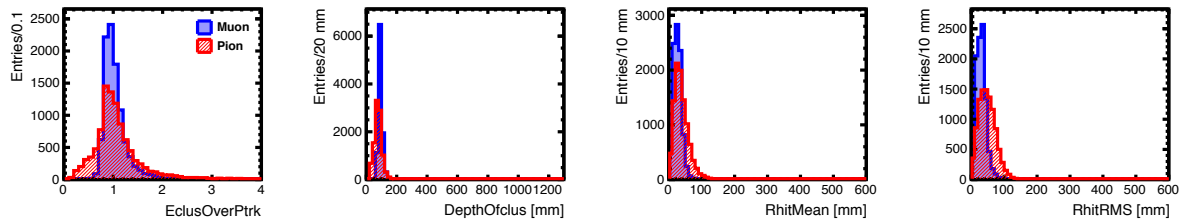
(b) 0.3 GeV P
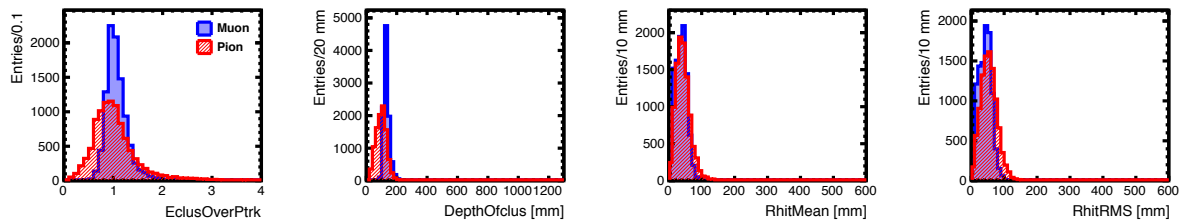
(c) 0.4 GeV P

Figure D.1 Input variables for momenta between 0.2 GeV and 0.4 GeV.
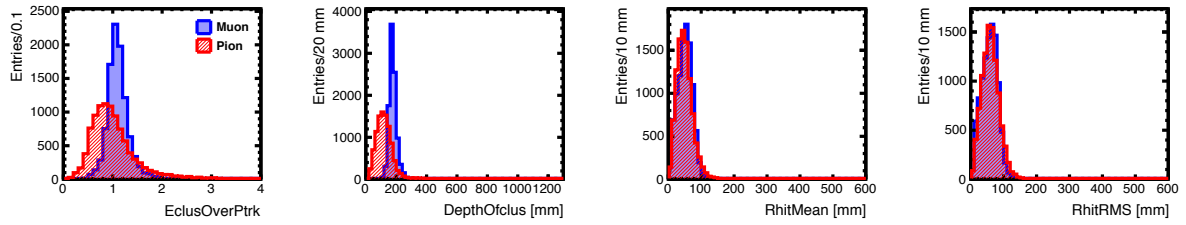
(a) 0.5 GeV P
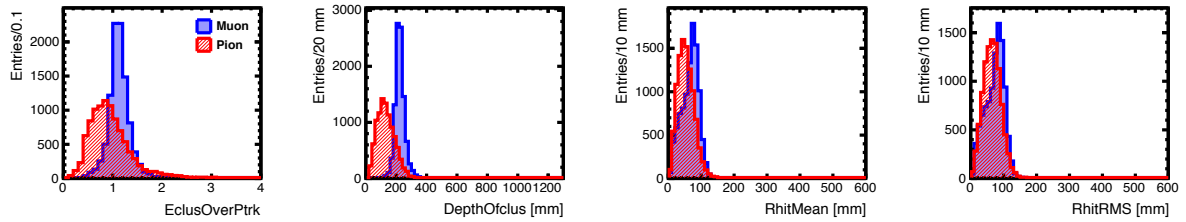
(b) 0.6 GeV P
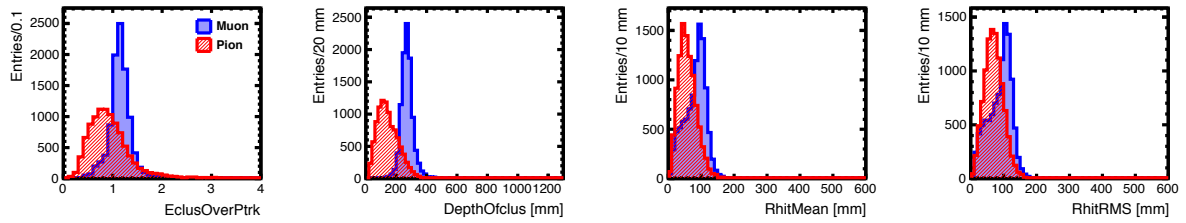
(c) 0.7 GeV P
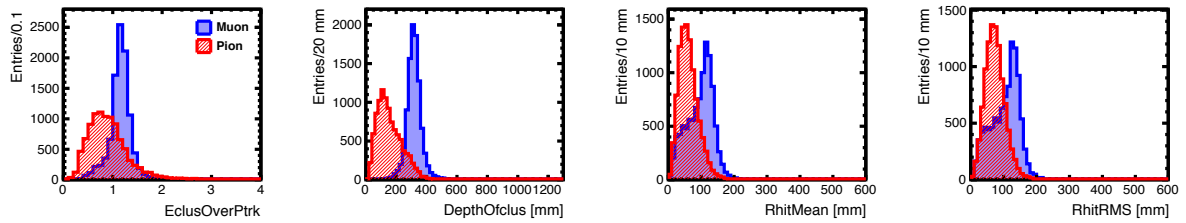
(d) 0.8 GeV P

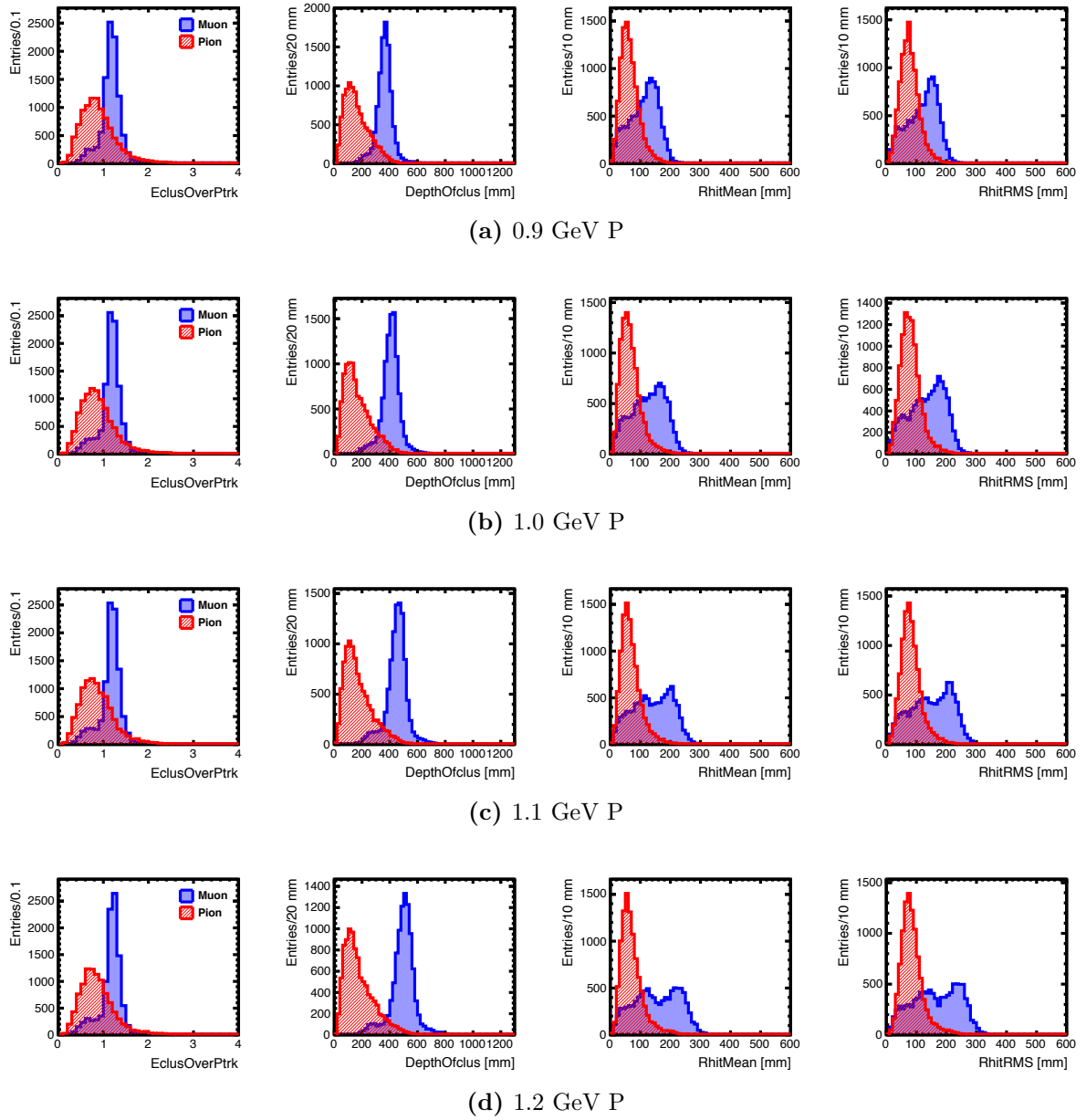**Figure D.2** Input variables for momenta between $0.5\,\mathrm{GeV}$ and $0.8\,\mathrm{GeV}$.

(a) 0.9 GeV P

(b) 1.0 GeV P

(c) 1.1 GeV P

(d) 1.2 GeV P

Figure D.3 Input variables for momenta between $0.9\,\mathrm{GeV}$ and $1.2\,\mathrm{GeV}$.

(a) 1.3 GeV P

(b) 1.4 GeV P

(c) 1.5 GeV P
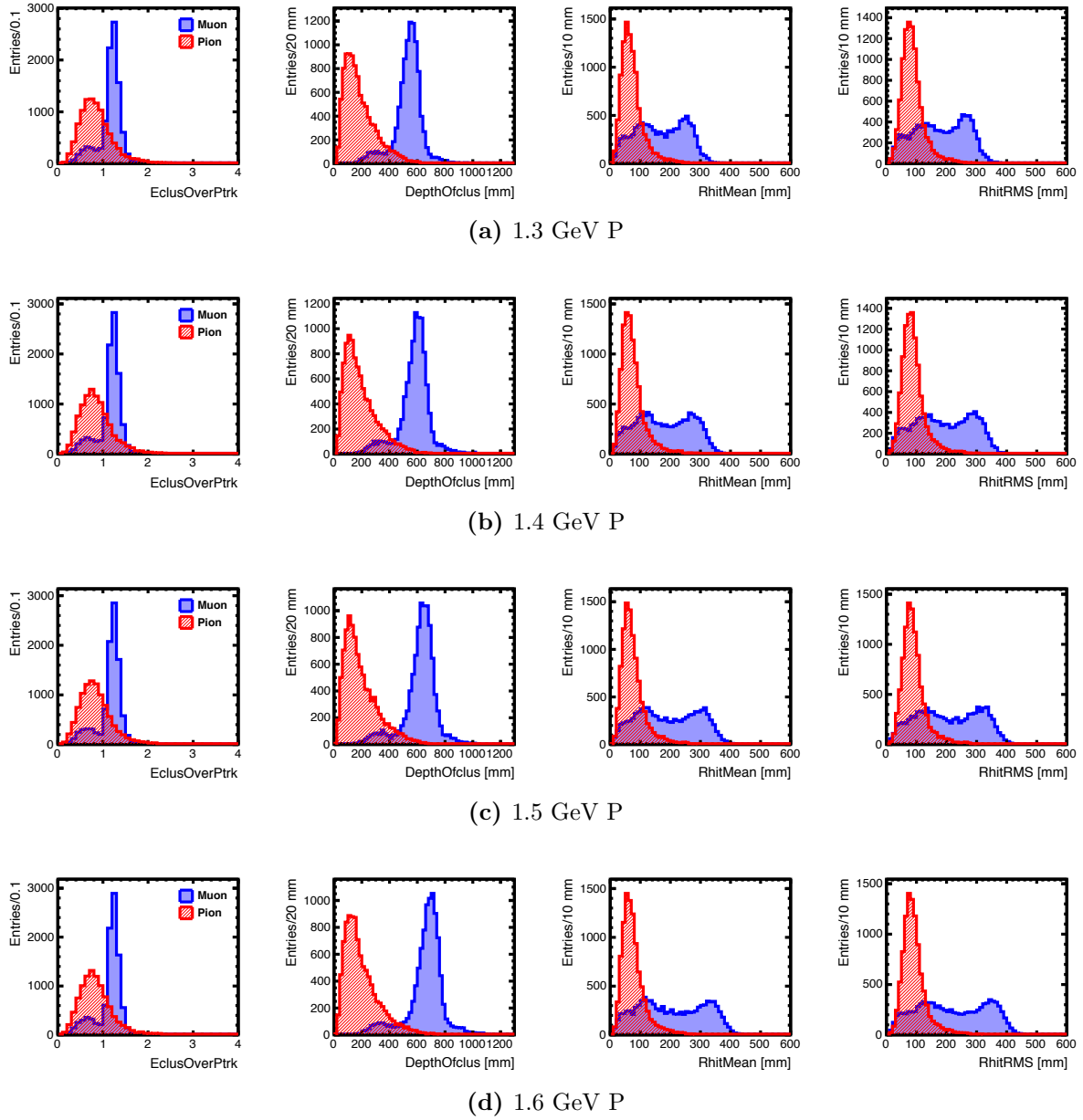
(d) 1.6 GeV P

Figure D.4 Input variables for momenta between 1.3 GeV and 1.6 GeV.

(a) 1.7 GeV P

(b) 1.8 GeV P

(c) 1.9 GeV P
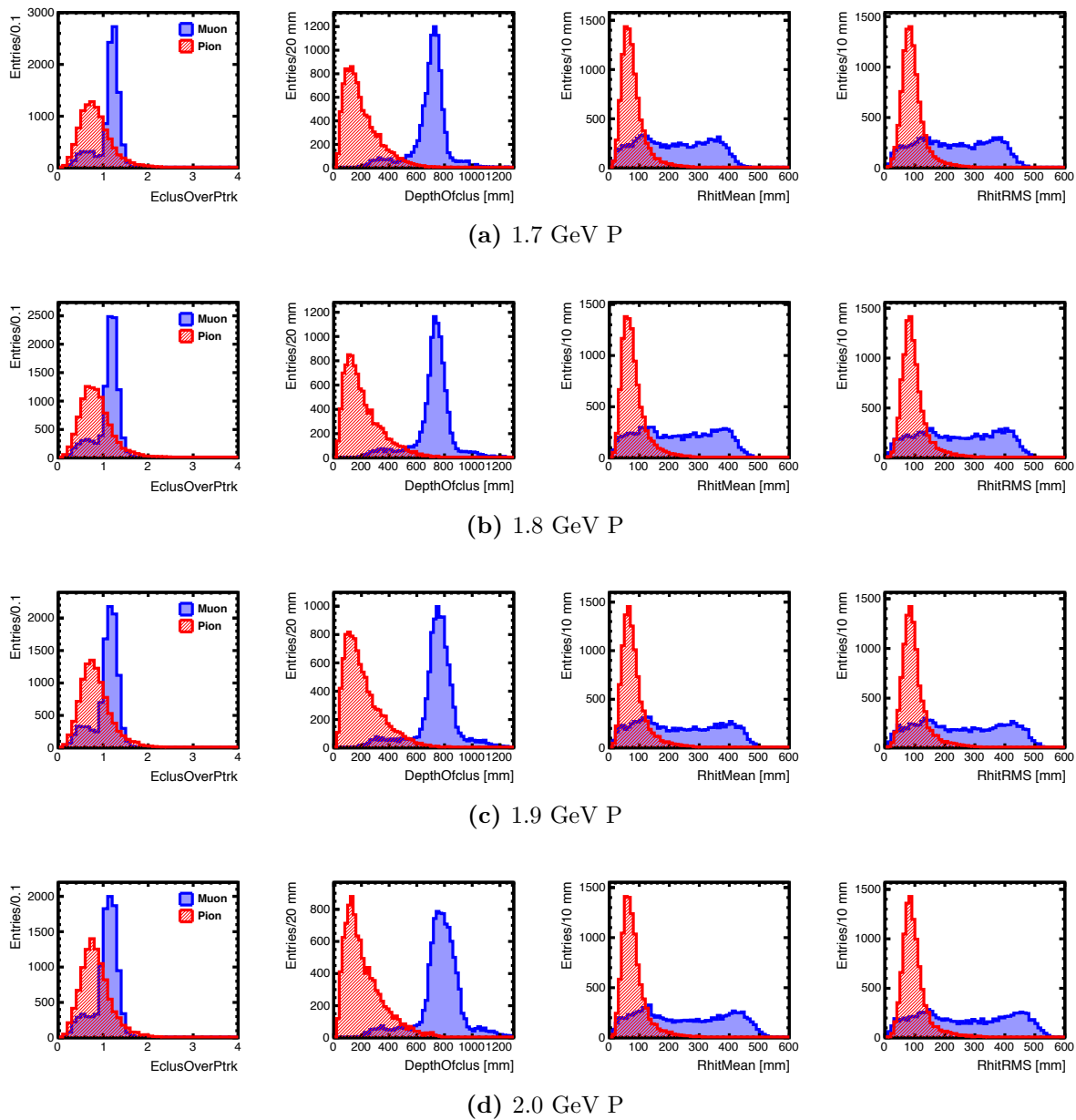
(d) 2.0 GeV P

Figure D.5 Input variables for momenta between 1.7 GeV and 2.0 GeV.

Acknowledgements

As most of PhD thesis projects, many people played an important role in the process of my PhD thesis. Therefore, I would like to send my special thanks to those people.

First of all, I am grateful to my supervisor Jenny List for providing me with such an exciting project. Working on this project was enlightening and enjoyable. I always felt her support and encouragement in each part of my project. I would like to thank her for her very informative guidance during my studies. I learned a lot under her supervision. Moreover, I want to thank her for her patience to read my thesis and her instructive suggestions.

Beside my supervisor, Mikael Berggen played an important role for further expanding my knowledge. I am thankful to him for his collaboration, time and willingness to share his knowledge with me.

Throughout my thesis, I had a chance to obtain an experience on detector development. I want to thank Astrid Münnich and especially Klaus Zenker for their supervision and guidance on detector development part of my thesis and for their proofreading of the related chapter of my thesis.

My special thanks go to Gudrid Moortgat-Pick for suggesting me this PhD position in the FLC group, as well as for being one of my mentors and one of my dissertation referees. I also would like to thank my other mentor Kerstin Tackmann for her support and for paying close attention to my studies. Moreover, I send my thanks to Ties Behnke, Peter Schleper and Dieter Horns for being members of my disputation committee.

In addition to those people whom I mentioned above, I would like to thank Ties Behnke, Karsten Büsser and Katja Krüger who took time to proofread part of my thesis. Moreover, I give my special thanks to Suvi Lehtinen who took kindly so much time to read most of my thesis. Furthermore, I want to thank Benedikt Vormwald, Dimitra Tsionou, Claude Dürig and Coralie Neubüser for their willingness to proofread some chapters of my thesis. I especially thank Moritz Habermehl and Annika Vauth for both their proofreading and translation of my abstract to German. I also would like to thank Georgios Voutsinas for his collaboration and for providing the plots related to tracking of low momentum particles.

During my time at DESY, I had a chance to work in a friendly environment in the FLC group. Thus, I want to thank the whole group for making me feel comfortable and cheerful, as well as those who took time to prepare my PhD hat. In particular, I would like to thank Annika Vauth, Claude Dürig, and my dear office mates: Benedikt Vormwald, Moritz Beckmann, Suvi Lehtinen, Moritz Habermehl and Madalina Chera for their friendship. I feel very lucky to have such kind

Eidesstattliche Versicherung

Declaration on oath

Hiermit erkläre ich an Eides statt, dass ich die vorliegende Dissertationsschrift selbst verfasst und keine anderen als die angegebenen Quellen und Hilfsmittel benutzt habe.

I hereby declare, on oath, that I have written the present dissertation by my own and have not used other than the acknowledged resources and aids.

Hale Sert
Hamburg, October 2015